

University of Nottingham
UK | CHINA | MALAYSIA

Contact line instabilities of rotating, viscous droplets

Tom W. Roper[†]

10028081

Supervisors: Matthew M. Scase[†], John Billingham[†], Barbara Turnbull[††]

School of Mathematical Sciences[†]
University of Nottingham

Faculty of Engineering[††]
University of Nottingham

Thesis submitted to The University of Nottingham for the degree of Doctor of Philosophy

August 2023

Abstract

In this thesis, we investigated the stability of the contact line of an initially axisymmetric, fixed volume of viscous fluid upon a flat rotating disc, centred on the axis of rotation. We performed an experimental analysis, concerning the onset and formation of the instabilities at the contact line. The instability at the contact line is characterised by an integer number of fingers given by the dominant wavenumber, which is found to be proportional to both the volume and rotation rate in the investigated parameter range.

To complement the experimental results, we performed a linear stability analysis within the lubrication limit of small contact angle. We determined the stability of the free surface for which the fluid is at rest within a rotating frame of reference, subject to small axisymmetric and non-axisymmetric perturbations. We found that the rotating droplet is unconditionally unstable, with the dominant wavenumber increasing with both rotational and gravitational effects when capillary effects are included. The growth rates of experimentally prevalent modes and equilibrium solutions both show good qualitative and quantitative agreement with the experimental data simultaneously.

We considered further cases where the contact angle is not small, meaning a lubrication approximation cannot be employed. Using a finite element method to solve the resulting system, we showed that under these circumstances the instability at the contact line is characterised by a rolling motion. This is found to be contrary to the form of instability under a lubrication approximation, where instability occurs via slip of the contact line radially outwards.

Contents

1 Introduction **1**

1.1 Background 1

1.2 Contact lines 3

1.2.1 Contact angles 4

1.2.2 Macroscopic slip 7

1.3 Centrifugally forced contact line instabilities 8

1.3.1 Experimental 8

1.3.2 Theoretical 12

1.4 Thesis outline 16

2 Experimental procedure and analysis **18**

2.1 Methodology 18

2.1.1 Experimental set-up 19

2.1.2 Experimental technique 22

2.2 Data analysis 23

2.2.1 Edge detection 23

2.2.2 Centre finding and polar representation 26

2.2.3 Fourier decomposition 27

2.2.4 Linear growth rate 28

2.2.5 Summary of the numerical method . . . 31
2.3 Results . . . 32
2.3.1 Qualitative observations . . . 33
2.3.2 Spin-up radius . . . 34
2.3.3 Axisymmetric spreading . . . 36
2.3.4 Non-axisymmetric spreading . . . 39
2.4 Summary . . . 43

3 Thin film model formulation and equilibrium solutions 45
3.1 Model . . . 45
3.1.1 Equations of motion . . . 45
3.1.2 Boundary conditions . . . 46
3.2 Nondimensionalisation . . . 49
3.3 Thin film equation . . . 53
3.4 Equilibrium solution . . . 55
3.4.1 Comparison to previous literature . . . 62
3.5 Summary . . . 63

4 Linear stability analysis of equilibrium solutions 64
4.1 Modelling . . . 64
4.1.1 Eigenvalue equation . . . 64
4.1.2 Velocity perturbation . . . 66
4.1.3 Boundary conditions . . . 67
4.1.3.1 Non-axisymmetric perturbations . . . 69
4.1.3.2 Axisymmetric perturbations . . . 70
4.1.3.3 Summary . . . 71

4.2 Quasi-steady limit, $C = 0$ . . . 71
4.2.1 Axisymmetric perturbations . . . 72
4.2.2 Non-axisymmetric perturbations . . . 73
4.2.3 Results . . . 74
4.3 Neutral stability . . . 77
4.4 General case, $C > 0$ . . . 79
4.4.1 Comparison to small capillary number limit . . . 85
4.5 Summary . . . 89

5 Further analysis and extensions of linear stability theory 91
5.1 Slip condition . . . 91
5.1.1 Local expansion . . . 92
5.1.2 General slip law . . . 93
5.1.3 Varying the slip length . . . 96
5.1.4 Summary . . . 96
5.2 Fixed contact angle model . . . 97
5.2.1 Model . . . 97
5.2.2 Neutral stability . . . 99
5.2.3 Results . . . 99
5.2.4 Comparison to Tanner model . . . 101
5.2.5 Summary . . . 106
5.3 Finite Ekman number . . . 107
5.3.1 Model . . . 107
5.3.2 Equilibrium solutions . . . 108
5.3.3 Linear stability . . . 109
5.3.3.1 Neutral stability . . . 111

5.3.3.2 Tanner law . . . 111
5.3.3.3 Fixed contact angle . . . 114
5.3.4 Summary . . . 114
5.4 Quasi-steady, axisymmetric spreading . . . 115
5.4.1 Model . . . 115
5.4.2 Equilibrium solutions . . . 116
5.4.3 Linear stability . . . 117
5.4.4 Comparison with numerical solution . . . 118
5.4.5 Summary . . . 120

6 O(1) Contact angle model; formulation and equilibrium solutions 121
6.1 Model . . . 122
6.2 Nondimensionalisation . . . 123
6.3 Equilibrium solutions . . . 126
6.3.1 Results . . . 128
6.3.2 Comparison to thin film solutions . . . 133
6.4 Finite element verification of equilibrium solutions . . . 137
6.4.1 Equations of motion . . . 137
6.4.2 Variational formulation . . . 138
6.4.3 Boundary conditions . . . 139
6.4.4 Solution method . . . 141
6.4.5 Results . . . 143
6.5 Summary . . . 147

7 O(1) Contact angle model; linear stability analysis 149
7.1 Linear stability formulation . . . 149

7.1.1 Equations of motion . . . 149
7.1.2 Boundary conditions . . . 151
7.1.3 Weak formulation . . . 153
7.1.4 Solution method . . . 157
7.2 Verification by comparison with thin film solutions . . . 161
7.2.1 Thin film solution . . . 161
7.2.2 Verification of implementation . . . 164
7.2.3 Comparison of eigensolutions . . . 171
7.3 Linear stability results . . . 175
7.4 Summary . . . 182

8 Comparison with experimental results and discussion 184
8.1 Equilibrium solutions . . . 184
8.1.1 Stationary solution . . . 185
8.1.2 Non-zero rotation . . . 187
8.2 Axisymmetric spreading . . . 191
8.3 Non-axisymmetric spreading . . . 191
8.3.1 Physical properties . . . 192
8.3.2 Nondimensional parameters . . . 193
8.3.3 Comparison to experimental data . . . 197
8.3.4 Contact angle varying with rotation . . . 201
8.4 Summary . . . 204

9 Conclusions and closing remarks 206
9.1 Thesis summary . . . 206
9.2 Closing remarks and future work . . . 211

Appendix A Derivation of Governing Equations **213**

Appendix B Discretisation of eigenvalue problem **216**

B.1 Non-axisymmetric perturbations 216

B.2 Axisymmetric perturbations 218

Appendix C Transformations for comparison of models **221**

References **224**

Chapter 1

Introduction

We begin with some background material on the subject of liquid spreading on solid surfaces and an introduction to the mathematical modelling of such systems. A literature review of previous work is presented, discussing both experimental and theoretical aspects of centrifugally forced instabilities, followed by a summary of the content of this thesis.

1.1 Background

The spreading of liquids placed on solid surfaces is a subject that has been widely studied. The motivation for much of this research is from industrial coating processes, where liquids are forced to spread on solids using an external force to drive the fluid front in a desired direction. A comprehensive review of wetting of solids in different circumstances is given by De Gennes [1], whereas further review articles by Myers [2] and Davis [3] discuss the the mathematical modelling of thin film flows with particular emphasis on the effect of external driving forces. Further applications of the spreading thin films are discussed in the review articles by Oron *et al.* [4] and Craster and Matar [5]. The flow behavior is often crucial in such applications demonstrating why understanding of the underlying physics of thin film flow is crucial.

The motivation for the work presented in this thesis is from an industrial process known as spin coating. Spin coating is a process used to coat a substrate with a thin, uniform layer of material typically of $\mathcal{O}(10^{-6})$ m and below [6, 7]. The appli-

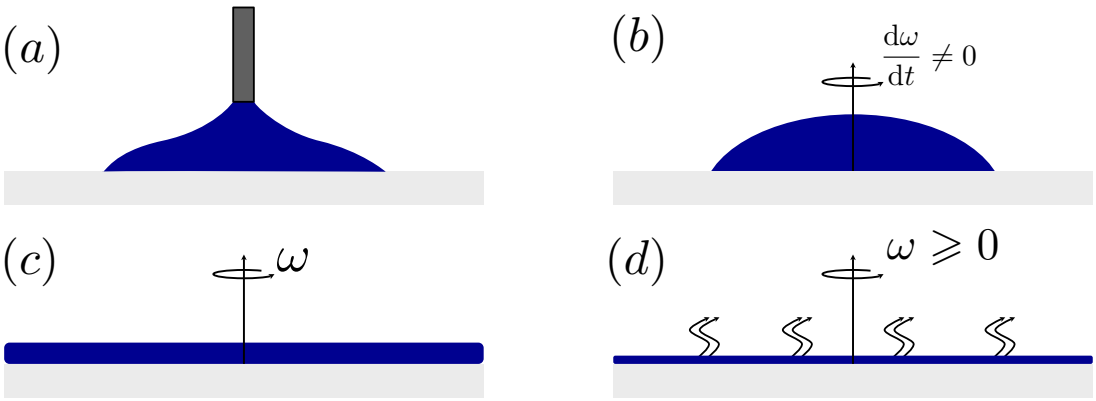


Figure 1.1: Phases of spin coating (reproduced from [17]), where $\omega(t)$ is the rotation rate of the substrate.

cations of spin coating in material science are wide and occur wherever smooth and uniform surfaces are required upon substrates [8]. Examples of such applications are in lithography [8, 9], generation of fuel cells [10] and solar cells [11, 12, 13], thermoelectrics [14, 15] and more recently biomedical applications [16].

The required material, commonly a polymer, is dissolved in a solvent creating a fluid, dispensed onto the substrate, spun at high rotational speeds and finally the solvent is evaporated to leave the desired material upon the substrate. The process is usually split into 4 distinct phases; dispensation, acceleration, constant rotation and evaporation [17]. Figure 1.1 demonstrates schematics of the four phases of spin coating.

The first phase is the dispensation phase, demonstrated by figure 1.1 (a). During this phase the fluid is placed onto the centre of rotation of the substrate and can be done statically or dynamically, referring to whether the substrate is in motion when dispensation occurs. The acceleration phase is demonstrated by figure 1.1 (b) and is characterised by large changes in rotational speed within very short times, causing fluid expulsion from the substrate [15, 18]. The substrate eventually reaches the desired speed at which point rotational accelerations are balanced by viscous forces, the fluid motion becomes steady in the rotating frame of reference and no differences in film thickness occur shown in figure 1.1 (b). The combination of spin speed and time over which this target rotation is achieved from stationary defines the final film thickness, generally higher spin speeds and longer spin times create decrease the film height. Once the target rotation rate is

reached, uniform thinning of the film gradually occurs [19]. Finally, when the fluid has reached a steady uniform desired thickness, evaporation of the constituting solvent becomes the dominant process [20], and is shown in figure 1.1 (d). In many applications heat is applied to quickly remove this solvent, leaving behind a uniform thin film of the desired material upon the substrate.

Emslie, Bonner and Peck [19] pioneered modelling of spin coating in the absence of evaporation effects by proposing a simple force balance between viscous and centrifugal forces showing that a film tends towards uniformity over time. The combined process of thinning due to both centrifugal force and evaporative effects has been extensively investigated in both experimental and theoretical studies [18, 21, 22, 23, 24, 25] however evaporation will not be addressed in this thesis. The early work of Emslie *et al.* [19] has been extended to include many other physical effects relevant to the spin coating process and will be discussed in more detail within § 1.3.2.

During spin coating it can be observed that when the circular fluid front reaches a critical radius, a fingering instability occurs, where the fluid flows preferentially through the formed fingers [26]. In this thesis, we theoretically and experimentally investigate the moving fluid front, known as the 'contact line' and formation of fingering instabilities when a fixed macroscopic volume of fluid is subject to centrifugal force.

1.2 Contact lines

A contact line is formed when a fluid-fluid interface meets a fluid-solid interface; any container that holds a fluid with a free surface must have a contact line. For example, in a stationary glass of water there is a static, closed contact line where water, air and glass meet. When you pick up the glass and drink from it, the contact line moves along the inner surface of the glass, changing shape and length as it does so. In the system we will consider, the contact line will be at the meeting of the free surface of an initially stationary droplet of fluid and a solid plate. The contact line is indicated on figure 1.2 at this meeting point. Since a contact line is formed at the meeting of three interfaces – liquid/solid, solid/gas and gas/liquid – it is often referred to as the 'common line' or 'tri-junction' in the

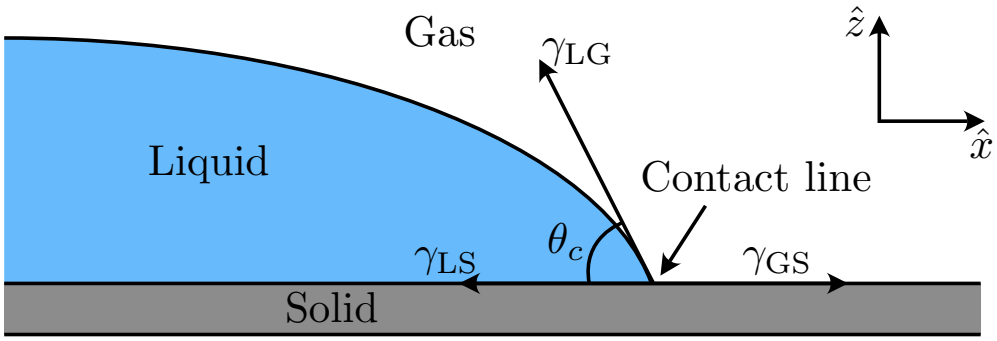


Figure 1.2: Young diagram (reproduced from [27]), where the static contact angle is denoted θ_c.

literature. The angle formed at the contact line is known as the 'contact angle' and is conventionally measured through the liquid rather than gaseous phase.

1.2.1 Contact angles

In this context, the static contact angle is defined when the droplet is stationary on the solid surface so that the contact line is not moving. Early investigations into static contact angles were performed by Young [28]. Young assumed that for a system to be static, the constant, horizontal interfacial tension components at each of three interfaces which meet at the contact line must be in equilibrium. Therefore, the Young equation reads

$$\gamma_{SG} - \gamma_{SL} - \gamma_{LG} \cos\theta_c = 0, \tag{1.2.1}$$

where γ denotes the interfacial tensions, the subscripts S, L, and G denote the solid, liquid and gas phases, respectively, and the static contact angle is denoted θ_c. Measurement of the static contact angle are often performed using an optical tensiometer. In practice, a droplet is placed on the solid surface and the image of the drop is recorded, and the surface tension, γ_{LG} is measured. The static contact angle is calculated using image analysis, while the difference $\gamma_{SG} - \gamma_{SL}$ is subsequently determined by fitting to Young's equation (1.2.1).

A dynamic contact angle is defined as the contact angle when the contact line is moving. Figure 1.3 shows typical experimental results for the dependence of the dynamic contact angle, θ, on the contact line speed, R_t [27]. We see that

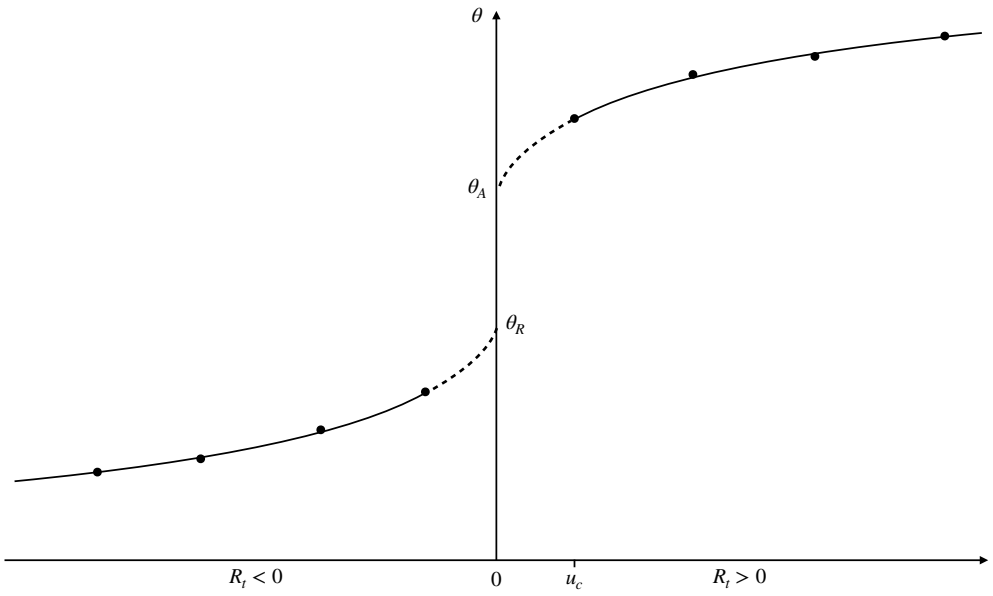


Figure 1.3: Typical experimental results for how the dynamic contact angle, θ, depends on the speed of the contact line, R_t. The angles θ_A and θ_R are the advancing and receding contact angles, respectively. The dashed line represents the prediction for the contact angle below the smallest contact line speed for which a contact angle can be measured, u_c (reproduced from [27]).

at $R_t = 0$ there is often a discontinuity in the contact angle, indicating that the contact line must remain stationary between the advancing contact angle, θ_A, and the receding contact angle, θ_R. This discontinuity in contact angle at $R_t = 0$ is known as contact angle hysteresis. Contact angle hysteresis is known to be caused by microscopic surface roughness, experimentally verified by Zisman [29], where only by coating very smooth surfaces can the advancing and receding contact angles be equal. The advancing and receding contact angles are measured from dynamic experiments where droplets are in movement, and are determined by the limiting behaviour as the contact line velocity tends to zero. In contrast, the equilibrium contact angle, θ_c, described by the Young equation (1.2.1) is measured from a static system, as described above. Values of the static contact angle lie between the advancing and receding contact angles and depend on variables such as drop volume.

In a cylindrical polar coordinate system (r, φ, z), the free surface is defined at time t as $z = h(r, \varphi, t)$, with the contact line at $r = R(\varphi, t)$. The contact angle, θ, is given by

$$\left.\frac{\partial h}{\partial r}\right|_{r=R(\varphi,t)} = -\tan(\theta). \tag{1.2.2}$$

This boundary condition must be coupled with a model for the contact angle, θ, itself. It is common in the literature to describe the experimental data such as in figure 1.3 by using a Tanner law [30]. The Tanner law couples the contact angle, θ, and to the contact line speed, R_t,

$$\frac{\partial R}{\partial t} = \begin{cases} \kappa_A \left(\theta^q - \theta_A^q\right) & \theta > \theta_A, \\ \kappa_R(\theta_R^q - \theta^q) & \theta < \theta_R, \\ 0 & \text{otherwise}, \end{cases} \tag{1.2.3}$$

where κ_A, κ_R, known as the advancing and receding contact line speeds, are positive with dimensions of velocity and are generally determined experimentally. The exponent q is also determined experimentally, and is commonly taken as either $q = 1$ or $q = 3$ [1, 31, 32, 33]. The Tanner contact line law (1.2.3) states that if the contact angle is above a critical value then the contact line will advance with a positive velocity, while if the contact angle is below a critical value, θ_R, then it will recede, otherwise remaining stationary.

Since these early studies there has been much interest into contact angle hysteresis [34, 35, 36, 37, 38, 39], and applications and underlying physics are discussed in the review articles by Eral *et al.* [40] and Extrand [41]. However, many of these studies do not provide a practical boundary which can be used in simple models involving moving contact lines. It is therefore common [32, 42, 43, 44] to restrict analysis to considering the Tanner law (1.2.3) in the case where no hysteresis is considered, so that

$$R_t = \kappa(\theta^q - \theta_c^q), \tag{1.2.4}$$

for all contact angles, where θ_c is the static or equilibrium contact angle; meaning the contact line can both advance and recede. Furthermore, since there is no discontinuity at $\theta = \theta_c$, we can safely linearise about this state. In this thesis we will also restrict our analysis to the case where contact angle hysteresis is neglected. Hoffman [45] and Kistler [46] also both suggest a cubic relationship between the contact line velocity and the dynamic contact angle, with slightly different form to (1.2.4).

Measurements of contact angles use visible light, which has a wavelength of approximately $\mathcal{O}(10^{-7})$ m, thousands of times bigger than a fluid molecule, hence the resolution of experimental images may be insufficient to measure the contact angle

accurately. Furthermore, microscopic surface roughness affects the contact angle meaning experimental data may not be accurate, especially on short lengthscales. This is demonstrated by contact angle hysteresis, shown in figure 1.3, whereby the advancing and receding contact angles have different values. An alternative condition to impose is that the contact angle is a constant [47, 48, 49, 50], and is given by its equilibrium value, θ_e, throughout the analysis. This method does not rely on the measure of contact line speed, κ, and exponent, q being determined empirically, rather just the equilibrium contact angle.

1.2.2 Macroscopic slip

In order to have a well-posed model for a moving contact line, we must also consider the macroscopic behaviour of the contact line. Application of standard no-slip boundary conditions in problems involving contact lines leads to singular components within the stress tensor, resulting in an apparent infinite force required for the contact line to move [3]. When considering a moving contact line, in order for the problem to be well-posed, it is common to introduce a macroscopic slip law at the boundary [51, 52, 31]. If (u, v, w) are velocity components, appropriate boundary conditions for a thin film of fluid on a plate at $z = 0$ are

$$u = s(h)\frac{\partial u}{\partial z}, \quad v = s(h)\frac{\partial v}{\partial z}, \quad w = 0, \tag{1.2.5}$$

for fluid height, h. The last of these conditions is the standard no-penetration condition. The slip conditions (1.2.5) (a, b) on the horizontal velocity components state that the velocity is directly proportional to the shear stress through a function, $s(h)$, depending on the height, h, of the free surface. If we take $s(h) = 0$ the classical no-slip and no-penetration boundary conditions, $\boldsymbol{u} = \mathbf{0}$ on $z = 0$, are recovered. The slip function is commonly chosen to be constant [27, 32, 42, 43], so that $s(h) = \beta$; known as the Navier slip law. This is justified since the shear stress at the plate is expected to be large at the contact line, so that the slip becomes most pronounced at these points [52]. Another common slip function to be $s(h) = \frac{\alpha}{3h}$ [2, 31, 51, 53]; known as the Greenspan slip law. Here, α is a small constant, so that the slip function, $s(h)$ is small except in the region close to the contact line where $h = \mathcal{O}(\alpha)$ and the slip becomes pronounced. Taking the slip to be proportional to $1/h$ forces the shear stress to be zero at the contact line, where

$h = 0$, correcting for the expected large stress contributions at the contact line. Myers' review of thin films with surface tension [2] discusses the different slip laws in more detail.

An alternative method of mitigating the stress singularity at the contact line is the use of a precursor film. In this case an assumption is made that a thin film of liquid is present upon the solid surface such that the free surface interacts with this layer rather than forming a contact line at the solid surface directly. This method is common in early literature [1, 2, 54, 55, 56, 57] however modelling presented within this thesis focuses only on the use of a slip law of the form (1.2.5) since introduction of a precursor film completely removes the contact line dynamics, and is not present within the experiments we performed, which we intend to model.

1.3 Centrifugally forced contact line instabilities

In an effort to understand the conditions for instability of centrifugally forced contact lines which occur during industrial processes such as spin coating, there have been a number of experimental and theoretical analyses of fixed volumes of fluid on rotating discs.

1.3.1 Experimental

There have been several experimental studies of contact line instabilities of viscous fluids on rotating substrates. An early investigation was performed by Melo *et al.* [26], who considered small volumes ($\mathcal{O}(10^{-2})$ ml) of silicon oils on silicon wafers, relevant to the electronics industry. They determined that in this configuration the spreading from an initially circular contact line is firstly axisymmetric during which a capillary ridge forms close to the contact line. When a critical radius is reached a fingering instability occurs. Figure 1.4 shows experimental images taken from [26] showing the onset of the fingering instability and the capillary ridge close to the contact line. It is suggested that the critical radius and the most unstable wavelength i.e., the number of fingers, is a function of the nondimensional parameter, $\beta = \gamma/(\rho\Omega^2 V)$, for rotation rate Ω, density ρ and volume V. However, for sufficiently large values of β, corresponding to lower rotation rates, the critical

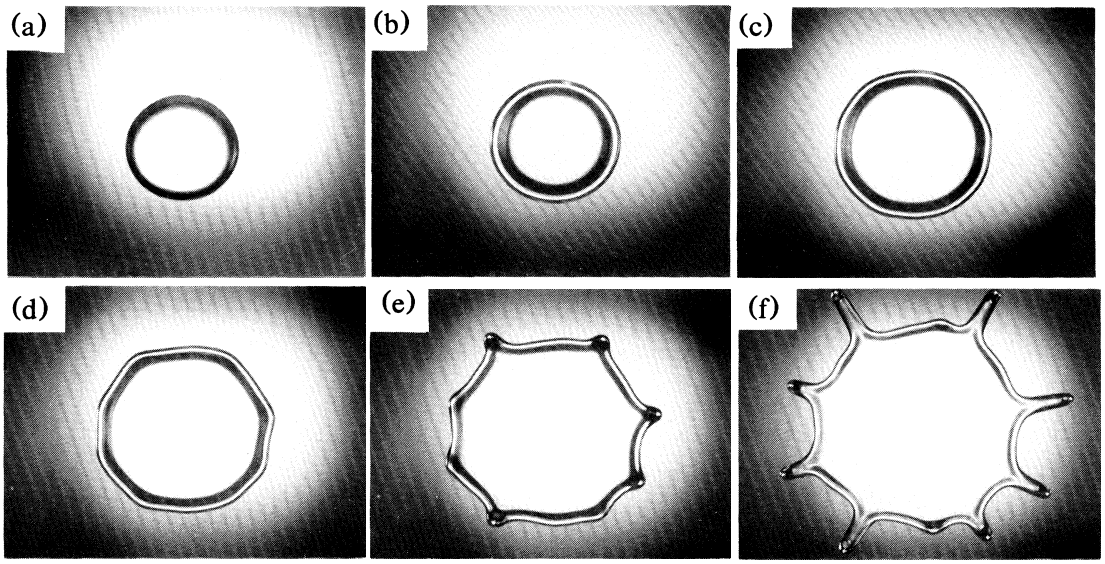


Figure 1.4: Experimental images taken from [26], showing the onset of the fingering instability from an initially circular configuration. The black areas within the fluid show areas of non-zero slope, indicating a ridge forms close to the contact line.

radius and number of fingers appeared to be independent of β, and therefore independent of the rotation rate and volume, whereas larger rotation rates were judged to be out of range of the lubrication approximation.

Fraysse and Homsy [58] performed similar experiments within the same parameter space, for three Newtonian fluids (silicone oils) of different viscosities and a non-Newtonian Boger fluid. They reported that the instability occurs in the same way as reported by Melo *et al.* [26], and further verified within the investigated range of parameters that the most unstable mode was independent of rotation rate and volume. Furthermore, Fraysse and Homsy found that the two-zone model of Troian *et al.* [59], where the free surface is modelled combining an inner region close to the moving contact line and an outer region of constant thickness, is in good agreement with their experimental data, both qualitatively and quantitatively, provided that the critical radius was taken from the experiment. However, Fraysse and Homsy determined that the most unstable mode and growth rates do depend on wetting properties, such as the contact angle and surface tension.

Spaid and Homsy [60] considered the effect of elasticity on the onset and evolution of the fingering instability by rotating small volumes ($\mathcal{O}(10^{-1})$ ml) of tricresyl phosphate either mixed with polystyrene polymer to form a viscoelastic fluid, and

on its own constituting a Newtonian fluid. They observed a qualitatively similar instability to Melo *et al.* [26] and Fraysse and Homsy [58], and demonstrated that viscoelastic fluids develop more fingers and coat a larger area than Newtonian fluids under comparable experimental conditions. Using similar Newtonian silicon oils Wang and Chou [61] performed experiments on larger volumes ($\mathcal{O}(1)$ ml); an order of magnitude larger than previous experiments. They determined that below a threshold value of rotation rate the dominant wavelength of the fingering instability is constant, whereas above this threshold the number of fingers increases rapidly, indicating that previous experiments [26, 58] may have been performed below critical rotation rates.

More recently, Holloway *et al.* [62] also reported contrasting results to Melo *et al.* [26] and Fraysse and Homsy [58], finding that within similar parameter regimes the number of fingers increases with both the rotation rate and the drop volume. It is suggested that this may be due to limited rotation rates being discussed in [26, 58]. Furthermore, power laws for axisymmetric spreading in time as functions of the rotation rate and volume were determined, finding that contact radius grows linearly in time, with speed $\kappa \propto \Omega^{2.47} V^{0.73}$. Holloway *et al.* [62] subsequently extended their experimental analysis to yield stress fluids [63]. Chou *et al.* [64] performed experiments using silicone oil for larger volumes, at $V = 0.3$ ml. They considered the dynamic contact angle, finding that a fingering instability occurs when the contact angle increases past a critical point, suggesting that contact angle hysteresis has an effect here. Furthermore, the reported contact angles can be as large as 150 °, meaning a small contact angle approximation may not be appropriate. The evolution of the free surface of small droplets of silicon oils with small capillary number was considered experimentally by Blank and Ehrhard [65]. They observed the formation of a capillary ridge forming close to the contact line in their experiments, agreeing qualitatively with previous investigations and the quasi-steady analysis of Boettcher and Ehrhard [44].

Veretennikov *et al.* [66] considered the spreading of relatively large volumes, $V \approx 0.6$ ml, of glycerol, a partially wetting fluid with an $\mathcal{O}(1)$ static contact angle. These experiments are in contrast to previous experiments detailed above which focused on microscopic volumes of perfectly wetting silicon oils, with contact angle close to zero. The authors considered rotation rates between 110 and 155 rpm, and observed a single finger forming in all experimental runs. Similarly

to Chou *et al.* [64], the authors suggest that movement of the contact angle occurs when the apparent contact angle exceeds a critical threshold, with the instability characterised by a rolling motion at the contact line, in contrast to the findings for perfectly wetting fluids [26, 58, 60]. Spin coating of suspension films was considered by Kulakarni *et al.* [67], using a glycerol and microscopic glass bead solution to create the suspension film. The results were compared to results of glycerol and silicon oil (PDMS), where they observed that the critical radius for the onset of instability for glycerol is much lower than PDMS for all rotation speeds. They assert that since glycerol has a greater surface tension of the two fluids, a droplet will break down into a lower number of fingers than PDMS in order to minimize surface energy. Sahoo *et al.* [68] study the simultaneous spreading of superimposed Newtonian fluids, comparing the results to the linear stability analysis of Fraysse and Homsy [58]. They found this model overpredicts the number of experimentally prevalent fingers.

The dynamics of droplets impinging on rotating planes has also been of recent scientific interest following much research into droplet impact on stationery disks [69] and references therein. Li *et al.* [70, 71] studied droplet impact patterns in detail, categorising patterns as a function of Reynolds, Weber, and Rossby numbers whereas Moghtadernejad *et al.* [72] were more interesting in the formation of a fingering instability following initial droplet impact. Pan *et al.* [73] investigated the axisymmetric spreading of a single droplet of approximately 8 μl of ethanol impinging on a rotating disk. They compared the results to numerical solutions using the Hoffman law [45] to model contact angle hysteresis demonstrating that the dynamic spreading process consists of an initial inertial spreading stage followed by a centrifugal thinning stage in good agreement with experiments. Dynamics of impinging droplets are not considered further within this thesis, however the above studies provide an excellent foundation for which to build similar experimental and numerical methods upon.

Overall, the majority of existing experimental analysis has been performed in a parameter range to reflect industrial spin coating, that is, very small volumes of silicone oils with small contact angles. However, it seems a surprising conclusion that the fingering instability is independent of rotation rate [26, 58], and may be a product of considering a limited extent of the parameter space, demonstrated by Wang and Chou [61] and Holloway [62]. Furthermore, the effect of rotation on

larger volumes ($\mathcal{O}(1)$ ml) of partially wetting fluids with potentially large contact angles has not been extensively studied, especially at high rotation rates.

1.3.2 Theoretical

Several mathematical models have been formulated to quantify and predict the axisymmetric spreading and subsequent fingering instabilities that occur at centrifugally forced contact lines. An early theoretical investigations into spin coating, performed by Emslie *et al.* [19], removed the need for contact line dynamics by considering a thin, axisymmetric fluid layer upon an infinitely large rotating disc. By considering a simple balance of the centrifugal and viscous forces, exact so lutions to the resulting evolution equation for the profile of the free surface are found for different cases. They found that liquid layers that are initially uniform remain so under rotation, while also showing that perturbed liquid layers also tend towards uniformity.

The analysis of Emslie has subsequently been extended to assess the individual and often combined effects of inertia [74], non-Newtonian fluids [75, 21], Coriolis force [76, 77, 78], surface roughness [79], evaporation and absorption [18, 23, 24, 25] and more recently multi-fluid systems [80, 81, 82]. Evaporation is commonly neglected in these studies and can be justified due to the timescale for volume loss due to evaporation being multiple orders of magnitude larger than that of the spreading process [83]. Tu [84] introduced the use of contact line dynamics to spin coating problems, using the inverse slip law of Greenspan [31] applied to a two dimensional viscous fluid under constant rotation and vanishing surface tension. Under these simplified conditions Tu determined that the axisymmetric contact line spreads exponentially in time. Wilson *et al.* [85] extended the analysis of Tu [84], considering axisymmetric spreading in spin coating problems, prior to the onset of fingering. However, as well as discussing the limit of vanishing surface tension, the asymptotic limit of weak surface tension and numerical solutions where surface tension effects are $\mathcal{O}(1)$ are also considered. The results of the latter case show good quantitative agreement to the axisymmetric phase of experiments by Fraysse and Homsy [58] and Spaid and Homsy [60]. Furthermore, the authors determined that both the fixed contact angle and Tanner boundary conditions can sufficiently reproduce the referenced experimental results. The weak surface

tension asymptotic solutions are found to capture the qualitative nature of the experiments described showing the same trend in the position of the contact line against time. Furthermore, the authors determined that both the fixed and Tanner (1.2.4) contact angle boundary conditions are capable of reproducing the experimental results well in each of the limits considered. Several authors have further investigated axisymmetric spreading, extending the analysis to non-Newtonian fluids [86, 87, 88].

Following the axisymmetric phase of experiments of centrifugally forced contact lines, a fingering instability occurs at the contact line [26, 58, 60]. Similar observations were made by Huppert while considering viscous flow down inclined planes [89] since in this configuration movement of the contact line is also driven by an external force, namely gravity. Troian *et al.* [59] and Moriarty *et al.* [90] developed the model of Huppert [89] applying the analysis in the context of centrifugally forced contact lines in the limit of small surface tension. Each set of authors considered the flow as two phase, asymptotically matching an outer region of thin uniform height with an inner region close to the contact line while using a precursor film to model contact line dynamics under a lubrication, or long wave, approximation. To verify the composite asymptotic solutions, Moriarty *et al.* [90] solved the derived lubrication equation numerically, showing good comparison for small surface tension. The solutions of Troian *et al.* were subsequently found to compare well to experiments performed by Fraysse and Homsy [58], and Holloway [62]. Spaid and Homsy [53] compared the use of an asymptotically matched precursor film to the use the Greenspan inverse slip law [31], finding that both methods can have quantitatively comparable results. Furthermore, they determine that the stability of the contact line is instability of the contact angle for sufficiently small angles. However, the asymptotic solutions detailed above [59, 90, 53] have limitations, such as that volume is only conserved within the outer region; an unphysical assumption for droplets of constant volume. Furthermore, Moriarty [90] assumes within his derivation that the body force driving instability is constant over the inner region, whereas in the context of spin coating the centrifugal force is a function of the radially distance from the axis of rotation.

McKinley *et al.* [42] considered the spreading of an incompressible fluid droplet that interacts with a vertical jet of air. They assert that the nondimensional equations of motion for this configuration are identical to those of a rotating fluid

in the absence of the Coriolis forces, up to the redefinition of a nondimensional group. They derive an evolution equation under a lubrication approximation, including gravitation effects, which in the small capillary limit and when combined with the Tanner law (1.2.4), reduces to a first order ordinary differential equation for the contact line position. A Navier slip condition, where the slip coefficient is constant, is used to allow the contact line to move. The equilibrium solutions are discussed and subsequently the stability of these solutions subject to axisymmetric perturbations is analyzed. They found that for each jet strength (or rotation rate) there is at most one physical equilibrium solution which is stable to axisymmetric perturbations, however for a small range of jet strengths there exist multiple physical solutions, where the solution with the larger radius is unstable. Annular solutions, where there exists a dry patch at the centre of the fluid droplet, are also considered in this work. A more recent effort into equilibrium solutions in the absence of a lubrication approximation was performed by Konan *et al.* [91]. The authors further demonstrated that equilibrium solutions exist only at sufficiently low rotation rates, where the limiting rotation rate depends on the Bond number. However, an assumption made during this analysis is that the contact angle is fixed at $\theta_c = \pi/2$.

McKinley and Wilson [43], motivated by a study concerning a linear stability analysis of a ridge of fluid [92] extend their previous analysis within the small capillary limit [42] to non-axisymmmetric perturbations to the free surface, h, and the contact line, R,

$$h = h_0(r) + h_1(r)\exp(\mathrm{i}m\varphi + \sigma_m t), \quad R = R_0 + R_1\exp(\mathrm{i}m\varphi + \sigma_m t) \tag{1.3.1}$$

for azimuthal wavenumber, m and corresponding growth rate, σ_m. In (1.3.1) h_0 and R_0 are the equilibrium free surface shape and contact line position, respectively. In this study, gravity is ignored due to the volumes under investigation making the Bond number negligibly small. The analysis is further extended to the general case with non-zero capillary number, solving a linear eigenvalue problem coupled with the Tanner law to produce growth rates for each mode. They find that when gravity is neglected all equilibrium solutions are unstable, both in the quasi-steady limit and in the general case for finite capillary numbers. Specifically, every equilibrium solution is unstable to $m = 1$ perturbations, corresponding to a translation from the axis of rotation, whereas higher modes are only unstable

above a critical rotation rate depending on the wavenumber. Each of the studies [42, 43, 92] constitute parts of the thesis of McKinley [93].

Schwartz and Roy [94] reported analytical and numerical solutions of the same evolution equation, again in the absence of gravitational effects. Their analytical results support those of McKinley and Wilson [43], recovering similar equilibrium solutions which they reaffirm to be universally unstable with respect to the displacement mode $m = 1$, while higher modes are only unstable beyond a critical rotation rate. Above rotation rates for which equilibrium solutions are possible the authors report a good comparison between their numerical solutions and the experiments of Fraysse and Homsy [58].

Boettcher and Ehrhard [44] performed a similar linear stability analysis to McKinley and Wilson [43], considering a rotating droplet of fluid including both gravity and non-axisymmetric perturbations, however only consider quasi-steady solutions. The base state for the linear stability are axisymmeteric quasi-steady solutions to the evolution equation neglecting the leading order contact angle condition, in contrast with McKinley and Wilson [42, 43] who discuss steady, axisymmetric solutions in equilibrium. Again, a combination of the Tanner and Navier slip boundary conditions are used to model the movement of the contact line, subsequently determining the growth rate of the system in the quasi-steady case. Each of the studies [42, 43, 44] resemble the modelling presented in chapters § 3, 4 and will therefore be discussed in more depth at relevant points in this thesis.

The effect of the Coriolis force on axisymmetric spreading was discussed by Myers and Charpin [77] and subsequently by Myers and Lombe [78]. Both studies conclude that in axisymmetric flow under a lubrication theory the Coriolis force does not affect the film height. Cho *et al.* [95] performed experiments on the subsequent fingering instability finding that the critical radius at which instability occurs is a function of only the rotational Reynolds number when Coriolis forces dominate. In a subsequent study Cho and Chou [96] performed further experiments finding that within the parameter range considered that the Coriolis force notably affects the critical radius at which a fingering instability occurs. Furthermore, for low rotation rates the effect of the Coriolis force is stabilizing, whereas above a threshold rotation rate the effect of Coriolis force becomes destabilising. In § 5 we will discuss the effect the Coriolis force has on the rate of fingering in

comparison to a theory in the absence of this inertial force.

1.4 Thesis outline

In chapter 2 we discuss the experimental procedure and methodology developed to analyse contact line instabilities of a viscous fluid, subject to rotation. We discuss the initial condition of the experiment as well as the stability, assessing axisymmetric and non-axisymmetric spreading using Fourier analysis.

In chapter 3 we develop a mathematical model for the experiment described in chapter 2. Assuming that the contact angle is small we make the lubrication approximation, deriving a thin film partial differential equation which governs the free surface height, and the contact line position. Subsequently, we consider equilibrium solutions to the thin film equation, assessing where solutions exist within the nondimensional parameter space, in an approach similar to McKinley and Wilson [42, 43].

Chapter 4 concerns the linear stability of the equilibrium solutions found in chapter 4, where a Tanner model (1.2.4) has been used to relate the contact angle to the contact line speed. We discuss axisymmetric and non-axisymmetric perturbations to the contact line, assessing the stability of the equilibrium solutions within the nondimensional space in which they exist; reproducing and extending the analysis of McKinley and Wilson [43]. In chapter 5 we discuss extensions to the linear stability theory, considering different limits of nondimensional parameters, and various modelling assumptions to those assumed in chapter 4.

In Chapters 3–5 we discuss solutions of the equations of motion under a lubrication approximation, where terms are neglected due to the radial length scale being larger than the vertical length scale. In chapter 6 we nondimensionalise the same set of equations and boundary conditions, no longer making this assumption. Again, we determine equilibrium solutions from the nondimensional equations, assessing where these solutions exist within the parameter space, comparing the results to those of the thin film theory.

Chapter 7 concerns the linear stability of the equilibrium solutions determined in chapter 6, where we develop a finite element method to solve the previously

derived perturbation equations and boundary conditions. We discuss the solutions and their trends as parameters, such as the contact angle, are varied in comparison to the thin film theory, and with reference to the experimental observations in chapter 2.

In chapter 8 we compare aspects of the experimental results from chapter 2 to solutions of the mathematical models studied in chapters 3–7, discussing the advantages and disadvantages of each model in relation to the modelling assumptions made. The important findings are summarised in chapter 9, along with a discussion on possible future research directions.

Chapter 2

Experimental procedure and analysis

In this chapter, we outline the experimental procedure developed to analyse the contact line instabilities of a viscous fluid under rotation. Specifically, we investigated the effect of rotation and gravity relative to that of surface tension, in a regime where inertia is negligible compared to viscosity. We detail an experiment whereby a fluid droplet of known viscosity and volume is placed in the centre of a flat, circular disc. This is spun up, at a chosen rate of acceleration, from rest to a prescribed rotation rate and the instability which occurs at the fluid front is analysed.

We first detail the equipment used to perform and record the experiments, and present the method used to analyse the data using Fourier analysis. Finally, the results of the experiment are described considering the mean radius of the fluid for both axisymmetric and non-axisymmetric spreading.

2.1 Methodology

First we detail the experimental method and equipment used, along with a description of the fluid chosen to perform the experiments and its properties.

Physical Quantity	Symbol	Units	Approximate Value
Density	ρ	$\mathrm{kg\,m^{-3}}$	1261
Surface tension	γ	$\mathrm{kg\,s^{-2}}$	69×10^{-3}
Rotation rate	Ω	$\mathrm{rad\,s^{-1}}$	5 – 90
Viscosity	μ	$\mathrm{kg\,m^{-1}\,s^{-1}}$	1.069
Volume	V	$\mathrm{m^3}$	1.5×10^{-7} – 1.6×10^{-6}
Contact angle	θ_c	rad	1.1 – 1.4

Table 2.1: Experimental values of physical quantities, with their respective symbol, units also shown. Each of the physical quantities are taken at a temperature of 20 °C. The reported values are for glycerol and the surface tension is determined using data from [97].

2.1.1 Experimental set-up

The experiment consisted of a 190 mm stainless steel disc, driven by a servo motor in rotation about its vertical axis, with control of the acceleration and rotation rate. The disc was covered with self adhesive sticky back plastic to ensure a uniform non-absorbent surface. We used glycerol to ensure the Reynolds number was small, and can be represented by taking the Stokes flow approximation adopted for the mathematical modelling in Chapter 3. The definition of the experimental Reynolds number varied depending on the modelling used, and is discussed further in Chapter 8.

The solution was prepared by combining glycerol with a small amount of dye. A peristaltic pump was used to accurately dispense a chosen volume of fluid onto the centre of the disc at a chosen flow rate. A slow pump flow rate was used to minimise non-axisymmetric spreading, achieving an initially circular fluid patch when viewed from above. The fluid was dispensed on the plate through a nozzle centred over the axis of rotation using a boom arm.

The disc was accelerated from rest to a chosen rotation rate. The spin-up timescale, over which the fluid adjusts to the rotation of the disc to achieve solid body-rotation is

$$\tau = \frac{\rho V^{2/3}}{\mu}\,\mathrm{s}. \tag{2.1.1}$$

We therefore accelerated the disc to the required rotation rate over ten times the

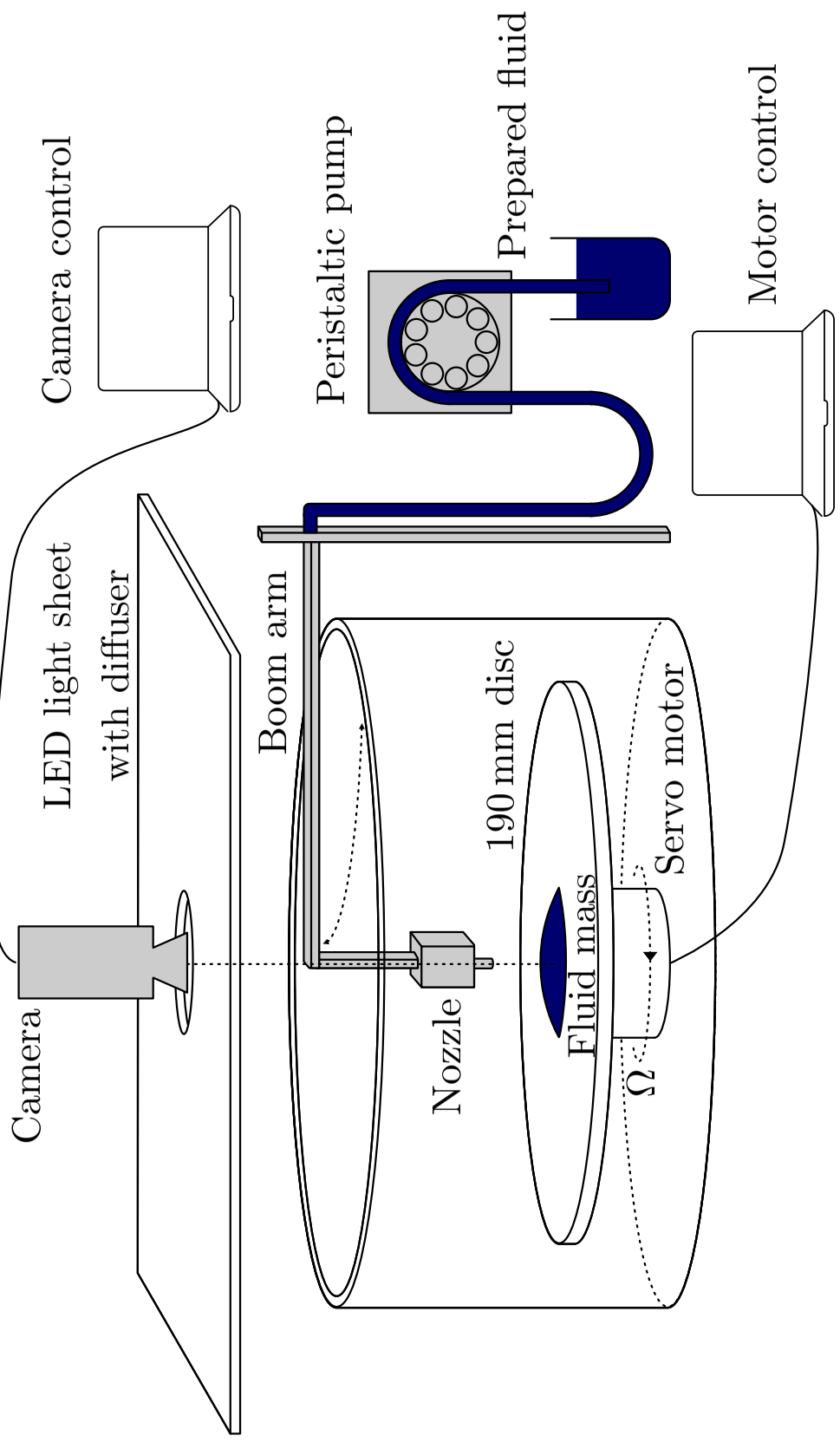


Figure 2.1: Schematic diagram showing the experimental set-up, side view.

spin-up time (2.1.1), mitigating any effects due to acceleration. Hence,

$$a = \frac{\Omega}{10\tau}\,\mathrm{rad\,s^{-1}} = \frac{\Omega\mu}{10\rho V^{2/3}}\,\mathrm{rad\,s^{-1}}. \tag{2.1.2}$$

where a is the acceleration. The dynamics were recorded using a high-speed Phantom Miro M340 camera, where exposure time, resolution and crucially the frame rate were optimised to resolve the fluid shape and dynamics. In each case the frame rate was scaled with the rotation rate, so that the number of frames per second matched the revolutions per minute of the disc. Therefore, in every experiment 60 frames corresponds to a single rotation of the disc. Since the exposure time is determined by the frame rate, it was important to have adequate lighting. In order for the light to be consistent across the disc, diffuse LED light sheets were mounted parallel to the disc surface, in the plane of the camera. This even, bright illumination facilitated systematic thresholding of the images to find the contact line. The experimental set-up is shown schematically in a side on view in figure 2.1 while the corresponding bird's-eye view in shown in figure 2.2.

All experiments were performed at a constant temperature of 20 °C to ensure physical properties of the fluid remained constant. The values and notation of each relevant physical fluid property are summarised in table 2.1. The surface tension and density reported in table 2.1 are for pure glycerol, whereas in our experiments the fluid is mixed with a small amount of dye. We used 0.25 ml of dye per 100 ml of glycerol to minimise any affect of the dye on the physical properties of the fluid, while providing sufficient contrast between fluid in background for pixel-scale resolution of the moving fluid boundary. The surface tension and density of the dye was measured as approximately equal to that of water, $\rho = 1000\,\mathrm{kg\,m^{-3}}$, $\gamma \approx 72 \times 10^{-3}\,\mathrm{kg\,s^{-2}}$. Although a small amount of dye was used to minimise the effect on the reported values while still providing an adequate contrast, there is evidence to suggest that introducing another fluid of differing surface tension can significantly affect the overall surface tension of the solution [97]. Specifically, the surface tension does not vary linearly according to the ratio of fluids used to make the solution, with the true value of surface tension being closer to that of the greater value of the constituent fluids. Therefore, the true surface tension coefficient may be larger than reported in table 2.1. Measurements of the surface tension coefficient of the glycerol-dye solution were taken using a capillary tube,

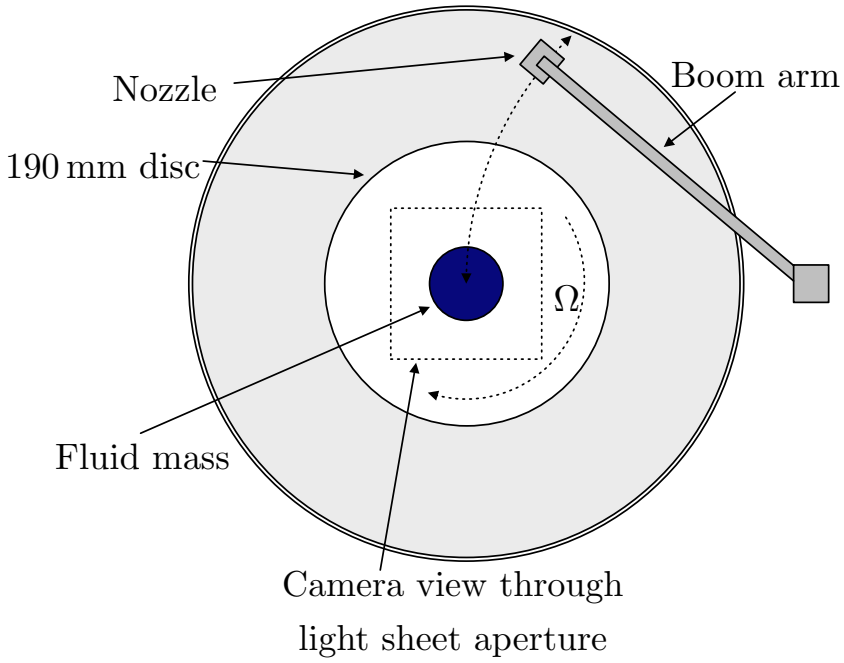


Figure 2.2: Schematic diagram showing the experimental set-up from a bird's-eye view.

finding the surface tension coefficient to be $\gamma = 70 \times 10^{-3} \pm 9 \times 10^{-3}\,\mathrm{kg\,s^{-1}}$. Furthermore, the density of the solution is calculated using the formulas given by Volk [98], with the resulting density being $0.4\,\mathrm{kg\,m^{-3}}$ less than reported in table 2.1. The inclusion of dye has a negligible effect on the overall viscosity of the fluid, again using calculations of Volk [98].

2.1.2 Experimental technique

The experimental technique is given as follows:

1. Prepare glycerol solution in the ratio of 100 ml with 0.25 ml of dye.
2. Using the peristaltic pump, flush glycerol solution through the pipe shown in figure 2.1.
3. Record reference video of a circle of a known radius printed on paper, this is later used to convert distances in terms of pixels into dimensional distances.
4. For each combination of rotation rate and volume:

- Calculate appropriate acceleration according to (2.1.2), and initialise motor with rotation rate and acceleration.
- Initialise high speed camera with a frame rate equal to the rotation rate in rpm, and exposure time of 1000 μs.
- Dispense volume of fluid onto the plate, taking care to centre the fluid mass on the axis of rotation.
- Allow fluid to relax to a circular, equilibrium state.
- Start rotation and video recording until instability occurs or maximum number of frames is reached and save video onto a hard drive.
- Clean plate with water and dry, ready for next run. The plate was cleaned using water since glycerol is water soluble.

2.2 Data analysis

The procedure detailed in § 2.1.2 was adopted to identify the influence of varying rotation rates and fluid volumes on the contact line for fixed viscosity, surface tension and densities of glycerol solution. Images from the video sequences were analysed to resolve the temporal evolution of the contact line. For each experiment we numerically analyzed the recorded dynamics using Fourier analysis, assessing how the contact line changes in time and determining the dominant Fourier mode of instability; the mode with the greatest associated growth rate.

2.2.1 Edge detection

The dynamics of each experiment were captured using a Phantom 4 MPixel camera producing a video file. The constituent frames were subsequently extracted using the MATLAB `VideoReader` package producing '.png' raw images such as figure 2.3 (a). We wish to understand how the contact line, that is, the visible boundary in the figure 2.3 (a), grows in time. In the literature, the boundary at which the pixel intensity changes with a large gradient is known as an 'edge' [99]. The Canny edge detection algorithm [100] is one of the most commonly used and rigorously tested methods for edge detection [101] and works by finding local maxima of the gradient of the image, where the gradient is calculated using the derivative

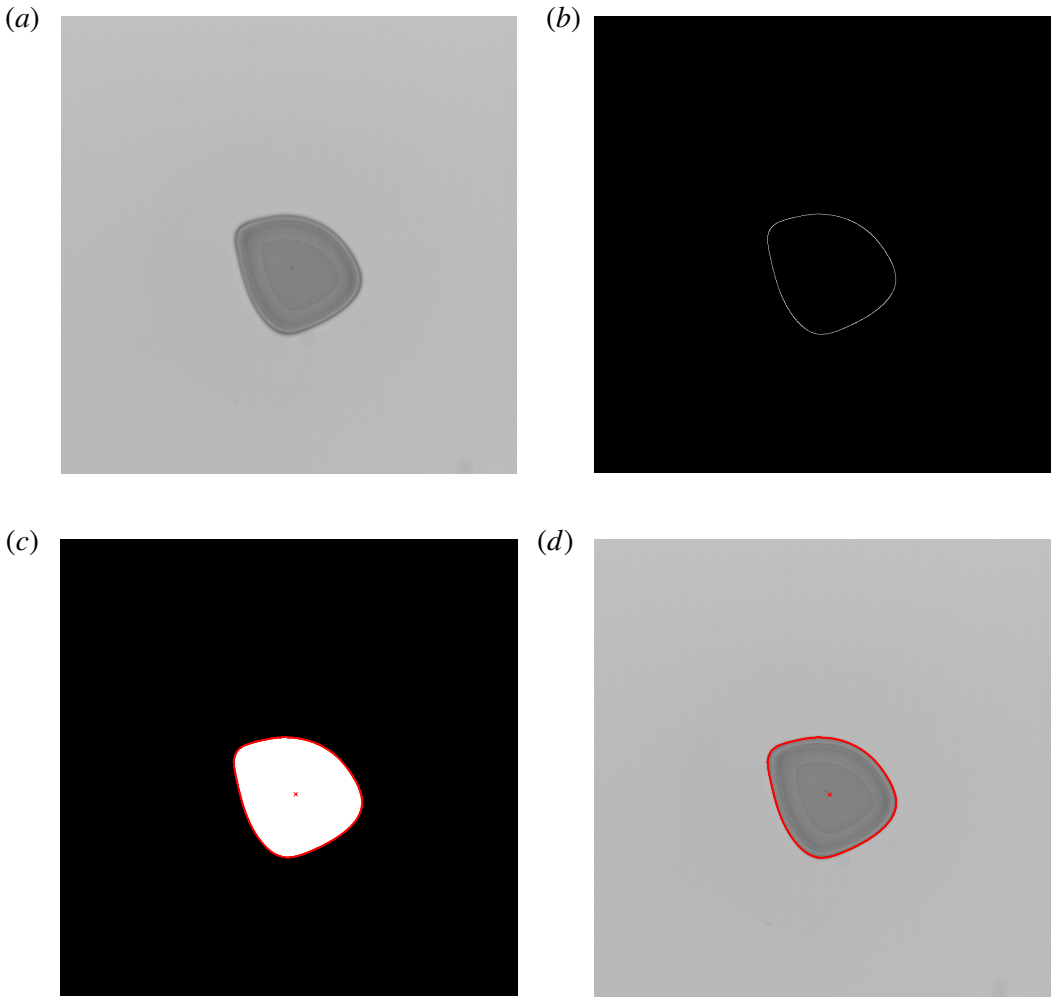


Figure 2.3: (a) Original image. (b) Gradient image, where the edge contour is shown in white. (c) Intensity matrix used for finding centre of mass, the boundary pixels are plotted in red and resulting centre of mass with a red cross. (d) Boundary and centre of mass plotted on the original image.

of a Gaussian filter. This method uses a higher and lower hysteresis threshold to detect both strong and weak edges. For each element in the gradient matrix, a value is accepted if the value lies above the prescribed upper threshold limit, and rejected if it lies below the lower threshold. Furthermore, points which lie between the upper and lower limits are accepted if they are adjacent to pixels whose value lies above the upper threshold. We chose the upper threshold value to be the minimum value such that the gradient matrix produces a single contour, while the lower value was taken such that the ratio between the upper and lower values is 2.5.

Comparable techniques such as Sobel [102] or Prewitt [103] methods use a single

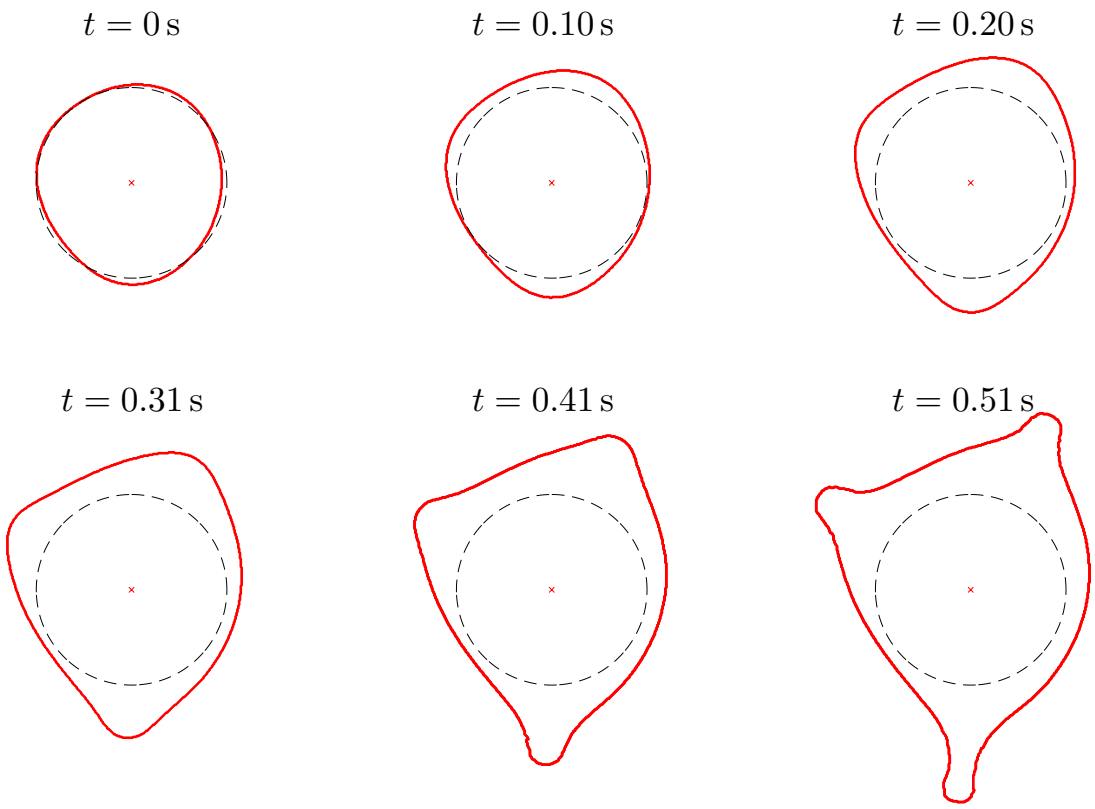


Figure 2.4: Results of an experiment of 0.35 ml of glycerol at being spun at 590 rpm, this figure shows the evolution of the boundary of the fluid mass in dimensional time, shown in red, while the mean initial radial extent of the fluid, R_0, is shown with a black dashed line.

threshold, which leads to the breaking up of the resulting contour caused by the gradient value fluctuating about the threshold along the length of an edge, known as streaking. Implementation of a hysteresis threshold reduces streaking, hence the Canny method is more robust to noise in the data [100]. Furthermore, our experiment was well lit by LED diffusive light sheets, meaning that any fluctuations in lighting across frames and experiments was minimised. Therefore, the Canny edge detection method is robust in calculating the evolution of the boundary.

Figure 2.3 (b) shows an example of the gradient image where areas of local maxima are shown in white, due to the chosen upper threshold we see a single contour is produced. Subsequently, the boundary pixels are identified and can be plotted on top of the original image, shown in figure 2.3 (d). Figure 2.4 shows an example of the evolution of the boundary over time in red in comparison to a circle of mean radius of the boundary at $t = 0$, shown with a dashed black line. In this case we can see the formation of three fingers evolving over time.

2.2.2 Centre finding and polar representation

Once the boundary has been detected using the method described in § 2.2.1, the location of the centre of mass of an individual frame can be calculated. Note, since the data is two-dimensional the centre of mass calculation neglects the free surface being a function of the vertical height. For each frame we created a matrix of intensities, I, where each pixel within the boundary was assigned the value 1 (white), whereas pixels outside the boundary assigned a 0 (black). Figure 2.3 (c) shows an example of the intensity matrix, where the boundary is shown in red. The centre (x_c, y_c) is calculated using the weighted average

$$(x_c, y_c) = \frac{\iint_A I\boldsymbol{x}\,\mathrm{d}A}{\iint_A I\,\mathrm{d}A} = \frac{\sum_{i=1}^{n}\sum_{j=1}^{m}(iI(i,j), jI(i,j))}{\sum_{i=1}^{n}\sum_{j=1}^{m} I(i,j)}, \tag{2.2.1}$$

where n and m are the number of pixels in the x and y directions, respectively. The centre of mass is shown in figure 2.3 (c) with a red cross.

To convert the boundary pixels into polar coordinates we require the position of the axis of rotation, denoted $(\bar{x}_c, \bar{y}_c)$. When the system is accelerated, the centre of mass of the boundary (2.2.1) of each frame will encircle the true centre of rotation. Therefore, the centre of rotation, $(\bar{x}_c, \bar{y}_c)$, was determined by fitting a circle through the centre of masses of each frame starting from when movement is first detected. The centre of the fitted circle gives the axis of rotation, $(\bar{x}_c, \bar{y}_c)$, and the radius was used as a measure of how well the fluid was centered on the disc. This process was repeated for each experiment to account for movement of the equipment between experimental runs. We found that accurately calculating the centre of rotation was important to reduce oscillations in the data when plotted over time.

Given the axis of rotation, $(\bar{x}_c, \bar{y}_c)$, the boundary pixels were expressed in two-dimensional polar coordinates, centred at $(\bar{x}_c, \bar{y}_c)$, by

$$\varphi_i = \tan^{-1}\left(\frac{y_i - \bar{y}_c}{x_i - \bar{x}_c}\right), \quad R_i(\varphi_i) = \sqrt{(x_i - \bar{x}_c)^2 + (y_i - \bar{y}_c)^2}. \tag{2.2.2}$$

The notation (x_i, y_i) denotes the Cartesian coordinates of each boundary pixel, and the angle $-\pi < \varphi \leqslant \pi$. Figure 2.5 (a) shows the boundary of the fluid at three different times which have been rotated so that the growth of fingers can

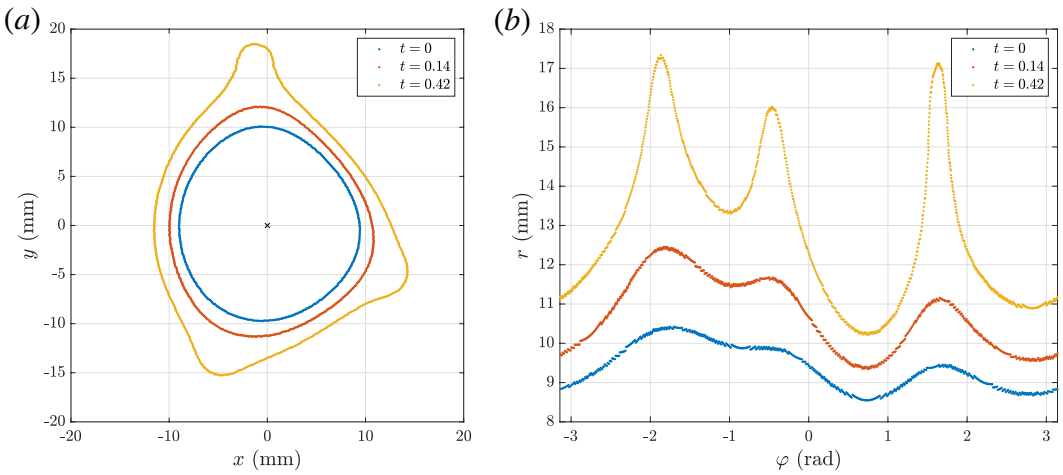


Figure 2.5: (a) Detected boundary in physical dimensions at three different times, translated so that the centre of mass is at on the origin. (b) Corresponding boundaries plotted in polar coordinates.

be viewed within a rotating frame of reference, and translated so the centre of rotation lies on the origin. Figure 2.5 (b) shows the boundary in polar form where the colours correspond to the same time in both parts of the figure. We see that the mean radius increases over time, indicating growth of the axisymmetric mode. Furthermore, we observe the growth of three distinct fingers in the boundary shown in figure 2.5 (a), which corresponds to three peaks in the polar representation in figure 2.5 (b).

Overall, at each timestep, corresponding to the inverse of the frame rate, the boundary was calculated and converted into a 2π periodic signal from the centre of rotation, which was found numerically. The signal evolves over time, as seen in figure 2.5 (b), and we can numerically analyse how the boundary, or contact line, grows in time.

2.2.3 Fourier decomposition

In previous sections we explained how for each frame the boundary of the fluid was obtained, and subsequently converted from Cartesian into polar coordinates, centered on the axis of rotation. The signal for each frame, $R(\varphi)$, is periodic and hence can be decomposed using Fourier analysis, and the resulting Fourier modes plotted as functions of time.

The signal $R(\varphi)$, as shown in figure 2.5 (b), can be represented by the truncated Fourier series

$$R(\varphi) = \frac{a_0}{2} + \sum_{m=1}^{N} \{a_m \cos(m\varphi) + b_m \sin(m\varphi)\}, \tag{2.2.3}$$

where the Fourier coefficients are given by

$$a_m = \frac{1}{\pi}\int_{-\pi}^{\pi} R(\varphi)\cos(m\varphi), \quad b_m = \frac{1}{\pi}\int_{-\pi}^{\pi} R(\varphi)\sin(m\varphi). \tag{2.2.4}$$

The number of terms, N, was chosen as the minimum value which returns root mean squared error between the boundary and Fourier series (2.2.3) below 0.3 pixels, approximately 0.0026 mm, for each frame. We find that $N = 25$ is the minimum to achieve this threshold, so that the boundary is well resolved without over-fitting the data. Hence, the Fourier coefficients are found by performing the required integrals of the pointwise, polar representation of the boundary pixels, $R_i(\varphi_i)$, at time t. The reference point for time is defined as the frame that the target rotation rate is first achieved after movement of the disc is detected. Specifically, $t = 0$ is defined as τ seconds after movement is first detected, rounded up to the closest frame, where τ is given by the spin-up timescale (2.1.1).

Repeating the above procedure for each frame returns the functions $a_m(t), b_m(t)$, where the timestep between frames is the inverse of the frame rate. Figure 2.6 shows how the amplitude, $A_m(t) = [a_m^2 + b_m^2]^{1/2}$, of the first seven non-axisymmetric modes grows over time for an experiment with 1.55 ml of fluid spun at 294 rpm, equivalent to $\Omega = 30.8\,\mathrm{rad\,s^{-1}}$. We observe that each Fourier mode grows over time at a different rate, with $m = 2$ appearing to grow the fastest and dominate the instability in this case. The $m = 6$ mode remains approximately constant indicating it does not participate in the instability.

2.2.4 Linear growth rate

Over time, in line with a linear theory, we suppose that the boundary, $R(\varphi, t)$, grows or decays exponentially with each wavenumber, $m \in \mathbb{N}_0$, growing with a

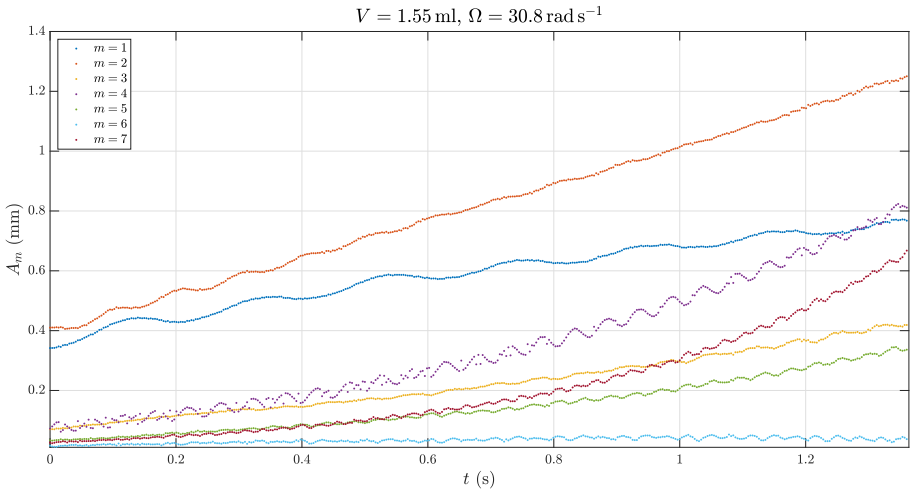


Figure 2.6: Dimensional amplitude, $A_m(t) = [a_m^2 + b_m^2]^{1/2}$, of non-axisymmetric Fourier modes, $m = 1, 2, ..., 7$ over time for an experiment in which 1.55 ml of fluid is spun at 294 rpm, corresponding to $30.8\,\mathrm{rad\,s^{-1}}$.

given complex growth rate, σ_m, hence

$$R(\varphi, t) = R_0 + \epsilon \sum_{m=0}^{\infty} R_{1m} e^{\mathrm{i}m\varphi + \sigma_m t}. \tag{2.2.5}$$

Therefore, we assume that a mode with wavenumber, m, grows or decays exponentially in time, t, with growth rate $\Re(\sigma_m) = \sigma_m^r$. Note that the growth rate, $\sigma_m \in \mathbb{C}$, is complex where the imaginary part, $\Im(\sigma_m) = \sigma_m^i$, controls precession of modes within the rotating frame. The contact line position is a function of the azimuthal angle, φ, and size of the perturbation is set by ϵ, which is assumed to be small. We take the unperturbed radius R_0 to be the mean radius at $t = 0$, the first frame in which the target rotation rate is achieved. Mathematically, (2.2.5) corresponds to taking a normal mode perturbation from a steady state solution, $r = R_0$, and superimposing linear components of different wavenumbers.

Notice that, the real part of the perturbation (2.2.5), gives

$$\Re\left[R(\varphi)\right] = R_0 + \epsilon \sum_{m=1}^{\infty} R_{1m} \left\{a_m \sin(m\varphi) + b_m \sin(m\varphi)\right\}, \tag{2.2.6}$$

where

$$a_m(t) = e^{\sigma_m^r t} \sin(\sigma_m^i t), \quad b_m(t) = e^{\sigma_m^r t} \cos(\sigma_m^i t). \tag{2.2.7}$$

Hence, the growth rate of each mode can be determined using the relationship

$$e^{\sigma_m^r t} = \left[a_m(t)^2 + b_m(t)^2\right]^{1/2} = A_m(t), \tag{2.2.8}$$

where the required amplitude, $A_m(t)$, of the Fourier series (2.2.6) is calculated from the data using the method described in § 2.2.3. For clarity we drop the superscript r and refer to the real part of the growth rate using σ_m, while being mindful that it is now a real quantity.

Figure 2.7 shows the amplitude of each of the non-axisymmetric Fourier modes for the experiment shown in figure 2.6, where amplitude is plotted on a logarithmic scale. The black line at $A_m \approx 0.08\,\text{mm}$ indicates the noise level of the data. The noise level is defined as the mean amplitude where a wavenumber, m, is required to assemble the boundary so that the mean average error between the boundary and assembled boundary is less than the size of a single pixel. The threshold of a single pixel is chosen since the Canny edge detection method defines the boundary to pixel precision and not below.

Any data below the noise level cannot be considered robust, and hence we restrict our analysis to data above this threshold. Specifically, the growth rate, σ_m, of a mode is taken as gradient of the log of amplitude of that mode as it crosses the noise level over a short time following this point since the relationship (2.2.8) predicts that the log of amplitude will be approximately linear in time.

On figure 2.7 the dashed lines illustrate the fitted curves where the gradient of each straight line gives the growth rate of each mode, $\sigma_m\,\text{s}^{-1}$, respectively. The colour of each dashed line corresponds to the wavenumber it is fitted to. The growth rate for any modes with amplitude above the noise level at $t = 0$, in this case $m = 1, 2$, are taken from this time. Whereas, the dashed lines corresponding to the $m = 5, 7$ modes are tangent to their respective curves at the point where the amplitude grows above the noise level. The $m = 6$ mode never rises above the noise level and therefore is ignored and we cannot determine its growth rate.

Overall, by assuming a normal mode perturbation for the contact line position about the spin-up radius, R_0, the linear growth rates for each Fourier mode can be extracted from the amplitudes of each mode of using the relationship (2.2.8). This will hold over a short time after $t = 0$, during which the perturbation is small

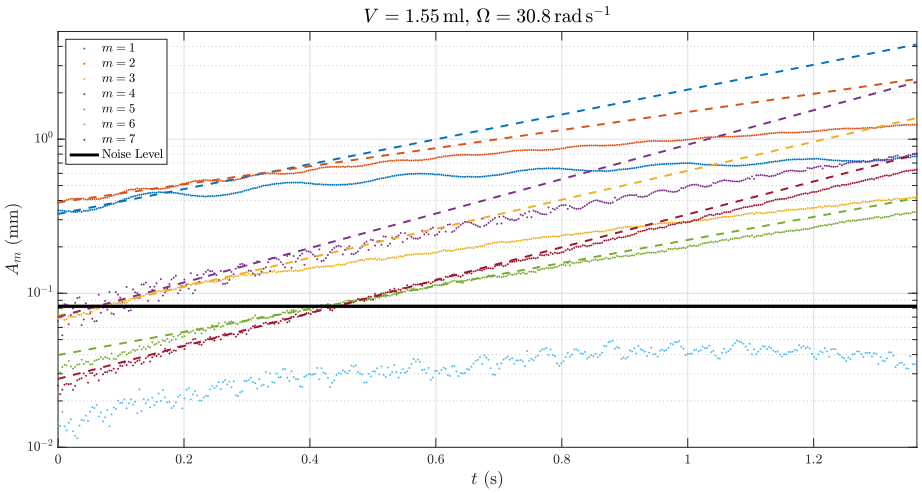


Figure 2.7: Dimensional amplitude of the first seven non-axisymmetric Fourier modes over time for the same experiment as in figure 2.6, but on a semi-logarithmic axes. Also shown are the noise level in black, and the fitted curves which have slope equal to the growth rate, σ_m, shown in dashed lines of the same colour as the wavenumber they are fitted to.

enough that a linear theory can be assumed.

2.2.5 Summary of the numerical method

Given a video file of each experiment with a chosen volume, V, and a target rotation rate, Ω, the method to analyse how the contact line of the fluid evolves in time is summarised as follows.

1. Extract all frames using MATLAB's `VideoReader` package.
2. Detect at which frame the system begins to accelerate from rest.
3. Using the known acceleration, determine the first frame where the target velocity, Ω, is achieved, defining this point as $t = 0$.
4. Find the axis of rotation using the method described in § 2.2.2.
5. For each frame:
    - Detect the pixels that lie on the contact line using the method described in § 2.2.1.

- Convert boundary points to two dimensional polar coordinates centred at the axis of rotation.
- Find the Fourier coefficients, a_m, b_m, for each mode so that the function $R(\varphi)$ is represented by the truncated Fourier series (2.2.6).
- Calculate the amplitude of each mode, $m = 0, 1, 2, ..., N$.

6. Determine the noise level of the data
7. Use the relationship involving the amplitude of Fourier modes over time (2.2.8) to calculate the growth rate, σ_m, for each mode over a short time after crossing the noise level.

2.3 Results

We considered six different volumes of dyed glycerol solution, performing 20 or more experiments for each volume for a range of rotation rates. To choose this range, we considered the equations of motion for a viscous fluid rotating in solid body rotation at rate, Ω, about the vertical axis in cylindrical polar coordinates (r, φ, z)

$$0 = -\nabla p + \rho\Omega^2 r + \mu\nabla^2 \boldsymbol{u} \tag{2.3.1}$$

for the pressure, p, and velocity, $\boldsymbol{u}$. Nondimensionalising such that the length scale is determined by the volume of fluid, V,

$$p = Pp', \quad r = V^{1/3}r', \quad z = V^{1/3}z' \quad \boldsymbol{u} = U\boldsymbol{u}', \tag{2.3.2}$$

and taking a viscous pressure scale, $P = \mu U/V^{1/3}$, leaves

$$0 = -\nabla p + \frac{\rho\Omega^2 V}{\mu U} r + \nabla^2 \boldsymbol{u}. \tag{2.3.3}$$

Therefore, the range of Ω was chosen so that $\Omega^2 V$ is similar between experimental sets. We will see in Chapter 3 that the nondimensional quantity ϕ is directly proportional to $\Omega^2 V$ and it is useful to define the quantity $\phi^* = \Omega^2 V$. Table 2.2 shows the range in the rotation rate, $\Omega, \mathrm{rad\,s^{-1}}$, for each volume considered.

The uncertainty in the volume calculation is determined by whether the final

Volume (ml)	Ω range ($\mathrm{rad\,s^{-1}}$)	Frame rate range (fps)	Resolution	Pixel length (mm)
0.15 ± 0.05	14.1 – 89.4	135 – 854	1024×1024	0.0873
0.35 ± 0.04	2.6 – 63.2	25 – 604	1024×1024	0.0868
0.57 ± 0.04	8.2 – 51.6	78 – 493	1024×1024	0.0876
0.73 ± 0.09	10.5 – 44.7	25 – 427	1024×1024	0.0878
1.20 ± 0.09	5.6 – 36.5	55 – 349	1024×1024	0.0874
1.55 ± 0.10	5.0 – 31.6	48 – 302	1408×1400	0.0872

Table 2.2: Summary of the six experimental sets performed for different volumes, showing the range of rotation rates, frame resolution and corresponding pixel length.

droplet within the nozzle is dispensed onto the disc or not. The rotation rate, Ω, fluctuates to a maximum of 0.02 rpm, which is equivalent to $2 \times 10^{-3}\,\mathrm{rad\,s^{-1}}$ and is therefore deemed negligible since $\Omega = \mathcal{O}(10)\,\mathrm{rad\,s^{-1}}$. For each experimental set, the resolution and corresponding pixel size was also recorded. The size of a single pixel was determined by taking a reference image of a circle of known radius, calculating the radius in pixels, and dividing this value by the known true radius in millimeters. A reference was taken for each experimental set to account for movement of the camera between sets. The error in the pixel length is defined by the 95% confidence interval in the calculation of the radius in pixels, and is less than 1×10^{-5} mm in each case.

2.3.1 Qualitative observations

Once the fluid was dispensed onto the disc, it was allowed to relax into an equilibrium state, with small amounts of axisymmetric spreading observed. The resultant the droplet had a circular shape centered on the axis of rotation with a radius determined by the fluids physical properties, contact angle and volume. This dependence will be discussed further in chapter 8.

When the motor is switched on and the target rotation rate is achieved, we observed that axisymmetry is broken almost immediately, leading quickly to the formation of distinct fingers. Kulakarni *et al.* [67] observed similarly short times to the onset of fingering in their experiments on glycerol solutions. Our qual-

itative observations are contrary to previous experiments on silicon oils where there is a long axisymmetric phase prior to the onset of a fingering instability [26, 58, 60, 62]. During the early stages following reaching the target rotation rate we observed the formation of a capillary ridge close to the contact line, with a flatter internal region. This is visible in figure 2.3 (a), and is in agreement with each previous experiment.

Following the short initial phase, we observed a fingering instability, where the number of fingers forming appeared to increase with both rotation rate and volume of fluid. Holloway *et al.* [62] and Wang and Chou [61] both reported similar observations for silicon oils, contrary to earlier experiments [26, 58]. Veretennikov *et al.* [66] reported the formation of only one finger forming for glycerol, however it appears these observations were due to a limited range of rotation rates investigated.

Overall, the qualitative nature of the experiments we performed was similar to previous experiments such that a fingering instability occurred. However, the long axisymmetric phase observed in previous experiments with silicon oils was not seen, with initial axisymmetry being quickly broken after reaching the target rotation rate.

2.3.2 Spin-up radius

The spin-up radius, R_0, is defined by the value of a_0 in the Fourier series (2.2.6) at the frame after which the target velocity has first been achieved, namely $t = 0$. In § 2.1.1 we stated that the acceleration was chosen according to the spin-up time (2.1.1) for each experiment. Therefore, to establish the frame in which the target velocity is achieved effectively, we require the frame in which movement is first detected. To find this point we consider the difference in the background image of successive frames, finding the minimum frame where the maximum value in the difference of pixel intensity is above a given threshold. The minimum frame is calculated for several thresholds, with larger thresholds capturing greater amounts of movement and *vice versa*. Lower thresholds are subject to greater amounts of noise in the image, and therefore can lead to false positives in the detection of true motion. Therefore, the frame at which movement is first detected is taken from using the minimum threshold where the detected frame is sufficiently close

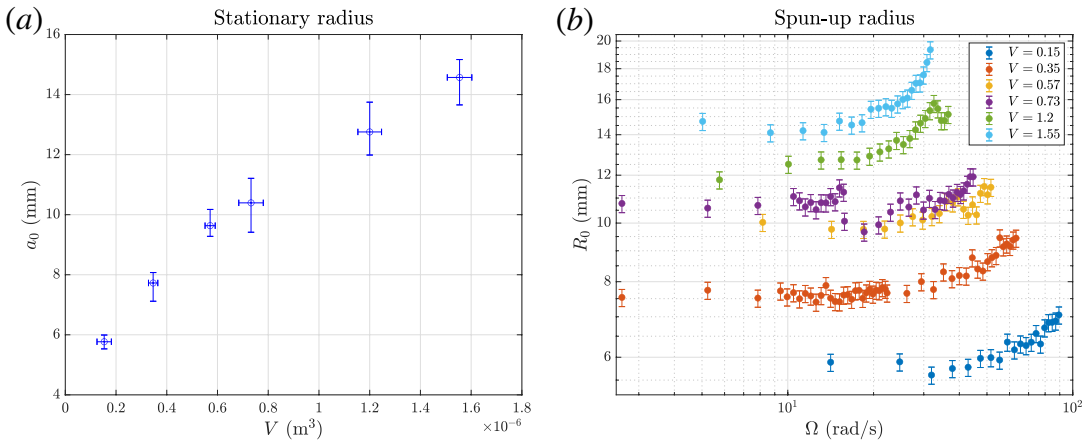


Figure 2.8: (a) The mean of the radii of each experimental set before spin-up, against volume, where the error bars show the skew in initial radii between experiments within a set. (b) The spin-up radius, defined as the size of the axisymmetric Fourier mode at the frame where the target velocity, Ω, is reached, plotted against rotation rate for each set of experiments in different colours.

to that from the largest threshold, since large thresholds are robust to noise.

Prior to any movement being detected the system is at rest. By calculating the first Fourier coefficient, a_0, of each frame where $t < -\tau$ we assess the initial condition of the experiments. Since we are considering the system prior to spin-up, the initial condition between experiments of the same volume should have comparable radii. Figure 2.8 (a) shows the radius of fluid masses before movement is detected for each volume, averaged over the constituent experiments. Note that, as expected, the droplet radius increases with volume. The horizontal error bars show the uncertainty in the volume, as presented in table 2.2, while the vertical error bars show the range of radii calculated for the same volume. It is observed that the error in the radii generally increases with volume, which is likely due to the greater error in the dispensed volume for greater volumes. Furthermore, larger droplets are more susceptible to non-axisymmetric perturbations when the fluid is dispensed onto the plate [32], leading to the range of radii calculated for different experiments.

Recall that the spin-up radius, R_0, is defined as the amplitude of the $m = 0$ mode at $t = 0$. Figure 2.8 (b) shows the spin-up radius for each experiment performed, with different volumes shown in different colours. We see that for each volume under consideration, the spin-up radius increases as the rotation rate, Ω, increases.

This result is anticipated since centrifugal force is directed radially outwards from the centre of mass, so that higher rotation rates cause the boundary of the fluid, or contact line, to be further from the axis of rotation. Furthermore, similar to the stationary case presented in figure 2.8 (a) we observe that R_0 increases with volume for the same rotation rate.

To assess the repeatability of the data, we repeated a single experiment where $V = 0.73\,\text{ml}$ and $\Omega = 34.2\,\text{rad}\,\text{s}^{-1}$ fifteen times, calculating the percentage errors of the maximum and minimum values of R_0 from the mean. We found the upper percentage error to be 3.1% while the lower -3.4%. The error bars shown on figure 2.8 (b) reflect the percentage error from the value calculated. There is also error associated in the detection of the frame at which movement begins, which can be as many as five frames. This error is one sided since the algorithm always detects movement, but is always greater than or equal to the true start frame, therefore, there is subsequently an error associated to each calculated R_0. The error in calculation is small and increases with rotation rate, with the maximum error over all experiments being approximately 0.2 mm which is negligible in comparison to the error in repeats.

2.3.3 Axisymmetric spreading

During the analysis in the previous section we identified the time at which spin-up occurs and subsequently the initial radius R_0, defined as the amplitude of the axisymmetric mode at the frame corresponding to $t = 0$. We now discuss how the amplitude of the axisymmetric mode, $a_0(t)$, grows over time from the initial condition at $r = R_0$.

Figure 2.9 (a) shows the difference between $a_0(t)$ and R_0 over time, with each axis plotted on a log scale. The specific experiment under consideration is when $V = 0.35\,\text{ml}$ and $\Omega = 61.8\,\text{rad}\,\text{s}^{-1}$. We see that $a_0 - R_0$ grows linearly over time when t is small, so that

$$a_0(t) = R_0 + \kappa_e t, \tag{2.3.4}$$

where κ_e is the contact line speed, determined from the data. Note that, this experimental contact line speed is not the same as the contact line speed used in the Tanner law (1.2.4), κ, however these values are directly proportional. We find

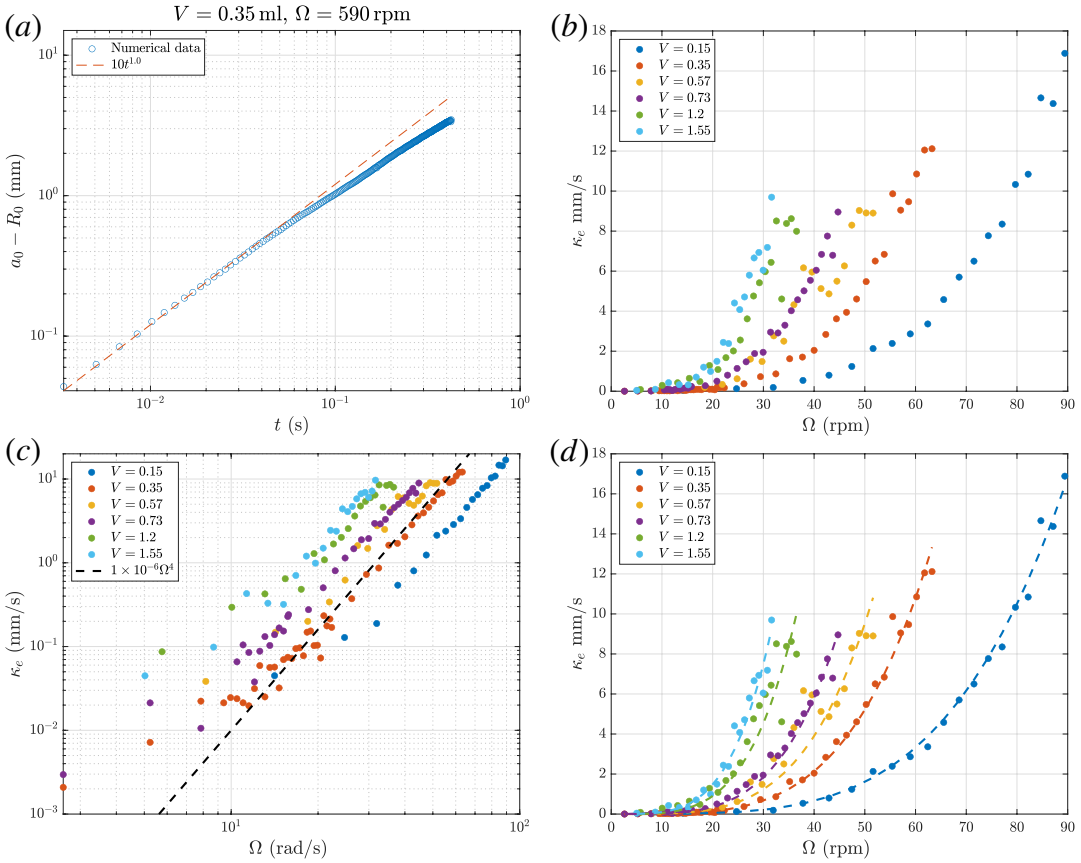


Figure 2.9: (a) Evolution of the axisymmetric mode, a_0, in time from the spin-up radius for a single experiment, plotted on logarithmic axes showing linear growth. (b) Contact line speed for each experiment, defined as the slope of the dashed red line in figure (a), for each experiment, plotted against the rotation rate. (c) Contact line speed plotted on logarithmic axes, showing that $\kappa_e \sim \Omega^4$, for each volume. The dashed black line is of the curve $\kappa_e = \Omega^4$, for reference. (d) Figure (c) with fitted power law model (2.3.6) plotted for comparison, with values taken from table 2.3, showing good agreement.

that for each volume and rotation rate considered, the growth of the axisymmetric mode remains linear over time, whereas the contact line speed varies so that, $\kappa_e = \kappa_e(\Omega, V)$. Figure 2.9 (b) shows the contact line speed, $\kappa_e(\Omega, V)$, as a function of the rotation rate, Ω, with each experimental set of constant volume shown in a different colour. For each volume, faster rotation speeds correspond to greater contact line speeds. Furthermore, to achieve the same rate of spreading smaller volumes require larger rotational speeds. Figure 2.9 (c) shows the same results plotted with logarithmic axes. We observe that for each volume, the contact line speed is linear on these axes, with a slope of approximately 4, as indicated by the black dashed line. Therefore, the data indicates that the contact line speed,

Volume (ml)	k	n	R^2 %
0.15	7.00	1.53	99.2
0.35	10.90	1.56	99.0
0.57	20.32	1.62	87.1
0.73	9.74	1.57	98.4
1.20	9.62	1.56	87.6
1.55	11.35	1.56	95.9
-	11.73	1.57	94.5

Table 2.3: Values of fitting coefficient, k, and exponent, n, from (2.3.6) for each volume, V. The R^2 percentage calculated from the residuals between the data and model are also presented showing good agreement in each case. The bottom row is shows the same values when the model is fitted to all of the data at once, again showing good agreement.

$\kappa_e(\Omega, V)$, is given by

$$\kappa_e(\Omega, V) = kV^n\Omega^4, \tag{2.3.5}$$

so that in time the mean radius of the contact line spreads like

$$a_0(t) = R_0 + kV^n\Omega^4 t. \tag{2.3.6}$$

The values of the coefficient k and power n are determined empirically using least squares fitting for each data set, and are summarised in table 2.3. The R^2 percentage, indicating the fit between the data and the model is also presented. We see that the exponent n is approximately constant between experimental sets, whereas the coefficient k is skewed. The experimental set where $V = 0.57\,\text{ml}$ returns a value of k twice that of the other experiments which are similar, indicating uncertainty in the data for this case. Furthermore, note that the R^2 percentage for this data set is the minimum achieved. In each case the R^2 percentage indicates that the fit between the data and model is good. Figure 2.9 (d) shows the fitted curves and the data on the same plot, confirming that the agreement is good. The final row of table 2.3 reports the values of k, n and associated R^2 value when the data is fitted all together, rather than in individual data sets. The R^2 value indicates that fitting with a single value of k and n for all experiments is appropriate.

Holloway *et al.* [62] reported a similar power law for axisymmetric spreading, also

reporting that the contact line radius grows linearly in time but with different contact line speed $\kappa_e \propto \Omega^{2.47} V^{0.73}$. However, it is likely that the difference in parameter regimes is responsible for the observed discrepancies, since Holloway *et al.* analysis focused on volumes $50\,\mu\text{l} \leqslant V \leqslant 250\,\mu\text{l}$ of silicone oil, whereas our analysis considered larger volumes of glycerol, reported in table 2.3. Furthermore, the difference in fluid and substrate combination used will alter the contact angle, resulting in differences in the contact line speed which is demonstrated by the Tanner law (1.2.4). In § 2.3.1 we noted that axisymmetry was broken very soon following the target rotation rate being met. As a result, the experimental data presented here does not lend well to the mathematical modelling developed by Wilson *et al.* [85] for axisymmetric spreading during spin coating, up to the onset of fingering.

2.3.4 Non-axisymmetric spreading

Next, we present the results for non-axisymmetric modes, that is, $m = 1, 2, 3, ...$ Recall from § 2.2.4 that the growth rate of a given Fourier mode, m, is found using the relationship (2.2.8). Specifically, the relationship (2.2.8) relates the growth rate of a linear perturbation in time with to the amplitude of Fourier modes, which are calculated from the data using the method described in § 2.2.1–2.2.6. The growth rates of each wavenumber with amplitude exceeding the noise level are calculated by using a linear least squares fit through the values corresponding to the first sixty frames following crossing the noise level. In figure 2.7 the only non-axisymmetric wavenumbers which exceed the noise level were modes $m = 1, 2, ..., 5$. Sixty frames corresponds to a single rotation of the disc, so this choice mitigates the effects of any disc oscillations on the data. The oscillations are caused by the small error in the calculation of the centre of rotation; in figure 2.7 the maximum amplitude of oscillation is small, being approximately 0.08 mm.

The assumption made in § 2.2.4 is that the perturbations to the initial condition at spin-up are small enough that a linear theory holds true. Therefore, we shall only consider the modes which have amplitude above the noise level a short time following the target rotation, Ω, being reached, referred to as 'accepted modes'.

The time post spin-up, t_c, is chosen to scale with the rotation rate, Ω, such that

$$t_c = \frac{T^*}{\Omega}. \tag{2.3.7}$$

The inverse scaling of the critical time with rotation rate is chosen to account for the fact that the instability occurs sooner following spin-up for experiments with larger rotation rates. Since the frame rate of recording is equal to the rotation rate, this scaling amounts to taking T^* frames post spin-up.

Figures 2.10 shows the accepted modes for $T^* = 120$ at each target rotation rate plotted with black circles, where each figure corresponds to a data set at a different volume. The solid red circles in each figure correspond to the dominant mode, that is, the wavenumber which has the greatest associated growth rate. We see in each case that larger rotation rates cause higher wavenumbers to become unstable within the same nondimensional time T^*, so that each mode has a rotation rate at which it becomes unstable. Furthermore, the dominant mode increases with Ω in each of the figures. There is indication that the dominant mode increases sequentially as Ω increases, particularly visible in figure 2.10 (f) when $V = 1.55\,\mathrm{ml}$ in qualitative agreement with previous mathematical modelling [43]. These results are in contrast to those reported by Melo *et al.* [26] and Fraysse and Homsy [58], who state that the number of fingers, and therefore the dominant wavenumber of the instability, is independent of the rotation rate. However, our results qualitatively agree with more recent experiments [62, 64, 67]. Furthermore, our results extend those of Veretennikov *et al.* [66] to greater rotation rates, where we observe the formation of multiple fingers for a glycerol solution, as stated in § 2.3.1. Our experiments consider a larger portion of the experimental parameter range than many studies, which is likely to be responsible for the aforementioned qualitative differences.

Comparing between figures 2.10 (a)–(f) we can also assess the effect of changing the volume. We observe for a fixed rotation rate that the dominant mode increases with volume. To illustrate this, consider the dominant mode at $\Omega \approx 30\,\mathrm{rad\,s^{-1}}$ in each figure; which increases from $m = 1$ when $V = 0.15\,\mathrm{ml}$ to $m = 5$ when $V = 1.55\,\mathrm{ml}$. Similarly, we observe that the threshold rotation rate for a mode to become dominant decreases as the volume increases.

The accepted modes are a subset of those which rise above the noise level. Fig-

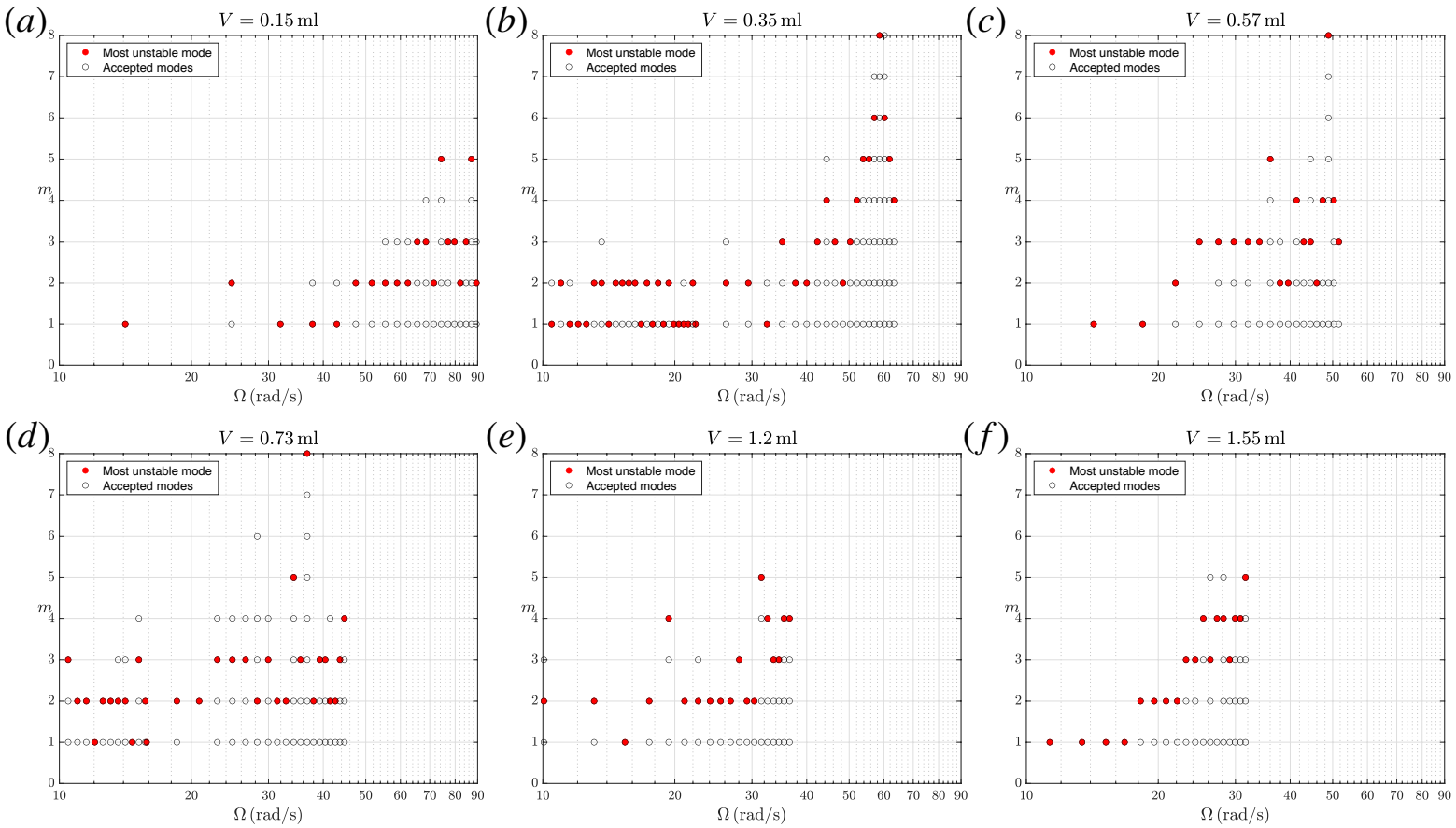


Figure 2.10: The accepted modes at $T^* = 120$, are shown in black circles against rotation rate for each volume on a separate figure. These are the Fourier modes required to reproduce the boundary at a nondimensional time T^* following spin-up. Also shown on each figure in solid red, are the dominant modes, that is, the wavenumber with the largest growth rate.

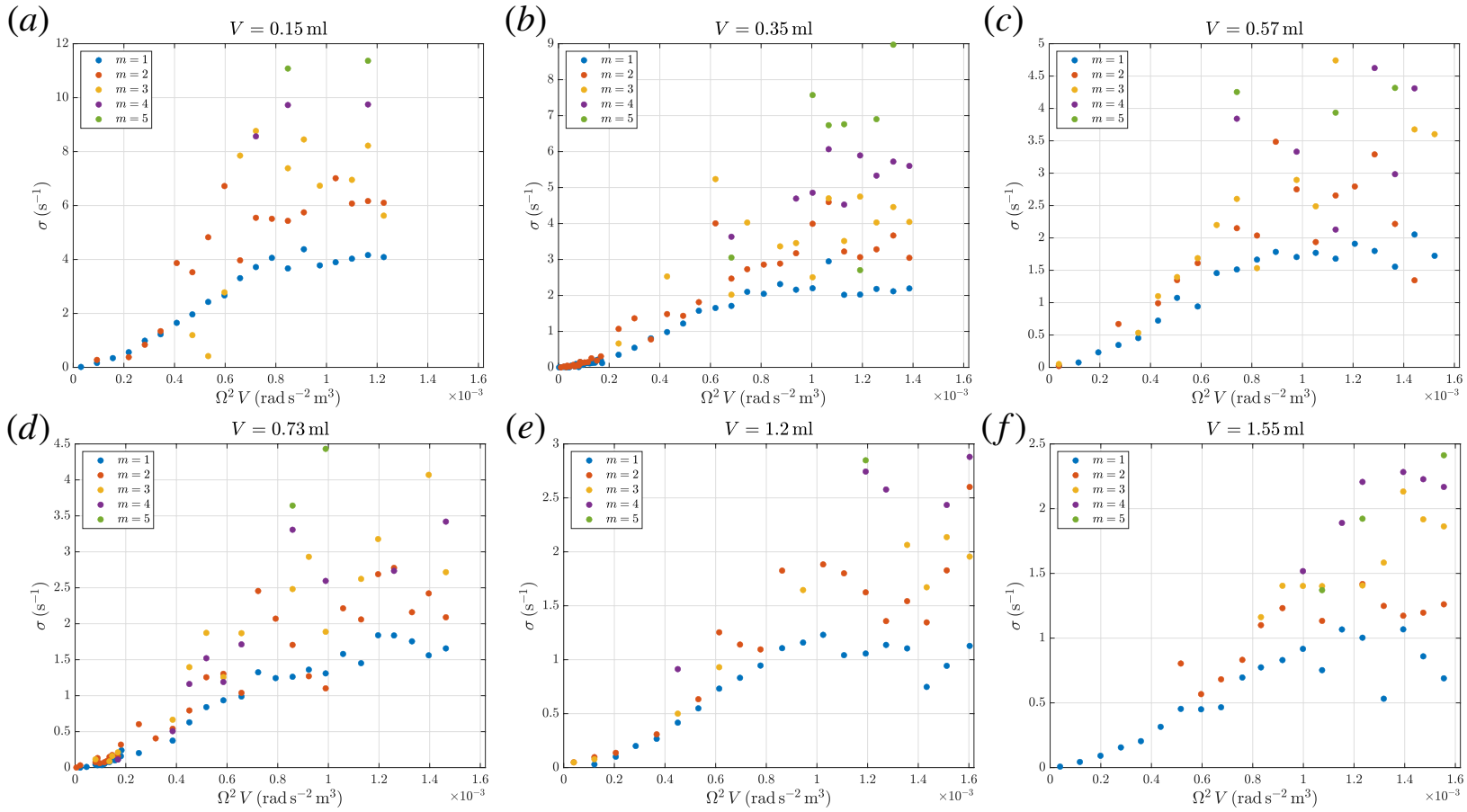


Figure 2.11: The growth rates, σ_m of the first five non-axisymmetric Fourier modes $m = 1, 2, ..., 5$, where they are accepted, according to figure 2.10 and shown in different colours. The x-axis is chosen to be $\phi^* = \Omega^2 V$, so that the figures are comparable to one another.

ures 2.11 shows the dimensional growth rates, σ_m, of the first five modes for each volume, where accepted. The x-axis is the same in each figure and is given by $\phi^* = \Omega^2 V$, which as shown in (2.3.3), is directly proportional to a nondimensional measure of the rotation rate, meaning the data is comparable between experiments. Note that, the y-axis in each figure is different. In each figure we see the general trend that as the rotation rate is increased that the growth rate of each mode increases. We observe that the rate at which this happens decreases as ϕ^* increases, this is particularly visible in the $m = 1$ mode with the curve in each figure flattening and in some cases decreasing as ϕ^* increases. A possible conclusion is that there exists an upper limit on the growth rate of each mode, which is dependent on the volume and physical properties of the fluid. As stated in the analysis of figure 2.10, greater wavenumbers become dominant as ϕ^* increases for each volume considered. Comparing between figures we see that for each mode, smaller volumes have larger growth rates for the same ϕ^*, demonstrated by the decreasing growth rate of the $m = 1$ mode at $\phi^* = 1$ across each subfigure. This could perhaps be predicted since larger rotation rates are required for the same ϕ^*, corresponding to greater contact line speeds.

2.4 Summary

In this chapter we investigated the contact line instability when a viscous fluid of a prescribed volume, V, is spun at a chosen rotation rate, Ω. Specifically, we discussed the relative effects of rotation and volume in a regime where inertia is assumed to be negligible compared to viscosity for droplets upon a rotating disc. To do so, we described a methodology for performing such experiments, where a glycerol solution was used to ensure a viscous regime. The recorded videos were analysed using Fourier analysis, first assessing the initial condition of the experiments.

We found that, as may be predicted physically, the initial radius R_0 increases with both rotation rate and volume. Next, we assessed the axisymmetric spreading from the initial condition, finding a power law for growth by fitting to the data using a non-linear least squares method showing good agreement to the data. The investigated range of volumes in our experiments were macroscopic, leading to the

observed qualitative differences in the axisymmetric phase of the experiments, and spreading rates in comparison to Holloway *et al.* [62] who considered microscopic volumes of silicon oils. Finally, we considered non-axisymmetric perturbations ascertaining that the dominant Fourier mode of instability increases with rotation and volume for each volume considered. Furthermore, we found that the threshold rotation rate for a mode to become dominant decreases as the volume increases, converse to findings in early experiments [26, 53, 58] into microscopic droplets of silicon oils and previous experiments into macroscopic volumes of glycerol [66].

Chapter 3

Thin film model formulation and equilibrium solutions

To begin our theoretical analysis, we derive a model to describe the experiments detailed in chapter 2. The model is derived directly from the governing Navier-Stokes equations within a rotating frame of reference, coupled with appropriate boundary conditions. The lubrication approximation is used to simplify the modelling. We derive an evolution equation governing the shape and position of a mass of fluid subject to rotation, the form of which is common in the literature for problems of this type [32, 42, 43, 31].

Finally, we discuss equilibrium solutions to the derived evolution equation, finding steady axisymmetric solutions which have zero velocity in the rotating frame of reference. We recover and further discuss the solutions of McKinley *et al.* [42] subject to a transformation of nondimensional variables.

3.1 Model

3.1.1 Equations of motion

We consider a fixed mass of fluid, on a flat plate, at constant temperature, in solid body rotation about the vertical axis with a free surface, which meets the solid plate at the contact line. A schematic diagram is shown in figure 3.1 showing the geometry and common notation used throughout this chapter. The coordinate

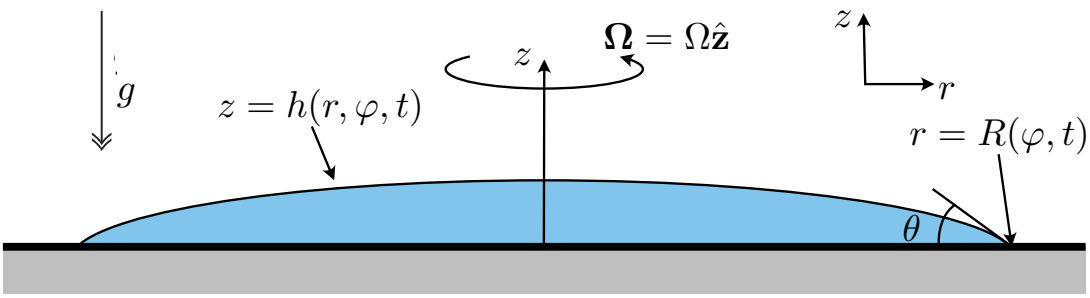


Figure 3.1: Schematic diagram of a viscous, incompressible fluid layer on a plate, spun about the vertical axis.

system used is cylindrical polar coordinates where a point in space is defined by a radial distance, r, from the origin, an azimuthal angle, φ, and a height, z. The governing dimensional set of equations for fluid velocity, $\boldsymbol{u} = (u, v, w)$, and pressure, p, are the Navier–Stokes equations in a rotating frame of reference including gravity,

$$\rho\frac{\mathrm{D}\boldsymbol{u}}{\mathrm{D}t} = -\nabla p - \rho\boldsymbol{\Omega} \times (\boldsymbol{\Omega} \times \boldsymbol{x}) - 2\rho\boldsymbol{\Omega} \times \boldsymbol{u} - \rho g\hat{\boldsymbol{z}} + \mu\nabla^2\boldsymbol{u}, \tag{3.1.1}$$

(see Appendix A for derivation), and the incompressibility condition,

$$\boldsymbol{\nabla} \cdot \boldsymbol{u} = 0. \tag{3.1.2}$$

Here $\boldsymbol{x} = r\hat{\boldsymbol{r}} + z\hat{\boldsymbol{z}}$ is the position vector where $\hat{\boldsymbol{r}}$ and $\hat{\boldsymbol{z}}$ are unit vectors in the radial and axial directions, respectively, while the constant rotation rate is given by $\boldsymbol{\Omega} = \Omega\hat{\boldsymbol{z}}$. The term on the left hand side of (3.1.1) is the force due to inertia, given by Newton's second law, while the first term on the right hand side is the pressure gradient. The second and third terms on the right hand side of (3.1.1) correspond to centrifugal and Coriolis forces, respectively, and arise when considering the Navier–Stokes equations within a rotating frame of reference. The fourth and fifth terms model gravitational and viscous forces.

3.1.2 Boundary conditions

We define the free surface of the fluid as

$$\mathscr{S} := z - h(r, \varphi, t) = 0, \tag{3.1.3}$$

on which we impose a kinematic condition and three continuity of stress conditions, one in each direction. The kinematic condition states that the fluid particles on the free surface should move with the fluid. Hence, the material derivative of the free surface (3.1.3) is zero on the free surface

$$\frac{\mathrm{D}}{\mathrm{D}t}\Big(z - h(r,\varphi,t)\Big)\Big|_{\mathscr{S}} = 0. \tag{3.1.4}$$

The continuity of stress condition is given at the free surface by the Young–Laplace equation

$$\big[\underline{\underline{\sigma}} \cdot \boldsymbol{n}\big]^{+}_{-} = \gamma(\nabla \cdot \hat{\boldsymbol{n}})\boldsymbol{n} \tag{3.1.5}$$

on $\mathscr{S}$, where $\hat{\boldsymbol{n}}$ is the outward pointing normal from the fluid volume into the atmospheric gas. The notation $[\,\cdot\,]^{+}_{-}$ indicates a jump across the free surface from the atmospheric gas into the fluid volume.

The boundary conditions at the solid plate, $z = 0$, are a no-penetration condition,

$$w = 0, \tag{3.1.6}$$

and two slip conditions for the tangential velocity components,

$$u = \frac{\alpha}{3h}\frac{\partial u}{\partial z}, \quad v = \frac{\alpha}{3h}\frac{\partial v}{\partial z}, \tag{3.1.7}$$

where α is the small slip length. We choose the same slip condition as Greenspan [31], where the slip is a function of the height of the interface rather than constant. This is the simplest model for slip in which the contact line velocity can be non-zero, and hence allowed to move. Further justification for this choice of slip coefficient is provided in § 5.1. In the limit $\alpha = 0$ we recover the usual no-slip condition.

The position of the contact line is given by $r = R(\varphi, t)$, at which we impose three physical conditions. First is the contact condition, which states that the height of the free surface is zero at the contact line

$$h(R(\varphi,t),\varphi,t) = 0. \tag{3.1.8}$$

Second is a contact angle condition, such that the angle at the contact line is

specified as part of the model,

$$\left.\frac{\partial h}{\partial r}\right|_{r=R(\varphi,t)} = -\tan\theta, \tag{3.1.9}$$

where the contact angle is denoted by θ. The contact line and contact angle are shown on the schematic diagram in figure 3.1. The model we use to describe the physics at the contact line is the Tanner law [27, 30], which in the form we consider is

$$\frac{\partial R}{\partial t} = \kappa(\theta^q - \theta_c^q), \tag{3.1.10}$$

where θ_c is the equilibrium contact angle and κ, q are empirically determined positive constants. The constant κ is a measure of the contact line speed. In chapter 1 we discussed how the simplified form (3.1.10) neglecting contact angle hysteresis results in the contact line being allowed to both advance and retreat.

The third physical condition is the contact line kinematic condition

$$\frac{\mathrm{D}}{\mathrm{D}t}\Big(r - R(\varphi,t)\Big) = 0, \tag{3.1.11}$$

at $r = R(\varphi,t), z = 0$, which similarly to the free surface kinematic condition (3.1.4) states the fluid particles at the interface should move with the fluid; the interface being the contact line.

We impose regularity conditions along the axis $r = 0$ so that the velocity at the origin is finite,

$$|\boldsymbol{u}(0,\varphi,z,t)| < \infty. \tag{3.1.12}$$

Furthermore, to ensure the shape of the free surface is differentiable at $r = 0$ we enforce that

$$\left.\frac{\partial h}{\partial r}\right|_{r=0} = 0. \tag{3.1.13}$$

Finally, since the mass of fluid placed on the plate is fixed we have the volume conservation condition

$$V_f = \int_0^{2\pi}\int_0^{R(\varphi,t)} rh(r,\varphi,t)\,\mathrm{d}r\,\mathrm{d}\varphi, \tag{3.1.14}$$

for a fixed volume of fluid, V_f.

3.2 Nondimensionalisation

We nondimensionalise the system, assuming that the horizontal lengthscale is much larger than the vertical lengthscale. The equilibrium contact angle, θ_c, is the natural choice of aspect ratio and is assumed small. Consequently, the following scales are introduced

$$r = Lr', \quad z = \theta_c L z', \quad u = Uu', \quad v = Vv', \quad w = Ww', \quad t = Tt', \quad p = Pp'. \tag{3.2.1}$$

Immediately from the incompressibility condition (3.1.2) we take the azimuthal and axial velocity scales to be $V = U, W = \theta_c U$, giving

$$\frac{1}{r'}\frac{\partial}{\partial r'}(r'u') + \frac{1}{r'}\frac{\partial v'}{\partial \varphi} + \frac{\partial w'}{\partial z'} = 0. \tag{3.2.2}$$

The lengthscale, L is determined from the volume equation (3.1.14) so that $L = (V_f/\theta_c)^{1/3}$, leaving

$$V_f' = \int_0^{2\pi}\int_0^{R'(\varphi,t')} r'h'(r',\varphi,t')\,\mathrm{d}r'\,\mathrm{d}\varphi. \tag{3.2.3}$$

Although due to the choice of lengthscale $V_f' = 1$, we will keep V_f' in our analytical formulation for clarity, while in numerical calculations, unless stated otherwise, it will be taken to be unity.

The free surface kinematic condition (3.1.4) gives us the timescale $T = L/U$ and simplifies to

$$w' = \frac{\partial h'}{\partial t'} + u'\frac{\partial h'}{\partial r'} + \frac{v'}{r'}\frac{\partial h'}{\partial \varphi} \tag{3.2.4}$$

at $z' = h'(r', \varphi, t')$. The contact line kinematic condition (3.1.11) simplifies to

$$u' = \frac{\partial R'}{\partial t'} + \frac{v'}{R'}\frac{\partial R'}{\partial \varphi} \tag{3.2.5}$$

at the contact line, $z' = 0, r' = R'(\varphi, t')$.

To nondimensionalise the stress continuity condition (3.1.5) we must first determine the unit normal to the free surface (3.1.3). Expressed in terms of nondimen-

sional quantities,

$$\hat{\boldsymbol{n}} = \frac{\nabla \mathscr{S}}{|\nabla \mathscr{S}|} = \hat{\boldsymbol{z}} - \theta_c \nabla'_H h' + \mathcal{O}(\theta_c^2), \tag{3.2.6}$$

where $\nabla_H = \partial_r \hat{\boldsymbol{r}} + r^{-1}\partial_\varphi \hat{\boldsymbol{\varphi}}$ denotes the gradient operator in two dimensional polar coordinates. Hence the curvature up to $\mathcal{O}(\theta_c^2)$, κ, of the free surface (3.1.3) is

$$\kappa = \nabla \cdot \hat{\boldsymbol{z}} - \left[\frac{\theta_c}{L}\right] \nabla' \cdot \nabla'_H h' = -\left[\frac{\theta_c}{L}\right] \nabla'^2 h'. \tag{3.2.7}$$

Note, since $h = h(r, \varphi, t)$ that $\nabla^2 h = \nabla_H^2 h$. The stress tensor, $\underline{\underline{\sigma}}$, is given by $\underline{\underline{\sigma}} = -p\underline{\underline{I}} + 2\mu \underline{\underline{e}}$ for rate of strain tensor $\underline{\underline{e}} = \frac{1}{2}(\nabla \boldsymbol{u} + \nabla \boldsymbol{u}^T)$. In cylindrical polar coordinates, the rate of strain tensor is

$$\underline{\underline{e}} = \left[\frac{U}{\theta_c L}\right] \begin{pmatrix} \theta_c \dfrac{\partial u'}{\partial r'} & \dfrac{\theta_c}{2}\left\{ r' \dfrac{\partial}{\partial r'}\left(\dfrac{v'}{r'}\right) + \dfrac{1}{r'}\dfrac{\partial u'}{\partial \varphi} \right\} & \dfrac{1}{2}\dfrac{\partial u'}{\partial z'} + \dfrac{\theta_c^2}{2}\dfrac{\partial w'}{\partial r'} \\ \dfrac{\theta_c}{2}\left\{ r' \dfrac{\partial}{\partial r'}\left(\dfrac{v'}{r'}\right) + \dfrac{1}{r'}\dfrac{\partial u'}{\partial \varphi} \right\} & \theta_c \left\{ \dfrac{1}{r'}\dfrac{\partial v'}{\partial \varphi} + \dfrac{u'}{r'} \right\} & \dfrac{1}{2}\dfrac{\partial v'}{\partial z'} + \dfrac{\theta_c^2}{2r'}\dfrac{\partial w'}{\partial \varphi} \\ \dfrac{1}{2}\dfrac{\partial u'}{\partial z'} + \dfrac{\theta_c^2}{2}\dfrac{\partial w'}{\partial r'} & \dfrac{1}{2}\dfrac{\partial v'}{\partial z'} + \dfrac{\theta_c^2}{2r'}\dfrac{\partial w'}{\partial \varphi} & \theta_c \dfrac{\partial w'}{\partial z'} \end{pmatrix} \tag{3.2.8}$$

so that in the normal direction to the free surface,

$$\underline{\underline{e}} \cdot \boldsymbol{n} = \left[\frac{U}{\theta_c L}\right] \begin{pmatrix} \dfrac{1}{2}\dfrac{\partial u'}{\partial z'} + \mathcal{O}(\theta_c^2) \\ \dfrac{1}{2}\dfrac{\partial v'}{\partial z'} + \mathcal{O}(\theta_c^2) \\ \mathcal{O}(\theta_c^2) \end{pmatrix}. \tag{3.2.9}$$

Hence, the three stress conditions are

$$[P]\frac{\partial h'}{\partial r'}[p']_-^+ - \left[\frac{U\mu}{L\theta_c^2}\right]\frac{\partial u'}{\partial z'} = \left[\frac{\gamma\theta_c}{L}\right]\frac{\partial h'}{\partial r'}\nabla'^2 h' + \mathcal{O}(\theta_c^2), \tag{3.2.10}$$

$$[P]\frac{1}{r'}\frac{\partial h'}{\partial \varphi}[p']_-^+ - \left[\frac{U\mu}{L\theta_c^2}\right]\frac{\partial v'}{\partial z'} = \left[\frac{\gamma\theta_c}{L}\right]\frac{1}{r'}\frac{\partial h'}{\partial \varphi}\nabla'^2 h' + \mathcal{O}(\theta_c^2), \tag{3.2.11}$$

$$[P][p']_-^+ = \left[\frac{\gamma\theta_c}{L}\right]\nabla'^2 h' + \mathcal{O}(\theta_c^2) \tag{3.2.12}$$

at $z' = h'$ in the radial, azimuthal and axial directions, respectively. Keeping a general velocity scale, U, we take a viscous pressure scale, so that $P = \mu U/L\theta_c^2$,

giving rise to a capillary number $C = U\mu/\gamma\theta_c^3$, a ratio of viscosity to surface tension. Furthermore, using the axial stress component (3.2.12) to simplify the radial and azimuthal stress components (3.2.10, 3.2.11) the three stress conditions are

$$0 = \frac{\partial u'}{\partial z'} + \mathcal{O}(\theta_c^2), \quad 0 = \frac{\partial v'}{\partial z'} + \mathcal{O}(\theta_c^2), \tag{3.2.13}$$

$$p' = p'_g - C^{-1}\nabla'^2 h' + \mathcal{O}(\theta_c^2) \tag{3.2.14}$$

at $z' = h'(r', \varphi, t')$ in the radial, azimuthal and axial directions, respectively. The atmospheric pressure is denoted p_g and is constant.

Next, we nondimensionalise the equations of motion (3.1.1) in component form,

$$\left[\frac{\rho U^2}{L}\right]\frac{\mathrm{D}u'}{\mathrm{D}t'} = -\left[\frac{P}{L}\right]\frac{\partial p'}{\partial r'} + [\rho\Omega^2 L]r' + 2[\rho\Omega U]v' + \left[\frac{\mu U}{L^2\theta_c^2}\right]\left\{\frac{\partial^2 u'}{\partial z'^2} + \mathcal{O}(\theta_c^2)\right\}, \tag{3.2.15}$$

$$\left[\frac{\rho U^2}{L}\right]\frac{\mathrm{D}v'}{\mathrm{D}t'} = -\left[\frac{P}{L}\right]\frac{1}{r'}\frac{\partial p'}{\partial \varphi} - 2[\rho\Omega U]u' + \left[\frac{\mu U}{L^2\theta_c^2}\right]\left\{\frac{\partial^2 v'}{\partial z'^2} + \mathcal{O}(\theta_c^2)\right\}, \tag{3.2.16}$$

$$\left[\frac{\rho\theta_c U^2}{L}\right]\frac{\mathrm{D}w'}{\mathrm{D}t'} = -\left[\frac{P}{\theta_c L}\right]\frac{\partial p'}{\partial z'} - [\rho g] + \left[\frac{\mu U}{L^2\theta_c}\right]\left\{\frac{\partial^2 w'}{\partial z'^2} + \mathcal{O}(\theta_c^2)\right\}. \tag{3.2.17}$$

Taking the viscous pressure scale for each equation results in two distinct pressure scales,

$$P_1 = P_2 = \frac{\mu U}{L\theta_c^2}, \quad P_3 = \frac{\mu U}{L} = \theta_c^2 P_1, \tag{3.2.18}$$

where the subscripts represent the component of the equations of motion (3.2.15)–(3.2.17) it arises from. We can see that the greatest pressure changes come from choosing $P = P_1$, since $\theta_c \ll 1$, consistent with our previous choice of pressure scale. Substituting into (3.2.15)–(3.2.17) we get

$$\theta_c^2\,\mathrm{Re}\frac{\mathrm{D}u'}{\mathrm{D}t'} = -\frac{\partial p'}{\partial r'} + \frac{\phi}{C}r' + \frac{2\theta_c^2}{\mathrm{Ek}}v' + \frac{\partial^2 u'}{\partial z'^2} + \mathcal{O}(\theta_c^2), \tag{3.2.19}$$

$$\theta_c^2\,\mathrm{Re}\frac{\mathrm{D}v'}{\mathrm{D}t'} = -\frac{1}{r'}\frac{\partial p'}{\partial \varphi} - \frac{2\theta_c^2}{\mathrm{Ek}}u' + \frac{\partial^2 v'}{\partial z'^2} + \mathcal{O}(\theta_c^2), \tag{3.2.20}$$

$$\theta_c^2\,\mathrm{Re}\frac{\mathrm{D}w'}{\mathrm{D}t'} = -\frac{1}{\theta_c^2}\left(\frac{\partial p'}{\partial z'} + \frac{G}{C}\right) + \frac{\partial^2 w'}{\partial z'^2} + \mathcal{O}(\theta_c^2), \tag{3.2.21}$$

where the Reynolds, Ekman, centrifugal, Bond and capillary numbers are

$$\mathrm{Re} = \frac{\rho U L}{\mu}, \quad \mathrm{Ek} = \frac{\mu}{\rho\Omega L^2}, \quad \phi = \frac{\rho\Omega^2 L^3}{\gamma\theta_c}, \quad G = \frac{\rho g L^2}{\gamma}, \quad C = \frac{U\mu}{\gamma\theta_c^3}, \tag{3.2.22}$$

respectively, for general velocity scale. We take the velocity scale from the Tanner law (3.1.10) so that $U = \kappa\theta_c^q$, where the contact angle $\theta = \theta_c\theta'$, and consequently

$$\frac{\partial R'}{\partial t'} = (\theta' - 1)^q. \tag{3.2.23}$$

We make the lubrication approximation by taking the limits

$$\theta_c \to 0, \quad \theta_c^2 \mathrm{Re} \to 0, \quad \frac{\theta_c^2}{\mathrm{Ek}} \to 0, \tag{3.2.24}$$

while assuming that the terms involving ϕ and G are not negligible, leaving a linear system. Dropping the dash notation, our equations of motion (3.2.19)–(3.2.21) and incompressibility condition (3.2.2) become

$$0 = -\frac{\partial p}{\partial r} + \frac{\phi}{C} r + \frac{\partial^2 u}{\partial z^2}, \tag{3.2.25}$$

$$0 = -\frac{1}{r}\frac{\partial p}{\partial \varphi} + \frac{\partial^2 v}{\partial z^2}, \tag{3.2.26}$$

$$0 = -\frac{\partial p}{\partial z} - \frac{G}{C}, \tag{3.2.27}$$

$$0 = \frac{1}{r}\frac{\partial}{\partial r}(ru) + \frac{1}{r}\frac{\partial v}{\partial \varphi} + \frac{\partial w}{\partial z}. \tag{3.2.28}$$

At $z = 0$, we have the slip and no-penetration and slip conditions (3.1.7, 3.1.6),

$$u = \frac{\alpha}{3h}\frac{\partial u}{\partial z}, \quad v = \frac{\alpha}{3h}\frac{\partial v}{\partial z}, \quad w = 0, \tag{3.2.29}$$

while on $z = h(r, \varphi, t)$, we have the continuity of stress (3.2.13, 3.2.14) and free surface kinematic conditions (3.2.4)

$$0 = \frac{\partial u}{\partial z}, \quad 0 = \frac{\partial v}{\partial z}, \quad p = p_g - C^{-1}\nabla^2 h, \tag{3.2.30}$$

$$w = \frac{\partial h}{\partial t} + u\frac{\partial h}{\partial r} + \frac{v}{r}\frac{\partial h}{\partial \varphi}. \tag{3.2.31}$$

At the contact line, $r = R(\varphi, t), z = 0$, we have the nondimensional contact (3.1.8) and contact angle (3.1.9) conditions,

$$h(r, \varphi, t) = 0, \quad \frac{\partial h}{\partial r} = -\theta, \tag{3.2.32}$$

where the contact angle condition (3.2.32) (b) has been simplified using the small angle approximation, $\tan\theta \approx \theta$. Furthermore, at the contact line we impose the Tanner law (3.2.23)

$$\frac{\partial R}{\partial t} = \theta^q - 1, \tag{3.2.33}$$

and the contact line kinematic condition

$$u = \frac{\partial R}{\partial t} + \frac{v}{r}\frac{\partial R}{\partial \varphi}. \tag{3.2.34}$$

Along the axis $r = 0$, we have the differentiability condition,

$$\frac{\partial h}{\partial r} = 0, \tag{3.2.35}$$

and the finite velocity regularity condition (3.1.12),

$$|\boldsymbol{u}(0, \varphi, z, t)| < \infty. \tag{3.2.36}$$

The volume condition (3.1.14) simplifies so that the double integral over the domain is equal to V_f, which due to the chosen lengthscale is always equal to one,

$$V_f = \int_0^{2\pi} \int_0^{R(\varphi,t)} rh(r, \varphi, t)\, \mathrm{d}r\, \mathrm{d}\varphi. \tag{3.2.37}$$

Equations (3.2.25)–(3.2.37), consisting of the equations of motion and boundary conditions, model a thin droplet of fluid rotating on a flat plate under a lubrication approximation, under the assumption that the contact angle is sufficiently small.

3.3 Thin film equation

Typically thin film flows driven by surface tension are described by a fourth-order nonlinear parabolic partial differential equations (PDEs) [2]. Examples of PDEs are given for flows down inclined plates [52, 89], and for stationary droplets on flat plates [32, 31]. McKinley and Wilson [42, 43], and Boettcher and Ehrhard [44] derive similar thin film equations in the context of droplets under the influence of centrifugal force.

Therefore, we derive a similar thin film equation by substituting the velocity and

pressure, returning a single partial differential equation for the free surface height, $h(r, \varphi, t)$. First, we integrate the incompressibility condition (3.2.28) across the thin layer from $z = 0$ to the free surface $z = h(r, \varphi, t)$, subsequently using the no-penetration condition (3.2.29) (c) and Leibniz's rule to give,

$$w|_h = -\frac{1}{r}\frac{\partial}{\partial r}\left[r\int_0^h u\mathrm{d}z\right] + u|_h\frac{\partial h}{\partial r} - \frac{1}{r}\frac{\partial}{\partial \varphi}\int_0^h v\mathrm{d}z + \frac{v}{r}\bigg|_h\frac{\partial h}{\partial \varphi}. \tag{3.3.1}$$

Substituting the kinematic condition (3.2.31) results in a thin film equation,

$$\frac{\partial h}{\partial t} + \frac{1}{r}\frac{\partial}{\partial r}\left[r\int_0^h u\mathrm{d}z\right] + \frac{1}{r}\frac{\partial}{\partial \varphi}\int_0^h v\mathrm{d}z = 0. \tag{3.3.2}$$

This can also be written

$$\frac{\partial h}{\partial t} + \nabla_H \cdot \left(\int_0^h \boldsymbol{u}_H\,\mathrm{d}z\right) = 0, \tag{3.3.3}$$

where $\boldsymbol{u}_H = u\hat{\boldsymbol{r}} + v\hat{\boldsymbol{\varphi}}$ and $\nabla_H = \nabla - \frac{\partial}{\partial z}\hat{\boldsymbol{z}}$. Solving the axial equation of motion (3.2.27) subject to the axial stress condition (3.2.30) (c) gives

$$p = p_g + \frac{G}{C}(h - z) - \frac{1}{C}\nabla_H^2 h. \tag{3.3.4}$$

Since $\nabla_H(Cp_g - Gz) = 0$, the radial and azimuthal equations of motion (3.2.25, 3.2.26) can be written in a single equation where the right hand side is independent of z,

$$\frac{\partial^2 \boldsymbol{u}_H}{\partial z^2} = -C^{-1}\nabla_H\left(\nabla_H^2 h - Gh + \frac{\phi r^2}{2}\right). \tag{3.3.5}$$

Solving (3.3.5) by integrating with respect to z twice subject to the two slip conditions (3.2.29) (a, b) and the radial and azimuthal stress conditions (3.2.30) (a, b) gives the fluid velocity,

$$\boldsymbol{u}_H = -C^{-1}\left\{\frac{z^2}{2} - hz - \frac{\alpha}{3}\right\}\nabla_H\left(\nabla_H^2 h - Gh + \frac{\phi r^2}{2}\right). \tag{3.3.6}$$

Note, at $z = 0$ the velocity is proportional to α, meaning that if $\alpha \neq 0$ then the fluid can have non-zero horizontal velocity. Finally, substituting the velocity (3.3.6) into the thin film equation (3.3.3) and multiplying through by C, we get

$$C\frac{\partial h}{\partial t} + \nabla_H \cdot \left(\left\{\frac{h^3}{3} + \frac{\alpha}{3}h\right\}\nabla_H\left[\nabla_H^2 h - Gh + \frac{\phi r^2}{2}\right]\right) = 0. \tag{3.3.7}$$

This is the evolution equation for the free surface $z = h(r, \varphi, t)$ under the lubrication approximation. When deriving this equation we used each of the equations (3.2.25)–(3.2.28) and boundary conditions (3.2.29)–(3.2.31). The remaining equations (3.2.32)–(3.2.37) are boundary conditions for the thin film equation (3.3.7), along with a contact line law (3.2.33). Notice that there are more boundary conditions than unknowns in (3.3.7), however, we will show that many are automatically satisfied under certain circumstances, leaving a well defined system.

3.4 Equilibrium solution

We seek the initial profile of the free surface, $\mathscr{S}$, when the fluid volume is spun-up into solid body rotation so that $\boldsymbol{u}_0 = \mathbf{0}$. Quantities with subscript 0 denote the leading order, hydrostatic equilibrium solutions. Immediately, since each velocity component is zero everywhere, the velocity regularity condition (3.2.36) is automatically satisfied. Substituting $\boldsymbol{u}_0 = \mathbf{0}$ into the momentum equations (3.2.25)–(3.2.27) and solving determines the equilibrium pressure

$$p_0(r, z) = p_{00} + \frac{\phi}{2C} r^2 - \frac{G}{C} z \tag{3.4.1}$$

for a constant p_{00}; the pressure at the origin. The pressure contours are therefore paraboloidal in profile. We impose axisymmetry for the free surface so that there is no dependence on the azimuthal coordinate, φ. Furthermore, using the kinematic condition (3.2.31) we see that the free surface solution is steady, so that $h(r, \varphi, t) = h_0(r)$. Since we are considering a steady, axisymmetric free surface, the contact line radius is constant and denoted by $R(\varphi, t) = R_0$. As a result, the contact line kinematic condition (3.2.34) is automatically satisfied, and the nondimensional contact angle is fixed at $\theta = \theta_0 = 1$ due to the Tanner law (3.2.33).

Substituting $h(r, \varphi, t) = h_0(r)$ into the evolution equation (3.3.7) gives the ordinary differential equation

$$\left(r \left\{ \frac{h_0^3}{3} + \frac{\alpha}{3} h_0 \right\} \left[h_0'' + \frac{h_0'}{r} - G h_0 + \frac{\phi}{2} r^2 \right]' \right)' = 0, \tag{3.4.2}$$

where primes denotes derivatives with respect to r. The non-trivial general solu-

tion depends on whether $G = 0$ or not,

$$h_0(r) = \begin{cases} c_1\mathcal{I}_0(\sqrt{G}r) + c_2\mathcal{K}_0(\sqrt{G}r) + \dfrac{\phi}{2G}r^2 + c_3, & G > 0 \qquad (3.4.3a) \\ -\dfrac{\phi}{32}r^4 + \dfrac{c_1}{2}r^2 + c_2 \log r + c_3, & G = 0 \qquad (3.4.3b) \end{cases}$$

where $\mathcal{I}_0$ and $\mathcal{K}_0$ are modified Bessel functions of the first and second kind, respectively, and c_1, c_2 and c_3 are constants to be determined in each case. An alternative way to find these solutions is by substituting the equilibrium pressure (3.4.1) into the solution of the axial stress condition (3.3.4) giving

$$C(p_g - p_{00}) = h_0'' + \frac{h_0'}{r} - Gh_0 + \frac{\phi}{2}r^2. \qquad (3.4.4)$$

This reproduces the above solutions, but with $c_3 = [GC(p_{00} - p_g) + 2\phi]/G^2$ in (3.4.3a) or $c_1 = C(p_g - p_{00})/2$ in (3.4.3b). The equilibrium free surface solutions (3.4.3a, 3.4.3b) must each satisfy four boundary conditions; differentiability at the origin (3.2.35),

$$h_0'(0) = 0, \qquad (3.4.5)$$

the contact condition (3.2.32) (a)

$$h_0(R_0) = 0, \qquad (3.4.6)$$

the contact angle condition (3.2.32) (b) with $\theta_0 = 1$

$$h_0'(R_0) = -1, \qquad (3.4.7)$$

and the volume condition (3.2.37),

$$V_f = 2\pi \int_0^{R_0} r h_0(r)\, \mathrm{d}r. \qquad (3.4.8)$$

The differentiability condition (3.2.35) determines in both cases that $c_2 = 0$, while applying the contact (3.4.6) and volume (3.4.8) conditions determines the remain-

ing constants, giving the solutions

$$h_0(r) = \begin{cases} \left(\frac{R_0^4\phi\pi + 4V_f G}{4\pi R_0\sqrt{G}}\right)\left[\frac{\mathcal{I}_0(\sqrt{G}r) - \mathcal{I}_0(\sqrt{G}R_0)}{2\mathcal{I}_1(\sqrt{G}R_0) - R_0\sqrt{G}\mathcal{I}_0(\sqrt{G}R_0)}\right] + \frac{\phi}{2G}(r^2 - R_0^2), & (3.4.9a) \\ -\frac{\phi}{32}(r^4 - R_0^4) + \frac{1}{24\pi R_0^4}(\pi\phi R_0^6 - 48V_f)(r^2 - R_0^2), & (3.4.9b) \end{cases}$$

when $G > 0$ and $G = 0$, respectively. Note that, the contact line position, R_0, remains unknown and is determined by the only remaining boundary condition; the contact angle condition (3.4.7). Specifically, (3.4.7) requires that $f(\phi, R_0, G) = h_0'(R_0) + 1 = 0$ where

$$f(\phi, R_0, G) = \begin{cases} \left(\frac{R_0^4\phi\pi + 4V_f G}{4\pi R_0}\right)\left[\frac{\mathcal{I}_1(\sqrt{G}R_0)}{2\mathcal{I}_1(\sqrt{G}R_0) - R_0\sqrt{G}\mathcal{I}_0(\sqrt{G}R_0)}\right] + \frac{\phi}{G}R_0 + 1, & (3.4.10a) \\ \frac{\pi\phi R_0^6 - 24\pi R_0^3 + 96V_f}{24\pi R_0^3}, & (3.4.10b) \end{cases}$$

in each case, respectively. Solutions of the contact angle condition (3.4.10a, 3.4.10b) determine values of the unknown contact line position, R_0, so that our equilibrium solution satisfies all boundary conditions. We further constrain solutions of (3.4.10a, 3.4.10b) such that we require a contact line position, $r = R_0$, where $h_0(r) \geqslant 0, \forall\, r \in [0, R_0]$, since the height of the fluid cannot be negative. This condition is satisfied if and only if $g(\phi, G, R_0) = h_0(0) > 0$, where

$$g(\phi, R_0, G) = \begin{cases} -\left(\frac{R_0^4\phi\pi + 4V_f G}{4\pi R_0\sqrt{G}}\right)\left[\frac{\mathcal{I}_0(\sqrt{G}R_0)}{2\mathcal{I}_1(\sqrt{G}R_0) - R_0\sqrt{G}\mathcal{I}_0(\sqrt{G}R_0)} - \frac{\phi}{2G}R_0^2\right], & (3.4.11a) \\ \frac{192V_f - \phi\pi R_0^6}{96\pi R_0^2}. & (3.4.11b) \end{cases}$$

Figure 3.2 shows the equilibrium solutions (3.4.9a), where R_0 was found using the contact angle condition (3.4.10a), for three different values of ϕ when $G = 10$.

Within the solution space there are two specific points of interest, the maximum value ϕ can take, denoted ϕ_m, and the maximum value R_0 can take, denoted R_{0m}. The associated other parameter is denoted with a subscript c, so that the points of interest are (ϕ_m, R_{0c}) and (ϕ_c, R_{0m}). Each of these points is a function of the Bond number, G. We find (ϕ_m, R_{0c}) by solving $f = 0$ and $\partial f/\partial R_0 = 0$ simultaneously. Hence, (ϕ_m, R_{0c}) is the point in the solution space where, for a given value of G, the nondimensional rotation rate for which a equilibrium thin film solution exists

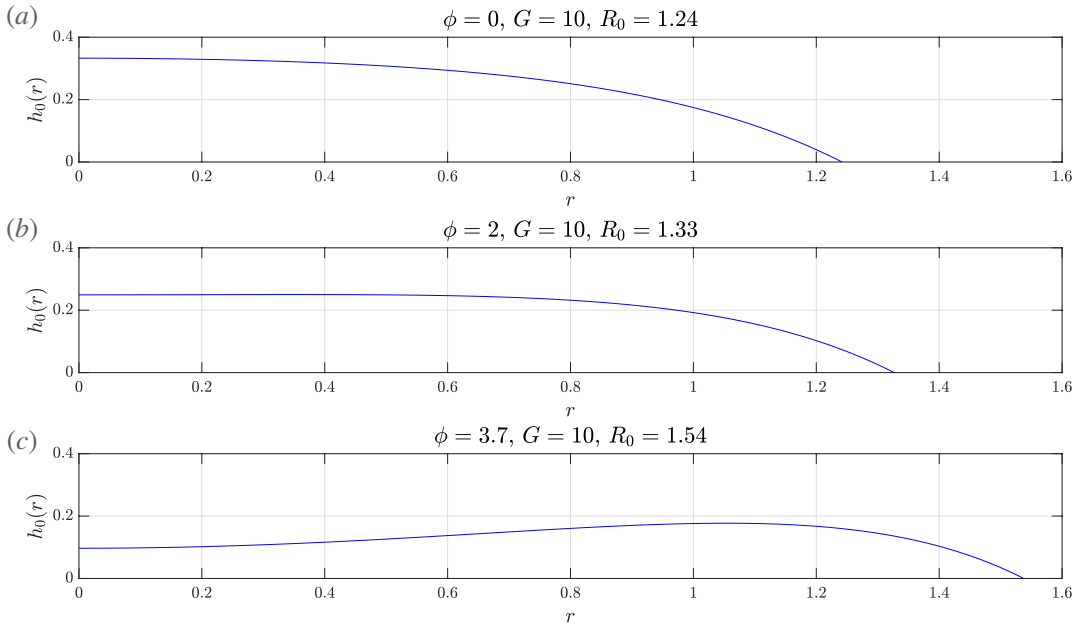


Figure 3.2: Comparison of $z = h_0(r)$ satisfying (3.4.9a, 3.4.10a, 3.4.11a) when $G = 10$ for different values of ϕ and therefore R_0.

is maximum. We find (ϕ_c, R_{0m}) by solving $f = 0$ and $g = 0$ together, giving the point in the solution space which corresponds to the film touching down at the centre. For $G > 0$, the solutions to the contact angle condition (3.4.10a) and the two bifurcation points are found numerically. When $G = 0$, the contact angle condition (3.4.10b) can be solved analytically giving equilibrium contact line position

$$R_0 = \left(\frac{24\pi \pm \sqrt{(24\pi)^2 - 384\pi\phi V_f}}{2\pi\phi} \right)^{\frac{1}{3}}, \tag{3.4.12}$$

where there are two solutions if $\phi < \phi_m = 3\pi/(2V_f)$, and a single maximum at $(\phi_m, R_{0c}) = (3\pi/(2V_f), 2(V_f/\pi)^{1/3})$. The point where the film touches down at the centre is $(\phi_c, R_{0m}) = (4\pi/(3V_f), (12V_f/\pi)^{1/3})$. The analytical solutions for the equilibrium free surface shape and contact line position (3.4.9b, 3.4.12) are equivalent to the solutions of McKinley and Wilson [42, 43] subject to a redefinition of the nondimensional groups.

Figure 3.3 shows the contour of the contact angle condition (3.4.10a) at zero in blue and the contour of the height of fluid condition (3.4.11a) at zero in red for various values of G. The region where the height of fluid at the origin is greater than zero, $g(\phi, R_0, G) > 0$, is shaded in grey. The bifurcation points (ϕ_m, R_{0c}) and

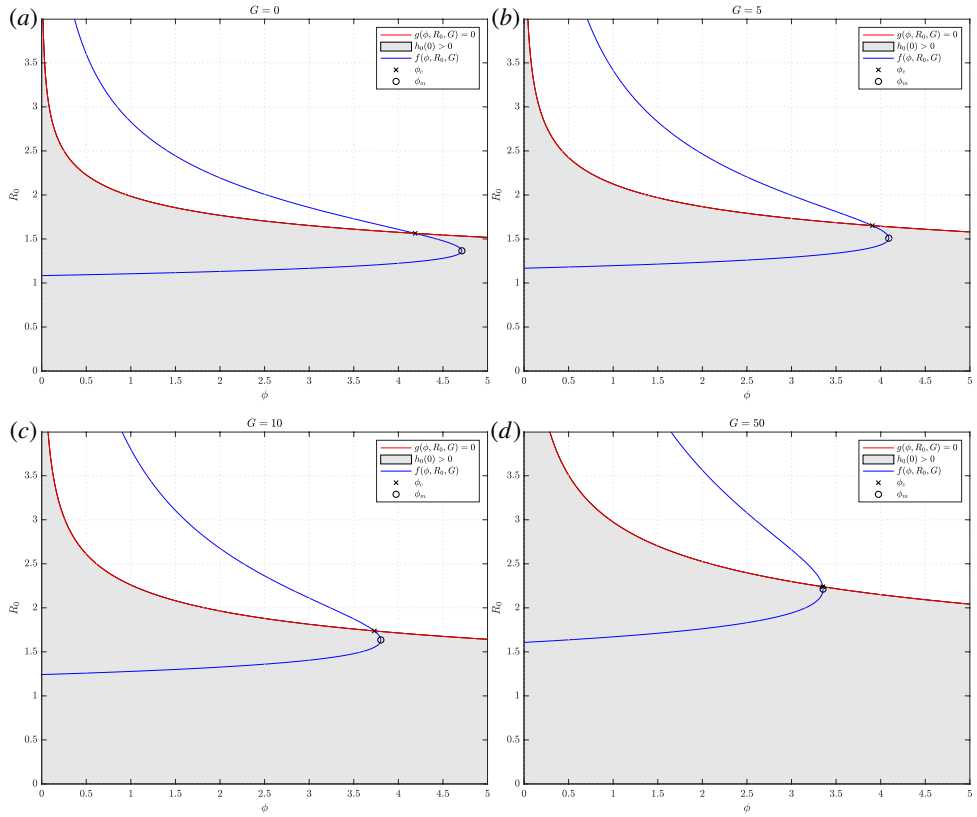


Figure 3.3: Contour of the contact angle condition, $f = 0$ (3.4.10a,3.4.10b), and the height of fluid condition, $g = 0$ (3.4.11a, 3.4.11b), for various values of the Bond number G.

(ϕ_c, R_{0m}) are plotted with a black circle and a black $\times$, respectively. Note that in the grey region when $\phi_c < \phi < \phi_m$ there exist multiple solutions for $R_0(\phi)$, whereas the function $\phi(R_0)$ is one-to-one. Furthermore, as G increases we see that the two bifurcation points converge. Figure 3.4 shows the solution space as G is varied, plotted in both the $G - \phi$ space (a, b), and the $G - R_0$ space (c). In each of these figures the bifurcation point (ϕ_m, R_{0c}) is plotted with a black solid line, while the point (ϕ_c, R_{0m}) is plotted with a red line. Figures 3.4 (a, c) show more clearly that the bifurcation points converge as G increases, with the ϕ coordinate converging quicker than the R_0 coordinate. Furthermore, both the functions $\phi_m(G)$ and $\phi_c(G)$ are decreasing as G increases, while both $R_{0m}(G)$ and $R_{0c}(G)$ are increasing. An interpretation of this is as G increases and the contact line is forced outwards, the height at zero decreases, increasing R_0 and requiring a lower value of ϕ to decrease the height at the origin to zero.

The shaded regions in each subfigure of figure 3.4 are where physical solutions to

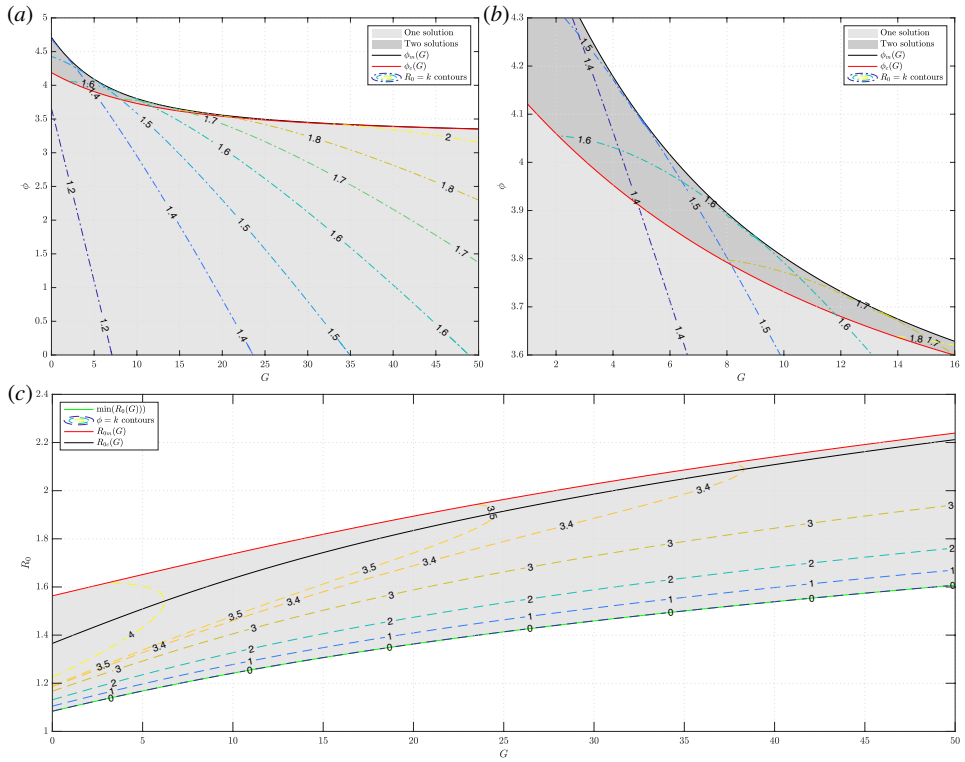


Figure 3.4: (a) The shaded region shows the $G - \phi$ parameter space, where the contours of constant R_0 are also plotted. (b) Zoomed area of figure (a). In each of (a, b) the darker region indicates multiple solutions, whereas the lighter shaded region indicates a single solution. (c) The shaded region indicates the $G - R_0$ parameter space, showing the contours of constant ϕ.

the contact angle condition exist, while in the unshaded regions no equilibrium solution exists in the thin film limit. In Figures 3.4 (a, b), within the region bounded by the red and black solid curves there exists two physical solutions for R_0, indicated with darker shading. Whereas, in the lighter shaded region only a single physical solution exists. This is further illustrated by plotting the contours of constant R_0 through the region, shown in the dashed coloured lines, where we see that contours can only cross within the darker shaded region. Figure 3.4 (b) is a zoomed in region of figure 3.4 (a) showing this feature more clearly. Following a contour as ϕ increases we pass through the maximum value of ϕ, touching the black line, and progressing onto the upper solution branch where the contour terminates when it reaches the red line since solutions are no longer physical. Note that contours only cross when one is on the upper branch and the other is on the lower branch of solutions.

Figure 3.4 (c) shows the region where solutions satisfying both the contact angle

condition is satisfied and physical solutions exist in $G - R_0$ space, where contours of constant ϕ are also shown. The region bounded by $R_{0c}(G)$ and $R_{0m}(G)$ corresponds to the upper solution branches of figure 3.3, while the region bounded by the minimum R_0 and R_{0c} corresponds to the lower branch. Note that the minimum value of R_0 is always achieved when $\phi = 0$, which is consistent with the centrifugal force being directed radially outwards. Physically, we expect that as the rotation is increased the fluid experiences a greater outward force and hence forms a ridge near the contact line, known as a capillary ridge [104]. Figure 3.4 (a) shows that for fixed G increasing the centrifugal number in the region $0 < \phi < \phi_c$ increases R_0, as anticipated, and, due to volume conservation decreases the height at $r = 0$ forming a ridge near the contact line. This is visualised in figure 3.2, where for fixed Bond number the centrifugal number is increased and the solution $h_0(r)$ is plotted. Note, each of these solutions belong to the lower branch of solutions on figure 3.3, where in this region the function $R_0(\phi)$ is one-to-one.

In the region where $\phi_c \leqslant \phi < \phi_m$, two solutions exist for each value of ϕ with R_0 greater than that on the lower branch of solution. Within this region, corresponding to the upper branch, increasing ϕ decreases R_0 from R_{0m} to R_{0c}. We might anticipate that the point (ϕ_m, R_{0c}) is a saddle node bifurcation point, where the upper branch of solutions in $\phi_c < \phi < \phi_m$ is unstable to axisymmetric perturbations, while the lower branch is stable.

The physical interpretation of increasing the Bond number, G, is increasing the constant vertical force acting downwards. We can see this in the axial component of the equations of motion (3.2.27) due to the $-G$ contribution. Hence, we would expect as we increase the Bond number for fixed centrifugal number the profile of the free surface flattens and the contact line position, R_0, increases. If $\phi < \phi_c(G)$ this is what we see in figure 3.4 (a), where for fixed ϕ each contour of constant R_0 is crossed successively. Furthermore, in figure 3.4 (c) we see along contours of constant ϕ, R_0 increases with G, while $\phi < \phi_m$. These solutions once again correspond to the lower branch of solutions in figure 3.3. On the upper branch when $R_{0c} < R_0 < R_{0m}$, the value of G is decreasing along contours of constant ϕ, again in contrast to the physical interpretation.

Overall, for a given volume, V_f, contact angle, θ_c, and rotation rate, Ω amongst other physical properties, we can calculate the nondimensional Bond and centrifu-

gal numbers, G, ϕ and solve the contact angle condition (3.4.10a) for R_0. If there are no solutions for R_0 while $\theta_c \ll 1$, this suggests that the lubrication approximation is not valid in these regimes, or that the assumption that an equilibrium solution exists where $\boldsymbol{u}_0 = \mathbf{0}$ is violated.

3.4.1 Comparison to previous literature

The equilibrium solutions detailed in the previous section are equivalent to the solutions of McKinley *et al* [42] subject to suitable transformations. The authors considered the case of nonzero gravity, $G > 0$, with both sessile and pendant cases considered as well as the special case where $C = 0$. The same problem as described in § 3.3 is nondimensionalised by taking the capillary lengthscale to make $G = 1$, subsequently varying the volume and centrifugal number producing equivalent plots to figure 3.3 under suitable transformations. Consequently, the authors also found that equilibrium solutions only exist below a critical rotation rate. By performing a linear stability analysis of these solutions subject to axisymmetric perturbations the authors observed that a saddle node bifurcation occurs at this point; (ϕ_m, R_{0c}) in our notation.

McKinley and Wilson [43] discuss the case of zero Bond number, $G = 0$, deriving solutions in the context of a vertical jet of air directed at a mass of fluid, for which the equations of motion are the same with the strength of the jet being analogous to rotation rate as discussed in chapter 1. They considered the case where $G = 0$ and took the lengthscale so that $\phi = 1$, solving the ODE (3.4.2) subject to the contact angle condition, leaving the volume, V_f, to be set by the chosen R_0. We can recover this solution by choosing V_f in (3.4.9b) such that the contact angle condition (3.4.7) is satisfied, so that

$$V_f = \frac{1}{4}R_0^3\pi - \frac{1}{96}\pi\phi R_0^6. \tag{3.4.13}$$

The volume (3.4.13) is (11) in [43] while substituting into (3.4.9b) gives the same solution as (10) in our notation

$$h_0(r) = \frac{1}{32R_0}(r^2 - R_0^2)\left[\phi R_0(R_0^2 - r^2) - 16\right]. \tag{3.4.14}$$

Schwartz and Roy [94] subsequently derived a similar result in the absence of

gravity including a small but variable contact angle.

When $\phi = 0, G \neq 0$ we recover the solution of Ehrhard and Davis [32], who consider find the solution by considering the quasi-steady limit, $C \to 0$, of a thin film equation analogous to (3.3.7). Within this limit they neglect the contact angle condition, and discuss axisymmetric spreading rather than considering equilibrium solutions as we have done here. Similarly, Boettcher and Ehrhard [44] considered the case where both $\phi, G \neq 0$, finding the same solution (3.4.9a), in the context of quasi-steady spreading and therefore also neglect the contact angle condition.

3.5 Summary

Overall, we have presented a mathematical model to describe the evolution of the free surface, $h(r, \varphi, t)$, and contact line, $R(\varphi, t)$, of a volume of fluid in solid body rotation on a solid plate. We modelled the contact line dynamics by imposing a macroscopic slip law and used the Tanner law to relate the contact angle to the speed of the contact line. The equations of motion were simplified using a lubrication approximation, assuming that the contact angle is small and subsequently a partial differential equation for the evolution of the free surface over time (3.3.7) is derived.

Finally, we recovered the equilibrium solutions of McKinley *et al.* [42] and McKinley and Wilson [43] up to a redefinition of nondimensional groups. The steady, axisymmetric free surface shape, $h_0(r)$, is derived under different scalings and presented as a function of nondimensional rotation rate and volume, subsequently solving the nondimensional contact angle condition (3.4.7) for the remaining unknown; the contact line position, R_0. We assessed how the contact line position varies with both the centrifugal number, ϕ, and the Bond number, G, clearly presenting the parameter space in which physical equilibrium solutions exist and discussing the trends as each parameter is varied. The key result is that for each Bond number there is a corresponding maximum value of ϕ below which solutions are possible. In terms of physical parameters, each volume has a maximum rotation rate beyond which no equilibrium solution is possible.

Chapter 4

Linear stability analysis of equilibrium solutions

The aim of performing the linear stability analysis is to understand the conditions for instability of a prescribed perturbation to the equilibrium solutions described in § 3.4, that is, whether the perturbation grows or decays in time. Specifically, we discuss how varying the nondimensional rotation speed, ϕ, and the Bond number, G, affects the growth rates of each mode, determining the dominant mode of instability in different limits of the capillary number, C.

4.1 Modelling

4.1.1 Eigenvalue equation

In § 3.3 we derived the thin film equation (3.3.7) and appropriate boundary condition under a lubrication approximation. The resultant evolution equation involves only the free surface shape $z = h(r, \varphi, t)$. We consider a small perturbation to the equilibrium solutions where the free surface, contact line and contact angle deform as $h = h_0(r) + \epsilon h_1(r, \varphi, t) + \mathcal{O}(\epsilon^2)$, $R = R_0 + \epsilon R_1(\varphi, t) + \mathcal{O}(\epsilon^2)$ and $\theta = \theta_0 + \epsilon\theta_1(\varphi, t) + \mathcal{O}(\epsilon^2)$, respectively, where $\epsilon \ll 1$ is the size of the perturbation. During this analysis all perturbation quantities have the subscript 1. We take

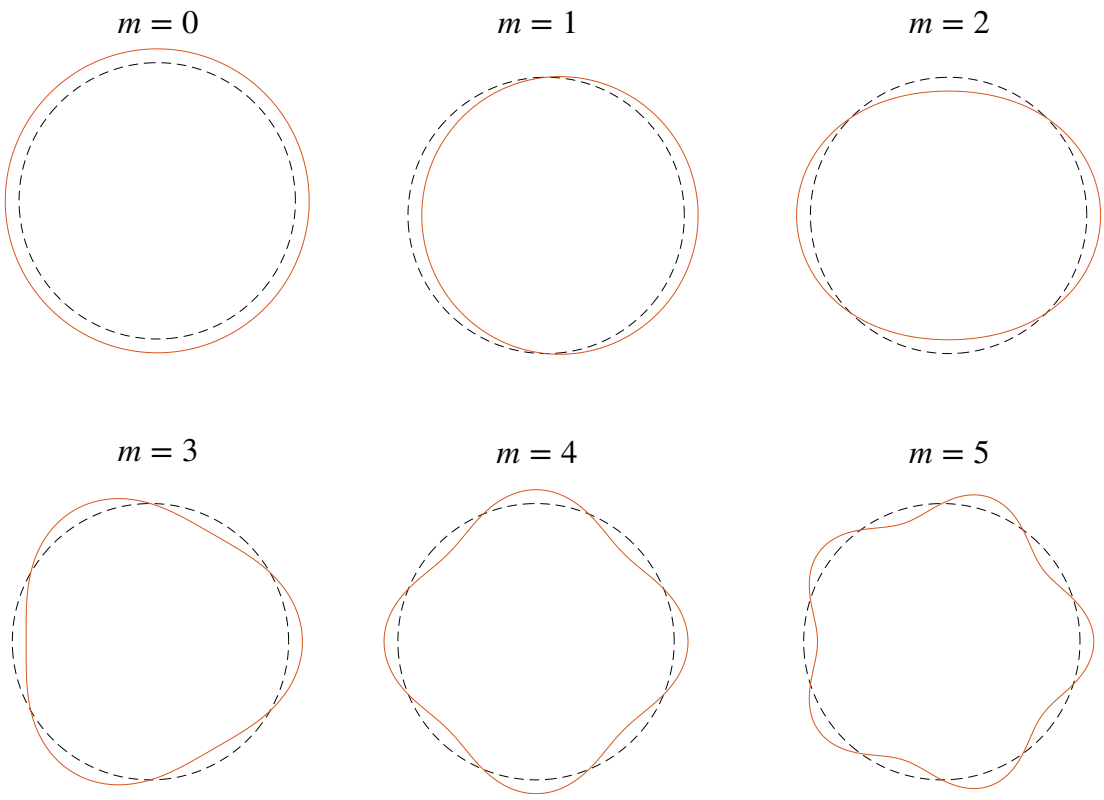


Figure 4.1: Plots of the contact line for different perturbations $m = 0, 1, 2, ..., 5$ when $\epsilon = 0.1$ and $R_0 = 1$, indicated in dashed black lines.

normal modes so that

$$h(r, \varphi, t) = h_0(r) + \epsilon h_1(r) e^{\mathrm{i}m\varphi + \sigma_m t}, \tag{4.1.1}$$

$$R(\varphi, t) = R_0 + \epsilon R_1 e^{\mathrm{i}m\varphi + \sigma_m t}, \tag{4.1.2}$$

$$\theta(\varphi, t) = \theta_0 + \epsilon \theta_1 e^{\mathrm{i}m\varphi + \sigma_m t} \tag{4.1.3}$$

for wavenumber, $m \in \mathbb{N}$, and associated growth rate, $\sigma_m \in \mathbb{C}$. Figure 4.1 shows the perturbation to the contact line (4.1.2) for wavenumbers $m = 0, 1, 2, ..., 5$ in red compared to the linearised contact line at $r = R_0$ which is shown with a black dashed line.

Note, the stability of this linear system depends on the sign of the real part of this frequency, $\Re(\sigma_m)$. The imaginary part, $\Im(\sigma_m)$, corresponds to precession of modes, meaning rotation about the $r = 0$ axis within the rotating frame. Given that we have scaled out the Coriolis force terms which account for this effect by taking $\mathrm{Ek} \to \infty$, we might expect the eigenvalues to be purely real. Substituting the perturbed free surface (4.1.1) into the evolution equation (3.3.7) gives a fourth

order linear eigenvalue equation at $\mathcal{O}(\epsilon)$

$$\mathcal{L}_2[\mathcal{L}_1(h_1)] = C\sigma_m h_1, \tag{4.1.4}$$

where the linear operators $\mathcal{L}_1$ and $\mathcal{L}_2$ are defined as,

$$\mathcal{L}_1[\Phi] = \left[\frac{\mathrm{d}^2}{\mathrm{d}r^2} + \frac{1}{r}\frac{\mathrm{d}}{\mathrm{d}r} - \frac{m^2}{r^2} - G\right]\Phi, \tag{4.1.5}$$

$$\mathcal{L}_2[\Phi] = -\left[\left\{\frac{1}{3}h_0^3 + \frac{\alpha}{3}h_0\right\}\frac{\mathrm{d}^2}{\mathrm{d}r^2} + \frac{1}{r}\left(r\left\{\frac{1}{3}h_0^3 + \frac{\alpha}{3}h_0\right\}\right)'\frac{\mathrm{d}}{\mathrm{d}r} - \frac{m^2}{r^2}\left\{\frac{1}{3}h_0^3 + \frac{\alpha}{3}h_0\right\}\right]\Phi, \tag{4.1.6}$$

respectively.

4.1.2 Velocity perturbation

When deriving the thin film equation in § 3.3, we found an expression for the fluid velocity (3.3.6). Substituting in the free surface perturbation (4.1.1) and simplifying using the ODE for the equilibrium free surface shape (3.4.4), gives

$$\boldsymbol{u}_H = -\frac{\epsilon}{C}\left\{\frac{z^2}{2} - h_0 z - \frac{\alpha}{3}\right\}\nabla_H\left(\left[h_1'' + \frac{h_1'}{r} - \left(m^2 + Gr^2\right)\frac{h_1}{r^2}\right]e^{\mathrm{i}m\varphi+\sigma_m t}\right). \tag{4.1.7}$$

Recall that the notation, $\boldsymbol{u}_H$, denotes the velocity in the radial and azimuthal directions so that $\boldsymbol{u}_H = u\hat{\boldsymbol{r}} + v\hat{\boldsymbol{\varphi}}$, while $\boldsymbol{u}$ is the velocity including the axial component, $\boldsymbol{u} = \boldsymbol{u}_H + w\hat{\boldsymbol{z}} = (u, v, w)$. The horizontal velocity, $\boldsymbol{u}_H$, given by (4.1.7), is an $\mathcal{O}(\epsilon)$ quantity, consistent with a perturbation from the hydrostatic equilibrium solution, $\boldsymbol{u}_0 = \boldsymbol{0}$. Hence, we posit $\boldsymbol{u} = \epsilon\boldsymbol{u}_1(r, z)e^{\mathrm{i}m\varphi+\sigma_m t}$, where $\boldsymbol{u}_1$ is the perturbed velocity, giving the radial and azimuthal velocity components

$$u_1(r, z) = -C^{-1}\left\{\frac{z^2}{2} - h_0 z - \frac{\alpha}{3}\right\}\mathcal{L}_1'[h_1], \tag{4.1.8}$$

$$v_1(r, z) = -C^{-1}\frac{\mathrm{i}m}{r}\left\{\frac{z^2}{2} - h_0 z - \frac{\alpha}{3}\right\}\mathcal{L}_1[h_1], \tag{4.1.9}$$

respectively. The linear operator $\mathcal{L}_1$ is defined as above (4.1.5). The axial velocity component, $w_1(r, z)$, is determined using the incompressibility condition (3.2.28)

subject to the no-penetration boundary condition (3.2.29) (c),

$$w_1(r,z) = \frac{z}{C}\left(\frac{z^2}{6} - \frac{h_0 z}{2} - \frac{\alpha}{3}\right)\left(\mathcal{L}_1^2(h_1) + G\mathcal{L}_1[h_1]\right) - \frac{h_0'}{2C}z^2\mathcal{L}_1'[h_1], \tag{4.1.10}$$

where the notation $\mathcal{L}_1^2[\Phi] = \mathcal{L}_1\left(\mathcal{L}_1[\Phi]\right)$. Notice that both the horizontal velocity components (4.1.8, 4.1.9) are non-zero at the linearised contact line, $r = R_0$, $z = 0$, due to choosing the Greenspan slip law (3.2.29) (a, b).

4.1.3 Boundary conditions

The fourth order linear eigenvalue equation (4.1.4) requires four boundary conditions to calculate the growth rate, σ_m for a given wavenumber, m. The remaining conditions to satisfy at $\mathcal{O}(\epsilon)$ are the contact (3.2.32 (a), contact angle (3.2.32) (b), Tanner (3.2.33), contact line kinematic (3.2.34), differentiability (3.2.35), regularity (3.2.36) and volume (3.2.37) conditions. We will show that these remaining boundary conditions can be reduced to the number required to find the eigenvalue, σ_m.

Substituting the perturbed free surface (4.1.1), contact line (4.1.2) and contact angle (4.1.3), into the contact and contact angle conditions (3.2.32) give

$$h_0'(R_0)R_1 + h_1(R_0) = 0, \quad \theta_1 = -R_1 h_0''(R_0) - h_1'(R_0) \tag{4.1.11}$$

at $\mathcal{O}(\epsilon)$, respectively. Recalling that the contact angle condition (3.2.32) (b) gives $h_0'(R_0) = -1$ at leading order in ϵ, we eliminate R_1 between the contact and contact angle conditions giving a combined boundary condition at the linearised contact line position, R_0,

$$\theta_1 = -h_0''(R_0)h_1(R_0) - h_1'(R_0), \tag{4.1.12}$$

provided that $R_1 \neq 0$. The contact condition at $\mathcal{O}(\epsilon)$ (4.1.11) (a), is simplified by the equilibrium contact angle condition (3.4.7) so that

$$R_1 = h_1(R_0). \tag{4.1.13}$$

Since we require $R_1 \neq 0$, without loss of generality we can normalise solutions by

choosing $R_1 = 1$, redefining the perturbation quantity ϵ to be set by the size of the contact line perturbation. We retain R_1 within the equations for clarity.

A consequence of the Tanner law (3.2.33) the contact line can both advance and recede depending on the contact angle. Furthermore, the Tanner law (3.2.33) can be linearised about the equilibrium contact angle, $\theta_0 = 1$. Substituting the normal mode perturbation for the contact line (4.1.2) and contact angle (4.1.3) gives the $\mathcal{O}(\epsilon)$ Tanner law at the unperturbed contact line $r = R_0$, $z = 0$,

$$\sigma_m R_1 = q\theta_1. \tag{4.1.14}$$

Substituting into the combined contact and contact angle condition (4.1.12) eliminates θ_1, leaving,

$$\sigma_m h_1(R_0) = -q\left\{h_0''(R_0)h_1(R_0) + h_1'(R_0)\right\}, \tag{4.1.15}$$

again provided $R_1 \neq 0$. The above boundary condition (4.1.15) is formed of the contact (3.2.32) (a), contact angle (3.2.32) (b) conditions and the Tanner (3.2.33) law, and will be subsequently referred to as the combined Tanner law.

The contact line kinematic condition (3.2.34) at $\mathcal{O}(\epsilon)$ simplifies to

$$\sigma_m R_1 = u_1(R_0, 0), \tag{4.1.16}$$

where the radial velocity at the contact line is given by (4.1.8), so that

$$u_1(R_0,0) = \frac{\alpha}{3C}\left[h_1''' + \frac{1}{r}h_1'' - \left(1 + m^2 + Gr^2\right)\frac{h_1'}{r^2} + 2m^2\frac{h_1}{r^3}\right]\Bigg|_{r=R_0}. \tag{4.1.17}$$

Substituting (4.1.17) into the contact line kinematic condition (4.1.16) shows that the contact line kinematic condition is exactly the eigenvalue equation (4.1.4) evaluated at the linearised contact line, R_0. When $\alpha = 0$, corresponding to no-slip boundary conditions, the radial contact line velocity is zero so that by the contact line kinematic condition $R_1 = 0$, meaning the contact line is pinned. Subsequently, the Tanner law (4.1.14) gives $\theta_1 = 0$ so that the contact angle remains constant. Hence, if the contact line velocity is zero the combined Tanner law (4.1.15) can no longer be applied and are replaced with (4.1.11) with $R_1 = \theta_1 = 0$ so that $h_1(R_0) = 0, h_1'(R_0) = 0$. Since in this case the contact line cannot move from its

linearised position at $r = R_0$ all modes are unconditionally stable. Interestingly, imposing Navier slip conditions at the contact line so that $u = \beta u_z, v = \beta v_z$ also results in the radial contact line velocity being zero, meaning the contact line cannot move. Previous analysis by McKinley and Wilson [43] neglected this fact, assuming that the perturbation to the contact line, R_1, was non-zero and deriving a boundary condition equivalent to (4.1.15). In summary, the contact line kinematic condition (4.1.16) is not required as a boundary condition since it replicates (4.1.4) at the contact line, but does provide important justification for the use of the Greenspan slip law (3.1.7) showing that the radial contact line velocity cannot be zero.

The volume conservation condition (3.2.37) under the perturbation to both the free surface (4.1.1), and the contact line (4.1.2) gives

$$V_f = 2\pi \int_0^{R_0} r h_0(r)\,\mathrm{d}r + \epsilon \int_0^{2\pi} e^{\mathrm{i}m\varphi+\sigma_m t}\,\mathrm{d}\varphi \int_0^{R_0} \left\{ r h_1(r) + \frac{2R_1}{R_0} r h_0(r) + \frac{R_1}{R_0} r^2 h_0'(r) \right\} \mathrm{d}r. \quad (4.1.18)$$

The volume conservation (4.1.18) and other remaining boundary conditions depend on the wavenumber, m, and are considered as separate cases; specifically, whether perturbations are axisymmetric or not.

4.1.3.1 Non-axisymmetric perturbations

For wavenumbers, $m = 1, 2, ...$, the integral

$$\int_0^{2\pi} e^{\mathrm{i}m\varphi+\sigma_m t}\,\mathrm{d}\varphi = \frac{e^{\sigma_m t}}{\mathrm{i}m}\left[(e^{2\pi\mathrm{i}})^m - 1\right] = 0, \quad (4.1.19)$$

so that the $\mathcal{O}(\epsilon)$ volume conservation condition (4.1.18) is satisfied automatically.

The remaining boundary conditions are at the origin $r = 0$, where the eigenvalue equation (4.1.4) is subject to the $\mathcal{O}(\epsilon)$ differentiability condition (3.2.35), and the velocity regularity (3.2.36) condition. The differentiability condition at $\mathcal{O}(\epsilon)$ is

$$h_1'(0) = 0, \quad (4.1.20)$$

provided that $m \neq 1$. When $m = 1$, the perturbation is a translation of the fluid

so that the the centre of mass is not on the axis of rotation, shown in figure 4.1, meaning at $r = 0$ we do not necessarily require h_1 to have zero slope.

The velocity regularity condition (3.2.36) states that magnitude of the velocity along $r = 0$ is finite, that is, each of the $\mathcal{O}(\epsilon)$ velocity components (4.1.8)–(4.1.10) are finite along $r = 0$. Each velocity component is a function of $\mathcal{L}_1$ (4.1.5) and therefore for the velocity to be regular, $\mathcal{L}_1(h_1)$ and its derivative must be finite at $r = 0$. Hence, solutions must behave like r^m when r is small. Substituting this form into the $\mathcal{O}(\epsilon)$ velocity components (4.1.8)–(4.1.10) gives

$$u_1(r,z) = k_m C^{-1}\left(\frac{z^2}{2} - h_0 z - \frac{\alpha}{3}\right) mGr^{m-1}, \tag{4.1.21}$$

$$v_1(r,z) = k_m C^{-1}\left(\frac{z^2}{2} - h_0 z - \frac{\alpha}{3}\right) \mathrm{i}mGr^{m-1}, \tag{4.1.22}$$

$$w_1(r,z) = k_m \frac{z^2}{2C} mGr^m, \tag{4.1.23}$$

respectively, where k_m are constants. The axial equation has been simplified using $h_0'(r) \sim r$ when $r \ll 1$. Taking the limit as $r \to 0$ of each of these equations shows that the regularity condition is satisfied for each positive wavenumber. Furthermore, when $m = 2, 3, 4, ...$, corresponding to perturbations in which the centre of mass lies on the origin, each velocity component is zero along $r = 0$. Therefore, the boundary conditions imposed on h_1 reflect the r^m behaviour close to the origin so that the non-axisymmetric boundary conditions at $r = 0$ are taken as

$$m = 1: \quad h_1(0) = 0, \quad h_1''(0) = 0, \quad h_1'''(0) = 0, \tag{4.1.24}$$

$$m = 2: \quad h_1(0) = 0, \quad h_1'(0) = 0, \quad h_1'''(0) = 0, \tag{4.1.25}$$

$$m \geqslant 3: \quad h_1(0) = 0, \quad h_1'(0) = 0, \quad h_1''(0) = 0. \tag{4.1.26}$$

4.1.3.2 Axisymmetric perturbations

If $m = 0$, corresponding to axisymmetric perturbations, the integral condition (4.1.18) is not satisfied automatically, and as a result we must impose

$$\int_0^{R_0} r h_1(r)\,\mathrm{d}r = 0, \tag{4.1.27}$$

to satisfy volume conservation. The remaining two conditions in addition to the combined contact and contact angle condition (4.1.15) and the above volume condition (4.1.27), are the differentiability condition (4.1.20) and a further symmetry condition

$$h_1'''(0) = 0. \tag{4.1.28}$$

4.1.3.3 Summary

To summarise, to solve the eigenvalue equation (4.1.4) we require four boundary conditions to find the eigenfunction, $h_1(r)$, and the eigenvalue, σ_m, which determine the linear stability of the system. One boundary condition is always the combined Tanner law (4.1.15), while the remaining three boundary conditions depend on the wavenumber, which are summarised below

$$m = 0: \quad h_1'(0) = 0, \quad h_1'''(0) = 0, \quad \int_0^{R_0} r h_1(r)\,\mathrm{d}r = 0, \tag{4.1.29}$$

$$m = 1: \quad h_1(0) = 0, \quad h_1''(0) = 0, \quad h_1'''(0) = 0, \tag{4.1.30}$$

$$m = 2: \quad h_1(0) = 0, \quad h_1'(0) = 0, \quad h_1'''(0) = 0, \tag{4.1.31}$$

$$m \geqslant 3: \quad h_1(0) = 0, \quad h_1'(0) = 0, \quad h_1''(0) = 0. \tag{4.1.32}$$

The resultant solutions are normalised using the contact condition (4.1.13), where without loss of generality we can choose $R_1 = 1$.

4.2 Quasi-steady limit, $C = 0$

First we will consider solutions in the limit $C \to 0$, corresponding to a flow where surface tension dominates viscous drag. Under this assumption the contact line speed, κ, is zero, so that the Tanner law (3.2.33) gives $R_t = 0$ and the contact line is pinned so the system remains in equilibrium. Therefore, taking $C = 0$ before deriving the combined Tanner law (4.1.15) gives a qualitatively different set of boundary conditions. We consider the model discounting the assumption that $R_1 \neq 0$ and calculate the growth rate, σ_m through the combined Tanner law (4.1.15). In the limit $C \to 0$ the eigenvalue is removed from the eigenvalue

equation (4.1.4) and we are left with a differential equation for $h_1(r)$

$$\mathcal{L}_2\left[\mathcal{L}_1(h_1)\right] = 0, \tag{4.2.1}$$

where the linear operators $\mathcal{L}_1, \mathcal{L}_2$ are defined in § 4.1.1. The differential equation (4.2.1) is subject to the combined Tanner law (4.1.15) and appropriate set of boundary conditions (4.1.29)–(4.1.32), depending on which wavenumber, m, is under consideration. The solution, $h_1(r)$, is then normalised using the contact condition (4.1.13). Note that the growth rate, σ_m, only appears in the combined Tanner law (4.1.15).

4.2.1 Axisymmetric perturbations

First we will consider the solutions to the eigenvalue equation (4.1.4) under axisymmetric perturbations where $m = 0$. We require nontrivial solutions to the differential equation (4.2.1) which, when both $C = 0$ and $m = 0$, reduces to

$$0 = h_1''' + \frac{1}{r}h_1'' - \frac{1}{r^2}h_1' - Gh_1' \tag{4.2.2}$$

subject to the boundary conditions (4.1.15, 4.1.29, (4.1.13)). Similarly to § 3.4, solutions depend on whether the Bond number is zero, so that the general solutions in each case are

$$h_1(r) = \begin{cases} c_1\mathcal{I}_0(\sqrt{G}r) + c_2\mathcal{K}_0(\sqrt{G}r) + c_3, & G > 0 \quad \text{(4.2.3a)} \\ c_1r^2 + c_2\log r + c_3. & G = 0 \quad \text{(4.2.3b)} \end{cases}$$

In each case the differentiability condition (4.1.29) (a) requires that $c_2 = 0$, and as a result the symmetry condition (4.1.29) (b) is automatically satisfied. The remaining two constants of integration are determined by the integral condition (4.1.29) (c) and the contact condition (4.1.13). Hence, the solutions of (4.2.2) satisfying (4.1.29) (a)–(c), and the contact condition (4.1.13) are

$$h_1(r) = \begin{cases} R_1\dfrac{R_0\sqrt{G}\mathcal{I}_0(\sqrt{G}r) - 2\mathcal{I}_1(\sqrt{G}R_0)}{R_0\sqrt{G}\mathcal{I}_0(\sqrt{G}R_0) - 2\mathcal{I}_1(\sqrt{G}R_0)}, & G > 0, \quad \text{(4.2.4a)} \\ R_1\left[2\left(\dfrac{r}{R_0}\right)^2 - 1\right], & G = 0. \quad \text{(4.2.4b)} \end{cases}$$

Finally, using the combined Tanner law (4.1.15) we determine the growth rate of the $m = 0$ mode, denoted σ_0, so that

$$\sigma_0 = \begin{cases} -q\left[h_0''(R_0) + \dfrac{R_0 G\mathcal{I}_1(\sqrt{G}R_0)}{R_0\sqrt{G}\mathcal{I}_0(\sqrt{G}R_0) - 2\mathcal{I}_1(\sqrt{G}R_0)}\right], & G > 0, \quad (4.2.5a) \\ -q\left[h_0''(R_0) + \dfrac{4}{R_0}\right], & G = 0, \quad (4.2.5b) \end{cases}$$

respectively, where $R_1 \neq 0$ has been cancelled throughout. Therefore, given a set of nondimensional parameters, ϕ, G we calculate the equilibrium contact line position, R_0, and free surface, $h_0(r)$, defined by (3.4.9a, 3.4.9b) and subsequently calculate the growth rate of the axisymmetric mode (4.2.5a, 4.2.5b).

4.2.2 Non-axisymmetric perturbations

When considering non-axisymmetric perturbations, for wavenumbers $m = 1, 2, 3, ...$, the eigenvalue equation (4.1.4) again simplifies to an ODE of lower order when avoiding trivial solutions, in this case where $\mathcal{L}_1(h_1) = 0$,

$$0 = h_1'' + \frac{1}{r}h_1' - \left(\frac{m^2}{r^2} + G\right)h_1, \quad (4.2.6)$$

which we solve subject to the regularity condition $h_1(0) = 0$, and the contact condition (4.1.13). The general solution is therefore

$$h_1(r) = \begin{cases} c_1\mathcal{I}_m(\sqrt{G}r) + c_2\mathcal{K}_m(\sqrt{G}r), & G > 0, \quad (4.2.7a) \\ c_1 r^m + c_2 r^{-m}, & G = 0, \quad (4.2.7b) \end{cases}$$

where $\mathcal{I}_m$ and $\mathcal{K}_m$ are mth order modified Bessel functions of the first and second kind, respectively. The regularity condition $h_1(0) = 0$ determines that $c_2 = 0$ in both cases, and as a result both solutions exhibit the required behaviour that $h_1 \sim r^m$ as $r \to 0$ to satisfy each velocity regularity condition (3.2.36) and, if appropriate when $m = 2, 3, 4, ...$, the differentiability condition (4.1.20). Applying

the contact condition (4.1.13) normalises the solutions so that

$$h_1(r) = \begin{cases} R_1 \dfrac{\mathcal{I}_m(\sqrt{G}r)}{\mathcal{I}_m(\sqrt{G}R_0)}, & G > 0, \quad (4.2.8a) \\ R_1 \left(\dfrac{r}{R_0}\right)^m, & G = 0. \quad (4.2.8b) \end{cases}$$

Subsequently, using the combined Tanner law (4.1.15) determines the growth rate of each mode,

$$\sigma_m = \begin{cases} -q \left[h_0''(R_0) + \sqrt{G} \dfrac{\mathcal{I}_{m+1}(\sqrt{G}R_0)}{\mathcal{I}_m(\sqrt{G}R_0)} + \dfrac{m}{R_0} \right], & G > 0, \quad (4.2.9a) \\ -q \left[h_0''(R_0) + \dfrac{m}{R_0} \right], & G = 0. \quad (4.2.9b) \end{cases}$$

In both cases the sign of $h_0''(R_0)$ is unconditionally negative within the parameter space where physical equilibrium solutions exist.

4.2.3 Results

Recall that, for each wavenumber $m = 0, 1, 2, ...$, the real part of the frequency, $\Re(\sigma_m)$, determines the linear stability of this system; if $\Re(\sigma_m) > 0$ the perturbation grows in time and the system is linearly unstable, while if $\Re(\sigma_m) < 0$ perturbations decay in time and the system is linearly stable. We find that $\sigma_m \in \mathbb{R}$ as expected due to the lack of the Coriolis force in the lubrication theory meaning there is no precession of modes within the rotating frame of reference.

Figures 4.2 (a)–(c) show the how the growth rate, σ_m, of each wavenumber $m = 0, 1, 2, ..., 6$ varies with the Bond number, G, for three different values of the centrifugal number, ϕ, while figures 4.2 (d)–(f) show the growth rates as ϕ is varied for different values of G. Each of the figures 4.2 were produced using the Tanner exponent, $q = 1$.

Figure 4.2 (a) shows that when no rotation occurs where $\phi = 0$, the $m = 1$ mode is neutrally stable. The $m = 1$ perturbation corresponds to a translation of the fluid away from the axis $r = 0$, as shown in figure 4.1. Therefore, when $\phi = 0$ this translation has no effect and the system remains in equilibrium, centered at a different point. Furthermore, we see that when no rotation occurs all modes

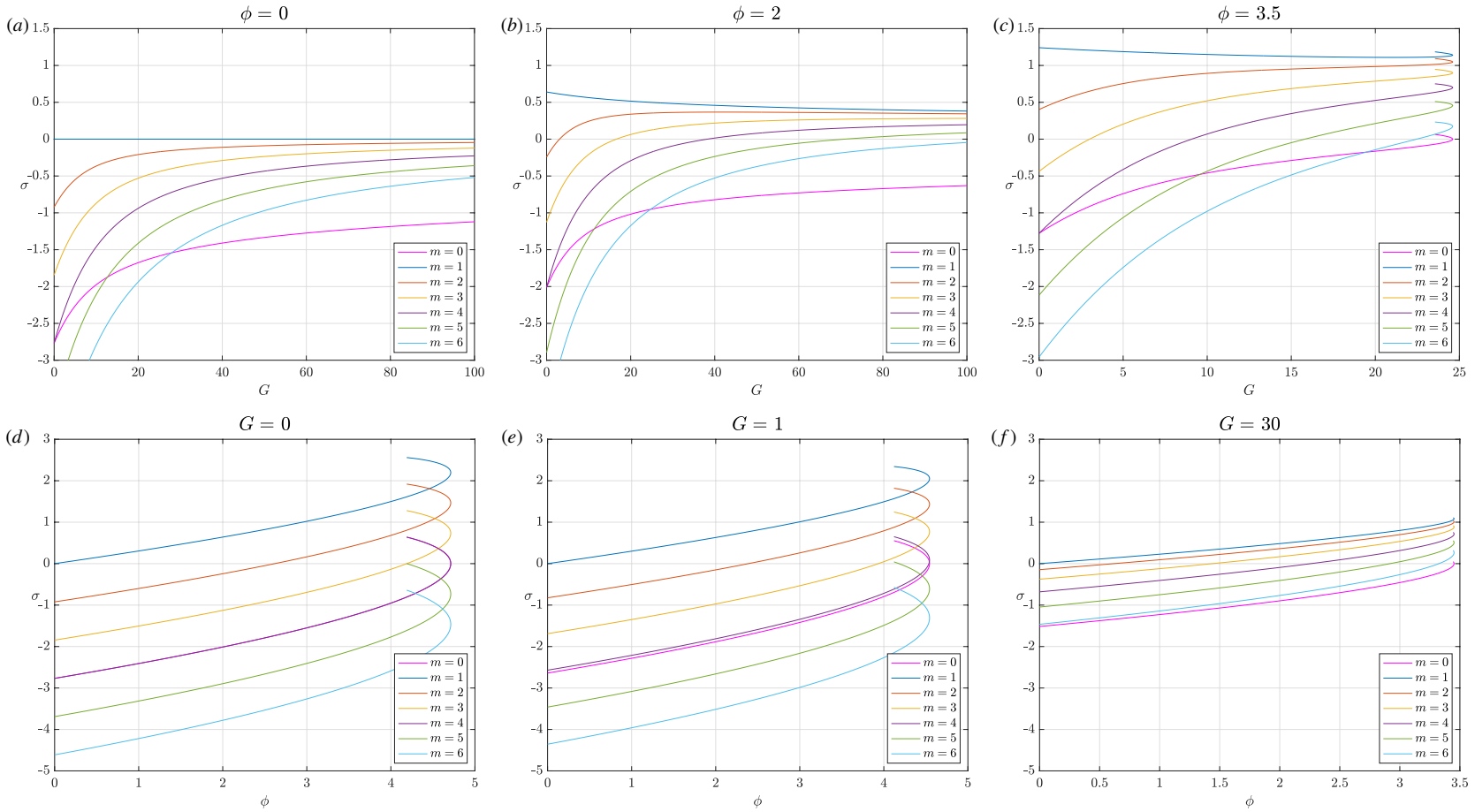


Figure 4.2: Growth rates in the $C = 0$ limit for each wavenumber $m = 0, 1, 2, ..., 6$ given by (4.2.5a, 4.2.5b, 4.2.9a, 4.2.9b). Figures (a)–(c) show growth rates as the Bond number G is varied for $\phi = 0, 2, 3.5$, respectively. Figures (d)–(f) show the growth rates as the centrifugal number, ϕ, is varied for $G = 0, 1, 30$, respectively.

are linearly stable and cannot be destabilised by increasing the Bond number. In terms of dimensional parameters; increasing the volume does not destabilise the stationary system.

In each of figures 4.2 (b)–(c), when $\phi > 0$, we observe that increasing the Bond number has a destabilising effect so that higher wavenumbers become unstable sequentially. This can be physically justified since larger wavenumbers have shorter wavelengths and hence larger curvature, so feel more effect due to surface tension. Therefore, larger wavenumbers require a greater gravitational effect to overcome the surface tension and hence a greater Bond number and so each mode becomes unstable sequentially. Notice that for $m = 1, 2, 3, ...$, the growth rates never cross each other and in each figure we see that the $m = 1$ mode, corresponding to a droplet translated off the axis off rotation, is always unstable when $\phi > 0$, and is unconditionally the most unstable mode when $C = 0$. When the Bond number is large the $m = 0$ mode becomes the most stable.

The growth rate of an unstable mode $m = 2, 3, 4, ...$ can rise to a maximum with G, so that increasing the Bond number further has a stabilising effect, where σ_m decreases as G increases. This is particularly visible in the $m = 2$ mode in figure 4.2 (b) where a maximum occurs at $G \approx 30$. The Bond number at which the maximum occurs increases with wavenumber and decreases with ϕ. In figures 4.2 (b)–(c) we see that growth rates of the $m = 1$ mode decrease as G increases up to its maximum value in the parameter space.

When the centrifugal number is beyond its critical value we enter the region where multiple solutions for R_0 exist, shown in figure 3.4 (a, b) in the darker shade of grey. Figure 4.2 (c) shows that within this region of the parameter space that the upper branch of solutions is always more unstable than the lower branch. Specifically, we see that axisymmetric perturbations are linearly stable on the lower branch and linearly unstable on the upper branch, meaning that the point (ϕ_m, R_{0c}) defined in § 3.4 is a saddle-node bifurcation point. This is shown more clearly in figures 4.2 (d)–(f) where the $m = 0$ mode always cross $\sigma_m = 0$ at the maximum value of ϕ possible for a given Bond number, G.

Figure 4.2 (d) shows the eigenvalues in the case that $G = 0$ (4.2.5b, 4.2.9b). We observe that the growth rates of the $m = 0$ and $m = 4$ mode are identical in this special case but not when $G > 0$. This is visible in figures 4.2 (a)–(c) where the

$m = 0$ and $m = 4$ growth rates converge at $G = 0$, and also in figures 4.2 (e)–(f) where the two lines are distinct. Furthermore, when $G = 0$ notice that the $m = 5$ mode reaches neutral stability at the point (ϕ_c, R_{0m}); the point where solutions become unphysical, but when $G > 0$ this is not the case. The results when $G = 0$ are equivalent to the findings of McKinley and Wilson [43], who reported the same features when $G = C = 0$. Boettcher and Ehrhard [44] reported similar findings when $G = 1 \times 10^{-3}$.

In each of the figures 4.2 (d)–(f) notice that the growth rates as ϕ is varied for constant G look qualitatively the same, with the modes $m = 1, 2, 3, ...$ becoming sequentially unstable as ϕ is increased. This is expected since larger values of ϕ correspond to greater rotation rates, and hence a greater destabilising force. A key point is that in each case the growth rates of modes $m = 1, 2, 3, ...$ at any fixed ϕ and G are in order of wavenumber. Specifically, crossing of growth rates for modes $m = 1, 2, 3, ...$ only occurs when the solutions corresponding to the upper branch of one mode crosses the lower branch of another, meaning again that the $m = 1$ mode is always dominant. Again we see that for larger G that the axisymmetric mode, $m = 0$, becomes the most stable for all values of values of ϕ.

Considering the growth rates (4.2.5a, 4.2.5b, 4.2.9a, 4.2.9b) we see in all cases that q is a multiplier of the growth rate and so does not affect the stability in the $C = 0$ limit, only the magnitude of σ_m.

4.3 Neutral stability

When considering the neutral stability of each mode, irrespective of the value of C the solutions for the perturbed free surface, $h_1(r)$, is given by solving the same ODE as when $C = 0$, (4.2.1), subject to the same boundary conditions associated with a given wavenumber (4.1.29)–(4.1.32). Hence, solutions for $h_1(r)$ along neutral stability curves will be identical as those in the axisymmetric and non-axisymmetric quasi-steady cases presented in § 4.2. The neutral stability curves of each mode are given by substituting solutions for the perturbed free surface, $h_1(r)$, (4.2.4a, 4.2.4b, 4.2.8a, 4.2.8b) into the combined Tanner law (4.1.15) and contouring at $\sigma_m = 0$. Notice that the solutions for $h_1(r)$ are independent of the slip length, α and also the Tanner exponent, q and therefore, the neutral stability

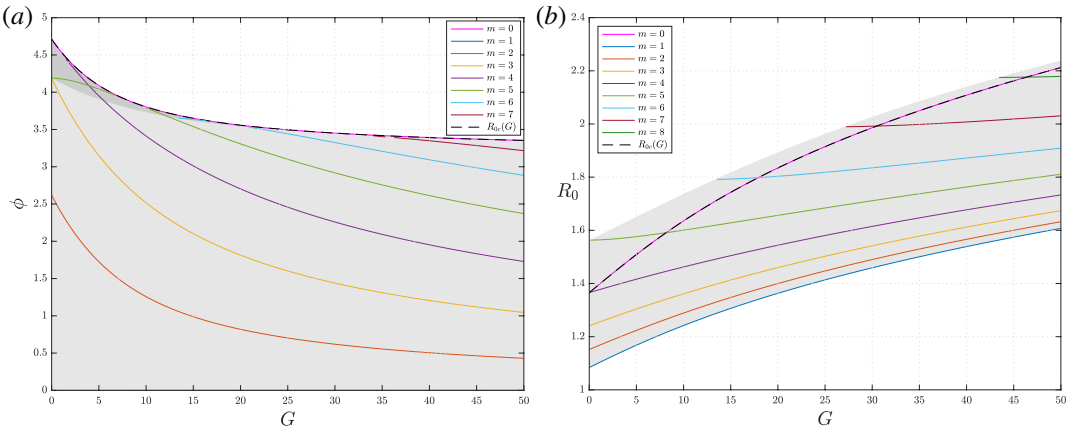


Figure 4.3: Neutral stability curves plotted within in each of the (a) $G - \phi$ and (b) $G - R_0$ parameter spaces for wavenumbers (a) $m = 0, 1, 2, ..., 7$, (b) $m = 0, 1, 2, ..., 8$.

curves are independent of the capillary number, C, the slip length, α, and the Tanner exponent, q.

Figure 4.3 shows the neutral stability curves plotted in the parameter space as in figure 3.4, where the area above a curve indicates instability of the labelled wavenumber. Immediately from each figure we see that the axisymmetric mode, $m = 0$, lies on top of the bifurcation point (ϕ_m, R_{0c}) where the centrifugal number, ϕ, is at its maximum. Therefore, we find that this point in parameter space is indeed a saddle node bifurcation point, where the upper branch of solutions as in figure 3.3 is linearly unstable, while the lower branch linearly stable. This is equivalent to the analysis of axisymmetric perturbations of equilibrium solutions performed by McKinley *et al* [42], who also showed a saddle-node bifurcation at the maximum rotation rate in a different nondimensional regime.

In each figure we see that the $m = 1$ mode, where the contact line is translated off the axis of rotation, is always unstable throughout the parameter space if any rotation is included. Hence, the neutral stability curve is simply $\phi = 0$, and therefore also where R_0 is minimum, as seen in figure 4.3 (b) where the $m = 1$ mode is the lower bound of the $G - R_0$ parameter space. In figure 4.3 when the Bond number, G, is increased for fixed ϕ each mode successively becomes unstable; as described in § 4.2 this is due to larger wavenumbers being subject to a greater effect due to surface tension. As the centrifugal number, ϕ, increases for fixed G each mode becomes successively unstable and higher modes can only become unstable for sufficiently large G. Again, an interpretation of this was

described in § 4.2 where it is argued that as the wavenumber is increased a greater centrifugal number is required to overcome the additional surface tension effects due to curvature, leading to greater wavenumbers becoming successively unstable for greater centrifugal numbers.

Each neutral stability curve for $m \neq 1$ decreases with G in figure 4.3 (a), meaning a lower centrifugal number, ϕ, is required to destabilise that mode. In terms of physical parameters, larger droplets require lower rotation rates for higher wavenumbers to become unstable in qualitative agreement with the experimental observations of chapter 2. We see that in each figure 4.3 (a, b) that the neutral stability curves of the $m = 0$ and $m = 4$ modes meet when $G = 0$ due to the growth rates, σ_0 (4.2.5b), and σ_4 (4.2.9b) being identical when $G = 0$. The neutral stability curves in figure 4.3 (a) in the $G - \phi$ space only cross in the region where multiple solutions exist for the same combination of (ϕ, G), indicated by a darker shade of grey. Interestingly, when $G = 0$ and R_0 is maximum, the $m = 5$ mode is neutrally stable and meets the lower branch of the $m = 3$ mode at this point in the solution space as shown in figure 4.2 (d).

4.4 General case, $C > 0$

We now consider the general case where $C > 0$ given by the eigenvalue equation (4.1.4) subject to the appropriate boundary conditions defined in § 4.1.3, depending on the wavenumber, m. The eigenvalue problem is solved numerically in all cases using a finite difference approximation to discretise the eigenvalue equation and boundary conditions and solve for the eigenfunction, $h_1(r)$, and the eigenvalue, σ_m, for a given set of nondimensional parameters, ϕ, G, C a wavenumber, m, and a slip length α. The boundary conditions used depend on the wavenumber, m, and are given by (4.1.29)–(4.1.32). The generalised eigenvalue problem $Ah_1 = \sigma_m B h_1$, is constructed from the eigenvalue problem (4.1.4) when $C > 0$. When, $m = 1, 2, 3, ...$, A and B are $N \times N$ matrices, where N is the number of uniformly spaced grid points. In the axisymmetric case when $m = 0$, A and B are $2N \times 2N$ matrices, since we must couple the system with the integral condition (4.1.27). Further detail on the finite difference discretisation is presented in appendix B

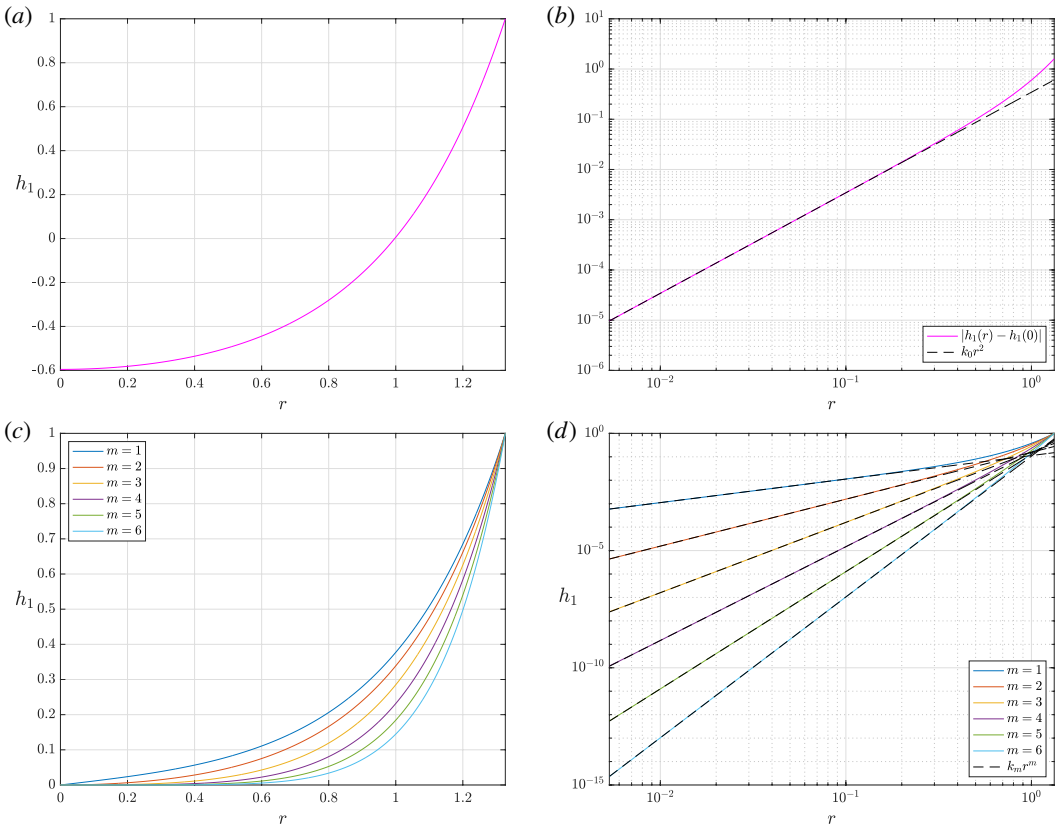


Figure 4.4: Normalised eigenvector $h_1(r)$, plotted on regular and log-log axes for $G = 10, \phi = 2, C = 0.01, q = 1$ and $\alpha = 1 \times 10^{-4}$, plotted for (a, b) $m = 0$, (c, d) $m = 1, 2, ..., 6$.

Figures 4.4 (a, c) show the eigenvectors, $h_1(r)$, when $G = 10, \phi = 2$, $C = 0.01$, $q = 1$ and the slip parameter, $\alpha = 1 \times 10^{-4}$, for (a) $m = 0$ and (c) $m = 1, 2, ..., 6$. The contact angle condition at leading order in ϵ, (3.4.10a), gives that $R_0 = 1.33$, and the equilibrium solution, $h_0(r)$, is presented in figure 3.2 (b). Figures 4.4 (b, d) show the same eigenfunctions, $h_1(r)$, plotted on logarithmic axes. In the axisymmetric case where $m = 0$, $h_1(0) < 0$ due to volume conservation, figure 4.4 (b) shows the difference in the eigenvector from its value at $r = 0$, $h_1(r) - h_1(0)$. We see that the solution close to $r = 0$ behaves like r^2, as shown by the linear relationship between values of r and $h_1(r)$ when plotted using logarithmic axes, with gradient equal to 2. In the $C = 0$ limit we see the same behaviour, since

when $r \ll 1$ (4.2.4a, 4.2.4b) become

$$h_1(r) - h_1(0) = \begin{cases} \dfrac{1}{4} \dfrac{R_1 R_0 G^{3/2}}{\sqrt{G} R_0 \mathcal{I}_0(\sqrt{G} R_0) - 2\mathcal{I}_1(\sqrt{G} R_0)} r^2 + \mathcal{O}(r^4) & G > 0, \quad (4.4.1a) \\ \dfrac{2R_1}{R_0^2} r^2, & G = 0. \quad (4.4.1b) \end{cases}$$

Hence, the behaviour near the origin for the axisymmetric eigenfunction is consistent with the findings in figure 4.4.

Figure 4.4 (c, d) show the eigenfunction in each case where $m = 1, 2, ..., 6$. We observe that near the origin, the solutions behave like r^m, with each eigenfunction showing a linear relationship between values of r and $h_1(r)$ with gradient equal to the wavenumber when plotted on a logarithmic axis in figure 4.4 (d). To further illustrate the behaviour near the origin, we consider the series expansion about $r = 0$ of the eigenvalue equation (4.1.4) satisfying $h_1'(0) = 0$ due to differentiability (4.1.20) when $m = 2, 3, 4, ...$

$$h_1(r) = \sum_{n=0}^{\infty} k_n r^n, \tag{4.4.2}$$

so that k_1 is equal to zero. Forcing the coefficients of each power of r present in the expansion of (4.1.4) to be zero, we find that all coefficients $k_n = 0$ for $0 \leqslant n < m$ and $m > 1$, so that

$$h_1(r) \sim k_m r^m + \mathcal{O}(r^{m+1}) \tag{4.4.3}$$

near the origin, agreeing with the numerical results in figure 4.4 (d). When $m = 1$ we find that $k_0 = 0$ while $k_1 \neq 0$. Therefore our numerical solutions satisfy the required velocity regularity condition (3.1.12) as argued in § 4.1.3.

Figures 4.5 (a)–(c) show how the eigenvalues vary, for each wavenumber $m = 1, 2, ..., 6$, as G is increased for $\phi = 0, 2, 3.5$, the same values as used in figures 4.2 (a)–(c), but when the capillary number, $C = 1$ so that viscous drag and surface tension are balanced. Figure 4.5 (a) shows the stationary case in which no rotation occurs and similarly to the solutions when $C = 0$, we again see that each mode is stable as $\sigma_m \leqslant 0$ for all G. The trend in the eigenvalues is qualitatively similar to that shown in figure 4.2 (a) when $C = 0$, but the numerical value of the growth rates has decreased significantly. Figures 4.5 (b, c) show the eigenvalues as the Bond number, G, is varied for non-zero centrifugal number, $\phi > 0$. We see

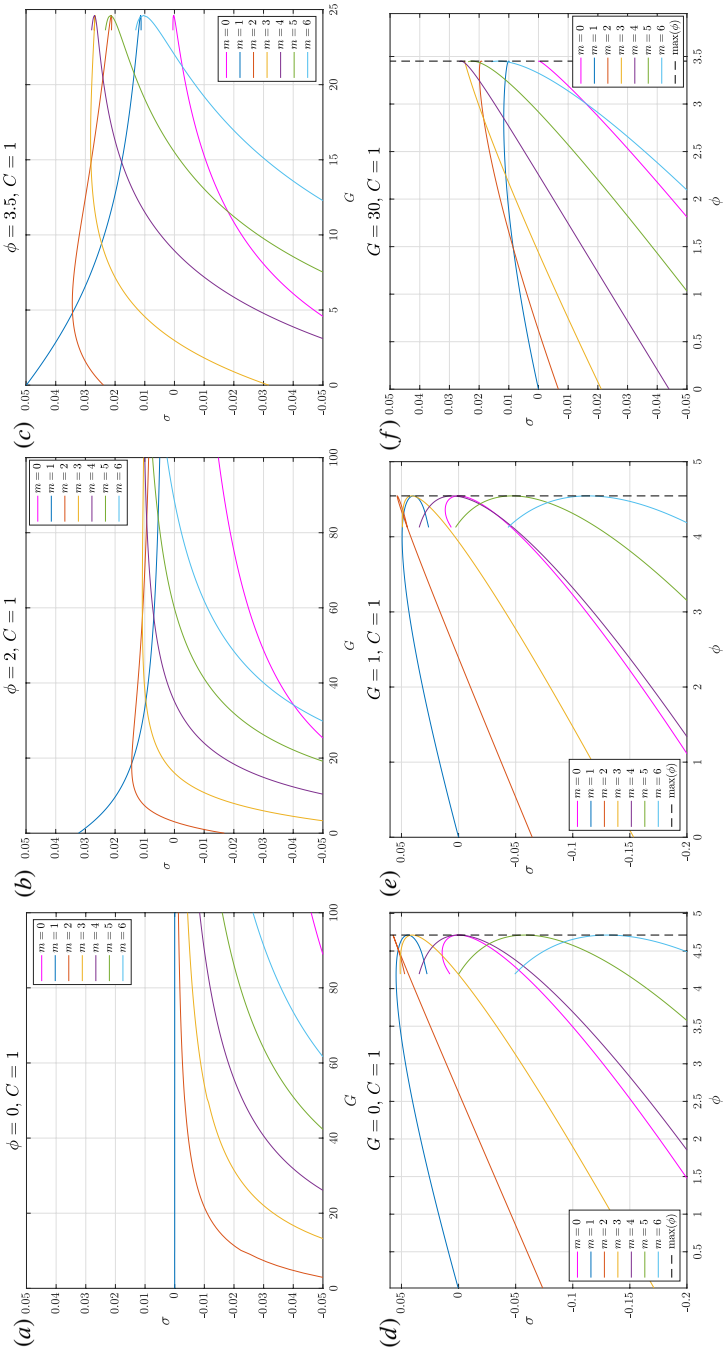


Figure 4.5: Eigenvalues of first seven wavenumbers, $m = 1, 2, ..., 6$ for $\alpha = 1 \times 10^{-6}$ and $C = 1$ as (a)–(c) G is varied for different values of ϕ and (d)–(f) as ϕ is varied for different values of G.

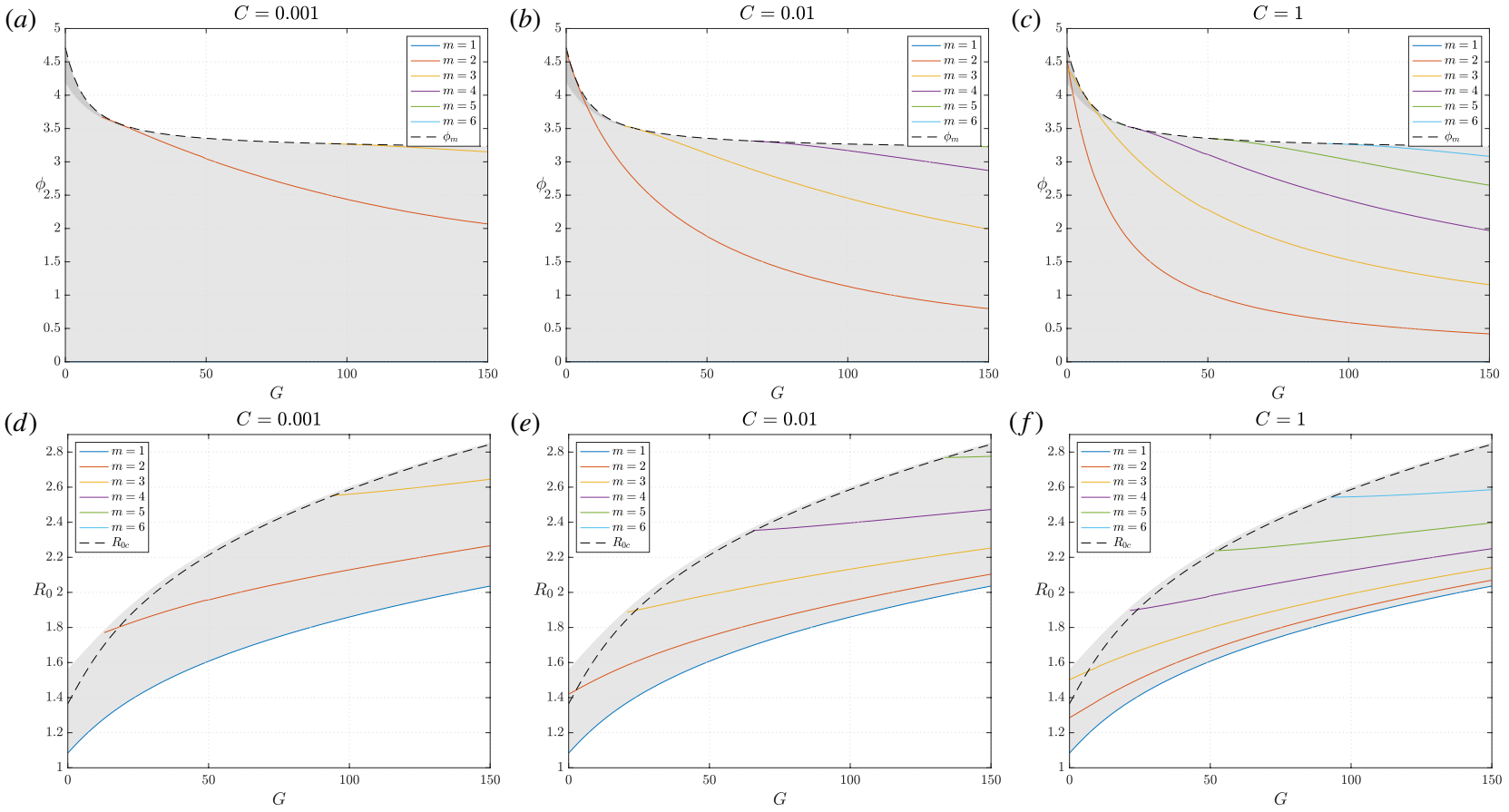


Figure 4.6: Thresholds where the most unstable modes changes for varying capillary number within both (a)–(c) the $G - \phi$ and (d)–(f) the $G - R_0$ parameter spaces when $\alpha = 1 \times 10^{-4}$.

that each mode becomes unstable sequentially, as shown by the neutral stability plots in figure 4.3. Similarly to when $C = 0$, σ_m can rise to a maximum and then decrease, meaning a slower growth rate above a critical point. In figures 4.2 (b, c), we saw the same behaviour when $C = 0$, but saw that eigenvalues of wavenumbers $m = 1, 2, 3, ...$ cannot cross, resulting in $m = 1$ as always the most unstable, or dominant, mode. When $C > 0$, eigenvalues can cross, allowing higher wavenumbers to become dominant sequentially, which is particularly visible in figure 4.5 (c). Furthermore, comparing figures 4.5 (b, c) indicates that increasing the centrifugal number, ϕ causes eigenvalues of each mode to be more unstable for the same Bond number, G.

Figures 4.5 (d)–(f) show the numerical eigenvalues when $C = 1$ as ϕ is varied for different values of G. In each figure we see that the eigenvalues of each mode in general become more unstable as the centrifugal number, ϕ, is increased. This is expected since larger values of ϕ correspond to of greater rotation rates, and hence a greater destabilising force. Hence, as the wavenumber is increased a greater centrifugal number is required to overcome the additional surface tension due to curvature. Perhaps surprisingly, we observe that the added capillary effects lead to growth rates decreasing as ϕ is increased. In figures 4.5 (d)–(f) the $m = 1$ mode grows to a maximum and subsequently decreases until $\phi = \phi_c$. This behaviour was observed experimentally for each volume considered in chapter 2. Furthermore, in contrast to the findings in § 4.2, notice that in each of figures 4.5 (d)–(f) in the region where multiple physical solutions of the contact angle condition (3.4.10a, 3.4.10b) exist, the lower branch of solutions is more unstable than the upper branch. This is also the case for the $m = 2$ mode in figure 4.5 (f). Furthermore, when $G = 0$, the result in the quasi-steady limit that $\sigma_0 = \sigma_4$ is lost. This is shown in figure 4.5 (d), where ϕ is varied and the eigenvalues for $m = 0$ and $m = 4$ are distinct, in contrast to figure 4.2 (d) where these growth rates are identical one another when $C = 0$. Overall, we find that increasing ϕ allows higher wavenumbers, starting from $m = 1$, to sequentially become the dominant mode.

Note that, as predicted by the analytical solutions when $C = 0$, the point of neutral stability of the axisymmetric mode is exactly at the point (ϕ_m, R_{0c}), where ϕ is maximum. This can be seen on each of figures 4.5 (d)–(f) as the $m = 0$ mode crosses $\sigma_m = 0$ tangent to the dashed line, indicating the maximum value of ϕ.

More specifically, by comparing figures 4.2 (a)–(f) to figures 4.5 (a)–(f) we recover the result from § 4.3 that the neutral stability of the system is independent of the capillary number, C, as each line crosses $\sigma_m = 0$ at the same point in like-for-like figures.

In § 4.2 we noted that figures 4.2 (a)–(f) show that when $C = 0$ the $m = 1$ mode is always the most unstable. In contrast, figures 4.5 (a)–(f) show that when the capillary number is larger, as either of ϕ or G are increased the dominant mode increases sequentially from $m = 1$. Figures 4.6 (a)–(c) show plots of the dominant mode within the $G - \phi$ parameter space for three different values of the capillary number, C, while figures 4.6 (d)–(f) show the same thresholds in $G - R_0$ parameter space. In each figure the area above the labelled curve is the region of parameter space which that respective mode is the most unstable. The $m = 1$ contour in figures 4.6 (a)–(c) lies at $\phi = 0$, and in (d)–(f) on the minimum R_0. As the capillary number, C, is decreased, the area of $G - \phi$ space for which $m = 1$ is the dominant mode increases, until the $m = 1$ mode dominates the parameter space when $C = 0$. Furthermore, increasing C allows for higher modes to dominate within the same $G - \phi$ parameter space. Specifically, as C is increased, higher modes require lower values of ϕ and G to become dominant and therefore the area where higher modes are unstable is to the upper right of the parameter space. We also see that the $m = 0$ is never the most dominant mode in either parameter space. In each of figures 4.6 (a)–(c), in the $G - \phi$ parameter space the contours where the most unstable mode changes are decreasing with G, while in the $G - R_0$ parameter space, shown in figures 4.6 (d)–(f) the contours increase with G. This can be seen by considering the crossing point of the $m = 1$ and $m = 2$ mode when comparing between figures 4.5 (b, c). When $\phi = 2$ the crossing point is at $G \approx 18$, whereas when $\phi = 3.5$, the crossing point is at $G \approx 5$. In terms of physical parameters, larger volumes require lower rotation rates in order for higher wavenumbers to become dominant. This result is supported by the experimental observations noted in chapter 2.

4.4.1 Comparison to small capillary number limit

When the capillary number is small but finite, corresponding to surface tension dominating viscous drag, we can compare the numerical eigenvalues, σ_m, and

eigenfunctions, $h_1(r)$, of the eigenvalue problem (4.1.4), to the analytical solutions found in § 4.2. Recall that in deriving the combined Tanner law (4.1.15) we assume that the $\mathcal{O}(\epsilon)$ contact line position, $R_1 \neq 0$, and taking $C = 0$ violates this. Whereas, the numerical solution for $C \ll 1$ is well founded as the contact line velocity is non-zero meaning that the contact line can move due to the Greenspan slip law (3.1.7).

The numerical method used to solve the generalised eigenvalue problem $Ah_1 = \sigma_m B h_1$ given by (4.1.4) subject to the combined Tanner boundary law (4.1.15) and further boundary conditions depending on the wavenumber (4.1.29)–(4.1.32) is described in appendix B. When $C = 0$, the eigenvalue, σ_m, only appears in the Tanner law (4.1.15) and therefore the square matrix B will have a single non-zero entry. Hence, the case where $C = 0$ can be solved numerically and the results compared with the analytical solutions in § 4.2 to verify our numerical method. Figure 4.7 shows the numerical solutions for $h_1(r)$ for centrifugal number, $\phi = 2$, slip parameter, $\alpha = 1 \times 10^{-4}$, and various values of capillary number, C, and Bond number, G for wavenumbers, $m = 0, 1, 2, ..., 6$. On each figure the corresponding analytical solution for $h_1(r)$ when $C = 0$ (4.2.8a, 4.2.8b) is shown in a black dashed line. Immediately, from figures 4.7 (a, b, e, f) we see that the numerical solutions when $C = 0$ and $G = 0, 10$ agree well with the analytical solutions derived in § 4.2. Figures 4.8 (a)–(c) show the numerical eigenvalues of each wavenumber, $m = 0, 1, 2, ..., 6$, as G is varied for $\phi = 2, \alpha = 1 \times 10^{-4}$ and increasing C across the three figures. Figures 4.8 (d)–(f) show the numerical eigenvalues for the same wavenumbers, slip number and capillary number but as ϕ is varied for $G = 10$. Once again the analytical solutions when $C = 0$ from § 4.2 are plotted in dashed black lines on each figure. We again see in figures 4.8 (a, d) when $C = 0$ the numerical eigenvalues show good agreement to the analytical growth rates found in § 4.2. Hence, both the eigenvalues and eigenfunctions agree with the analytical solutions when $C = 0$, verifying the numerical method.

When $C = 0.1$, figures 4.7 (c, d, g, h) show that the numerical eigenfunctions differ from the analytical solutions while retaining the r^m behaviour near the origin. This is demonstrated in figures 4.4 (b, d) where the solutions are plotted using logarithmic axes. In each of figures 4.8 (a)–(f) where $C \neq 0$, we see that the point of neutral stability is independent of C so that for each mode the numerical and respective analytic growth rates only cross when $\sigma_m = 0$, consistent with

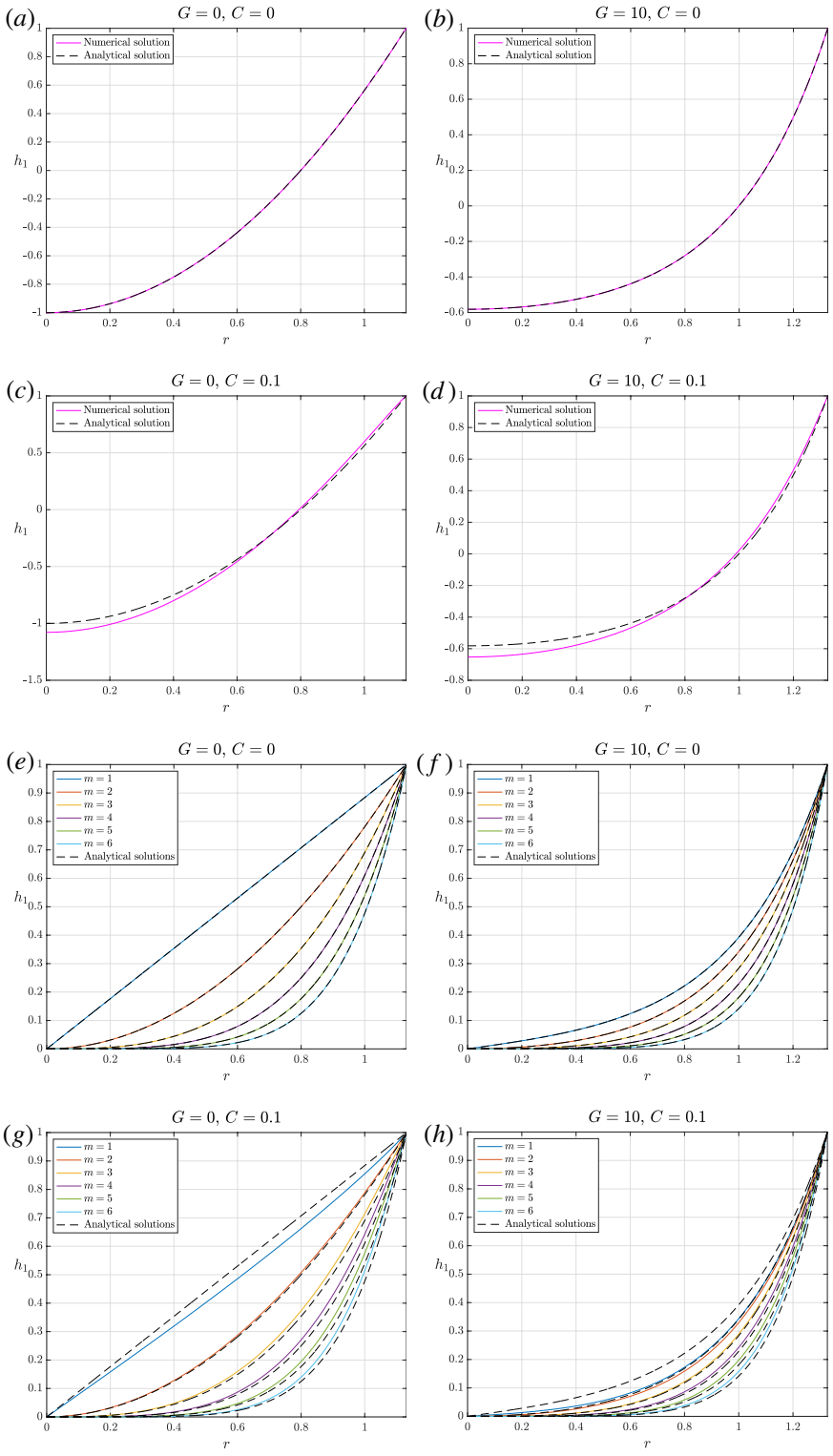


Figure 4.7: Comparisons of the eigenfunction h_1 when $\phi = 2$, $\alpha = 1 \times 10^{-4}$, (a)–(d) $m = 0$, (e)–(h) $m = 1, 2, ..., 6$ with the exact analytical solutions when $C = 0$ and $C = 0.1$.

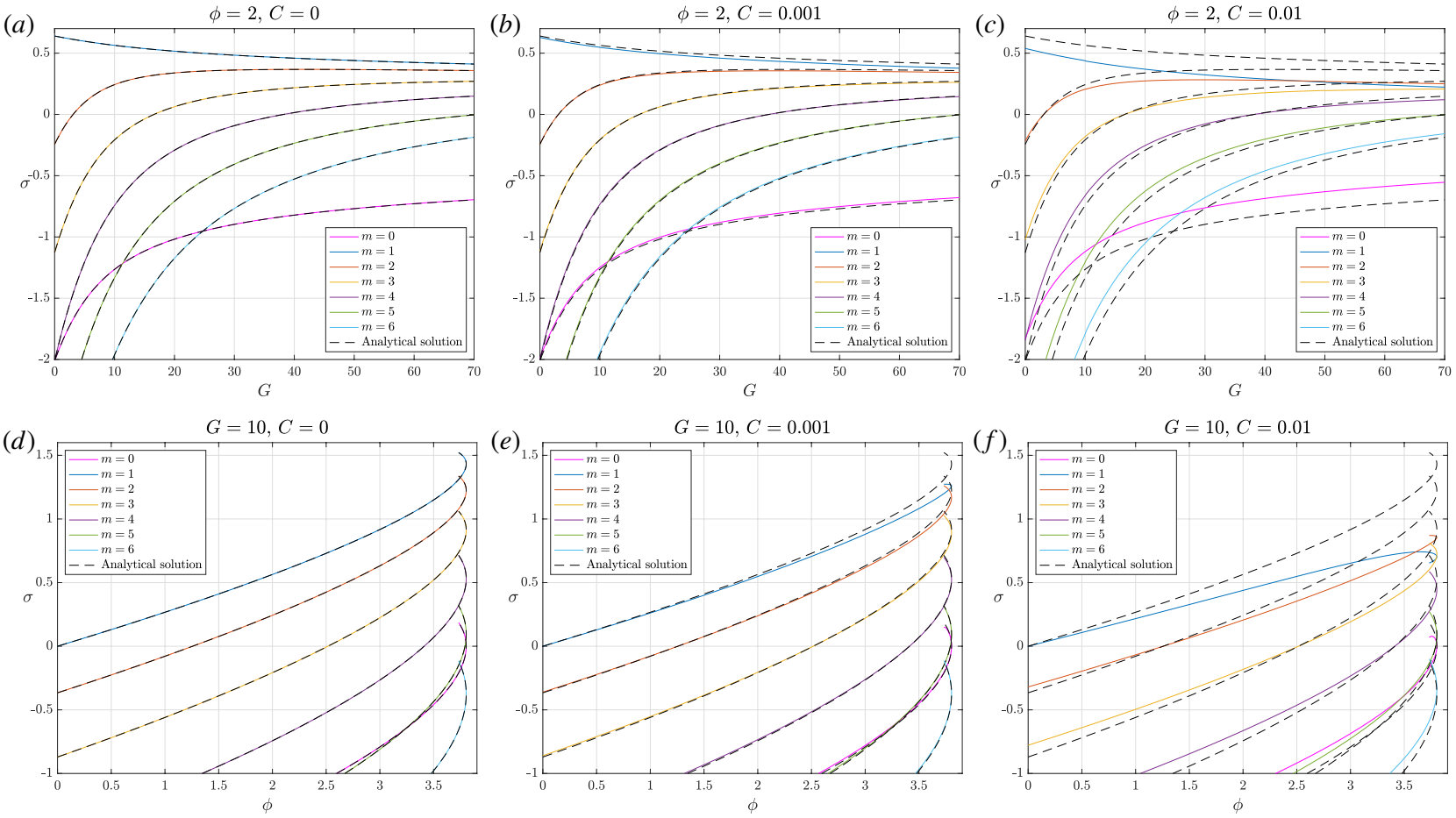


Figure 4.8: Comparison of eigenvalues between the analytical solutions when $C = 0$, shown in black dashed lines, and numerical solutions, shown in solid lines, for small capillary numbers. Figures (a)–(c) show the comparison when $\phi = 2$ and $0 \leqslant G \leqslant 70$ for $C = 0, 0.001, 0.01$, whereas (d)–(f) show the comparison for the same capillary numbers when $G = 10$ and $0 \leqslant \phi \leqslant \phi_m(10)$.

the findings in § 4.3. Consequently, in figures 4.8 (b, c, e, f) the eigenvalues are deflected away from the analytical solution towards the axis $\sigma_m = 0$, with greater deflection as C increases. We again see that as the capillary number C increases the growth rates of different wavenumbers $m = 1, 2, 3, ...$ can cross, meaning higher modes can become dominant.

4.5 Summary

In this chapter we have analysed the linear stability of the equilibrium solutions found in § 3.4 using the Tanner law, discussed in chapter 1, to model the contact line dynamics and the Greenspan slip condition [31] in replacement of the classical no-slip condition. Previous modelling of the same system use a Navier slip law [42, 43], which leads to a zero contact line speed and a qualitative change in the boundary conditions, discussed further in § 5.1.

We found analytical solutions for the perturbed free surface, $h_1(r)$, in the quasi-steady limit, $C \to 0$, for different wavenumbers, m, analysing the unexplored cases when $G > 0$ and $m = 1, 2, 3, ...$ as well as recovering the solutions of McKinley *et al.* [42] where $m = 0$ and McKinley and Wilson [43] when $G = 0$, $m = 1, 2, 3, ...$ Subsequently, the growth rates were determined using the combined Tanner law (4.1.15) and we saw how varying both the centrifugal number, ϕ, and Bond number, G, affected the growth rates within this limit. The main result being that in this limit the $m = 1$ mode is unconditionally dominant provided $\phi > 0$.

We determined that the neutral stability curves are independent of the capillary number, C, slip length, α, and Tanner exponent, q. Specifically, we found that the point in the parameter space (ϕ_m, R_{0c}), where the centrifugal number is maximum, is a saddle-node bifurcation point with axisymmetric perturbations, $m = 0$, being unstable on the upper branch of solutions, and stable on the lower branch. Furthermore, for non-axisymmetric perturbations $m = 1, 2, 3, ...$ we found that as both ϕ and G are increased, higher modes become unstable sequentially.

Next we considered the general case where $C > 0$, where the previously derived eigenvalue equation was solved numerically using a finite difference scheme. Previous modelling only consider on the case where $G = 0$ [43], in § 4.4 novel solutions

for the case where $G > 0$ are presented and the differences from previous solutions are demonstrated. We discussed how varying each parameter affects the eigenvalues, seeing that including capillary dynamics allows the dominant mode to change as both ϕ and G are varied, unlike when $C = 0$. We found that in the small capillary limit that the eigenvalues approach the analytical solutions previously found within the quasi-steady limit.

Chapter 5

Further analysis and extensions of linear stability theory

In this chapter we discuss further analysis and three extensions to the modelling of the linear stability problem detailed in chapter 4. First, in § 5.1 we discuss the effect of imposing the slip condition (3.1.7) along with alternative slip coefficient functions. Next, in § 5.2 we assess the linear stability of equilibrium solutions when an alternative model for the contact angle is employed, namely the fixed contact angle condition. Following this, in § 5.3 we present an extended model where previously neglected terms representing the Coriolis effect are now included. We discuss the linear stability results for this extended model subject to the Tanner law and fixed contact angle condition, evaluating the quality of the assumption in neglecting Coriolis terms. Finally, in § 5.4 we discuss axisymmetric, numerical solutions to the thin film equation (3.3.7) in the quasi-steady limit, comparing the results to the linear stability analysis presented in § 4.2.

In this chapter the term 'Tanner model' refers to the linear stability analysis with subject to the Tanner law (3.1.10), discussed in § 4.4.

5.1 Slip condition

In this section we justify the imposition of the Greenspan slip law (3.2.29) (a, b). We consider the local expansion of the eigenvalue equation (4.1.4) to demonstrate the regularising effect of imposing said slip law in comparison to the classical no-

slip and common Navier slip laws. Finally, we discuss the effect of varying the slip length, α, on the eigenvalues of the general Tanner model which was discussed in § 4.4.

5.1.1 Local expansion

We demonstrate the effect of introducing a slip law (3.2.29) by expanding the eigenvalue equation (4.1.4) locally about the linearised contact line position, $r = R_0$. First, we change coordinate system so that

$$r = R_0 + \varepsilon\hat{r}, \quad h_0(r) = \varepsilon\hat{h}_0(\hat{r}), \quad h_1(r) = \hat{h}_1(\hat{r}), \tag{5.1.1}$$

where $\varepsilon \ll 1$ is different from the perturbation parameter used in the previous chapter, ϵ. The scaling (5.1.1) is justified since we know in the region surrounding $r = R_0$ we have $h_0(r) \ll 1$ due to the contact boundary condition. Upon substitution into the eigenvalue equation (4.1.4) the leading order, $\mathcal{O}(\varepsilon^{-1})$, gives

$$0 = \alpha\hat{h}_0\frac{\mathrm{d}^4\hat{h}_1}{\mathrm{d}\hat{r}^4} + \alpha\frac{\mathrm{d}\hat{h}_0}{\mathrm{d}\hat{r}}\frac{\mathrm{d}^3\hat{h}_1}{\mathrm{d}\hat{r}^3} = \alpha\frac{\mathrm{d}}{\mathrm{d}\hat{r}}\left(\hat{h}_0\frac{\mathrm{d}^3\hat{h}_1}{\mathrm{d}\hat{r}^3}\right). \tag{5.1.2}$$

The equilibrium shape $h_0(r)$ approaches zero as $r \to R_0$ hence $h_0(r) \sim r - R_0$. In our modified coordinate system (5.1.1), $\hat{h}_0(\hat{r}) \sim \hat{r}$ and (5.1.2) becomes,

$$0 = \alpha\frac{\mathrm{d}}{\mathrm{d}\hat{r}}\left(\hat{r}\frac{\mathrm{d}^3\hat{h}_1}{\mathrm{d}\hat{r}^3}\right). \tag{5.1.3}$$

This has general solution, given in the original coordinate system

$$h_1(r) = a_1(r - R_0)^2\log(r - R_0) + a_2(r - R_0)^2 + a_3(r - R_0) + a_4, \tag{5.1.4}$$

where the coefficients, a_i, are constants. In the case when $\alpha = 0$, i.e. the classical no-slip conditions are applied, the leading order terms of the eigenvalue equation (4.1.4) are

$$0 = \frac{1}{3}\hat{h}_0^3\frac{\mathrm{d}^4\hat{h}_1}{\mathrm{d}\hat{r}^4} + \hat{h}_0^2\hat{h}_0'\frac{\mathrm{d}^3\hat{h}_1}{\mathrm{d}\hat{r}^3}, \tag{5.1.5}$$

which, following the same procedure as above, admits the general solution,

$$h_1(r) = a_1 \log(r - R_0) + a_2(r - R_0)^2 + a_3(r - R_0) + a_4. \tag{5.1.6}$$

Taking the limit as $r \to R_0$ demonstrates the effect of imposing the slip law. For $\alpha > 0$ the limit of (5.1.4) is zero, whereas, for $\alpha = 0$ the limit of (5.1.6) is $\pm\infty$ depending on the sign of a_1, assuming a_1 is non-zero. Therefore, the solution close to the contact line for $h_1(r)$ is more regular for the case where slip is imposed, $\alpha > 0$, than for the classical no-slip boundary conditions, $\alpha = 0$.

5.1.2 General slip law

Consider a general slip law,

$$u = s(h)\frac{\partial u}{\partial z}, \quad v = s(h)\frac{\partial v}{\partial z}. \tag{5.1.7}$$

The horizontal velocity, $\boldsymbol{u}_H$, analogous to (3.3.6), subject to the slip condition (5.1.7) is

$$\boldsymbol{u}_H = -\frac{\epsilon}{C}\left\{\frac{z^2}{2} - (z + s(h_0))h_0\right\}\nabla_H\left(\left[h_1'' + \frac{h_1'}{r} - \left(\frac{m^2}{r^2} + G\right)h_1\right]e^{\mathrm{i}m\varphi + \sigma_m t}\right). \tag{5.1.8}$$

We will consider three cases of the slip function,

$$s(h) = 0, \quad s(h) = \beta, \quad s(h) = \frac{\alpha}{3h}, \tag{5.1.9}$$

with each of these boundary conditions common in the literature as discussed in detail in chapter 1.

At the linearised contact line $r = R_0$, $z = 0$, the contact condition at leading order in ϵ is that $h_0(R_0) = 0$ and so the coefficient of $\nabla_H(\,\cdot\,)$ in (5.1.8) is zero, unless $s(h) \propto 1/h$ at $r = R_0$. Hence, in the case of no slip and constant slip, the velocity is zero at the contact line. In contrast, in the third case, where the Greenspan slip law is used, the contact line velocity can be non-zero, allowing movement. The contact line kinematic condition at $\mathcal{O}(\epsilon)$ (4.1.16) is,

$$\sigma_m R_1 = u_1(0, R_0), \tag{5.1.10}$$

therefore if the $\mathcal{O}(\epsilon)$ radial velocity, u_1, at the contact line is zero, as in the no-slip and Navier slip cases (5.1.7) (a, b), the contact line kinematic condition gives $R_1 = 0$ or $\sigma_m = 0$. If $\sigma_m = 0$ the system is neutrally stable and therefore the perturbation neither grows or decays. If $R_1 = 0$, the contact line is pinned at $r = R_0$, with contact angle $\theta = 1$ and remains in equilibrium. Furthermore, if $R_1 = 0$ the $\mathcal{O}(\epsilon)$ contact and contact angle conditions (4.1.11) (a, b) become

$$h_1(R_0) = 0, \quad h_1'(R_0) = 0, \tag{5.1.11}$$

respectively. The eigenvalue equation subject to the general slip law (5.1.7) has the same form as (4.1.4) but where the linear operator $\mathcal{L}_2$ is redefined so that

$$\mathcal{L}_2[\Phi] = \left[f(h_0)\frac{\mathrm{d}^2}{\mathrm{d}r^2} + \frac{1}{r}\left(r f(h_0)\right)' \frac{\mathrm{d}}{\mathrm{d}r} - \frac{m^2}{r^2} f(h_0) \right] \Phi, \tag{5.1.12}$$

where the function, $f(h)$, is defined as

$$f(h) = \frac{h^3}{3} + s(h)h^2. \tag{5.1.13}$$

When the appropriate eigenvalue equation (4.1.4) for the no-slip and Navier slip cases is solved numerically subject to (5.1.11) and suitable regularity conditions at $r = 0$, depending on the wavenumber, all eigenvalues are negative, and hence stable. This is the case for all allowed values of ϕ, G and m. Hence, there is no benefit in imposing the slip law with constant slip over a no-slip model, since although it will give a more regular solution at the contact line, the velocity at the contact line is zero in both cases making instability at the contact line impossible, and hence all perturbations decay in time. In fact, any slip function which does not have $s(h) \propto 1/h$ near $r = R_0$ will cause either a velocity singularity at the contact line, or zero velocity at the contact line. It is for this reason we chose (5.1.7) (c) as our slip function throughout.

The effect of choosing the Greenspan slip law is demonstrated when comparing the eigenvalues and eigenvectors of the linear problem between the chosen Greenspan slip function (5.1.7) (c) and the no-slip condition (5.1.7) (a). We see that there is a qualitative change between the shape of the normalised eigenvector, $h_1(r)$, from figures 4.4 (a, c) to figures 5.1 (a, c). Furthermore, the eigenvalue of each mode is stable when $\alpha = 0$, whereas for $\alpha > 0$ eigenvalues can be positive, and the

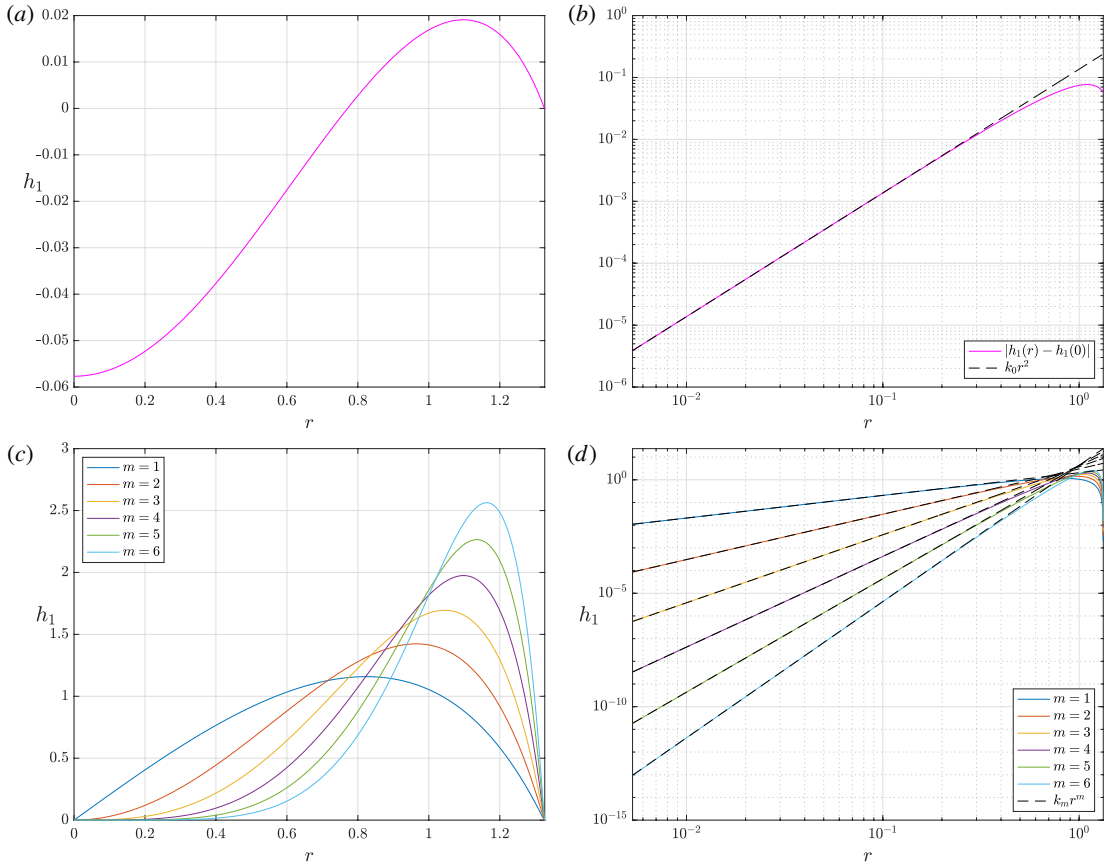


Figure 5.1: Figures (a, c) show the normalised eigenvectors $h_1(r)$ when (a) $m = 0$ and (c) $m = 1, 2, ..., 6$. Figures (b, d) show a the normalised eigenvector on logarithmic axes for (b) $m = 0$ and (d) $m = 1, 2, ..., 6$. Each eigenvector is calculated using the parameters $G = 10, \phi = 2$, $\alpha = 0$ and $C = 0.01$.

system unstable. Therefore, changing only the slip length from $\alpha = 1 \times 10^{-6}$ to $\alpha = 0$ produces a significant change in results and stability of the system due to the difference in boundary conditions. Figures 5.1 (b, d) show that the behaviour near the origin is retained for each wavenumber. If we overlook that $R_1 = 0$ when deriving the boundary conditions, then the combined Tanner condition (4.1.15) is recovered and both the no-slip and Navier slip models are capable of reproducing qualitatively similar results to those presented in § 4.4, as is done by McKinley and Wilson [43]. In the cases of different slip laws the eigenvalue equation (4.1.4) is solved with an appropriate linear operator, $\mathcal{L}_2$, defined in (5.1.12).

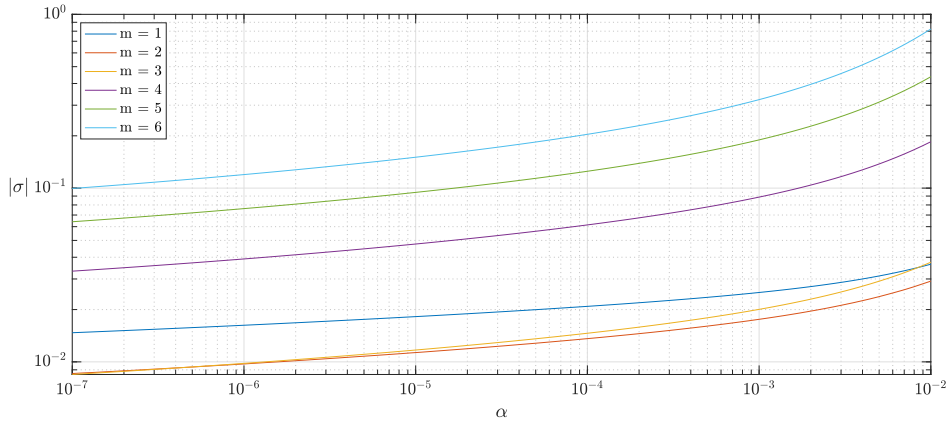


Figure 5.2: Absolute value of the eigenvalues of the model described in § 4.4 where the Tanner law is imposed when the slip length α is varied when $\phi = 2, G = 10, C = 1$ for wavenumbers $m = 1, 2, ..., 6$.

5.1.3 Varying the slip length

Next, we can consider how the nondimensional slip length, α, for the Greenspan slip law (3.2.29) (a, b) affects the eigenvalues when G and ϕ are fixed. The slip length is a numerically small number, so we consider values less than 0.01. In § 4.3 we established that varying $\alpha > 0$ cannot alter the stability of a given system, meaning the neutral stability curves shown in figure 4.3 are independent of the slip length, α. Furthermore, when α increases, the region in which the slip becomes significant also increases and therefore we expect that the absolute value of the eigenvalues increases with α. Figure 5.2 demonstrates this for a specific case when $\phi = 2$, $G = 10$ for each mode $m = 1, 2, ..., 6$, when $C = 1$. We find that this behaviour is independent of each parameter, ϕ, G and C. Furthermore, we find that the slip length, α, has a negligible effect on the dominant mode of instability over the solution spaces, consistent with the analysis of Hocking and Miksis [104] when $\alpha \ll 1$.

5.1.4 Summary

In this section, we first considered a local expansion of the eigenvalue equation (4.1.4). We showed that the Greenspan slip law regularises the eigenfunction, $h_1(r)$, whereas imposing the classical no-slip condition can lead to singular solu-

tions.

Next, we analysed the horizontal perturbation velocity, $\boldsymbol{u}_H$, under three common forms of the slip function; no-slip, Navier slip, and Greenspan slip. We showed that for the former two cases the radial velocity at the contact line is zero and therefore the perturbation to the contact line, R_1 is also zero, leading to a qualitative change in the boundary conditions and purely stable eigenvalues. Previous stability analyses of the equilbrium solutions defined in § 3.4 use a Navier slip law [42, 43] to model slip, however overlook the qualitative change caused in the boundary conditions. Therefore, we have demonstrated that the growth rates found using the Greenspan slip law, produced in chapter 4, are well founded and consistent with the derived contact line velocity.

Finally, we assessed the effect of varying the Greenspan slip coefficient, α, finding that the absolute value of eigenvalues increases as α increases, while the neutral stability curves remain unchanged when $\alpha \ll 1$.

5.2 Fixed contact angle model

Previously we used the Tanner law (3.1.10) to couple the contact angle, θ, and the equilibrium contact angle, θ_c, to the contact line speed, R_t. As discussed in § 1.2, an alternative condition to impose is that the contact angle is constant, and in our case small so that, $\theta = \theta_c \ll 1$. In this section we use the fixed contact angle condition and perform a similar linear stability analysis, comparing the results to those of the Tanner model. This model will subsequently be referred to as the 'Fixed contact angle model'.

5.2.1 Model

We are assuming that the contact angle is constant, so that the contact angle is $\theta = \theta_c$. Furthermore, we are also assuming that the contact angle is not directly related to the contact angle speed, meaning the Tanner contact line (3.2.33) is replaced with

$$\theta = 1, \tag{5.2.1}$$

after scaling the contact angle with the equilibrium contact angle, θ_c. All other boundary conditions remain unchanged. As a result of this assumption, the contact angle condition (3.2.32) (b) can immediately be simplified to

$$\frac{\partial h}{\partial r} = -1. \tag{5.2.2}$$

In § 3.2 the velocity scale is taken from the Tanner law so that $U = \kappa\theta_c^q$, but since we are no longer applying this boundary condition we must take a new velocity scale. Instead, we take the velocity scale $U = \gamma\theta_c^3/\mu$ making the capillary number, $C = 1$, and removing it from this formulation entirely. Therefore, the thin film equation analogous to (3.3.7) is

$$\frac{\partial h}{\partial t} + \nabla_H \cdot \left(\left\{ \frac{h^3}{3} + \frac{\alpha}{3} h \right\} \nabla_H \left(\nabla_H^2 h - Gh + \frac{\phi r^2}{2} \right) \right) = 0. \tag{5.2.3}$$

At leading order in ϵ, corresponding to the system in equilibrium, the thin film equation (5.2.3) and contact angle condition (5.2.2) are identical to that of the Tanner model (3.4.2,3.4.7), respectively, while all other boundary conditions remain the same. Hence, the equilibrium solutions presented in § 3.4 are identical when applying either the Tanner law (3.2.33) or the fixed contact angle condition (5.2.1).

To analyse the linear stability subject to the fixed contact angle condition (5.2.2) we again substitute the perturbed free surface (4.1.1), contact line (4.1.2) into the new contact angle condition (5.2.2), giving

$$R_1 h_0''(R_0) + h_1'(R_0) = 0. \tag{5.2.4}$$

Comparing the $\mathcal{O}(\epsilon)$ contact angle condition of the fixed contact angle model (5.2.4) to the Tanner model (4.1.11) (b) demonstrates the difference between imposing different contact angle models; because the contact angle is fixed there is no perturbation to it so that $\theta_1 = 0$ and the right hand side of (5.2.4) is zero. Subsequently, we again eliminate R_1 between the contact angle condition (5.2.4) and the contact condition (4.1.11) (a), giving the combined contact angle condition

$$h_0''(R_0) h_1(R_0) + h_1'(R_0) = 0, \tag{5.2.5}$$

again provided $R_1 \neq 0$. This is analogous to the combined Tanner condition (4.1.15), however notice that the eigenvalue, σ_m, no longer appears in the boundary condition (5.2.5). Substituting the free surface perturbation (4.1.1) into the evolution equation (5.2.3) gives another fourth order linear eigenvalue problem at $\mathcal{O}(\epsilon)$ analogous to (4.1.4),

$$\mathcal{L}_2\left[\mathcal{L}_1(h_1)\right] = \sigma_m h_1, \tag{5.2.6}$$

where the linear operators $\mathcal{L}_1$ and $\mathcal{L}_2$ are defined as before (4.1.5, 4.1.6). The eigenvalue equation (5.2.6) is subject to the combined contact angle condition (5.2.5) and one of the sets of boundary conditions (4.1.29)–(4.1.32) depending on the wavenumber, m, so that the velocity regularity (3.2.36) and differentiability (3.2.35) conditions are satisfied.

5.2.2 Neutral stability

When $\sigma_m = 0$, the eigenvalue equations (4.1.4, 5.2.6) and combined boundary conditions (4.1.15, 5.2.5) of the respective contact angle models are identical. Hence, the neutral stability curves for the fixed contact angle model are identical to those of the Tanner model. Therefore, the analysis and results of the neutral stability which is presented in § 4.3 is also valid for the fixed contact angle model.

5.2.3 Results

The generalised eigenvalue problem $Ah_1 = \sigma_m B h_1$ (5.2.6) subject to appropriate boundary conditions is solved using a method largely similar to that presented in appendix B for the Tanner model. The difference reflects the fact that the combined contact angle condition (5.2.5) differs from the combined Tanner condition (4.1.15). When $q = 1$, the difference amounts to a single entry in the matrix B, changing from -1 to zero on the row where the respective combined boundary condition is discretised.

Figures 5.3 (a)–(c) show the eigenvalues of each wavenumber $m = 0, 1, 2, ..., 6$ as the Bond number, G, is varied for increasing values of the centrifugal number, ϕ, across the figures, while figures 5.3 (d)–(f) show the eigenvalues as ϕ is varied for increasing G across figures. The results are qualitatively similar to those described

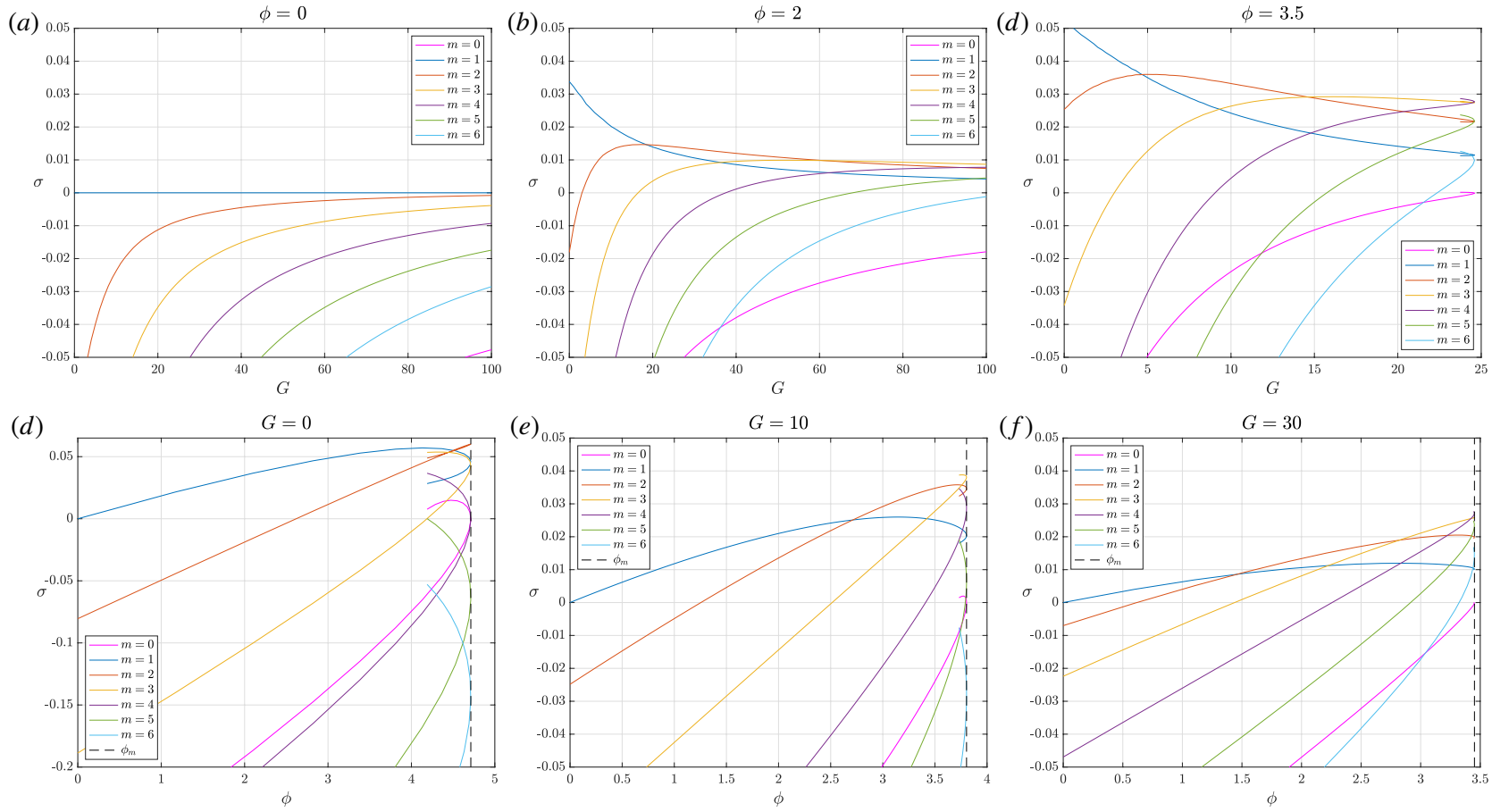


Figure 5.3: Eigenvalues of the fixed contact angle model, (a)–(c) as G is varied for $\phi = 0, 2, 3.5$ and (d)–(f) as ϕ is varied for $G = 0, 10, 30$. This figure is analogous to figure 4.5.

in § 4.4 and figures 4.5 (a)–(f). Specifically, we see that for $\phi = 2, 3.5$, shown in figures 5.3 (b, c) respectively, as G is increased that each mode $m = 2, 3, 4, ...$ is destabilized and rises to a maximum, decreasing after that point. As a result, as G is increased higher wavenumbers become dominant.

Similarly, considering figures 5.3 (d)–(f) we see a similar trend that as ϕ increases, corresponding to increased rotation, higher modes become dominant in each case. Furthermore, looking across the figures we see again that when G is large the most unstable wavenumber is greater. As mentioned in § 5.2.2 the neutral stability curves for each mode are unaffected, specifically we can still see that the axisymmetric mode, $m = 0$, is again neutrally stable at the maximum value of ϕ.

Figures 5.4 (a, b) show the regions of parameter space in which each mode is dominant, with area bounded above the labelled curves being the area in which it is the most unstable mode in (a) the $G - \phi$ (b) the $G - R_0$ parameter spaces, respectively. As stated above, we see in figure 5.4 (a) that as G increases for fixed ϕ the dominant wavenumber increases sequentially from $m = 1$, which is unconditionally unstable provided $\phi > 0$. Similarly, as ϕ increases for fixed G we see the same behaviour. Furthermore, we observe that each dominant threshold decreases as G increases meaning a lower ϕ is required to destabilise higher wavenumbers. In terms of dimensional quantities, this indicates that larger droplets require lower rotation rates for higher wavenumbers to become dominant, a feature observed in the experiments detailed in chapter 2. Figure 5.4 (b) shows that as G increases for fixed R_0 that the dominant mode decreases. Considering the contours of constant ϕ in the parameter space shown in figure 3.4 (c) this is consistent with decreasing ϕ.

5.2.4 Comparison to Tanner model

Ehrhard and Davis [32] noted that when considering a Tanner law to model the contact angle if we rescale nondimensional time so that $\tau = C^{-1}T$ the thin film equation (3.3.7) and Tanner condition (3.2.33) become

$$\frac{\partial h}{\partial t} + \nabla_H \cdot \left(\left\{ \frac{h^3}{3} + \frac{\alpha}{3} h \right\} \nabla_H \left(\nabla_H^2 h - Gh + \frac{\phi r^2}{2} \right) \right) = 0, \tag{5.2.7}$$

$$C^{-1} \frac{\partial R}{\partial t} = \theta^q - 1, \tag{5.2.8}$$

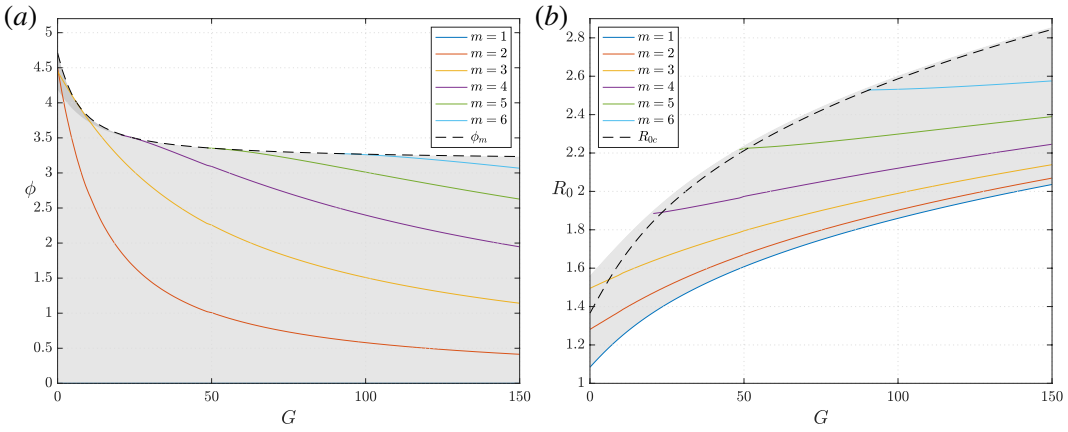


Figure 5.4: Thresholds for the most unstable modes of the fixed contact angle condition in both (a) G–ϕ and (b) G–R_0 parameter spaces for $m = 1, 2, ..., 6$.

respectively. Hence, the limiting behaviour $C \to \infty$ recovers the evolution equation (5.2.3) and the fixed contact angle condition, $\theta = 1$, from the Tanner law. Therefore, solutions with large capillary number will be comparable to those where the contact angle is assumed fixed from the start. Hence, at $\mathcal{O}(\epsilon)$ when C is sufficiently large

$$\sigma_F(\phi, G, m, \alpha) \approx C\sigma_T(\phi, G, m, \alpha, C), \tag{5.2.9}$$

where subscript F and T denote the fixed contact angle model and Tanner model, respectively.

In § 4.4 we noted that increasing C deflects eigenvalues towards $\sigma_m = 0$, meaning the absolute value of an eigenvalue decreases as C increases, for a given set of parameters. The limiting behaviour as $C \to \infty$ (5.2.9) supports this observation since rearranging gives $\sigma_T \approx \sigma_F/C$, and so increasing C decreases the absolute value of σ_T.

Figures 5.5 (a)–(f) show the comparison between the left and right hand side of (5.2.9) with C increasing across each row of figures. Eigenvalues of the Tanner model, described in § 4.4, are plotted in coloured lines for $m = 0, 1, 2, ..., 6$, whereas the fixed contact angle eigenvalues are plotted for the same wavenumbers in black dashed lines and are independent of C. Figures 5.5 (a)–(c) show the growth rates as the Bond number is varied $0 \leqslant G \leqslant 250$, when $\phi = 2$ and $C = 0.1, 1, 10$. Figures 5.5 (d)–(f) show the growth rates as the centrifugal number is varied when $G = 10$, so that $0 \leqslant \phi \leqslant \phi_m(10)$ for the same capillary numbers.

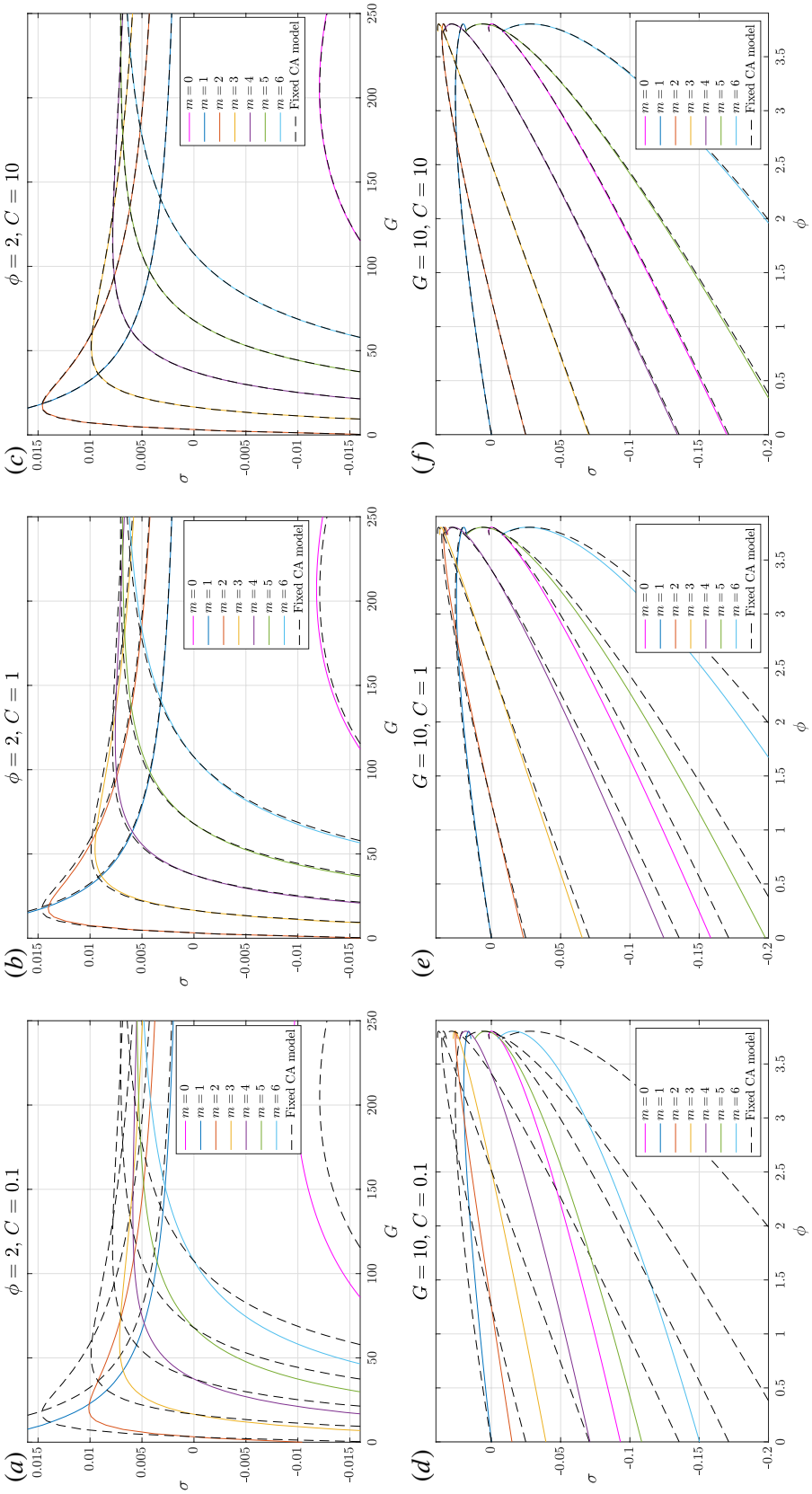


Figure 5.5: Comparison of eigenvalues between the fixed contact angle solutions, shown in black dashed lines, and Tanner model eigenvalues, shown in solid lines, for small capillary numbers and modes $0 \leqslant m \leqslant 6$.

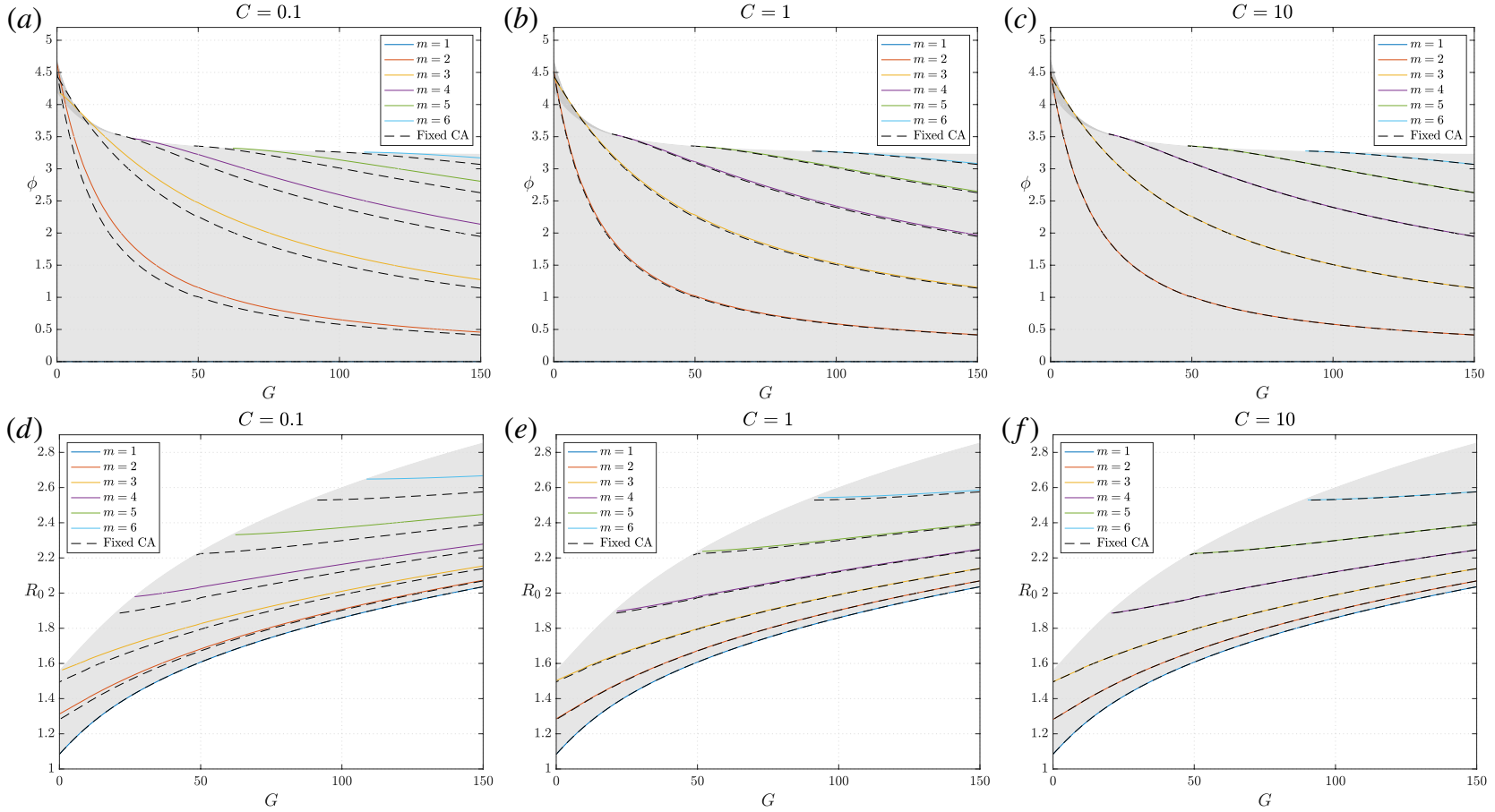


Figure 5.6: Thresholds where most unstable modes changes in the Tanner model for varying capillary number within both the (a)–(c) $G-\phi$ and (d)–(f) $G-R_0$ parameter spaces. Also shown in black dashed lines are the thresholds from figure 5.4.

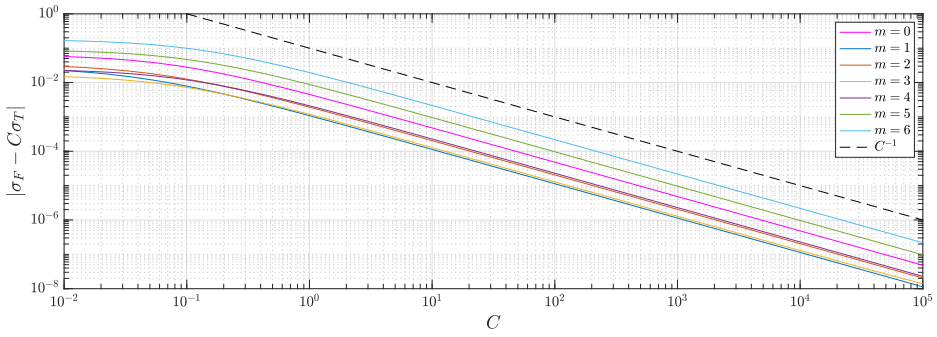


Figure 5.7: Convergence of the capillary number multiplied by the Tanner eigenvalues to fixed contact angle eigenvalues for $\phi = 2, G = 10, q = 1, \alpha = 1 \times 10^{-3}$ in the range $C \in [10^{-2}, 10^{5}]$.

In § 5.2.2 we established the neutral stability of each mode is independent of the contact angle model due to the same system of equations and boundary conditions being solved in each case. This feature is observed in each figure 5.5 (a)–(f) but is most visible in (a, c) where the coloured and dashed lines cross at $\sigma_m = 0$ for each mode, respectively. As C is increased each of the eigenvalues of the Tanner model are deflected away from $\sigma_m = 0$.

We see in each row of figures that as the capillary number, C, increases the equivalency (5.2.9) holds true; the capillary number multiplied by the Tanner eigenvalues, $C\sigma_T$, approaches the eigenvalues of the fixed contact angle model, σ_F, as C increases. At relatively low capillary number $C = 1$, shown in figures 5.5 (b, d), the agreement is good both quantitatively and qualitatively. Furthermore, when $C = 10$ in figures 5.5 (c, f) the agreement is improved.

Figures 5.6 (a)–(f) show the most unstable wavenumber within both the $G - \phi$ and $G - R_0$ parameter spaces in (a)–(c) and (d)–(f). In each figure both the Tanner model as C varies, shown in coloured lines, and the fixed contact angle model, shown in dashed lines are plotted. Similarly to figure 4.6, the area of parameter space bounded above each line is the region where that mode is the most unstable, respectively. Again, the equivalency (5.2.9) holds true since as C increases across each row of figures the dominant mode thresholds for each model lie on top of one another. Note that, at relatively low capillary numbers, $C \geqslant \mathcal{O}(1)$, the dominant mode thresholds of the Tanner model agree well with those of the fixed contact angle model.

Figure 5.7 shows the convergence of the Tanner model eigenvalues towards the eigenvalues of the fixed contact angle model as C increases for a specific set of parameters. We see that for each wavenumber the convergence looks like C^{-1} when $C \geqslant \mathcal{O}(1)$ for the parameters shown. This is the case generally for any set of parameters within the space for which equilibrium solutions satisfying the contact angle condition (3.4.7) exist.

5.2.5 Summary

In this section we modelled the contact angle by assuming that it is fixed and small, replacing the Tanner law previously used (3.2.33). In the literature the Tanner law (3.2.33) is commonly used to model the contact angle in rotating thin film flow, [42, 43, 44]. The fixed contact angle condition has been used in a similar fashion to assess the spreading of non-rotating droplets [48, 49, 50], and to assess axisymmetric spreading rates of a rotating droplet [85]. However, modelling the resultant fingering instability of droplets subject to rotation using a fixed contact angle has not been previously analysed, and is therefore a novel contribution.

The equilibrium solutions are unchanged by changing the contact line law, with differences only occurring within the linear stability analysis of these solutions. We derived the combined contact angle condition (5.2.5), replacing the previously used combined Tanner condition (4.1.15), and solved the rescaled eigenvalue equation (5.2.6) numerically subject to this new boundary condition. We found that, due to the formulation of the equations and boundary conditions, that the neutral stability curves within the parameter space are unchanged from those for the Tanner model.

We determined that solutions of the fixed contact angle model agree qualitatively with the results of the Tanner model when $C > 0$, showing that the dominant mode rises sequentially as both the Bond number and centrifugal number are increased. Furthermore, we observed that larger droplets require lower rotation rates for higher wavenumbers to become dominant. Each of these qualitative features was observed in the experiments we performed, detailed in chapter 2.

Finally, we demonstrated that the equivalency between eigenvalues of the Tanner and fixed contact angle models (5.2.9) holds true when the capillary number,

C, is sufficiently large. Therefore, the fixed contact angle model is the limiting behaviour of the Tanner model as $C \to \infty$. Specifically, the dominant mode of the Tanner model for a given set of parameters is predicted accurately when the capillary number is $\mathcal{O}(1)$ and above.

5.3 Finite Ekman number

In § 3.2, when nondimensionalising the equations of motion we made the assumption that the Ekman number, Ek, is sufficiently large such that terms involving its reciprocal can be neglected in the equations of motion (3.2.19)–(3.2.21). Therefore, in the analysis presented up to this point in chapters 3 and 4 the Coriolis force has been neglected. In this section we redefine the Ekman number so it is no longer necessarily negligible and perform similar linear stability analyses to previous cases. Subsequently, we compare the results to those in the limit $\mathrm{Ek} \to \infty$, therefore assessing the validity of the assumption previously made.

5.3.1 Model

Consider the system of nondimensional equations, (3.2.19)–(3.2.21). We can redefine the Ekman number, Ek, so that terms involving Ek are no longer assumed negligible,

$$\mathrm{Ek} = \frac{\mathrm{Ek}'}{\theta_c^2} = \frac{\mu}{\rho U L \theta_c^2}, \tag{5.3.1}$$

where Ek' is defined as the Ekman number from § 3.2 and the velocity scale, U, depends on whether the Tanner or fixed contact angle boundary conditions are imposed. Hence, we have an extra term in each of the radial and azimuthal components of the Navier-Stokes equations,

$$0 = -\frac{\partial p}{\partial r} + \frac{\phi}{C} r + \frac{2}{\mathrm{Ek}} v + \frac{\partial^2 u}{\partial z^2}, \tag{5.3.2}$$

$$0 = -\frac{1}{r}\frac{\partial p}{\partial \varphi} - \frac{2}{\mathrm{Ek}} u + \frac{\partial^2 v}{\partial z^2}, \tag{5.3.3}$$

$$0 = -\frac{\partial p}{\partial z} - \frac{G}{C}, \tag{5.3.4}$$

subject to the same boundary conditions as in § 3.2. Due to the extra terms arising we can no longer derive a thin film equation as in § 3.3, from the thin film equations (5.3.2)–(5.3.4) and must instead solve these equations directly.

5.3.2 Equilibrium solutions

We find the equilibrium solutions by again looking for a hydrostatic solution such that $\boldsymbol{u}_0 = \mathbf{0}$. Substituting into (5.3.2)–(5.3.4), gives an identical leading order pressure to that in § 3.4

$$p_0(r, z) = p_{00} + \frac{\phi}{2C} r^2 - \frac{G}{C} z, \tag{5.3.5}$$

for reference pressure at the origin, p_{00}. We consider steady, axisymmetric equilibrium solutions such that the free surface shape is a function of r only, $h(r, \varphi, t) = h_0(r)$, the contact line is at a constant position, $R(\varphi, t) = R_0$, and the contact angle is constant at $\theta = \theta_0 = 1$. Notice that, the incompressibility (3.2.28), slip and no-penetration (3.2.29), radial and azimuthal stress conditions (3.2.30) (a, b), free surface kinematic condition (3.2.31), velocity regularity condition (3.2.36), and contact line kinematic condition (3.2.34) are all satisfied automatically. To find the free surface shape, we must solve the axial stress condition (3.2.30) (c), which simplifies to

$$C(p_{00} - p_g) + h_0'' + \frac{h_0'}{r} - G h_0 + \frac{\phi}{2} r^2 = 0, \tag{5.3.6}$$

subject to the contact (3.2.32) (a), contact angle (3.2.32) (b), differentiability (3.2.35) and volume (3.2.37) conditions. The equation for the free surface (5.3.6) and boundary conditions are identical to those previously derived in § 5.1.2, which is as expected since the additional terms here do not have an effect when the velocity is zero and consistent with previous analysis by Myers *et al.* [77, 78]. Hence, the above stress condition (5.3.6) has solution identical to that in § 3.4, and all the analysis is equally valid when Coriolis forces are included.

5.3.3 Linear stability

In § 3.3 we derived a thin film equation (3.3.7) in terms of a single quantity, h, which we perturbed along with the contact line position, R, and contact angle, θ. In this analysis we also perturb each of the variables involved in the equations and boundary conditions since a thin film equation is not derived in this case. Hence, consider a small perturbation to the background initial condition of the form $\boldsymbol{u} = \epsilon \boldsymbol{u}_1(\boldsymbol{x}, t) + \mathcal{O}(\epsilon^2)$ for the velocity and $p = p_0(r, z) + \epsilon p_1(\boldsymbol{x}, t) + \mathcal{O}(\epsilon^2)$ for the pressure. The free surface deforms as before, $h = h_0(r) + \epsilon h_1(r, \varphi, t) + \mathcal{O}(\epsilon^2)$, while the contact line and contact angle again deform as $R = R_0 + \epsilon R_1(r, \varphi, t) + \mathcal{O}(\epsilon^2)$, and $\theta = \theta_0 + \epsilon\theta_1(\varphi, t) + \mathcal{O}(\epsilon^2)$, respectively. During this analysis all perturbation quantities have the subscript 1. We take normal modes

$$\boldsymbol{u}_1 = \hat{\boldsymbol{u}}_{\mathbf{1}}(r, z)e^{\mathrm{i}m\varphi+\sigma_m t}, \quad p_1 = \hat{p}_1(r, z)e^{\mathrm{i}m\varphi+\sigma_m t}, \tag{5.3.7}$$

$$h_1 = \hat{h}_1(r)e^{\mathrm{i}m\varphi+\sigma_m t}, \quad R_1 = \hat{R}_1 e^{\mathrm{i}m\varphi+\sigma_m t}, \quad \theta_1 = \hat{\theta}_1 e^{\mathrm{i}m\varphi+\sigma_m t} \tag{5.3.8}$$

for wavenumber, $m \in \mathbb{N}$, and frequency, $\sigma_m \in \mathbb{C}$. Due to the inclusion of the Coriolis force term in the governing equations, we expect that the growth rate, σ_m, will be complex and precession of modes within the rotating frame of reference will occur. At $\mathcal{O}(\epsilon)$ we have the following linear system, written component-wise and dropping the hats

$$0 = -\frac{\partial p_1}{\partial r} + \frac{2}{\mathrm{Ek}}v_1 + \frac{\partial^2 u_1}{\partial z^2}, \tag{5.3.9}$$

$$0 = -\frac{\mathrm{i}mp_1}{r} - \frac{2}{\mathrm{Ek}}u_1 + \frac{\partial^2 v_1}{\partial z^2}, \tag{5.3.10}$$

$$0 = -\frac{\partial p_1}{\partial z}, \tag{5.3.11}$$

$$0 = \frac{1}{r}\frac{\partial}{\partial r}(ru_1) + \frac{\mathrm{i}mv_1}{r} + \frac{\partial w_1}{\partial z}. \tag{5.3.12}$$

The centrifugal and gravitational forces are conservative hence appear in the hydrostatic pressure (5.3.5), rather than appearing in the above perturbation equations. Immediately we can solve the axial component (5.3.11) so that the pressure perturbation quantity is a function of the radial distance from the origin only, $p_1 = p_1(r)$. Applying the axial stress condition (3.2.30) (c) defines the $\mathcal{O}(\epsilon)$ pressure

$$p_1 = -h_1'' - \frac{1}{r}h_1' + \left(G + \frac{m^2}{r^2}\right)h_1 = -\mathcal{L}_1(h_1), \tag{5.3.13}$$

using the definition of $\mathcal{L}_1$ (4.1.5). To find the radial and azimuthal velocities, u_1 and v_1 we solve the coupled linear partial differential equations (5.3.9, 5.3.10), subject to slip conditions (3.2.29) (a, b), and stress conditions (3.2.30) (a, b). Subsequently, to find the vertical velocity, w_1, we solve the incompressibility condition (5.3.12) subject to the no-penetration condition (3.2.29) (c). The solutions for u_1, v_1 and w_1, multiplied by the capillary number, C, are

$$Cu_1(r,z) = -\frac{\mathrm{Ek}}{2}\frac{\mathrm{i}mp_1}{r} + f_1(r)\cos\lambda_1 z + f_2(r)\sin\lambda_1 z + f_3(r)\cos\lambda_2 z + f_4(r)\sin\lambda_2 z, \tag{5.3.14}$$

$$Cv_1(r,z) = \frac{\mathrm{Ek}}{2}p_1' + \mathrm{i}[f_1(r)\cos\lambda_1 z + f_2(r)\sin\lambda_1 z - f_3(r)\cos\lambda_2 z - f_4(r)\sin\lambda_2 z], \tag{5.3.15}$$

$$\begin{aligned} Cw_1(r,z) = {} & \frac{(m-1)f_1(r) - rf_1'(r)}{\lambda_1 r}\sin\lambda_1 z - \frac{(m-1)f_2(r) - rf_2'(r)}{\lambda_1 r}[\cos\lambda_1 z - 1] \\ & - \frac{(m+1)f_3(r) - rf_3'(r)}{\lambda_2 r}\sin\lambda_2 z + \frac{(m+1)f_4(r) - rf_4'(r)}{\lambda_2 r}[\cos\lambda_2 z - 1], \end{aligned} \tag{5.3.16}$$

where

$$f_1(r) = \frac{\mathrm{iEk}}{4}\left(\frac{mp_1}{r} + p_1'\right)\left[1 - \frac{\alpha\lambda_1}{3h_0}\tan\lambda_1 h_0\right]^{-1}, \quad f_2(r) = f_1(r)\tan\lambda_1 h_0, \tag{5.3.17}$$

$$f_3(r) = \frac{\mathrm{iEk}}{4}\left(\frac{mp_1}{r} - p_1'\right)\left[1 - \frac{\alpha\lambda_2}{3h_0}\tan\lambda_2 h_0\right]^{-1}, \quad f_4(r) = f_3(r)\tan\lambda_2 h_0, \tag{5.3.18}$$

and

$$\lambda_1 = \sqrt{\frac{2}{\mathrm{Ek}}}e^{\frac{\mathrm{i}\pi}{4}}, \quad \lambda_2 = \sqrt{\frac{2}{\mathrm{Ek}}}e^{-\frac{\mathrm{i}\pi}{4}}. \tag{5.3.19}$$

The free surface kinematic condition (3.2.31) at $\mathcal{O}(\epsilon)$ is

$$w_1(r, h_0(r)) = \sigma_m h_1 + h_0'(r)u_1(r, h_0(r)). \tag{5.3.20}$$

Therefore, if we substitute the expressions for u_1 and w_1 (5.3.14, 5.3.16) into the kinematic condition (5.3.20) and subsequently substitute for the $\mathcal{O}(\epsilon)$ pressure (5.3.13), the resulting equation is a linear eigenvalue equation for the growth rate, σ_m, and eigenfunction, $h_1(r)$. The form of this eigenvalue equation depends on which contact angle model is used, and, as argued in § 5.2 results in whether the

capillary number appears, so that

$$\mathcal{L}_3\left[\mathcal{L}_1(h_1)\right] = C\sigma_m h_1, \quad \text{(Tanner)}, \tag{5.3.21}$$

$$\mathcal{L}_3\left[\mathcal{L}_1(h_1)\right] = \sigma_m h_1, \quad \text{(Fixed)}, \tag{5.3.22}$$

where the linear operator, $\mathcal{L}_3$, is the same in each eigenvalue equation. The leading order asymptotic expansion in the Ekman number returns the previous eigenvalue equation (4.1.4). The eigenvalue equations (5.3.21, 5.3.22) are each subject to the same wavenumber dependent regularity and symmetry boundary conditions at the origin (4.1.29)–(4.1.32), enforcing that $h_1 \sim r^m$ near $r = 0$. Finally, we impose either the combined Tanner condition (4.1.15) or the combined contact angle condition (5.2.5) at the contact line, depending on which contact angle model is used. Therefore, inclusion of the Coriolis force doesn't affect stability of a prescribed mode.

5.3.3.1 Neutral stability

The neutral stability curves, when $\sigma_m = 0$, are solutions of

$$\mathcal{L}_3\left[\mathcal{L}_1(h_1)\right] = 0, \tag{5.3.23}$$

subject to

$$h_0''(R_0)h_1(R_0) + h_1'(R_0) = 0, \tag{5.3.24}$$

and are independent of which contact angle model is used. Nontrivial solutions of (5.3.23) are independent of the linear operator $\mathcal{L}_3$, and are solutions of $\mathcal{L}_1(h_1) = 0$. This is also the case in § 4.3, and therefore the neutral stability curves within the parameter space are also independent of the inclusion of Coriolis effects. Hence, the analysis performed in § 4.3 is equally valid here since an identical set of equations and boundary conditions are being analysed in each case, depending on whether G is zero.

5.3.3.2 Tanner law

We find that, as expected, introducing the Ekman terms to the system allows for precession of modes within the rotating frame of reference through the imaginary

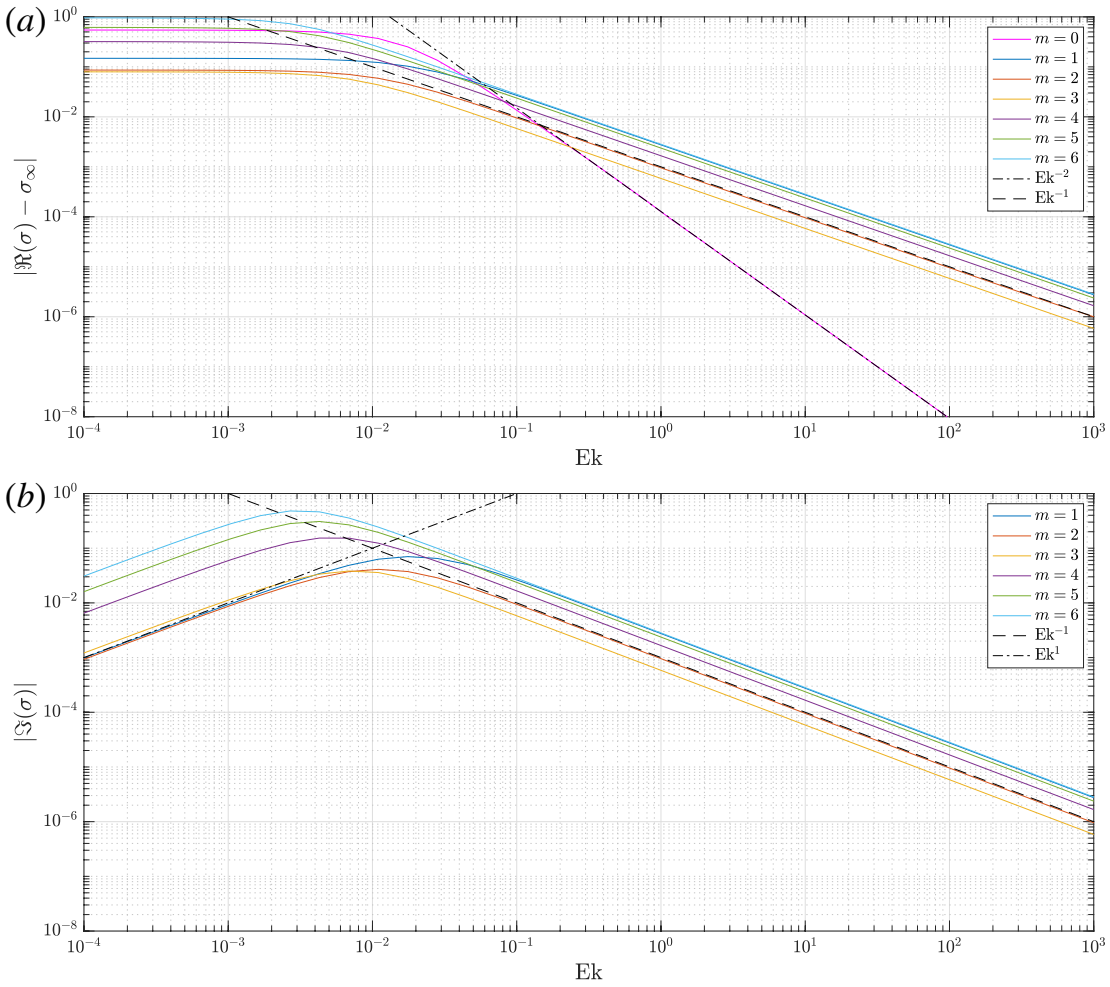


Figure 5.8: Convergence of finite Ekman to infinite Ekman eigenvalues in the range $\mathrm{Ek} \in [10^{-2}, 10^{3}]$ for both the (a) real and (b) imaginary parts. Here $\phi = 2$, $C = 0.1$, $G = 10$, $\alpha = 10^{-6}$ and $m = 0, 1, 2, ..., 6$ in (a) and $m = 1, 2, ..., 6$ in (b).

part of the growth rate, $\Im(\sigma_m)$.

When the capillary number, C, is zero, the analysis including Coriolis effects is identical to the that within the quasi-steady limit in the absence of Coriolis forces, presented in § 4.2. This is due to identical equations and boundary conditions are being solved when looking for nontrivial solutions. Hence, the analysis within this limit, presented in § 4.2 is equally valid for the current model. We can also solve the case where $C = 0$ numerically using the finite difference scheme described in appendix B but for one of the eigenvalue equations (5.3.21). Numerically we find that the real part of the numerical eigenvalues and eigenvectors are equal to the analytical solutions from § 4.2, while the imaginary part of the eigenvalues are zero, for any ϕ, G combination, as is the case in § 4.4.

When $C > 0$ we solve the eigenvalue equation (5.3.21) numerically using the finite difference scheme detailed in appendix B. We find that the analysis and results for positive wavenumber, $m = 1, 2, 3, ...$, are qualitatively similar to those in the infinite Ekman limit, presented in § 4.4. As $C \to 0$ the real part of the growth rate, σ_m, tends to the analytical solutions from § 4.2, while the imaginary part of the growth rate, σ_m, tends to zero. For the axisymmetric case, where $m = 0$, we find that for any combination of parameters the solutions are real, specifically, $\Im(\sigma_m) = 0$, meaning no precession of modes in the rotating frame. Therefore, the inclusion of Coriolis forces has no effect on axisymmetric solutions, consistent with the results of Myers and Charpin [77].

Figure 5.8 (a) demonstrates the convergence with the Ekman number of the absolute value of the difference between the real part of the finite Ekman eigenvalue and the infinite Ekman eigenvalue considered in § 4.4 and denoted σ_∞. In the range $\mathrm{Ek} \in [10^{-2}, 10^3]$ there is a linear relationship when plotted with logarithmic axes with slope of -1 for $m = 1, 2, ..., 6$ and -2 for $m = 0$, indicated with dashed lines. The slope, indicating rate of convergence with Ek, is independent of the choice of C, ϕ, G and α. Figure 5.8 (b) shows the corresponding convergence of the absolute value the imaginary part of the growth rates vary with Ekman number. The axisymmetric mode has no imaginary part and therefore does not appear on this figure. We observe that the imaginary part of the each eigenvalue converges to zero like Ek^{-1}, in the range $[10^{-2}, 10^3]$, the same rate observed for the real part. The convergence rate of imaginary parts of σ_m is also independent of the parameters chosen. The convergence to zero is expected since increasing the Ekman number decreases the effect of the Coriolis force, meaning that within the rotating frame there is less precession of modes, and hence a smaller imaginary part of the eigenvalue. Notice that, for small Ekman number, the imaginary part of the growth rates converge to zero like Ek^1. The case where $\mathrm{Ek} \ll 1$ is an inertial limit and is therefore unrealistic due too our modelling assumption that the Reynolds number is small. Therefore, although this case can be solved numerically and is shown as part of figure 5.8 (a, b) it is unfounded in reality. The dominant mode of instability for a given set of parameters is found to be unaffected by the inclusion of Ekman terms of $\mathcal{O}(1)$ and above. When $\mathrm{Ek} \ll 1$ solutions the Reynolds number will be large, violating the Stokes flow approximation, therefore this limit is unfounded and we discount these cases.

Overall, we see that the Tanner model, in which we assumed that $\mathrm{Ek}' \gg 1$, performs well for small values of the Ekman number. Therefore, taking the limit $\mathrm{Ek}' \to \infty$, as done in § 3.2, is well founded and the real part of solutions agree well provided that $\mathrm{Ek}' = \mathrm{Ek}/\theta_c^2 > 0.1$.

5.3.3.3 Fixed contact angle

Similarly to the analysis of the fixed contact angle model in the limit where $\mathrm{Ek} \to \infty$, presented in § 5.2.4, we find that the fixed contact angle exhibits the limiting behaviour of the Tanner model as $C \to \infty$ through the equivalency (5.2.9). Specifically, we again find that that eigenvalues of the Tanner model converge to eigenvalues of the fixed contact angle model like C^{-1} for each combination of ϕ, G, α, m and Ek.

The convergence of eigenvalues of the present model, for finite Ek towards the fixed contact angle model in the infinite Ekman limit, presented in § 5.2 are similar in nature to that of the Tanner model. Specifically, the rate of convergence of the real and imaginary parts of each mode $m = 1, 2, 3, ...$ is negative one, and negative two for $m = 0$. Each convergence rate is again independent of other parameters. Hence, the convergence plots are very similar to figure 5.8 and therefore are not presented.

5.3.4 Summary

In this section we presented novel solutions of the governing equations of motion including Coriolis force terms at $O(\epsilon)$, while demonstrating that in equilibrium, the solutions are unchanged from those found by McKinley *et al.* [42, 43], presented in § 3.4. Previous analysis in the literature [19, 90] neglected Coriolis force terms by reasoning that this force is negligible in comparison to the centrifugal force within a viscous regime. We have shown that taking the limit $\mathrm{Ek}' \to \infty$ in § 3.2 is a reasonable approximation to make, by directly comparing the solutions with and without inclusion of the Coriolis terms. Specifically, we found that even for relatively small Ekman numbers the differences between the presented model and the infinite Ekman models discussed in chapter 4, are negligible. Furthermore, we have shown that the Coriolis force has no effect on equilibrium solutions and

growth rates within the quasi-steady limit in agreement with Myers and Charpin [77] and Myers and Lombe [78].

5.4 Quasi-steady, axisymmetric spreading

In this section we consider axisymmetric solutions of the evolution equation (3.3.7), within the quasi-steady limit, $C = 0$, using the Tanner law to model the contact angle. We derive an ordinary differential equation (ODE) for the contact line position, and subsequently analyse the linear stability, relating back to the analysis performed in § 4.2 by comparing numerical solutions of the derived ODE to the results of the linear stability analysis.

5.4.1 Model

Consider the thin film equation (3.3.7) in the quasi-steady limit, $C = 0$, where axisymmetry is imposed so that the free surface is defined as $z = h(r, t)$,

$$\frac{1}{r}\frac{\partial}{\partial r}\left[r\left\{\frac{h^3}{3}+\frac{\alpha}{3}h\right\}\frac{\partial}{\partial r}\left(\frac{1}{r}\frac{\partial}{\partial r}\left(r\frac{\partial h}{\partial r}\right)-Gh+\frac{\phi r^2}{2}\right)\right]=0. \tag{5.4.1}$$

Nontrivial solutions of this equation satisfy the third order partial differential equation

$$0 = h_{rrr} + \frac{h_{rr}}{r} - \frac{h_r}{r^2} - Gh_r + \frac{\phi}{2}r^2, \tag{5.4.2}$$

where subscript r denoted partial differentiation with respect to the radial coordinate. The PDE (5.4.2) is solved, similarly to § 3.4, subject to the contact (3.2.32) (a), differentiability (3.2.35) and volume conservation (3.2.37). Note that, the PDE (5.4.2) is independent of the slip model used. The solution depends on whether G is non-zero, and the solutions are

$$h(r,t) = \begin{cases} \dfrac{R^4\phi\pi + 4V_f G}{4\pi R\sqrt{G}}\dfrac{\mathcal{I}_0(\sqrt{G}r) - \mathcal{I}_0(\sqrt{G}R)}{2\mathcal{I}_1(\sqrt{G}R) - R\sqrt{G}\mathcal{I}_0(\sqrt{G}R)} + \dfrac{\phi}{2G}(r^2 - R^2), & \text{(5.4.3a)} \\ -\dfrac{\phi}{32}(r^4 - R^4) + \dfrac{1}{24\pi R^4}(\pi\phi R^6 - 48V_f)(r^2 - R^2), & \text{(5.4.3b)} \end{cases}$$

respectively. The solutions (5.4.3a, 5.4.3b) have same form as the equilibrium solutions in § 3.4 but with the important difference that the free surface is a func-

tion of time through the contact line position, $R = R(t)$. Boettcher and Ehrhard [44] derived (5.4.3a) as the base state for their stability analysis within the quasi-steady limit, $C = 0$. McKinley and Wilson [42] derive an equivalent expression to (5.4.3b) under a different nondimensionalisation.

The contact angle condition (3.2.32) (b) defines the contact angle so that

$$\theta(t) = \begin{cases} -\dfrac{R^4\phi\pi + 4V_f G}{4\pi R}\dfrac{\mathcal{I}_1(\sqrt{G}R)}{2\mathcal{I}_1(\sqrt{G}R) - R\sqrt{G}\mathcal{I}_0(\sqrt{G}R)} - \dfrac{\phi}{G}R, & G > 0 \qquad (5.4.4a) \\ -\dfrac{\pi\phi R_0^6 + 96V_f}{24\pi R_0^3}, & G = 0, \qquad (5.4.4b) \end{cases}$$

where $G > 0$ and $G = 0$, respectively. The final boundary condition is the Tanner law, where we again make the simplification that there is no contact angle hysteresis so that

$$\frac{\mathrm{d}R}{\mathrm{d}t} = \theta(t)^q - 1, \qquad (5.4.5)$$

for all contact angles. Substitution of the contact angles (5.4.4a, 5.4.4b) into the Tanner law (5.4.5) results in two ODEs for $R(t)$, depending on whether G is zero,

$$\frac{\mathrm{d}R}{\mathrm{d}t} = \begin{cases} \left[-\dfrac{R^4\phi\pi + 4V_f G}{4\pi R}\dfrac{\mathcal{I}_1(\sqrt{G}R)}{2\mathcal{I}_1(\sqrt{G}R) - R\sqrt{G}\mathcal{I}_0(\sqrt{G}R)} - \dfrac{\phi}{G}R\right]^q - 1, & (5.4.6a) \\ \left[-\dfrac{\pi\phi R_0^6 + 96V_f}{24\pi R_0^3}\right]^q - 1, & (5.4.6b) \end{cases}$$

to be solved subject to an appropriate initial condition. Since the fixed contact angle condition does not relate the contact line position to the contact angle and contains no time derivative, similar analysis cannot be carried out in that case. McKinley and Wilson [42] derived and solved a similar expression for general Tanner laws, nondimensionalising the problem in an alternative way.

5.4.2 Equilibrium solutions

The system is at equilibrium and steady when $\theta = 1$, and the Tanner law (5.4.5) is solved to give $R(t) = R_0$. This means the position of the contact line position is constant at $r = R_0$, and is found by solving the contact angle condition (3.2.32) (b), for R_0 which becomes

$$\left.\frac{\mathrm{d}h}{\mathrm{d}r}\right|_{r=R_0} = -1. \qquad (5.4.7)$$

Therefore, the previous discussion of equilibrium solutions, performed in § 3.4, is valid in this case and the equilibrium contact line position can be determined given a centrifugal number, ϕ, and a Bond number, G.

5.4.3 Linear stability

The method of performing the linear stability analysis differs from the method presented in chapter 4. In this case, instead of assuming the form of the perturbation to the free surface as done in chapter 3, we have solved the evolution equation (5.4.1) directly and therefore know the height of the free surface as a function of the unknown contact line position, $R(t)$ (5.4.3a, 5.4.3b). The position of the contact line is subsequently found by solving (5.4.6a, 5.4.6b).

We perturb the contact line and contact angle in an axisymmetric fashion from the equilibrium contact line position R_0 according to

$$R(t) = R_0 + \epsilon R_1(t), \quad \theta(t) = \theta_0 + \epsilon\theta_1(t), \tag{5.4.8}$$

where $\epsilon \ll 1$. The contact angle condition (3.2.32) (b) at $\mathcal{O}(\epsilon)$ determines the perturbed contact angle

$$\theta_1 = -R_1(t)\,\frac{\partial}{\partial R}\left(\left.\frac{\partial h}{\partial r}\right|_{r=R(t)}\right)\Bigg|_{R(t)=R_0} = -\lambda R_1(t). \tag{5.4.9}$$

The Tanner law (5.4.5) at $\mathcal{O}(\epsilon)$ is

$$\frac{\mathrm{d}R_1}{\mathrm{d}t} = q\theta_1 = -q\lambda R_1, \tag{5.4.10}$$

after substituting the $\mathcal{O}(\epsilon)$ contact angle (5.4.9). Hence, the solution of the ODE (5.4.10) subject to initial condition that $R_1(0) = \bar{R}_1$, is

$$R_1(t) = \bar{R}_1 e^{-q\lambda t}, \tag{5.4.11}$$

showing that, as assumed in § 4.1, the perturbation to the contact line grows or

decays exponentially in time. In the notation of chapter 4 the growth rate σ_0 is

$$\sigma_0 = -q \frac{\partial}{\partial R} \left(\left. \frac{\partial h}{\partial r} \right|_{r=R(t)} \right) \Bigg|_{R(t)=R_0}, \tag{5.4.12}$$

which is a more general expression for the eigenvalues calculated in § 4.2, both when $G > 0$ (4.2.5a) and when $G = 0$ (4.2.5b). In § 4.3 we established that the point in the parameter space where the centrifugal number is maximum, (ϕ_m, R_{0c}), is a saddle node bifurcation point for fixed Bond number. Similarly if ϕ is large enough the maximum value of G, at the point (G_m, R_{0c}) is also a saddle-node bifurcation point for fixed ϕ, demonstrated by the neutral stability curve of $m = 0$ in figure 4.3. The form of the growth rate (5.4.12) gives interpretation to this feature, since we see that $\sigma_m = 0$ corresponds where a turning point of $h_r(R(t), t)$ occurs in R_0 within the parameter space, which is exactly the definition of the point (ϕ_m, R_{0c}) or (G_m, R_{0c}).

5.4.4 Comparison with numerical solution

The linear stability analysis assumes a small, axisymmetric perturbation from the equilibrium contact line position, R_0. We compare the growth rates, σ_m, from the linear stability problem (5.4.12) to the numerical solutions of (5.4.5) for sufficiently small perturbations. Recall that (5.4.12) is a more general expression for the explicitly defined growth rates (4.2.5a, 4.2.5b), derived in § 4.2. The linear, axisymmetric perturbation grows in time from the equilibrium solutions like

$$R(t) - R[0] = \epsilon \bar{R}_1 \exp \sigma_0 t, \tag{5.4.13}$$

demonstrated by the solution (5.4.11).

The derived ordinary differential equation depends on whether G is positive or zero, and is given by (5.4.6a, 5.4.6b), respectively. The appropriate initial condition to compare with the linear stability analysis is the perturbed equilibrium contact line position at $t = 0$, $R(0) = R_0 + \epsilon \bar{R}_1$ where $\epsilon \ll 1$. If the system is not perturbed from the equilibrium contact line position, then it will remain in equilibrium for all time. Without loss of generality we can take $\bar{R}_1 = 1$, so that ϵ defines the size of the perturbation to the contact line, rather than being a

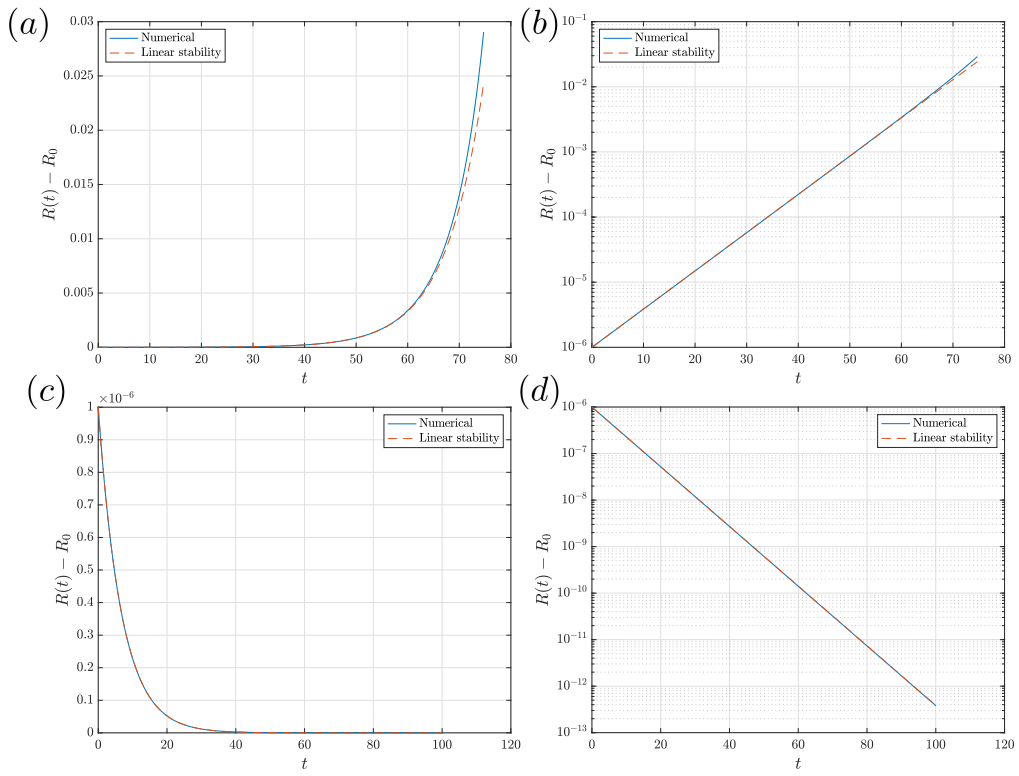


Figure 5.9: Comparison between the exponential growth with rate given by (5.4.12) and the numerical solution of (5.4.6a) with initial condition $R(0) = R_0 + \epsilon$ where $\epsilon = 1 \times 10^{-6}$. The cases where $\phi = 3.77$, $G = 10$ are presented, (a, b) show the unstable upper branch of solutions on normal and semi-logarithmic axis, whereas (c, d) show the stable lower branch of solutions.

small arbitrary constant. The ODE (5.4.6a, 5.4.6b) is solved numerically using a forward Euler scheme with a small timestep, δt,

$$R(t_0 = 0) = R_0 + \epsilon, \tag{5.4.14}$$

$$R(t_{n+1}) = R(t_n) + \delta t \left[\theta(t_n)^q - 1\right], \quad n \geqslant 0. \tag{5.4.15}$$

For brevity the numerical scheme is formulated from the more general ODE (5.4.5), where the contact angle, θ, at timestep t_n is given by (5.4.4a, 5.4.4b), depending on where G is non-zero. Furthermore, for solutions to be physical we require that the height of the free surface is everywhere positive at each point timestep. The first point on the free surface to reach $z = 0$ will be at $r = 0$, therefore we require $h(0, t_n) > 0$.

Figures 5.9 (a)–(d) show the comparison between numerical solutions of (5.4.4a)

and the exponential growth of the contact line position (5.4.13), for two cases. The specific cases presented are for $G = 10$, $\epsilon = 10^{-6}$ and $\phi = (\phi_m(G) + \phi_c(G))/2 = 3.77$. The value of ϕ is chosen to ensure two physical solutions for the contact line position exist, one on either side of the saddle node bifurcation point, (ϕ_m, R_{0c}). Figures 5.9 (a, b) show the unstable case where $R_0 = 1.71$ on both regular and semi-logarithmic axes, whereas figures 5.9 (c, d) show the stable case where $R_0 = 1.58$ on equivalent axes. We see that in each case the agreement between solutions is good. This is the case generally provided $\epsilon \leqslant \mathcal{O}(10^{-2})$.

5.4.5 Summary

To summarise, in the quasi-steady limit, $C = 0$, where axisymmetry is imposed, we solved the evolution equation (3.3.7) directly and subsequently derived an ODE for the position of the contact line as a function of time from the Tanner law (3.1.10). We derived an alternative, more general, form of the growth rate, σ_m, than in § 4.2, the form of which gives interpretation to the results that the point (ϕ_m, R_{0c}) is a saddle-node bifurcation point. Finally, we compared numerical solutions of the derived ODE to the solutions of the linear stability problem, showing good agreement when the size of the contact line perturbation, ϵ, is sufficiently small.

Chapter 6

O(1) Contact angle model; formulation and equilibrium solutions

In this chapter we formulate a model no longer making the assumption that the static contact angle, θ_c, is small, in contrast to the previous modelling in chapters 3, 4 and 5. Therefore, we present an alternative nondimensionalisation for the system of equations and boundary conditions including terms previously neglected when making the lubrication approximation in § 3.2.

Similarly to § 3.4, we discuss the hydrostatic, equilibrium case where the velocity is zero within the rotating frame, and solve the resulting equations numerically, determining the free surface shape and contact line position as before. Subsequently, in the small contact angle limit solutions are compared to those found in § 3.4. Due to limitations in the numerical method the contact angle is limited to $0 < \theta_c < \pi/2$.

Finally, we develop a finite element method to solve a set of Stokes equations on a domain defined by the previously determined numerical solutions for the free surface shape when the contact angle is not small. We validate the method by recovering the the equilibrium pressure, p_0 and velocity, $\boldsymbol{u}_0$, given a set of predetermined boundary conditions.

6.1 Model

We consider the same system described in chapter 3, modelling the experiments of chapter 2; a fixed mass of fluid, on a flat plate, at constant temperature, in solid body rotation about the vertical axis with a free surface. A schematic diagram is shown in figure 3.1. The dimensional Navier–Stokes equations within a rotating frame of reference (3.1.1) and incompressibility condition (3.1.2) still apply. The derivation of the equations of motion within the rotating frame is shown in appendix A.

The dimensional boundary conditions at the free surface

$$\mathscr{S} := z - h(r, \varphi, t) = 0, \tag{6.1.1}$$

are the kinematic condition (3.1.4) and three continuity of stress conditions (3.1.5), one in each direction. At the solid plate, $z = 0$, we again impose slip conditions in the horizontal directions, instead of the classical no-slip conditions. We leave the slip law general

$$u = s(h)\frac{\partial u}{\partial z}, \quad v = s(h)\frac{\partial v}{\partial z}, \tag{6.1.2}$$

so that the Navier, Greenspan or another slip model can be discussed depending on $s(h)$. It is useful to write (6.1.2) in terms of a metric tensor and hence in a single equation

$$\boldsymbol{u}^T \cdot (\underline{\underline{I}} - \hat{\boldsymbol{n}}\hat{\boldsymbol{n}}^T) + s(h)\hat{\boldsymbol{n}}^T \cdot \underline{\underline{\sigma}} \cdot (\underline{\underline{I}} - \hat{\boldsymbol{n}}\hat{\boldsymbol{n}}^T) = 0, \tag{6.1.3}$$

where the radial and azimuthal components of this equation recover each of the conditions (6.1.2) when $\hat{\boldsymbol{n}} = -\hat{\boldsymbol{z}}$, respectively. At $z = 0$ we again apply the no-penetration condition (3.1.6), which can be written more generally as

$$\boldsymbol{u} \cdot \hat{\boldsymbol{n}} = 0. \tag{6.1.4}$$

At the contact line, $r = R(\varphi, t)$, there are three physical conditions; the contact condition (3.1.8), the contact angle condition (3.1.9), and the contact line kinematic condition (3.1.11). As discussed in § 3.1, the contact angle condition (3.1.9) must be coupled with a modelling assumption the contact angle itself. For this

model we choose the fixed contact angle condition, investigated in § 5.2 for small contact angles, so that the contact angle condition (3.1.9) immediately becomes

$$\left.\frac{\partial h}{\partial r}\right|_{r=R(\varphi,t)} = -\tan\theta_c \tag{6.1.5}$$

for fixed contact angle, θ_c. On the axis $r = 0$ we impose the velocity regularity (3.1.12), and differentiability (3.1.13) conditions. Finally, since the mass of fluid placed on the plate is fixed we again impose the volume conservation condition (3.1.14).

6.2 Nondimensionalisation

In contrast to the nondimensionalisation performed in § 3.2, here we nondimensionalise the system of equations making no assumption about the comparative size of the radial and axial length scales. Hence, we introduce the following scales

$$\boldsymbol{x} = L\boldsymbol{x}', \quad u = Uu', \quad v = Vv', \quad w = Ww', \quad t = Tt', \quad p = Pp', \tag{6.2.1}$$

where $\boldsymbol{x} = r\hat{\boldsymbol{r}} + z\hat{\boldsymbol{z}}$ is a position vector. We take the velocity scales to be equal, $U = V = W$, so that the each term in the incompressibility condition (3.1.2) balances

$$\nabla' \cdot \boldsymbol{u}' = 0. \tag{6.2.2}$$

We again take the lengthscale, L, to be determined by the volume conservation condition (3.1.14) so that $L = V_f^{1/3}$, leaving

$$1 = \int_0^{2\pi} \int_0^{R'(\varphi,t')} r'h'(r', \varphi, t')\, \mathrm{d}r'\mathrm{d}\varphi. \tag{6.2.3}$$

The free surface kinematic condition (3.1.4) determines the timescale $T = L/U$ and simplifies to

$$w' = \frac{\partial h'}{\partial t'} + u'\frac{\partial h'}{\partial r'} + \frac{v'}{r'}\frac{\partial h'}{\partial \varphi} \tag{6.2.4}$$

on $\mathscr{S}$. Whereas, the contact line kinematic condition (3.1.11) simplifies to

$$u' = \frac{\partial R'}{\partial t'} + \frac{v'}{r'}\frac{\partial R'}{\partial \varphi} \tag{6.2.5}$$

at the contact line, $z' = 0, r' = R'(\varphi, t')$.

$$-[P]p'\hat{\boldsymbol{n}} + 2\left[\frac{\mu U}{L}\right]\underline{\underline{e}}' \cdot \hat{\boldsymbol{n}} = -[P]\left(p'_g + \left[\frac{\gamma}{PL}\right](\nabla' \cdot \hat{\boldsymbol{n}})\right). \tag{6.2.6}$$

Since the experiment described in chapter 2 is characterised by smooth, laminar flow we take a viscous pressure scale so that $P = \mu U/L$, hence

$$-p'\hat{\boldsymbol{n}} + 2\underline{\underline{e}}' \cdot \hat{\boldsymbol{n}} = -\left(p'_g + \frac{1}{C}(\nabla' \cdot \hat{\boldsymbol{n}})\right)\hat{\boldsymbol{n}}. \tag{6.2.7}$$

Here we define the capillary number $C = \mu U/\gamma$ as the ratio between viscous and surface tension effects, as done previously for the fixed contact angle condition discussed in § 5.2. Next, we consider the equations of motion (3.1.1), keeping a general velocity scale, U. Since our length scales for each direction are identical we can consider the equations in vector form so that

$$\left[\frac{\rho U^2}{L}\right]\frac{\mathrm{D}\boldsymbol{u}'}{\mathrm{D}t'} = -\left[\frac{P}{L}\right]\nabla' p' + [\rho\Omega^2 L]r'\hat{\boldsymbol{r}} - 2[\rho\Omega U]\hat{\boldsymbol{z}} \times \boldsymbol{u} - [\rho g]\hat{\boldsymbol{z}} + \left[\frac{\mu U}{L^2}\right]\nabla'^2\boldsymbol{u}'. \tag{6.2.8}$$

Substituting the viscous pressure scale $P = \mu U/L$, gives the nondimensional equations of motion,

$$\mathrm{Re}\frac{\mathrm{D}\boldsymbol{u}'}{\mathrm{D}t'} = -\nabla' p' + \frac{\phi}{C}r'\hat{\boldsymbol{r}} - \frac{2}{\mathrm{Ek}}\hat{\boldsymbol{z}} \times \boldsymbol{u} - \frac{G}{C}\hat{\boldsymbol{z}} + \nabla'^2\boldsymbol{u}', \tag{6.2.9}$$

with Reynolds, Ekman, centrifugal, Bond and capillary numbers defined as

$$\mathrm{Re} = \frac{\rho U L}{\mu}, \quad \mathrm{Ek} = \frac{\mu}{\rho\Omega L^2}, \quad \phi = \frac{\rho\Omega^2 L^3}{\gamma}, \quad G = \frac{\rho g L^2}{\gamma}, \quad C = \frac{\mu U}{\gamma}, \tag{6.2.10}$$

respectively. We again take the velocity scale as $U = \gamma/\mu$, as in § 5.2.2, so that each term in the stress condition matches, coresponding to taking $C = 1$. For clarity we will include C in all of our analytical calculations but set $C = 1$ in all numerical calculations.

The nondimensional equations of motion are therefore identical to those in the previous thin film model prior to taking the limit $\theta_c \to 0$, but with the aspect ratio $\theta_c = 1$ so that the vertical and horizontal lengths are scaled in the same way. Hence, in the equations of motion we cannot discard terms arising from the Laplacian operator previously deemed to be negligible in the thin film model. We

make a Stokes flow approximation by taking the limits

$$\mathrm{Re} \to 0, \quad \mathrm{Ek} \to \infty. \tag{6.2.11}$$

Dropping the dash notation leaves a set of Stokes flow equations which include centrifugal and gravitational forces,

$$\mathbf{0} = -\nabla p + \frac{\phi}{C} r\hat{\boldsymbol{r}} - \frac{G}{C}\hat{\boldsymbol{z}} + \nabla^2 \boldsymbol{u}, \quad \nabla \cdot \boldsymbol{u} = 0. \tag{6.2.12}$$

At the solid plate $z = 0$ the equations of motion (6.2.12) are subject to the slip (6.1.3) and no-penetration (6.1.4) conditions,

$$\boldsymbol{u}^T \cdot (\underline{\underline{I}} - \hat{\boldsymbol{n}}\hat{\boldsymbol{n}}^T) + s(h)\hat{\boldsymbol{n}}^T \cdot \underline{\underline{\sigma}} \cdot (\underline{\underline{I}} - \hat{\boldsymbol{n}}\hat{\boldsymbol{n}}^T) = 0, \quad \boldsymbol{u} \cdot \hat{\boldsymbol{n}} = 0, \tag{6.2.13}$$

where the slip functions have been nondimensionalised appropriately. At the free surface $z = h$ the continuity of stress conditions (6.2.7) and kinematic condition (6.2.4) apply

$$-p\hat{\boldsymbol{n}} + 2\underline{\underline{e}} \cdot \hat{\boldsymbol{n}} = -\left(p_g + \frac{\kappa}{C}\right)\hat{\boldsymbol{n}}, \quad \frac{\partial h}{\partial t} = w - u\frac{\partial h}{\partial r} - \frac{v}{r}\frac{\partial h}{\partial \varphi}, \tag{6.2.14}$$

where $\hat{\boldsymbol{n}}$ is the unit outward pointing normal from the fluid into atmospheric gas, $\kappa = \nabla \cdot \hat{\boldsymbol{n}}$ is the curvature of the free surface and p_g is the atmospheric pressure. At the contact line $r = R(\varphi, t)$ we impose the contact (3.1.8), contact angle (3.1.9) and the contact line kinematic conditions (6.2.5)

$$h(r, \varphi, t) = 0, \quad \frac{\partial h}{\partial r} = -\tan(\theta_c), \tag{6.2.15}$$

$$\frac{\partial R}{\partial t} = u - \frac{v}{r}\frac{\partial R}{\partial \varphi}, \tag{6.2.16}$$

respectively. At $r = 0$ the free surface must have zero gradient so that

$$\frac{\partial h}{\partial r} = 0, \tag{6.2.17}$$

and the velocity must be regular along the axis,

$$|\boldsymbol{u}(0, \varphi, z, t)| < \infty. \tag{6.2.18}$$

Finally, we impose the volume conservation condition

$$1 = \int_0^{2\pi} \int_0^{R(\varphi,t)} rh(r,\varphi,t)\,\mathrm{d}r\mathrm{d}\varphi. \tag{6.2.19}$$

6.3 Equilibrium solutions

Similarly to the analysis performed in § 3.4, we look for a steady, axisymmetric solution in a hydrostatic regime, so that $h = h_0(r)$, and $\boldsymbol{u}_0 = \mathbf{0}$. Solving the Stokes equations (6.2.12) under these conditions determines the equilibrium pressure. In comparison to the thin film formulation, all additional terms in this model are dependent on the velocity, which is zero. Therefore, the equilibrium pressure is identical to that in the thin film model (3.4.1),

$$p_0(r,z) = p_{00} + \frac{\phi}{2C}r^2 - \frac{G}{C}z, \tag{6.3.1}$$

where p_{00} is the constant pressure at the origin. Note that both the free surface kinematic (6.2.14) (b) and contact line kinematic condition (6.2.16) are satisfied automatically due to $\boldsymbol{u}_0 = \mathbf{0}$ and the equilibrium solutions being independent of time. To find the equilibrium free surface shape, $h_0(r)$, we use the continuity of stress condition (6.2.14) (a), where the unit normal to the free surface (6.1.1) is defined as

$$\hat{\boldsymbol{n}} = \frac{\nabla\mathscr{S}}{|\nabla\mathscr{S}|} = \frac{-h_0'\,\hat{\boldsymbol{r}} + \hat{\boldsymbol{z}}}{(1+h_0'^2)^{1/2}}, \tag{6.3.2}$$

where prime notation denotes differentiation with respect to the radial coordinate, r. The stress condition (6.2.14) simplifies to

$$C(p_0 - p_g) = \nabla\cdot\hat{\boldsymbol{n}} \tag{6.3.3}$$

in both the radial and axial directions. Substituting the equilibrium pressure (6.3.1) and the expressions for the normal and unit normal (6.3.2) into the stress condition (6.2.7) results in,

$$C(p_{00} - p_g) + \frac{\phi}{2}r^2 - Gh_0 = -\frac{h_0'^3 + rh_0'' + h_0'}{r(1+h_0'^2)^{3/2}}, \tag{6.3.4}$$

a nonlinear, second order, ordinary differential equation (ODE) for the equilibrium shape, $h_0(r)$. The ODE (6.3.4) is subject to four boundary conditions; the volume condition (6.2.19),

$$1 = 2\pi \int_0^{R_0} r h_0(r)\, \mathrm{d}r, \tag{6.3.5}$$

the contact condition (6.2.15) (a),

$$h_0(R_0) = 0, \tag{6.3.6}$$

the contact angle condition (6.2.15) (b),

$$h_0'(R_0) = -\tan\theta_c, \tag{6.3.7}$$

and finally the differentiability condition (6.2.17),

$$h_0'(0) = 0. \tag{6.3.8}$$

Note that the volume, contact and differentiability conditions are identical to those used in the thin film model, whereas the contact angle condition (6.3.7) cannot be simplified as in § 3.4, since the contact angle is no longer necessarily small. The four boundary conditions determine the four unknowns in the problem; two constants of integration from (6.3.4), the constant pressure difference $p_{00} - p_g$, and the position of the contact line, R_0. Furthermore, we require that solutions are physical, that is, the height of the free surface is everywhere non-negative. We solve the system (6.3.4)–(6.3.8) numerically using the Chebfun package [105], giving the solution $h_0(r)$ and the contact line position, R_0. Our numerical method assumes that the solution, $h_0(r)$, is not multivalued, restricting the analysis of the contact angle to $0 < \theta_c < \pi/2$. At $\theta_c = \pi/2$ the contact angle condition (6.3.7) is singular and so cannot be included. Figure 6.1 shows three examples of the equilibrium solution, $z = h_0(r)$, for different values of the Bond number G, when the contact angle, $\theta_c = \pi/3$, for which we see that the contact line position, R_0, increases with G.

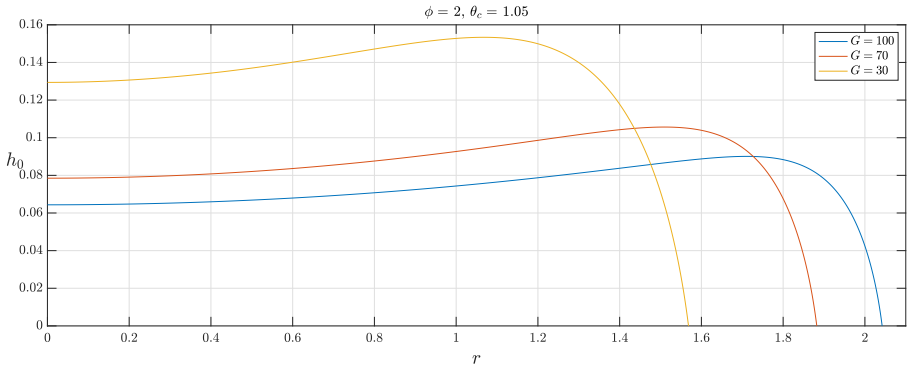


Figure 6.1: Equilibrium free surface shape $h_0(r)$ in the region $0 \leqslant r \leqslant R_0$, which are solutions of (6.3.4)–(6.3.8), when $G = 0, 30, 70, 100$ for $\phi = 2$ and $\theta_c = \pi/3$.

6.3.1 Results

Similarly to the thin film solutions in § 3.4, we identify two important points in the parameter space; the maximum value the centrifugal number, ϕ, can take and the maximum value the contact line position, R_0, can take. Recall that the former is denoted (ϕ_m, R_{0c}), where R_{0c} is the corresponding value of R_0, while the latter is denoted (ϕ_c, R_{0m}). The same notation was used in § 3.4.

Above the maximum contact line position, R_{0m}, solutions are unphysical, such that the height at the origin is negative. Therefore, given the contact angle, θ_c, and the Bond number, G, we impose the extra boundary condition $h_0(0) = 0$ and can determine an extra unknown. Specifically, the extra unknown is the critical centrifugal number, ϕ_c, at which the free surface touches down at the origin, determining the point (ϕ_c, R_{0m}). The minimum value of R_0 always corresponds to where no rotation occurs so that, $\phi = 0$. Physically, this could be anticipated since the centrifugal force is directed radially outwards from the centre of rotation and moves the contact line in this direction as ϕ increases. Therefore, given a Bond number, $G \geqslant 0$, and a contact angle, $0 < \theta_c < \pi/2$, we can determine the maximum and minimum values of R_0, and subsequently construct the parameter space within which equilibrium solutions exist.

Figures 6.2 (a)–(d) show how the contact line position varies with centrifugal number for increasing values of the contact angle, θ_c, across each figure. In each figure solutions are shown for $G = 0, 10, 30$ in different colours. The point (ϕ_c, R_{0m}) is shown with a black cross, below which solutions are physical and shown in solid

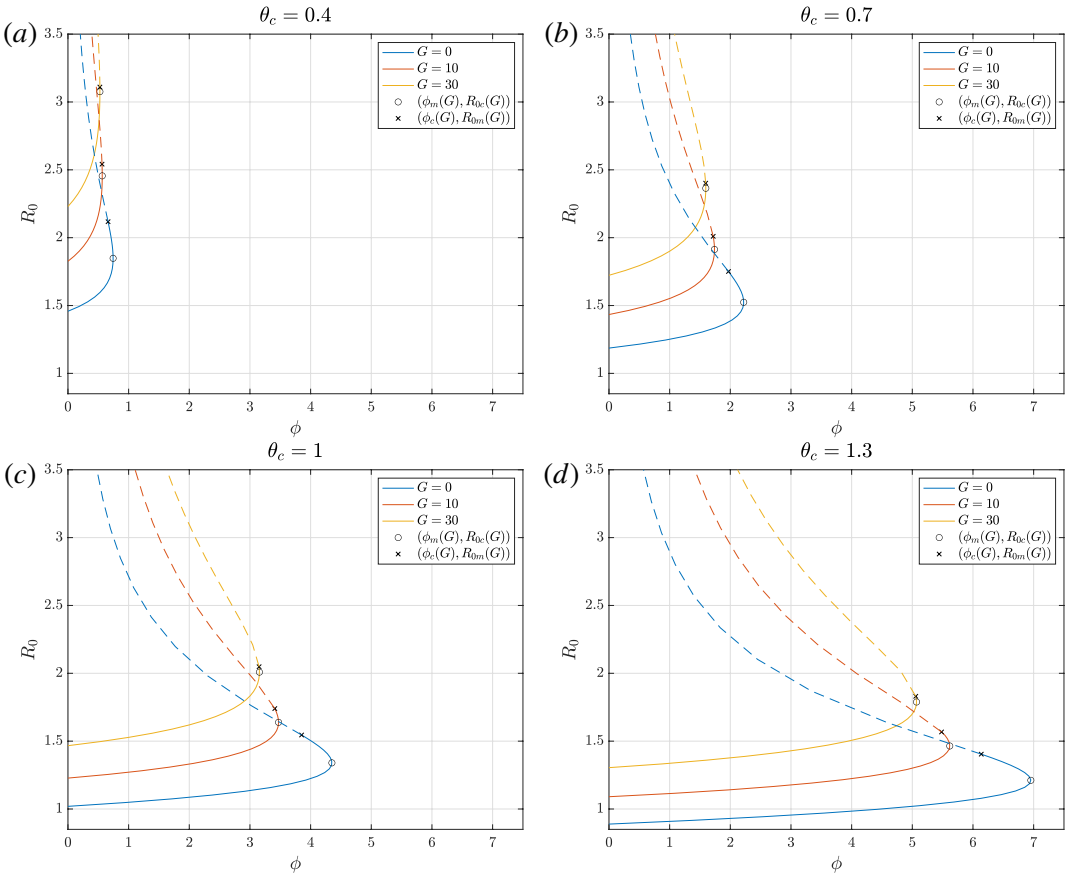


Figure 6.2: Plots showing the contact line position as a function of centrifugal number, ϕ, for various contact angles. On each sub-figure solutions for $G = 0, 10, 30$ are shown, where a solid line indicates a physical solution, and dashed line unphysical solutions. The bifurcation points (ϕ_m, R_{0c}) and (ϕ_c, R_{0m}) are indicated with a black circle or cross, respectively.

coloured lines and above which solutions are unphysical indicated with dashed lines. Similarly to the results in the thin film limit, for each Bond number, G, and contact angle, θ_c, increasing the centrifugal number increases R_0, which is consistent with the physical interpretation given in § 3.4. But, beyond the critical value, ϕ_c we find for a given set of parameters the solution is multivalued as the centrifugal number is varied. Specifically, when $\phi_c \leqslant \phi < \phi_m$ a single value of ϕ gives two solutions which are physical. Conversely, the centrifugal number, ϕ, as a function of the contact line position, R_0, is one-to-one. Hence, to ensure all solutions are found, it is instructive to calculate the maximum and minimum values of R_0 as described above, and subsequently edit the numerical scheme to solve for ϕ, given R_0 which lies in this range.

In the thin film limit previously considered, the free surface shape, $h_0(r)$, was known analytically and subsequently the point at which ϕ is maximum (ϕ_m, R_{0c}) was calculated by numerically solving two coupled transcendental equations. The solutions to the full equilibrium problem including previously neglected terms described here is purely numerically, and so the maximum is found using a golden-section search [106]. This algorithm finds any extremum within a prescribed interval, successively narrowing the range in which the extremum lies using the golden ratio, giving the algorithm its name. The initial interval in R_0 is taken as the two solutions when $\phi = \phi_c$, since the maximum value of ϕ always lies in this range. On each of the sub-figures in figure 6.2 the point (ϕ_m, R_{0c}) is shown with a black circle.

In each figure 6.2 (a)–(d) we observe that as the Bond number, G, increases for fixed centrifugal number and contact angle that the equilibrium contact line position, R_0, increases. This feature is consistent with the findings within the thin film limit, discussed in § 3.4 where a physical interpretation was provided. Furthermore, as G is increased the maximum centrifugal number at which equilibrium solutions exist, ϕ_m, decreases. Overall, the contour plots shown in figure 6.2 are qualitatively comparable to those previously discussed within the thin film limit in figure (3.3), in terms of the trends of varying both the centrifugal and Bond numbers.

The two points of interest, along with the minimum value of R_0 bound the space in which solutions exist for a fixed contact angle as G is varied. Figures 6.3 (a)–(c) show the region where solutions exist in the $G - \phi$ space, while figures 6.3 (d)–(f) show the $G - R_0$ space, for increasing contact angle across the row. These sets of figures are analogous to figures 3.4 (a, c), respectively and show the two points of interest as G is varied in each figure. The point (ϕ_m, R_{0c}) is traced with a black line while the point (ϕ_c, R_{0m}) is traced with a red line. We see that there is no qualitative difference in the parameter space when the contact angle is taken to be $\mathcal{O}(1)$ and when it is small in § 3.4. Therefore, the analysis and interpretation of varying both the centrifugal and Bond numbers for a fixed contact angle is as stated in § 3.4 for the thin film solutions. However, increasing the contact angle does change the numerical parameter ranges in which equilibrium solutions exists.

Figures 6.2 (a)–(d) show that increasing the contact angle increases the maximum

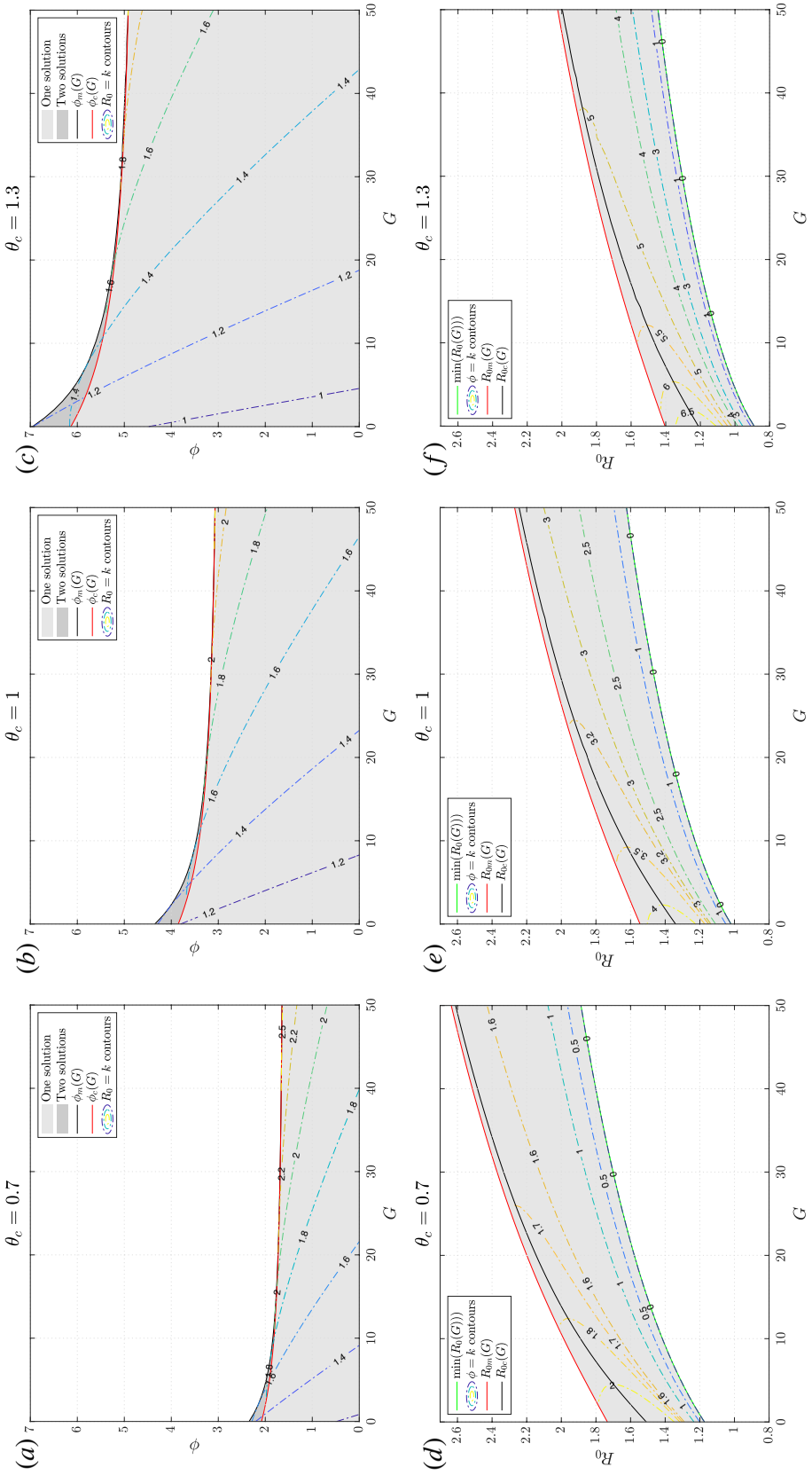


Figure 6.3: Solution spaces for three $theta_c = 0.7, 1, 1.3$, shown in the $G - \phi$, space in (a)–(c), and the $G - R_0$ space in (d)–(f). The figures are analogous to figure 3.4.

value of the centrifugal number, ϕ_m, while decreasing the corresponding value of R_{0c}. Physically, this means that systems with larger contact angles can sit at equilibrium with zero velocity at greater rotation rates than those with lower contact angles. This is visualised in the solution spaces in figures 6.3 (a)–(c) where as the contact angle increases across the row the parameter space encapsulates greater values of ϕ. Moreover, for any point where G and R_0 are fixed increasing the contact angle results in a greater value of ϕ at which the solution is in equilibrium. Furthermore, we see in figures 6.2 (a)–(d) that increasing the contact angle decreases R_0 for the same combination of ϕ and G. This is more clearly visualised across figures 6.3 (d)–(f) where the shaded region within which solutions exist moves down as the contact angle is increased. This is demonstrated by the $\phi = 1$ contour which moves down for each value of G shown. The position of the contact line decreasing as the contact angle is increased is consistent with volume being conserved.

Note that, the model for the contact angle presented within this chapter is the fixed contact angle model, introduced in § 5.2. When analysing equilibrium solutions for the fixed contact angle condition in § 5.2 we established that equilibrium solutions are identical to those when the Tanner law is used, under a thin film approximation. Recall that the Tanner law is

$$\frac{\partial R}{\partial t} = \kappa \left(\theta^q - \theta_c^q\right), \tag{6.3.9}$$

which is coupled with contact angle condition (3.1.9), repeated as

$$\left.\frac{\partial h}{\partial r}\right|_{r=R(\varphi,t)} = -\tan\theta. \tag{6.3.10}$$

Therefore, when in equilibrium, $\theta = \theta_c$, so that equilibrium solutions when the Tanner law is imposed also satisfy the contact angle condition (6.3.7). Hence, a model subject to the Tanner law and one subject to the fixed contact angle condition (5.2.1) give identical equilibrium solutions, as is the case for the thin film models discussed in chapters 3, 4 and 5.

6.3.2 Comparison to thin film solutions

In our derivation of the thin film equation (3.3.7) in § 3.2–3.3, we neglected terms of $\mathcal{O}(\theta_c^2)$. The nondimensionalisation of the $\mathcal{O}(1)$ contact angle model described in § 6.2 differs from the one performed for the thin film model in § 3.2, since each nondimensional quantity does not involve the contact angle. Instead, the contact angle appears only in the contact angle boundary condition (6.3.7). Therefore, there exists a transformation between the two models involving the contact angle, where each nondimensional variable and number will be transformed so that the models will be comparable. These transformations are derived in appendix C. Subsequently, we can assess the quality of the previously made assumption that the contact angle is small, and the equilibrium solutions between models. In § 5.2.2 we stated that the equilibrium solutions are independent of whether the Tanner law or fixed contact angle is imposed. Hence, although we are only considering the fixed contact angle model in the current regime, solutions will also be comparable to the equilibrium solutions when the Tanner law (3.1.10) is imposed instead.

The most important transformations derived in appendix C are that on the nondimensional centrifugal number, ϕ, the Bond number, G, the free surface, h_0, and the contact line position, R_0, which are

$$\phi_{\mathrm{II}} = \theta_c^2 \phi_{\mathrm{I}}, \quad G_{\mathrm{II}} = \theta_c^{2/3} G_{\mathrm{I}}, \tag{6.3.11}$$

$$h_{0\mathrm{II}}(r_{\mathrm{II}}) = \theta_c^{2/3} h_{0\mathrm{I}}(\theta_c^{-1/3} r_{\mathrm{I}}), \quad R_{0\mathrm{II}} = \theta_c^{-1/3} R_{0\mathrm{I}}, \tag{6.3.12}$$

respectively. The subscript notation is consistent with that in appendix C and denotes (I) the thin film model and (II) the $\mathcal{O}(1)$ contact angle model.

Figures 6.4 (a)–(d) show the equilibrium solutions shape for both the $\mathcal{O}(1)$ model and the thin film model for different contact angles. In each figure the thin film solution when $\phi_{\mathrm{I}} = 2$, $G_{\mathrm{I}} = 10$ is shown with red dashed lines whereas the transformed $\mathcal{O}(1)$ contact angle solutions are shown with a solid blue line. Each function is plotted in the thin film regime, so that the thin film solution is invariant between figures. Immediately we observe that when the contact angle is small in figure 6.4 (a), the comparison between solutions is good, in both the free surface, h_0, and the position of the contact angle, R_0. The contact angle is increased over figures 6.4 (a)–(d) and as the contact angle gets larger the error between the

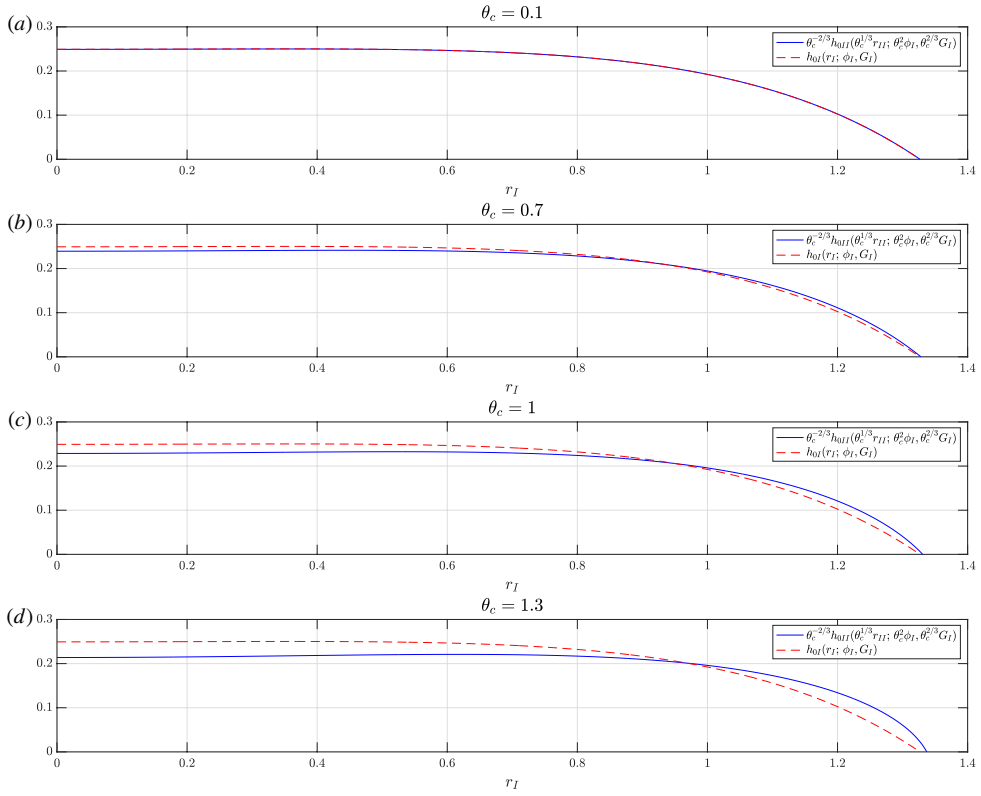


Figure 6.4: Solutions of (6.3.4) when $\phi_{\mathrm{I}} = 2$ and $G_{\mathrm{I}} = 10$ for $\theta_c = 0.1, 0.7, 1, 1.3$, shown in blue. Also shown with the red dashed lines is the thin film solution obtained in § 3.4.

free surface solutions becomes apparent. The discrepancy in the apparent contact angle increases across figures 6.4 (a)–(d) and is representative of the small angle approximation, $\tan(\theta_c) \approx \theta_c$, breaking down for large contact angles. Although the contact angle is large, the thin film solution performs well in calculating the contact line position, R_0.

Figures 6.5 (a)–(d) show how the contact line, R_0, varies with ϕ for different contact angles for the two models. Similarly to figure 6.4, the $\mathcal{O}(1)$ contact angle model solutions are shown with a solid blue line, whereas the thin film solutions are shown with a red dashed line. The solutions for R_0 are plotted in the parameter space of the thin film model when $G_{\mathrm{I}} = 5$, so that these solutions are invariant as the contact angle is increased across sub-figures. The points of interest are also plotted for each solution in their respective colours, whereas in figure 6.2 (ϕ_m, R_{0c}) is plotted with a circle while (ϕ_c, R_{0m}) is plotted with a cross. The non-physical solutions previously shown in figure 6.2 are not included in this figure.

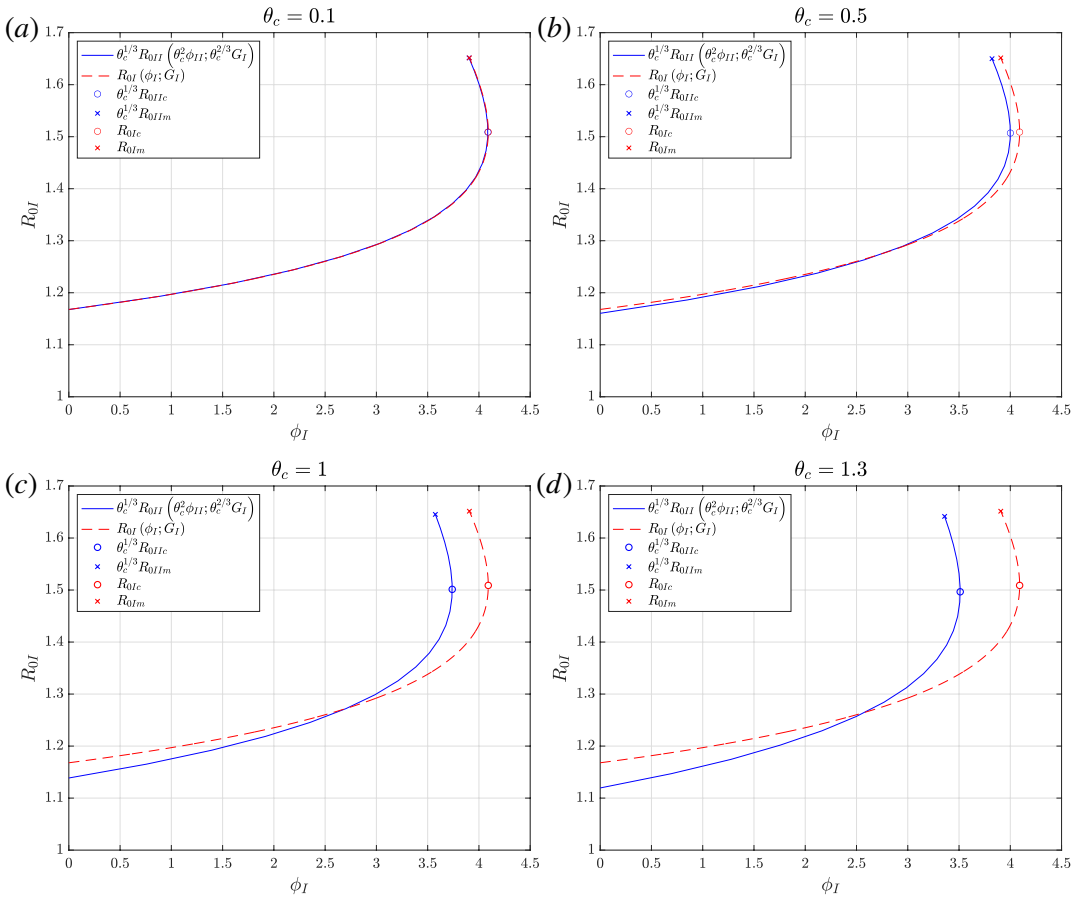


Figure 6.5: Contact line position, R_0, as a function of ϕ for various contact angles, for both the thin film model I, and the current model II. Each plot is within the scaling for model I, showing the case where $G_\mathrm{I} = 5$, where transformed solutions of model II are shown in blue, while solutions of model I are shown in red.

In figure 6.5 (a), when the contact angle is small, we see that the agreement between solutions is good. This is expected since the previously neglected terms should have a smaller effect when included if the contact angle is small. Across figures 6.5 (a)–(d) the contact angle increases, and we observe the agreement gets worse. This feature is also anticipated since in the thin film scaling the previously neglected terms are $\mathcal{O}(\theta_c^2)$, and so the effect of including them will increase with the contact angle. Although the agreement between solutions decreases as the contact angle increases, we note that the thin film solution performs well in predicting the range of R_0 possible, even when the contact angle is not small.

In figures 6.5 (a)–(d) as the contact angle is increased it can be observed that the range in which solutions exists decreases, which at first glance is contrary to the findings above, where we stated that larger contact angles can support equilibrium

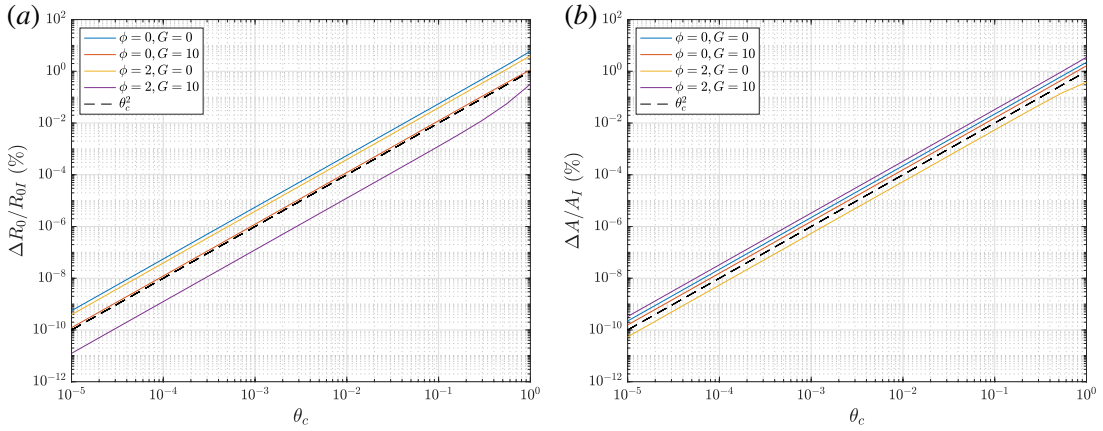


Figure 6.6: Convergence of percentage error between full model including $\mathcal{O}(\theta_c^2)$ terms and thin film model for the measures (a) ΔR_0 and (b) ΔA, defined in (6.3.13).

solutions at larger rotation rates. It is important to remember that in the thin film model, the centrifugal number, ϕ, defined in (3.2.22) contains the contact angle, so that the x-axis of each figure is scaled with the contact angle. If each figure was plotted on axes independent of the contact angle we would see that the larger contact angles support greater rotation rates as seen in figures 6.2 (a)–(d). However, we can say that for large rotation rates the thin film model always overestimates the possible range of ϕ; more specifically, $\theta_c^2\phi_{mI} > \phi_{mII}$.

To measure the error between the semi-analytical thin film solution described in § 3.4 and the full numerical solution including all terms, we consider the error in the contact line position R_0, and the area bounded between the two curves. The first of these measures how well the equivalency (6.3.12) (b) holds. Since the domain of the two solutions are different, to calculate the bounded area each solution is transformed onto a fixed domain $\tilde{r} = [0, 1]$, and the area bounded below each curve is calculated. Therefore, the two measures of the error are defined as

$$\Delta R_0 = \left|R_{0\mathrm{I}} - \theta_c^{1/3} R_{0\mathrm{II}}\right|, \quad \Delta A = |A_{\mathrm{I}} - A_{\mathrm{II}}| = \left|\int_0^1 R_{0\mathrm{I}}\tilde{h}_{0\mathrm{I}}(\tilde{r}) - \theta_c^{1/3} R_{0\mathrm{II}}\tilde{h}_{0\mathrm{II}}(\tilde{r})\mathrm{d}\tilde{r}\right|. \tag{6.3.13}$$

Figure 6.4 (a) shows the comparison between the analytical thin film solutions (3.4.9a, 3.4.9b) and the numerical solution of (6.3.4) when $\theta_c = 0.1$; the maximum contact angle for which the error in the small angle approximation $\tan\theta_c = \theta_c$ is less than 1%. We see the agreement between the analytical and numerical solutions is good, with the percentage error in ΔR_0 compared to R_{0I} being less

than 0.09%.

Figure 6.6 shows percentage error of both (a) ΔR_0 and (b) ΔA, as the contact angle is varied for various combinations of centrifugal number, ϕ, and Bond number, G. We find that each of the percentage error decreases as the contact angle decreases like θ_c^2. This could be anticipated since the terms neglected when deriving the thin film equation are $\mathcal{O}(\theta_c^2)$. When the contact angle is $\mathcal{O}(1)$ we see that the percentage error in both ΔR_0 and ΔA can be $\mathcal{O}(1)$. Hence, the lubrication approximation produces equilibrium solutions with surprisingly good agreement with the full numerical equilibrium solutions when the contact angle is sufficiently small, while if the contact angle is $\mathcal{O}(1)$ the neglected terms have a more noticeable effect on the equilibrium solutions.

6.4 Finite element verification of equilibrium solutions

In this section we develop a numerical method of solving a set of Stokes equations on a domain defined by the numerical solution for $h_0(r)$ found in § 6.3. Specifically, we use a finite element method, solving for the equilibrium pressure, p_0 and velocity, $\boldsymbol{u}_0$, given boundary conditions described in § 6.2.

6.4.1 Equations of motion

The equations of motion (6.2.12) written in component form and assuming axisymmetry to reflect axisymmetric solutions found in § 6.3, so that $p = p_0(r, z, t)$ and $\boldsymbol{u} = \boldsymbol{u}_0(r, z, t)$ are

$$0 = \frac{\partial p_0}{\partial r} + \frac{\phi}{C} r + \nabla^2 u_0 - \frac{u_0}{r^2}, \tag{6.4.1}$$

$$0 = \nabla^2 v_0 - \frac{v_0}{r^2}, \tag{6.4.2}$$

$$0 = \frac{\partial p_0}{\partial z} - \frac{G}{C} z + \nabla^2 w_0, \tag{6.4.3}$$

$$0 = \frac{1}{r}\frac{\partial}{\partial r}(r u_0) + \frac{\partial w_0}{\partial z}, \tag{6.4.4}$$

where the subscript 0 denotes equilibrium quantities. The solution we expect to recover is that found in § 6.3,

$$p_0 = p_{00} + \frac{\phi}{2C} r^2 - \frac{G}{C} z, \quad \boldsymbol{u}_0 = \boldsymbol{0}. \tag{6.4.5}$$

We begin with the equilibrium free surface shape, $h_0(r)$, and therefore the contact (6.2.15) (a), contact angle (6.2.15) (b), differentiability (6.2.17) and volume (6.2.19) conditions are automatically satisfied. The equations of motion for the leading order system (6.4.1)–(6.4.3) can be written in the form

$$\boldsymbol{0} = \nabla \cdot \underline{\underline{\sigma}}_0 + \boldsymbol{f}_0, \quad \nabla \cdot \boldsymbol{u} = 0, \tag{6.4.6}$$

where $\boldsymbol{f}_0 = (\phi r \hat{\boldsymbol{r}} - G\hat{\boldsymbol{z}})/C$, and the stress tensor is defined as

$$\underline{\underline{\sigma}}_0 = -p_0 \underline{\underline{I}} + 2\underline{\underline{e}}_0 = -p_0 \underline{\underline{I}} + \nabla \boldsymbol{u}_0 + (\nabla \boldsymbol{u}_0)^T. \tag{6.4.7}$$

6.4.2 Variational formulation

To implement the finite element method we must formulate the equations of motion (6.4.6) in weak form. To do so, we first define the inner product appropriate to the geometry,

$$(\boldsymbol{u}, \boldsymbol{v}) = \int_\Omega \boldsymbol{u} \cdot \boldsymbol{v}\, r \,\mathrm{d}r\mathrm{d}\varphi\mathrm{d}z. \tag{6.4.8}$$

The domain, Ω, is defined as the region bounded by the curves $z = 0$, $r = 0$, and $z = h_0(r)$, and is shown in figure 6.7.

The weak formulation is derived by taking the inner product (6.4.8) of a vector test function, $\boldsymbol{t}$, and the equations of motion (6.4.6) (a), giving

$$\begin{aligned}
0 &= \int_\Omega \left(\boldsymbol{\nabla} \cdot \underline{\underline{\sigma}}_0 + \boldsymbol{f}_0 \right) \cdot \boldsymbol{t} \,\mathrm{d}\boldsymbol{x} && (6.4.9)\\
&= \int_\Omega \frac{\partial}{\partial x_j} [(\sigma_0)_{ij}] t_i + (f_0)_i t_i \,\mathrm{d}\boldsymbol{x} && (6.4.10)\\
&= \int_\Omega \frac{\partial}{\partial x_j} [(\sigma_0)_{ij} t_i] - (\sigma_0)_{ij} t_{i,j} + (f_0)_i t_i \,\mathrm{d}\boldsymbol{x} && (6.4.11)\\
&= \int_{\partial\Omega} (\sigma_0)_{ij} (n_0)_j t_i \,\mathrm{d}S - \int_\Omega (-p_0 \delta_{ij} + 2(e_0)_{ij}) t_{i,j} + (f_0)_i t_i \,\mathrm{d}\boldsymbol{x} && (6.4.12)\\
&= \int_{\partial\Omega} \left(\underline{\underline{\sigma}}_0 \cdot \hat{\boldsymbol{n}}_0 \right) \cdot \boldsymbol{t} \,\mathrm{d}S - \int_\Omega \left(-p_0 \boldsymbol{\nabla} \cdot \boldsymbol{t} + 2\underline{\underline{e}}_0 : \nabla \boldsymbol{t} + \boldsymbol{f}_0 \cdot \boldsymbol{t} \right) \mathrm{d}\boldsymbol{x}, && (6.4.13)
\end{aligned}$$

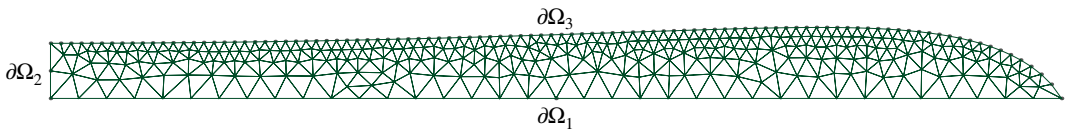


Figure 6.7: A mesh defined by the free surface $z = h_0(r)$ for $\phi = 2$, $G = 50$ and $\theta_c = \pi/3$. The mesh is more refined at the free surface so that the element size is smaller along this curve.

where $\hat{\boldsymbol{n}}_0$ is the unit normal to the surface $\partial\Omega$. We then take the inner product (6.4.8) of the incompressibility condition (6.4.6) (b) with a scalar test function, q, and sum the result with (6.4.13) leaving the general weak formulation

$$0 = \int_\Omega \left(-p_0 \boldsymbol{\nabla} \cdot \boldsymbol{t} + 2\underline{\underline{e}}_0 : \nabla \boldsymbol{t} + q \boldsymbol{\nabla} \cdot \boldsymbol{u}_0 + \boldsymbol{f}_0 \cdot \boldsymbol{t} \right) \mathrm{d}\boldsymbol{x} - \int_{\partial\Omega} \left(\underline{\underline{\sigma}}_0 \cdot \hat{\boldsymbol{n}}_0 \right) \cdot \boldsymbol{t} \, \mathrm{d}S, \tag{6.4.14}$$

which is yet to have any boundary conditions applied.

6.4.3 Boundary conditions

The equilibrium problem is axisymmetric and therefore we have three boundaries to consider, the r-axis, the z-axis and the free surface which we label

$$\partial\Omega_1 : z = 0, \quad \partial\Omega_2 : r = 0, \quad \partial\Omega_3 : z = h_0(r), \tag{6.4.15}$$

respectively, as shown in figure 6.7. Hence, the boundary term in (6.4.14) is rewritten as the sum of each individual boundary term

$$\int_{\partial\Omega} \left(\underline{\underline{\sigma}}_0 \cdot \hat{\boldsymbol{n}}_0 \right) \cdot \boldsymbol{t} \, \mathrm{d}S = \sum_{i=1}^{3} \int_{\partial\Omega_i} \left(\underline{\underline{\sigma}}_0 \cdot \hat{\boldsymbol{n}}_0 \right) \cdot \boldsymbol{t} \, \mathrm{d}S_i. \tag{6.4.16}$$

If we first consider the solid boundary $\partial\Omega_1$, we need to incorporate both the slip and no-penetration conditions (6.2.13) in our weak formulation. John [107] gives a method of implementing both the slip and no-penetration conditions weakly. First, we rewrite the test function, $\boldsymbol{t}$, in terms of its normal and tangential parts,

$$\boldsymbol{t} = (\boldsymbol{t} \cdot \hat{\boldsymbol{n}}_0)\hat{\boldsymbol{n}}_0 + (\underline{\underline{I}} - \hat{\boldsymbol{n}}_0 \hat{\boldsymbol{n}}_0^T)\boldsymbol{t}, \tag{6.4.17}$$

so that the boundary integral term on $\partial\Omega_1$ can be rewritten as

$$\int_{\partial\Omega_1} \left(\underline{\underline{\sigma}}_0 \cdot \hat{\boldsymbol{n}}_0\right) \cdot \boldsymbol{t}\, \mathrm{d}S = \int_{\partial\Omega_1} \left(\hat{\boldsymbol{n}}_0^T \cdot \underline{\underline{\sigma}}_0 \cdot \hat{\boldsymbol{n}}_0\right) \hat{\boldsymbol{n}}_0 \cdot \boldsymbol{t}\, \mathrm{d}S + \int_{\partial\Omega_1} (\hat{\boldsymbol{n}}_0^T \cdot \underline{\underline{\sigma}}_0) \cdot \left[(\underline{\underline{I}} - \hat{\boldsymbol{n}}_0\hat{\boldsymbol{n}}_0^T) \cdot \boldsymbol{t}\right] \mathrm{d}S. \tag{6.4.18}$$

The no-penetration boundary condition (6.2.13) (b) is reformulated by instead imposing the boundary condition

$$\boldsymbol{u}_0 \cdot \hat{\boldsymbol{n}}_0 + \xi \hat{\boldsymbol{n}}_0^T \cdot \underline{\underline{\sigma}}_0 \cdot \hat{\boldsymbol{n}}_0 = 0, \tag{6.4.19}$$

where the penetration parameter $\xi \ll 1$. Note that taking $\xi = 0$ recovers (6.2.13) (b) exactly, whereas choosing $\xi \to \infty$ prescribes free penetration conditions. Therefore, in our numerical scheme we choose $\xi = 10^{-12}$ to ensure the no-penetration condition is satisfied. Hence, following substitution of the slip (6.2.13) (a) and no-penetration conditions (6.4.19) the boundary integral term on $\partial\Omega_1$ becomes

$$\int_{\partial\Omega_1} \left(\underline{\underline{\sigma}}_0 \cdot \hat{\boldsymbol{n}}_0\right) \cdot \boldsymbol{t}\, \mathrm{d}S = -\int_{\partial\Omega_1} \xi^{-1} (\boldsymbol{u}_0 \cdot \hat{\boldsymbol{n}}_0)(\boldsymbol{t} \cdot \hat{\boldsymbol{n}}_0)\, \mathrm{d}S_1 - \int_{\partial\Omega_1} s(h_0)^{-1} \boldsymbol{u}_0^T \cdot (\underline{\underline{I}} - \hat{\boldsymbol{n}}_0\hat{\boldsymbol{n}}_0^T) \cdot \boldsymbol{t}\, \mathrm{d}S_1. \tag{6.4.20}$$

Next we consider the boundary $\partial\Omega_2$, the axis $r = 0$. Here we impose a stress free boundary condition so that the boundary term is

$$\int_{\partial\Omega_2} \left(\underline{\underline{\sigma}}_0 \cdot \hat{\boldsymbol{n}}_0\right) \cdot \boldsymbol{t}\, \mathrm{d}S = 0, \tag{6.4.21}$$

and the velocity regularity conditions are satisfied, since any stress singularity at $r = 0$ is avoided. Finally, on $\partial\Omega_3$ we impose the continuity of stress boundary condition (6.2.7). This boundary condition can be rewritten in terms of the stress tensor,

$$\underline{\underline{\sigma}}_0 \cdot \hat{\boldsymbol{n}}_0 = -\left(P_g + \frac{\kappa_0}{C}\right)\hat{\boldsymbol{n}}_0, \tag{6.4.22}$$

and then directly substituted into the boundary term, giving

$$\int_{\partial\Omega_3} \left(\underline{\underline{\sigma}}_0 \cdot \hat{\boldsymbol{n}}_0\right) \cdot \boldsymbol{t}\, \mathrm{d}S_3 = -\int_{\partial\Omega_3} \left(P_g + \frac{\kappa_0}{C}\right)\hat{\boldsymbol{n}}_0 \cdot \boldsymbol{t}\, \mathrm{d}S_3. \tag{6.4.23}$$

An alternative method to impose the stress condition is to use a Dirichlet boundary condition, imposing that the pressure along the free surface is exactly given by $\kappa_0 + p_g$ (6.3.3). The results of this yield smaller L^2-norms between the numerical and exact velocity and pressure solutions for the same number of elements, and hence computational cost. The problem with this method is that within (6.3.3) the assumption that $\boldsymbol{u_0} = \boldsymbol{0}$ is implicit. Therefore, it is more natural to impose the stress condition in full, with no knowledge of the velocity solution, as has been presented.

Substituting the three boundary terms (6.4.20, 6.4.21, 6.4.23) into (6.4.16) gives the boundary integral term from (6.4.14),

$$\int_{\partial\Omega} \left(\underline{\underline{\sigma}}_0 \cdot \hat{\boldsymbol{n}}_0\right) \cdot \boldsymbol{t}\,\mathrm{d}S = -\int_{\partial\Omega_1} \xi^{-1}(\boldsymbol{u}_0 \cdot \hat{\boldsymbol{n}}_0)(\boldsymbol{t} \cdot \hat{\boldsymbol{n}}_0)\,\mathrm{d}S_1 - \int_{\partial\Omega_3} \left(P_g + \frac{\kappa_0}{C}\right)\hat{\boldsymbol{n}}_0 \cdot \boldsymbol{t}\,\mathrm{d}S_3 - \int_{\partial\Omega_1} s(h_0)^{-1}\boldsymbol{u}_0^T \cdot (\underline{\underline{I}} - \hat{\boldsymbol{n}}_0\hat{\boldsymbol{n}}_0^T) \cdot \boldsymbol{t}\,\mathrm{d}S_1. \tag{6.4.24}$$

Hence, the weak formulation of the equations of motion (6.4.6), subject to the no-penetration, slip, free surface stress and regularity conditions is

$$0 = \int_\Omega \left(-p_0 \boldsymbol{\nabla}\cdot\boldsymbol{t} + 2\underline{\underline{e}}_0 : \nabla\boldsymbol{t} + q\boldsymbol{\nabla}\cdot\boldsymbol{u}_0 + \boldsymbol{f}_0 \cdot \boldsymbol{t}\right)\mathrm{d}\boldsymbol{x} + \int_{\partial\Omega_3} \left(P_g + \frac{\kappa_0}{C}\right)\hat{\boldsymbol{n}}_0 \cdot \boldsymbol{t}\,\mathrm{d}S_3 + \int_{\partial\Omega_1} \xi^{-1}(\boldsymbol{u}_0 \cdot \hat{\boldsymbol{n}}_0)(\boldsymbol{t} \cdot \hat{\boldsymbol{n}}_0)\,\mathrm{d}S_1 + \int_{\partial\Omega_1} s(h_0)^{-1}\boldsymbol{u}_0^T \cdot (\underline{\underline{I}} - \hat{\boldsymbol{n}}_0\hat{\boldsymbol{n}}_0^T) \cdot \boldsymbol{t}\,\mathrm{d}S_1. \tag{6.4.25}$$

The remaining boundary conditions are the free surface kinematic (6.2.14) (b) and contact line kinematic conditions (6.2.16), which are

$$w_0(r, h_0(r)) - u_0(r, h_0(r))h_0'(r) = 0, \quad u_0(R_0, 0) = 0, \tag{6.4.26}$$

respectively.

6.4.4 Solution method

First, we must determine the numerical solution for $h_0(r)$, using the method described in § 6.3 given each set of parameters under consideration. Following this,

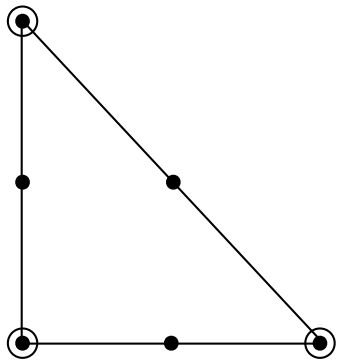


Figure 6.8: Velocity • and pressure ∘ nodes for a triangular Taylor–Hood finite element, reproduced from [109].

we use the GMSH finite element mesh generator [108] to produce a mesh defined by $h_0(r)$, to a given maximum element size, δ_+. GMSH provides the ability to refine the mesh about specified curves or points to maximise the efficiency of our code, that is, achieving a more accurate answer for the same numerical cost. If refinement is used, the minimum element size is denoted by δ_-. Since we are considering an axisymmetric problem, our mesh is two-dimensional meaning our elements are triangles; an example of a mesh for $\phi = 2, G = 50$ and $\theta_c = \pi/3$ is shown in figure 6.7, where the mesh is refined about the free surface, $\partial\Omega_3$.

In order to apply the stress conditions we require the curvature of the free surface, κ_0, which is calculated from the numerical solution for $h_0(r)$,

$$\kappa_0 = -\frac{h_0'^3 + r h_0'' + h_0'}{r(1 + h_0'^2)^{3/2}}. \tag{6.4.27}$$

As described in § 6.3, we use the Chebfun numerical computing package to obtain the function $h_0(r)$. Using the package we can accurately compute the numerical derivatives required to calculate the curvature, including at the endpoints of the domain. The curvature is calculated on a finer grid than the minimum element size, δ_-, and then interpolated at the free surface nodes produced from the mesh. An alternative method of calculating the curvature is for each point to fit a circle through itself and a point either side, and adding the inverse of this radius to a correction term due to the coordinate system. We found that this method breaks down at the end points, $r = 0$ and $r = R_0$, since there isn't a point either side, hence the curvature cannot be calculated accurately, increasing the error in the final velocity and pressure solutions.

We use the FEniCS package [110] to implement the finite element method to solve the weak formulation (6.4.25). The benefit of using a package such as FEniCS is the use of unified form language (UFL) during the implementation, meaning we can easily choose finite element spaces and define expressions for weak forms in familiar mathematical notation [111]. The specific finite element we use is the Taylor–Hood element [112, 113], since it approximates both velocity and pressure well, is not too numerically costly, and satisfies the discrete inf-sup condition [109]. The Taylor–Hood element consists of a continuous piecewise quadratic approximation of each velocity component combined with a continuous piecewise linear approximation of the pressure. Hence, the velocity space and pressure spaces are

$$V_h = \{v \in [C^0(\Omega)]^d : v|_K \in [P^2(K)]^d\}, \tag{6.4.28}$$

$$Q_h = \{v \in C^0(\Omega) : v|_K \in P^1(K)\}, \tag{6.4.29}$$

respectively, for a finite element K, and spatial dimension d. In (6.4.28,6.4.29), $C^0(\Omega)$ denotes the set of continuous functions on Ω, while P^n denotes nth order polynomials. Figure 6.8 shows the positions of the velocity and pressure nodes for a triangular Taylor–Hood element.

The mesh is converted into the correct format and imported, meaning we can define the function space, and hence the trial and test functions. Next, using UFL notation we define the weak form (6.4.25) ensuring that the correct inner product for the geometry (6.4.8) is used by multiplying each term by rdx. Finally, we call the solve function, which assembles and inverts the linear problem, returning the velocity and pressure solutions.

6.4.5 Results

Figure 6.9 shows representative velocity and pressure solutions for the case that $\phi = 2$, $G = 50$ and $\theta_c = \pi/3$. The mesh used to produce these figures had 23711 elements, with the element sizes being uniform, that is, no refinement is used. A simulation of this resolution takes approximately 8.8 seconds to run on a desktop computer. The velocities in the radial, $u_0(r, z)$, and axial, $w_0(r, z)$, directions are shown in figures 6.9 (a, b), respectively. The azimuthal velocity, $v_0(r, z)$, is not shown but is exactly zero everywhere. Conversely, the radial and

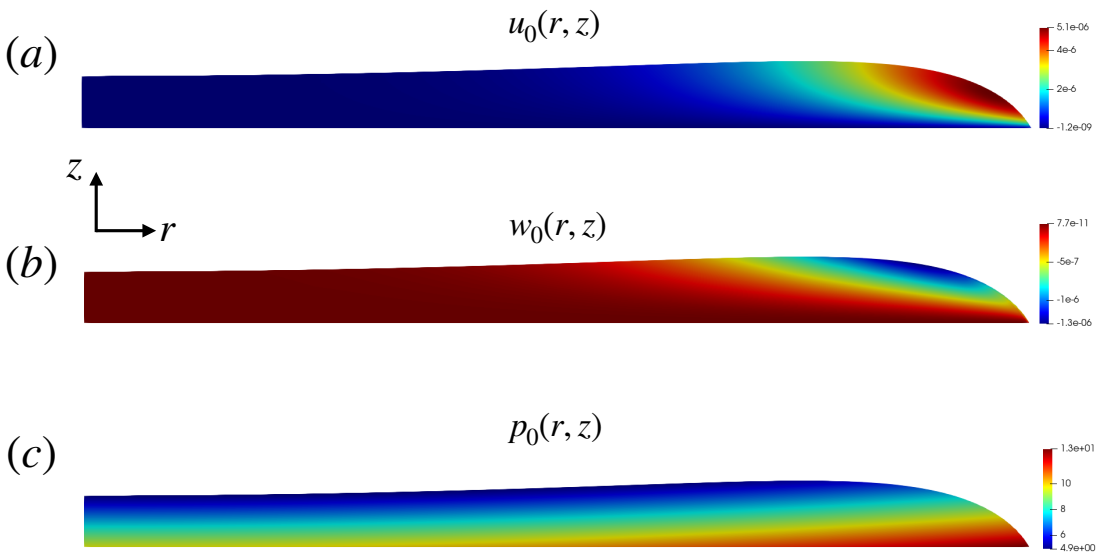


Figure 6.9: Numerical solutions of the axisymmetric equations of motion (6.4.6) when $\phi = 2$, $G = 10$, $\theta_c = \pi/3$. The radial and axial velocities, and the pressure are shown.

axial velocity components are small but non-zero. For the case presented the maximum radial and axial velocities are $\mathcal{O}(10^{-6})$. We see that in both cases the largest velocity magnitude appears where the curvature is greatest, due to the piece-wise element approximation of the free surface being poorer in this region. Furthermore, the axial velocity along the $z = 0$ axis is $\mathcal{O}(10^{-11})$ and constant, satisfying the no-penetration condition (6.1.4) closely. Therefore, we observe the solution for the velocity is close to hydrostatic, $\boldsymbol{u}_0 \approx \mathbf{0}$, satisfying the kinematic conditions (6.4.26).

The numerical pressure solution, $p_0(r, z)$, is shown in figure 6.9 (c) and matches the expected pressure distribution (6.3.1) very well. We see that contours of constant pressure are parabolic, which again is expected given the exact equilibrium pressure (6.3.1). Figure 6.10 (a) shows the difference between the pressure solution along the $z = 0$ axis and the reference pressure at the origin plotted on logarithmic axes. Also shown is the exact pressure solution (6.3.1). The numerical solution aligns well with the expected solution in that the pressure is quadratic along lines of constant height, with a linear function with slope 2. Along any axis $z = k$ with k less than the maximum height of the free surface, the numerical results are the same. Figure 6.10 (b) is similar but shows the difference in pressure solution along the $r = 0$ axis along with the expected solution. We again observe that

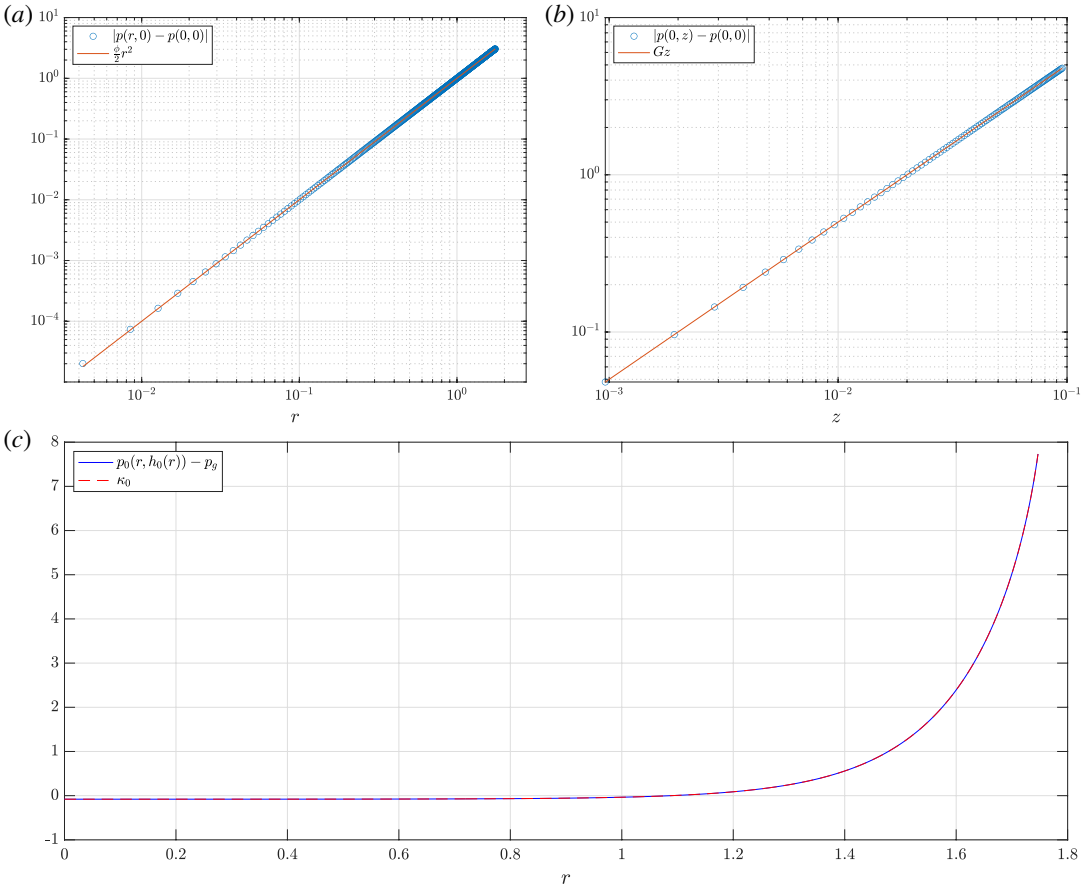


Figure 6.10: Pressure difference along (a) $z = 0$, and (b) $r = 0$, demonstrating that the solution (6.4.5) (b) is recovered. (c) Pressure jump across the free surface in comparison to the curvature, κ_0, showing the the stress condition (6.4.22) is satisfied.

the numerical and exact solutions align well with the pressure rising linearly as z increases. The same numerical results are produced along any axis $r = k$, where $k < R_0$.

Figure 6.10 (c) shows the numerical jump in pressure at the free surface $z = h_0(r)$ in comparison to the curvature of the free surface, κ_0. The pressure jump and curvature are the left and right hand side of the stress condition (6.3.3), respectively, and are shown to agree well. It is consistent that the agreement between these quantities is good, provided that (6.2.7) is implemented correctly. Therefore, figure 6.10 (c) demonstrates that the stress condition (6.2.7) is being applied properly at the free surface.

Solutions for the velocity and pressure converge to their respective analytical solutions (6.4.5) as the maximum element size δ_+ decreases, so that the resolution of

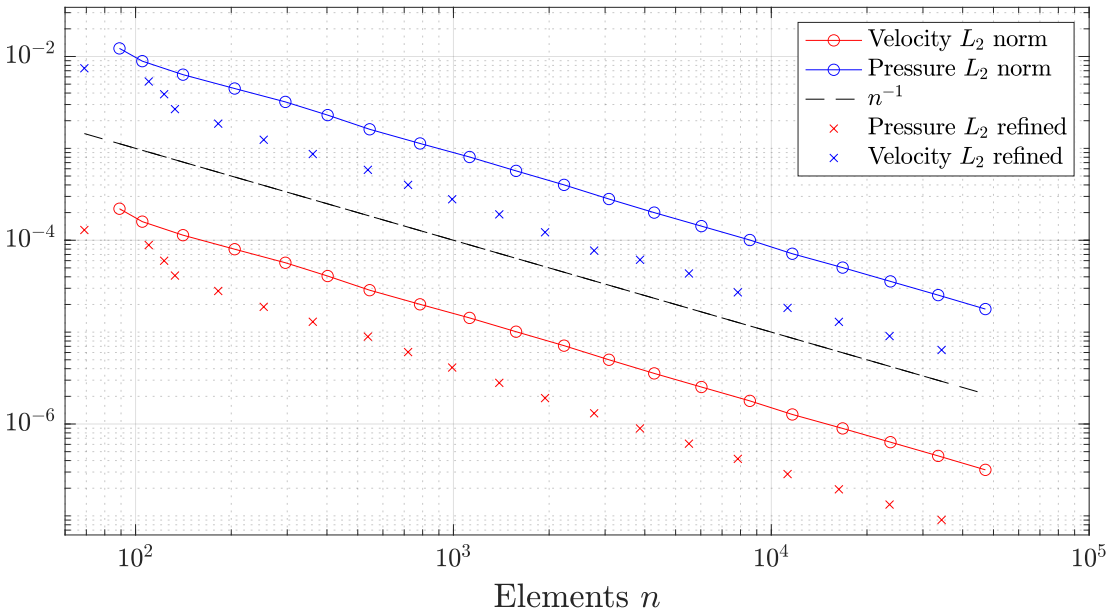


Figure 6.11: Convergence of L2-norm of the pressure and velocity solution of (6.4.25), subject to stress, regularity, slip and no-penetration conditions for $\phi = 2$, $G = 50$. The constant slip function used is $s(h) = \beta = 1 \times 10^{-3}$. Solutions on refined meshes are also plotted for reference.

the mesh increases. This should be expected since increasing the resolution results in a greater number of nodes on the free surface, hence a better approximation of the free surface, $h_0(r)$, and its curvature, κ_0. Figure 6.11 shows the convergence of the L^2–norm of velocity and pressure solution to the exact solution given by (6.4.5) for a specific ϕ and G. We find that on a uniform sized mesh where $\delta_+ = \delta_-$ the velocity and pressure solution both converge like n^{-1}, where n is the number of elements.

The meshing software GMSH allows for refinement of the mesh about a curve or point, as mentioned in § 6.4.4. We can refine about the free surface, so that on $\partial\Omega_3$, the element size is δ_-, rising to δ_+ after a given distance. Therefore, when the mesh is refined in this way, the curvature (6.4.27) of the free surface is better approximated on an overall coarser mesh and the stress boundary conditions are applied more accurately. This results in the same level of accuracy of the solution for fewer elements, meaning lower computational expense. Figure 6.11 also shows the L^2–norm of pressure and velocity solutions on meshes where the target size of elements on the free surface is five times smaller than the maximum element size, so that $\delta_- = \delta_+/5$. We see that for the same number of elements that the error in

both the pressure and velocity is lower, and converges at the same rate.

6.5 Summary

In this chapter we formulated a model no longer assuming that the contact angle is small, θ_c, in contrast to the previous modelling in chapter 3 and much of the literature detailed in chapter 1. The existing literature focuses on thin film solutions of the governing equations, where equilibrium solutions were determined by McKinley *et al.* [42, 43]. Consequently, the analysis presented in this chapter concerning equilibrium solutions when the contact angle is no longer small, and subsequent comparison to the thin film equilibrium solutions of McKinley *et al.* [42, 43], reproduced in § 3.4, are novel contributions to the literature.

We nondimensionalised the system of equations and boundary conditions in an alternative way, with the contact angle functioning as an arbitrary boundary condition, rather than within the nondimensional quantities as before. The resultant equations of motion and boundary conditions contain all terms previously neglected when taking the lubrication approximation in § 3.2.

We found steady, axisymmetric, equilibrium solutions for the free surface, $h_0(r)$, and the constant equilibrium contact line position, R_0. The analysis in this chapter differs from that in § 3.4 since we now include terms previously neglected under the lubrication approximation of (3.2). Therefore, we use a purely numerical scheme to solve the derived ODE (6.3.4), for both $h_0(r)$ and R_0 simultaneously.

We established that for fixed Bond number, G, the results as ϕ is varied is qualitatively the same as the analysis in § 3.4 and to the results of McKinley [42, 43]; for a given Bond number, there exists a maximum nondimensional rotation rate, ϕ_m, beyond which equilibrium solutions do not exist. Furthermore, we determined the effect of varying the contact angle, finding that larger contact angles can support equilibrium solutions at greater rotation rates. Subsequently, we assembled a parameter space in which physical, equilibrium solutions exist which are qualitatively similar to those presented in § 3.4.

Next, we compared the numerical solutions of the full model to the semi-analytical solutions determined by McKinley *et al.* [42, 43] and detailed in § 3.4, finding that

the lubrication approximation compares well to the full model including previously neglected terms for contact angles less than $\theta_c = \pi/2$. However, the thin film solutions detailed within § 3.4 have the advantage of providing an analytical form rather than the purely numerical solutions found within this chapter. We found that, as may be anticipated, when transformed appropriately solutions converge like θ_c^2; the magnitude of neglected terms in the thin film analysis.

We developed a numerical method of solving a set of Stokes equations on a domain defined by the numerical solution for $h_0(r)$ found in § 6.3. Specifically, we used a finite element method and solving for the equilibrium pressure, p_0 and velocity, $\boldsymbol{u}_0$, given the curvature of the free surface, κ_0, calculated from the free surface, $h_0(r)$. We used the FEniCS package to implement the finite element method, and show that the expected equilibrium solutions for velocity and pressure are recovered. Finally, we show that the L^2–norm of the velocity and pressure converge to the exact solution at a rate of n^{-1}, where n is the number of elements in the finite element mesh. The implementation of this method gives a good foundation for solving the subsequent perturbation equations to assess the linear stability of equilibrium solutions.

Chapter 7

O(1) Contact angle model; linear stability analysis

In this chapter we discuss a method of assessing the linear stability of the equilibrium solutions described in § 6.3. Similarly to chapter 4 we first derive the equations of motion and boundary conditions at $\mathcal{O}(\epsilon)$, given a normal mode perturbation, defined by a wavenumber, m. We then present a method of solving the perturbation equations using a finite element method, subsequently discussing the solutions and results.

7.1 Linear stability formulation

In this section we formulate a model to assess the linear stability of the equilibrium solutions discussed in § 6.3, including the terms previously neglected in the thin film model of chapters 4 and 5. We make a normal mode assumption and describe a method to solve the perturbed equations of motion for the $\mathcal{O}(\epsilon)$ velocity and pressure, using a finite element method similar to that described above in § 6.4 but with the added complexity of an unknown free surface perturbation, $h_1(r)$.

7.1.1 Equations of motion

We consider a small perturbation to the initial condition (6.4.5) of the form $\boldsymbol{u} = \epsilon \boldsymbol{u}_1(\boldsymbol{x}, t) + \mathcal{O}(\epsilon^2)$ for the velocity and $p = p_0(r, z) + \epsilon p_1(\boldsymbol{x}, t) + \mathcal{O}(\epsilon^2)$ for the pressure,

where $\epsilon \ll 1$. The free surface and contact line deform as $h = h_0(r) + \epsilon h_1(r, \varphi, t) + \mathcal{O}(\epsilon^2)$, and $R = R_0 + \epsilon R_1(\varphi, t) + \mathcal{O}(\epsilon^2)$, respectively. Since we are considering a model where the contact angle is fixed, no perturbation is applied to the contact angle. During this analysis all perturbation quantities have the subscript 1 and satisfy

$$0 = -\nabla p_1 + \nabla^2 \boldsymbol{u}_1, \quad \boldsymbol{\nabla} \cdot \boldsymbol{u}_1 = 0, \tag{7.1.1}$$

which are the incompressible Stokes flow equations. Note that, the centrifugal and gravitational forces are conservative and appear in the hydrostatic pressure (6.3.1), rather than in the perturbation equations (7.1.1). We make a normal mode assumption, so that the velocity and pressure perturbations are given by

$$\boldsymbol{u}_1(r, \varphi, z, t) = \hat{\boldsymbol{u}}_{\boldsymbol{1}}(r, z) e^{\mathrm{i}m\varphi + \sigma_m t}, \quad p_1(r, \varphi, z, t) = \hat{p}_1(r, z) e^{\mathrm{i}m\varphi + \sigma_m t}, \tag{7.1.2}$$

while the perturbed free surface and contact line deform like

$$h_1(r, \varphi, t) = \hat{h}_1(r) e^{\mathrm{i}m\varphi + \sigma_m t}, \quad R_1(\varphi, t) = \hat{R}_1 e^{\mathrm{i}m\varphi + \sigma_m t} \tag{7.1.3}$$

for wavenumber, $m \in \mathbb{N}$, and comlex growth rate, $\sigma_m \in \mathbb{C}$. Substitution of (7.1.2) into the equations of motion (7.1.1) yields a linear system, written component-wise and dropping the hats

$$0 = -\frac{\partial p_1}{\partial r} + \nabla^2 u_1 - \frac{m^2 u_1}{r^2} - \frac{2\mathrm{i}m v_1}{r^2} - \frac{u_1}{r^2}, \tag{7.1.4}$$

$$0 = -\frac{\mathrm{i}m p_1}{r} + \nabla^2 v_1 - \frac{m^2 v_1}{r^2} + \frac{2\mathrm{i}m u_1}{r^2} - \frac{v_1}{r^2}, \tag{7.1.5}$$

$$0 = -\frac{\partial p_1}{\partial z} + \nabla^2 w_1 - \frac{m^2 w_1}{r^2} \tag{7.1.6}$$

$$\frac{1}{r}\frac{\partial}{\partial r}(r u_1) + \frac{\mathrm{i}m v_1}{r} + \frac{\partial w_1}{\partial z} = 0, \tag{7.1.7}$$

for velocity components as $\boldsymbol{u}_1 = (u_1, v_1, w_1)$. Furthermore, since the velocity components, $\boldsymbol{u}_1 = (u_1, v_1, w_1)$, are functions of r and z only, the Laplacian operator $\nabla^2(\,\cdot\,)$, only involves radial and axial derivatives. The domain in which we solve equations (7.1.4)–(7.1.7), Ω, is defined by the equilibrium free surface solution, $z = h_0(r)$. Therefore, Ω is the domain bounded by $r = 0$, $z = 0$, and $z = h_0(r)$, as was defined in § 6.4.2, an example of which is shown in figure 6.7.

7.1.2 Boundary conditions

Next, we apply the perturbations (7.1.3) to the boundary conditions, giving their $\mathcal{O}(\epsilon)$ forms. Firstly, the free surface (6.1.1) following perturbation is

$$\mathscr{S} := z - [h_0(r) + \epsilon h_1(r) e^{\mathrm{i}m\varphi + \sigma_m t}] = 0, \tag{7.1.8}$$

on which the kinematic boundary condition (6.2.14) (b) is

$$w_1(r, h_0) = \sigma_m h_1(r) + u_1(r, h_0)\frac{\mathrm{d}h_0}{\mathrm{d}r} \tag{7.1.9}$$

at $\mathcal{O}(\epsilon)$. Under the assumptions made by perturbing and taking normal mode form (7.1.2, 7.1.3) the rate-of-strain tensor, $\underline{\underline{e}} = \frac{1}{2}(\nabla \boldsymbol{u} + (\nabla \boldsymbol{u})^T)$, the outward unit normal, $\hat{\boldsymbol{n}}$, and the curvature, κ, each deform like

$$\underline{\underline{e}} = \underline{\underline{e}}_0 + \epsilon \underline{\underline{e}}_1 e^{\mathrm{i}m\varphi + \sigma_m t}, \quad \hat{\boldsymbol{n}} = \hat{\boldsymbol{n}}_0 + \epsilon \hat{\boldsymbol{n}}_1 e^{\mathrm{i}m\varphi + \sigma_m t}, \quad \kappa = \kappa_0 + \epsilon \kappa_1 e^{\mathrm{i}m\varphi + \sigma_m t}, \tag{7.1.10}$$

where, due to the hydrostatic equilibrium velocity solution, $\underline{\underline{e}}_0 = 0$. Subsequently, the stress condition (6.2.14) (a) gives (6.3.3) at leading order in ϵ and

$$\Big[-p_1(r, h_0) + 2\underline{\underline{e}}_1(r, h_0) + G h_1\Big] \cdot \hat{\boldsymbol{n}}_0 = -\frac{\kappa_1}{C}\hat{\boldsymbol{n}}_0 \tag{7.1.11}$$

at $\mathcal{O}(\epsilon)$, where the $\mathcal{O}(1)$ stress condition (6.3.3) has been used to simplify (7.1.11). The $\mathcal{O}(\epsilon)$ curvature κ_1 in terms of $h_0(r), h_1(r)$ is,

$$\kappa_1(r) = \boldsymbol{\nabla} \cdot \hat{\boldsymbol{n}}_1 = \frac{[1 + h_0'^2]^2 m^2 h_1 - r\{r[1 + h_0'^2]h_1'' + [1 + h_0'^2 - 3r h_0' h_0'']h_1'\}}{r^2[1 + h_0'^2]^{5/2}}, \tag{7.1.12}$$

and only varies with the radial coordinate, r, with dashes denoting derivatives with respect to this coordinate. Note that, both the kinematic (7.1.9) and the stress condition (7.1.11) are evaluated at the equilibrium free surface, $z = h_0(r)$.

At the solid plate $z = 0$, the slip and no-penetration boundary conditions (6.2.13) are imposed, which at $\mathcal{O}(\epsilon)$ are

$$u_1 = s(h_0)\frac{\partial u_1}{\partial z}, \quad v = s(h_0)\frac{\partial u_1}{\partial z}, \quad \boldsymbol{u}_1 \cdot \hat{\boldsymbol{n}}_0 = 0, \tag{7.1.13}$$

respectively.

At the contact line, $r = R_0 + \epsilon R_1 e^{\mathrm{i}m\varphi+\sigma_m t}$, we impose the contact (6.2.15) (a) and contact angle (6.2.15) (b) conditions, which at $\mathcal{O}(\epsilon)$ are

$$h_0'(R_0)R_1 + h_1(R_0) = 0, \quad R_1 h_0''(R_0) + h_1'(R_0) = 0, \tag{7.1.14}$$

respectively. Recalling the contact angle condition at leading order in ϵ (6.3.7), we can eliminate R_1 between the contact and contact angle conditions (7.1.14) leading to a combined boundary condition and an expression for R_1,

$$h_1'(R_0) + \cot(\theta_c)h_1(R_0)h_0''(R_0) = 0, \tag{7.1.15}$$

$$R_1 = h_1(R_0)\cot(\theta_c), \tag{7.1.16}$$

respectively, under the assumption that $R_1 \neq 0$. The combined condition (7.1.15) is analogous to (5.2.5) in the thin film theory. We also impose the contact line kinematic condition (6.2.16) at $\mathcal{O}(\epsilon)$,

$$\sigma_m R_1 = u_1(0, R_0). \tag{7.1.17}$$

Similarly to the boundary conditions at the free surface, we note that each of the boundary conditions at the contact line are evaluated at the equilibrium solution, $r = R_0$.

On the axis $r = 0$, the $\mathcal{O}(\epsilon)$ differentiability condition (6.2.17) is

$$h_1'(0) = 0. \tag{7.1.18}$$

In § 4.1.3 we discussed how the $m = 1$ perturbation corresponds to a translation of the centre of mass away from the axis of rotation at $r = 0$. Therefore, the differentiability condition (7.1.18) only applies to perturbations $m \neq 1$, where the centre of mass lies on $r = 0$. We impose the velocity regularity condition (6.2.18) at $r = 0$

$$|\boldsymbol{u}_1(0, z)| < \infty, \tag{7.1.19}$$

stating that the magnitude of the $\mathcal{O}(\epsilon)$ velocity is finite on the axis of rotation, $r = 0$. Finally, as argued in § 4.1.3, due to the form of the perturbation the volume condition (6.2.19) is satisfied automatically for $m = 1, 2, 3, ...$, whereas if $m = 0$,

corresponding to purely axisymmetric spreading, we require

$$\int_0^{R_0} r h_1(r)\,\mathrm{d}r = 0. \tag{7.1.20}$$

7.1.3 Weak formulation

In § 6.4, for the equilibrium solutions, corresponding to solutions at leading order in ϵ, we derived a weak formulation (6.4.14) from the equations of motion in vector form (6.4.6). We cannot employ a similar method for the perturbation equations (7.1.4)–(7.1.7), due to the normal mode assumption and must instead derive the weak formulation directly from the equations. Therefore, we take the inner product (6.4.8) of each component of the perturbation equations (7.1.4)–(7.1.6), and each component of the vector test function, $\boldsymbol{t} = (t_r, t_\varphi, t_z)$, and sum the results giving

$$\begin{aligned} 0 = \int_\Omega \Bigg\{ &\left[-\frac{\partial p_1}{\partial r} + \nabla^2 u_1 - \frac{m^2 u_1}{r^2} - \frac{2\mathrm{i}m v_1}{r^2} - \frac{u_1}{r^2} \right] t_r \\ &+ \left[-\frac{\mathrm{i}m p_1}{r} + \nabla^2 v_1 - \frac{m^2 v_1}{r^2} + \frac{2\mathrm{i}m u_1}{r^2} - \frac{v_1}{r^2} \right] t_\varphi \\ &+ \left[-\frac{\partial p_1}{\partial z} + \nabla^2 w_1 - \frac{m^2 w_1}{r^2} \right] t_z \Bigg\}\,\mathrm{d}\boldsymbol{x}. \end{aligned} \tag{7.1.21}$$

The numbered subscripts indicate whether the quantity is $\mathcal{O}(1)$ or $\mathcal{O}(\epsilon)$, whereas the coordinate subscript denote the component in that coordinate respectively, not to be confused with partial derivatives. Since the weak formulation is defined on Ω, the outward pointing unit normal, subsequently referred to as $\boldsymbol{n} = (n_r, 0, n_z)$, is a quantity at leading order in ϵ which only has components in the radial and axial directions; on the free surface $\partial\Omega_3$ $\boldsymbol{n} = \hat{\boldsymbol{n}}_0$ as defined in (7.1.10). The second order velocity derivatives and the pressure derivatives in (7.1.21) are integrated by parts, and summed with the inner product of the incompressibility condition

(3.2.28) and scalar test function, q, to give

$$
\begin{aligned}
0 = \int_\Omega \Bigg\{ & p_1 \left[\nabla^* \cdot \boldsymbol{t}^* - \frac{\mathrm{i}m t_\varphi}{r} \right] - q \left[\nabla^* \cdot \boldsymbol{u}_1^* + \frac{\mathrm{i}m v_1}{r} \right] - \nabla^* u_1 \cdot \nabla^* t_r \\
& - \nabla^* v_1 \cdot \nabla^* t_\varphi - \nabla^* w_1 \cdot \nabla^* t_z + \left[-\frac{m^2 u_1}{r^2} - \frac{2\mathrm{i}m v_1}{r^2} - \frac{u_1}{r^2} \right] t_r \\
& + \left[-\frac{m^2 v_1}{r^2} + \frac{2\mathrm{i}m u_1}{r^2} - \frac{v_1}{r^2} \right] t_\varphi - \frac{m^2 w_1}{r^2} t_z \Bigg\} \, \mathrm{d}\boldsymbol{x} \\
& + \int_{\partial\Omega} [(-p_1 n_r + \nabla^* u_1 \cdot \boldsymbol{n}^*) t_r + (\nabla^* v_1 \cdot \boldsymbol{n}^*) t_\varphi \\
& \qquad + (-p_1 n_z + \nabla^* w_1 \cdot \boldsymbol{n}^*) t_z] \, \mathrm{d}S. \qquad (7.1.22)
\end{aligned}
$$

The starred quantities in (7.1.22) denote those in the (r, z) plane, so that $\nabla^*(\,\cdot\,) = (\partial/\partial r[\,\cdot\,], \partial/\partial z[\,\cdot\,])$, $\boldsymbol{n}^* = (n_r, n_z)$ and $\boldsymbol{t}^* = (t_r, t_z)$.

The boundary conditions to be applied to the weak formulation (7.1.22) are the stress (7.1.11), slip (7.1.13) (a, b), no-penetration (7.1.13) (b) and regularity (7.1.19) conditions. The boundary integral of the weak formulation (7.1.22), denoted B, is a sum over the contributing boundaries, B_i where $i = 1, 2, 3$, as in (6.4.16). On the solid boundary at $z = 0$, the outward unit normal is $\boldsymbol{n}^* = (0, -1)$ so that the boundary integral contribution, B_1 is

$$
B_1 = \int_{\partial\Omega_1} \left\{ -\frac{\partial u_1}{\partial z} t_r - \frac{\partial v_1}{\partial z} t_\varphi + \left(p_1 - \frac{\partial w_1}{\partial z} \right) t_z \right\} \mathrm{d}S_1. \qquad (7.1.23)
$$

The no-penetration condition (7.1.13) (c) is formulated as in § 6.4 according to John [107], so that

$$
0 = \boldsymbol{u}_1 \cdot \boldsymbol{n} + \xi \boldsymbol{n}^T \cdot \left(-p_1 \underline{\underline{I}} + 2 \underline{\underline{e}}_1 \right) \cdot \boldsymbol{n} = w_1 + \xi \left(-p_1 + 2 \frac{\partial w_1}{\partial z} \right) \qquad (7.1.24)
$$

at $z = 0$. Substituting the no-penetration condition (7.1.24) and the two slip conditions (7.1.13) (a, b) into the expression for B_1 (7.1.23) gives the boundary integral

$$
B_1 = \int_{\partial\Omega_1} \left\{ -\frac{u_1}{s(h_0)} t_r - \frac{v_1}{s(h_0)} t_\varphi + \left(\frac{w_1}{\xi} + \frac{\partial w_1}{\partial z} \right) t_z \right\} \mathrm{d}S_1. \qquad (7.1.25)
$$

At the free surface, $z = h_0(r)$, we apply the $\mathcal{O}(\epsilon)$ continuity of stress condition (7.1.11). Under the normal mode assumption, the $\mathcal{O}(\epsilon)$ strain tensor,

$\underline{\underline{e}}_1 = \frac{1}{2}(\nabla \boldsymbol{u}_1 + (\nabla \boldsymbol{u}_1)^T)$, is

$$2\underline{\underline{e}}_1 = \begin{pmatrix} 2\dfrac{\partial u_1}{\partial r} & \dfrac{\partial v_1}{\partial r} - \dfrac{v_1}{r} + \dfrac{\mathrm{i}mu_1}{r} & \dfrac{\partial u_1}{\partial z} + \dfrac{\partial w_1}{\partial r} \\ \dfrac{\partial v_1}{\partial r} - \dfrac{v_1}{r} + \dfrac{\mathrm{i}mu_1}{r} & 2\left(\dfrac{\mathrm{i}mv_1}{r} + \dfrac{u_1}{r}\right) & \dfrac{\partial v_1}{\partial z} + \dfrac{\mathrm{i}mw_1}{r} \\ \dfrac{\partial u_1}{\partial z} + \dfrac{\partial w_1}{\partial r} & \dfrac{\partial v_1}{\partial z} + \dfrac{\mathrm{i}mw_1}{r} & 2\dfrac{\partial w_1}{\partial z} \end{pmatrix}. \tag{7.1.26}$$

Substituting into the $\mathcal{O}(\epsilon)$ continuity of stress condition (7.1.11), with the unit normal to the free surface $\boldsymbol{n} = (n_r, 0, n_z)$, gives the three stress components

$$-\frac{\kappa_1}{C}n_r = -p_1 n_r + 2\frac{\partial u_1}{\partial r}n_r + \left(\frac{\partial u_1}{\partial z} + \frac{\partial w_1}{\partial r}\right)n_z + Gh_1 n_r, \tag{7.1.27}$$

$$0 = \left[\frac{\partial v_1}{\partial r} - \frac{v_1}{r} + \frac{\mathrm{i}mu_1}{r}\right]n_r + \left[\frac{\partial v_1}{\partial z} + \frac{\mathrm{i}mw_1}{r}\right]n_z, \tag{7.1.28}$$

$$-\frac{\kappa_1}{C}n_z = -p_1 n_z + \left(\frac{\partial u_1}{\partial z} + \frac{\partial w_1}{\partial r}\right)n_r + 2\frac{\partial w_1}{\partial z}n_z + Gh_1 n_z, \tag{7.1.29}$$

where the $\mathcal{O}(\epsilon)$ curvature, κ_1, is defined in (7.1.12). The normal vector is left in more general form since each component varies with r along the free surface. Rearranging and substituting into the boundary integral term from (6.4.14) determines the contribution from $\partial\Omega_3$,

$$\begin{aligned} B_3 = \int_{\partial\Omega_3} \Bigg\{ & \left[-\left(\frac{\kappa_1}{C} + Gh_1 + \frac{\partial u_1}{\partial r}\right)n_r - \frac{\partial w_1}{\partial r}n_z\right]t_r \\ & + \left[\left(\frac{v_1}{r} - \frac{\mathrm{i}mu_1}{r}\right)n_r - \frac{\mathrm{i}mw_1}{r}n_z\right]t_\varphi \\ & + \left[-\frac{\partial u_1}{\partial z}n_r - \left(\frac{\kappa_1}{C} + Gh_1 + \frac{\partial w_1}{\partial z}\right)n_z\right]t_z \Bigg\}\, \mathrm{d}S_3. \end{aligned} \tag{7.1.30}$$

Finally, on the axis $r = 0$, we again apply a stress free boundary condition so that $B_2 = 0$. Substituting each of the boundary integrals, B_{1-3}, into the weak formulation (7.1.22) determines the full weak formulation of equations of motion (7.1.4)–(7.1.7) subject to continuity of stress (7.1.11), slip (7.1.13) (a, b), no-penetration

(7.1.13) (c) and regularity (7.1.19) conditions

$$
\begin{aligned}
0 = \int_\Omega \Bigg\{ & p_1 \left[\nabla^* \cdot \boldsymbol{t}^* - \frac{\mathrm{i}m t_\varphi}{r} \right] - q \left[\nabla^* \cdot \boldsymbol{u}_\mathbf{1}^* + \frac{\mathrm{i}m v_1}{r} \right] - \nabla^* u_1 \cdot \nabla^* t_r \\
& - \nabla^* v_1 \cdot \nabla^* t_\varphi - \nabla^* w_1 \cdot \nabla^* t_z + \left[-\frac{m^2 u_1}{r^2} - \frac{2\mathrm{i}m v_1}{r^2} - \frac{u_1}{r^2} \right] t_r \\
& + \left[-\frac{m^2 v_1}{r^2} + \frac{2\mathrm{i}m u_1}{r^2} - \frac{v_1}{r^2} \right] t_\varphi - \frac{m^2 w_1}{r^2} t_z \Bigg\} \, \mathrm{d}\boldsymbol{x} + \int_{\partial\Omega_1} \Bigg\{ - \frac{u_1}{s(h_0)} t_r - \frac{v_1}{s(h_0)} t_\varphi \\
& + \left(\frac{w_1}{\xi} + \frac{\partial w_1}{\partial z} \right) t_z \Bigg\} \, \mathrm{d}S_1 + \int_{\partial\Omega_3} \Bigg\{ \left[- \left(\frac{\kappa_1}{C} + G h_1 + \frac{\partial u_1}{\partial r} \right) n_r - \frac{\partial w_1}{\partial r} n_z \right] t_r \\
& + \left[\left(\frac{v_1}{r} - \frac{\mathrm{i}m u_1}{r} \right) n_r - \frac{\mathrm{i}m w_1}{r} n_z \right] t_\varphi + \left[- \frac{\partial u_1}{\partial z} n_r - \left(\frac{\kappa_1}{C} + G h_1 + \frac{\partial w_1}{\partial z} \right) n_z \right] t_z \Bigg\} \, \mathrm{d}S_3.
\end{aligned}
\tag{7.1.31}
$$

Note that, derivatives with respect to φ have introduced complex parts due to the form of the perturbations (7.1.2). One option to solve the complex weak formulation (7.1.31) is to separate each variable into real and imaginary parts, and subsequently solve the real and imaginary parts of (7.1.31) simultaneously. A more efficient option is to notice that the transformation

$$
v_1 = \mathrm{i} v_1^\dagger, \quad t_\varphi = -\mathrm{i} t_\varphi^\dagger,
\tag{7.1.32}
$$

where $v_1^\dagger, t_\varphi^\dagger$ are real functions, removes the imaginary contributions from the problem resulting in the real weak formulation

$$
\begin{aligned}
0 = \int_\Omega \Bigg\{ & p_1 \left[\nabla^* \cdot \boldsymbol{t}^* - \frac{m t_\varphi^\dagger}{r} \right] - q \left[\nabla^* \cdot \boldsymbol{u}_\mathbf{1}^* - \frac{m v_1^\dagger}{r} \right] - \nabla^* u_1 \cdot \nabla^* t_r \\
& - \nabla^* v_1^\dagger \cdot \nabla^* t_\varphi^\dagger - \nabla^* w_1 \cdot \nabla^* t_z + \left[-\frac{m^2 u_1}{r^2} + \frac{2m v_1^\dagger}{r^2} - \frac{u_1}{r^2} \right] t_r \\
& + \left[-\frac{m^2 v_1^\dagger}{r^2} + \frac{2m u_1}{r^2} - \frac{v_1^\dagger}{r^2} \right] t_\varphi^\dagger - \frac{m^2 w_1}{r^2} t_z \Bigg\} \, \mathrm{d}\boldsymbol{x} + \int_{\partial\Omega_1} \Bigg\{ - \frac{u_1}{s(h_0)} t_r - \frac{v_1^\dagger}{s(h_0)} t_\varphi^\dagger \\
& + \left(\frac{w_1}{\xi} + \frac{\partial w_1}{\partial z} \right) t_z \Bigg\} \, \mathrm{d}S_1 + \int_{\partial\Omega_3} \Bigg\{ \left[- \left(\frac{\kappa_1}{C} + G h_1 + \frac{\partial u_1}{\partial r} \right) n_r - \frac{\partial w_1}{\partial r} n_z \right] t_r \\
& + \left[\left(\frac{v_1^\dagger}{r} - \frac{m u_1}{r} \right) n_r - \frac{m w_1}{r} n_z \right] t_\varphi^\dagger + \left[- \frac{\partial u_1}{\partial z} n_r - \left(\frac{\kappa_1}{C} + G h_1 + \frac{\partial w_1}{\partial z} \right) n_z \right] t_z \Bigg\} \, \mathrm{d}S_3.
\end{aligned}
\tag{7.1.33}
$$

The transformation on v_1 (7.1.32) could have been made from the perturbation

equation (7.1.5), where the transformation of the test function t_φ accounts for division by i through this transformed equation. Incidentally, if the complex weak formulation (7.1.31) was solved by simultaneously solving for the real and imaginary parts we would find that the real part of v_1 and imaginary parts of u_1, w_1, and p_1 are zero.

In summary, we have derived the weak formulation of the $\mathcal{O}(\epsilon)$ perturbation equations (7.1.4)–(7.1.7) subject to stress (7.1.11), slip (7.1.13) (a, b), no-penetration (7.1.13) (c) and regularity (7.1.19).

7.1.4 Solution method

The method of solution is somewhat similar to that in § 6.4.4, in which we first determine the numerical solution for $h_0(r)$, and then use GMSH [108] to produce our finite element mesh.

In order to apply the stress conditions we require the $\mathcal{O}(\epsilon)$ curvature (7.1.12), which in turn requires the perturbed free surface, $h_1(r)$. The function $h_1(r)$ is required to satisfy the remaining boundary conditions; the combined contact angle condition (7.1.15), the differentiability condition (7.1.18) and the normalisation condition on R_1 (7.1.16). Furthermore, although we take a stress free boundary condition on $\partial\Omega_2$, the regularity condition (7.1.19) must also be satisfied along the free surface, $\partial\Omega_3$, as $r \to 0$. Specifically, the curvature of the free surface must tend to a finite limit, that is

$$\lim_{r\to 0} \kappa_1(r) = \lim_{r\to 0} \left(h_1'' + \frac{1}{r} h_1' - \frac{m^2}{r^2} h_1. \right) < \infty, \tag{7.1.34}$$

where the differentiability condition at leading order in ϵ, $h_0'(0) = 0$, has been used to simplify (7.1.34). Specifically, when $m = 2, 3, ...$ we require that the limit (7.1.34) is equal to zero to ensure differentiability of the perturbed free surface, so that

$$h_1(r) \sim A r^m \tag{7.1.35}$$

as $r \to 0$, where A is an unknown constant. Therefore, for $m = 2, 3, ...$ the behaviour near the origin satisfies the differentiability condition (7.1.18). When $m = 1$ the differentiability need not be applied, as argued in § 4.1.3, since $m = 1$

represents a translation of the centre of mass. The behaviour (7.1.35) is consistent with that found for the perturbed free surface within the thin film limit, detailed in § 5.2.

To satisfy the combined contact angle condition (7.1.15) while retaining the behaviour close to $r = 0$, we construct the function $h_1(r)$ using a Fourier–Bessel series, known as a Dini series [114]. The perturbed free surface, $h_1(r)$, is expressed as

$$h_1(r) = B_0(r) + \sum_{n=1}^{\infty} a_n \mathcal{J}_m\left(\gamma_n \frac{r}{R_0}\right), \tag{7.1.36}$$

where $\mathcal{J}_m$ is the mth order Bessel function of the first kind, and γ_n are the solutions of

$$x\mathcal{J}_m'(x) + R_0 \cot(\theta_c) h_0''(R_0)\mathcal{J}_m(x) = 0. \tag{7.1.37}$$

The function $B_0(r)$ is defined as

$$B_0(r) = \begin{cases} 0 & m + R_0 \cot(\theta_c) h_0''(R_0) > 0, \\ a_0 \mathcal{I}_m\left(\gamma_0 \dfrac{r}{R_0}\right) & m + R_0 \cot(\theta_c) h_0''(R_0) < 0, \\ a_0 \left(\dfrac{r}{R_0}\right)^m & m + R_0 \cot(\theta_c) h_0''(R_0) = 0, \end{cases} \tag{7.1.38}$$

where $\mathcal{I}_m$ is the mth order modified Bessel function of the first kind, and γ_0 is the solution of

$$x\mathcal{I}_m'(x) + R_0 \cot(\theta_c) h_0''(R_0)\mathcal{I}_m(x) = 0. \tag{7.1.39}$$

Therefore, each term in the series (7.1.36) satisfies the regularity condition (7.1.35) and the combined contact angle condition (7.1.15) by construction. Notice that, if the Tanner law (4.1.14) was used, as in chapter 4, then the right hand side of the resultant combined Tanner law, analogous to (4.1.15), would be non-zero. Hence, in this case we could not construct a similar Fourier–Bessel series satisfying the boundary conditions.

Finally, to reflect the contact condition (7.1.16) we normalise each function in the series so that its value at the contact line is $\tan(\theta_c)$. This amounts to defining new coefficients k_n such that

$$k_0 = a_0 \cot(\theta_c)\mathcal{I}_m(\gamma_0), \quad k_n = a_n \cot(\theta_c)\mathcal{J}_m(\gamma_0), \tag{7.1.40}$$

for all $n = 1, 2, 3, ...$ Overall, we have a set of normalised functions, $f_{(m,n)}$, for each Fourier mode, m, and Bessel mode, n,

$$f_{(m,0)}(r) = \tan(\theta_c)\frac{\mathcal{I}_m(\gamma_0 \frac{r}{R_0})}{\mathcal{I}_m(\gamma_0)}, \quad f_{(m,n)}(r) = \tan(\theta_c)\frac{\mathcal{J}_m(\gamma_n \frac{r}{R_0})}{\mathcal{J}_m(\gamma_n)}, \tag{7.1.41}$$

which each satisfy the combined contact angle (7.1.15) and velocity regularity conditions (7.1.35). The functions sum to assemble $h_1(r)$, such that

$$h_1(r) = f_{(m,0)}(r) + \sum_{n=1}^{\infty} k_n f_{(m,n)}(r) \tag{7.1.42}$$

for each wavenumber, m, provided $m + R_0 \cot(\theta_c) h_0''(R_0) < 0$. If this quantity is greater than zero so that $m + R_0 \cot(\theta_c) h_0''(R_0) > 0$ then $f_{(m,0)} = 0$. Note that defining $R_1 = 1$ so that ϵ is the size of the contact line perturbation the $\mathcal{O}(\epsilon)$ contact condition results in the coefficients summing to one,

$$R_1 = 1 = \sum_{n=0}^{\infty} k_n. \tag{7.1.43}$$

Figures 7.1(a)–(d) each show the normalised functions, $f_{(m,n)}$, for Bessel modes $n = 0, 1, 2, 3$, with each figure showing a different wavenumber $m = 1, 2, 3, 4$ when $\phi = 2$, $G = 10$ and $\theta_c = \pi/3$. In each figure $m + R_0 \cot(\theta_c) h_0''(R_0) < 0$ so that there exists a real root to (7.1.39) and $n = 0$ returns a non-zero function. In all figures each function is normalised such that $h_1(R_0) = \tan(\theta_c) = \sqrt{3}$, where each function has the same gradient at $r = R_0$ due to satisfying the combined contact angle condition (7.1.15). Furthermore, the behaviour near $r = 0$ is demonstrated, where each function is of the form r^m close to the origin. This is particularly visible in the Bessel modes when $m = 1$, where each function approaches the origin linearly. When $m + R_0 \cot(\theta_c) h_0''(R_0) < 0$ we observe that the Bessel mode, n, corresponds to the number of extremum within $[0, R_0]$, so that $f_{(m,0)}$ is a monotonically increasing function. The function $f_{(m,n)}$ initially increases close the $r = 0$ if n is even, whereas decreases if n is odd. If $m + R_0 \cot(\theta_c) h_0''(R_0) > 0$ then there are $n - 1$ turning points within $[0, R_0]$ for the nth Bessel mode, and functions with odd n initially increase and those with even n decrease close to $r = 0$.

When $m = 0$, a further boundary condition is required to conserve volume (7.1.20). Using this method we cannot also satisfy (7.1.20), and therefore restrict our anal-

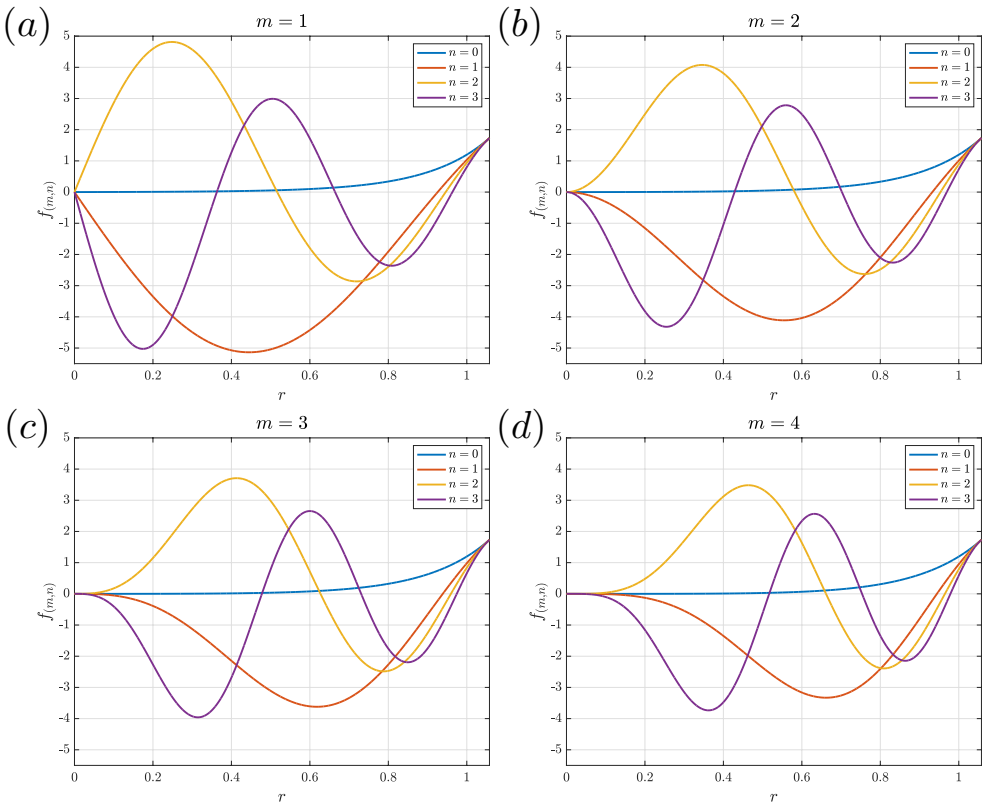


Figure 7.1: The first four normalised Bessel functions (7.1.41) $n = 0, 1, 2, 3$ for $m = 1, 2, 3, 4$. The presented case is for $\phi = 2$, $G = 10$ and $\theta_c = \pi/3$, so that $R_0 = 1.293$.

ysis to the non-axisymmetric cases, $m = 1, 2, 3, ...$, where volume is conserved automatically.

We are now in a position to calculate the $\mathcal{O}(\epsilon)$ velocity and pressure using a similar method to that described in § 6.4.4, but instead solving the derived weak formulation (7.1.31). The variational form (7.1.31) requires the $\mathcal{O}(\epsilon)$ curvature for each wavenumber, m, and Bessel mode, n,

$$\kappa_{1(m,n)}(r) = \frac{[1 + h_0'^2]^2 m^2 f_{(m,n)} - r\{r[1 + h_0'^2] f''_{(m,n)} + [1 + h_0'^2 - 3r h_0' h_0''] f'_{(m,n)}\}}{r^2 [1 + h_0'^2]^{5/2}}, \tag{7.1.44}$$

where $f_{(m,n)}(r)$ is each normalised function (7.1.41). The curvature is calculated on a finer grid than the minimum element size, δ_- and then interpolated at the free surface nodes produced from the finite element mesh.

We again use the FEniCS package to implement the finite element method, solving

the weak formulation (7.1.33) on the mesh defined by the equilibrium solution, for the $\mathcal{O}(\epsilon)$ velocity, $\boldsymbol{u}_1$, and pressure, p_1. More specifically, we are solving for the real parts of the radial and axial components of the velocity and the imaginary part of the azimuthal velocity, due to the transformation (7.1.32). Once again, Taylor-Hood elements are used as our finite elements (see figure 6.8).

Once the $\mathcal{O}(\epsilon)$ velocity has been determined, the growth rate $\sigma_{m,n}$ associated with a wavenumber m and a mode n is given by the contact line kinematic condition (7.1.17),

$$\sigma_{m,n} = u_{1(m,n)}(R_0, 0). \tag{7.1.45}$$

Since the system of equations is linear, if the coefficients for the Fourier–Bessel series are known the growth rate for a given wavenumber can be assembled by

$$\sigma_m = \sum_{n=0}^{\infty} k_n \sigma_{m,n}. \tag{7.1.46}$$

The coefficients are unknown, in which case we can determine the linear stability of a perturbation given by wavenumber m and Bessel mode, n, by considering sign and magnitude of the radial velocity at the contact line.

7.2 Verification by comparison with thin film solutions

Prior to describing the linear stability results of systems with $\mathcal{O}(1)$ contact angles, we first verify the numerical method used. To do this we use known numerical solutions found using the thin film approximation also subject to the fixed contact angle condition, previously described in § 5.2, and test our numerical implementation when the contact angle is small.

7.2.1 Thin film solution

Recall from § 4.1 that the linear stability problem is formulated by making a normal mode assumption, reducing the equations of motion and boundary conditions to an eigenvalue problem. In this chapter we studied the system subject to a fixed

contact angle condition, and to reflect this we discuss its thin film equivalent here, studied previously in § 5.2. In the thin film limit, the eigenvalue problem (5.2.6) is subject to the regularity, differentiability, contact, contact angle and contact line kinematic conditions which is solved to give the eigenvalue, $\sigma_{m\mathrm{I}}$, and a corresponding eigenfunction, $h_{1\mathrm{I}}(r)$. The subscript I denotes the thin film solutions, while the subscript m in $\sigma_{m\mathrm{I}}$ denotes the wavenumber as before.

The $\mathcal{O}(\epsilon)$ pressure and velocity components are defined in terms of the linear operator, $\mathcal{L}_1$, acting on the eigenfunction, $h_{1\mathrm{I}}(r)$,

$$p_{1\mathrm{I}}(r) = -\mathcal{L}_1[h_{1\mathrm{I}}], \tag{7.2.1}$$

$$u_{1\mathrm{I}}(r,z) = -\left(\frac{z^2}{2} - h_{0\mathrm{I}}z - \frac{\alpha_{\mathrm{I}}}{3}\right)\mathcal{L}_1'[h_{1\mathrm{I}}], \tag{7.2.2}$$

$$v_{1\mathrm{I}}(r,z) = -\frac{\mathrm{i}m}{r}\left(\frac{z^2}{2} - h_{0\mathrm{I}}z - \frac{\alpha_{\mathrm{I}}}{3}\right)\mathcal{L}_1[h_{1\mathrm{I}}], \tag{7.2.3}$$

$$w_{1\mathrm{I}}(r,z) = z\left(\frac{z^2}{6} - \frac{h_{0\mathrm{I}}z}{2} - \frac{\alpha_{\mathrm{I}}}{3}\right)\left(\mathcal{L}_1^2(h_1) + G\mathcal{L}_1[h_{1\mathrm{I}}]\right) - \frac{h_{0\mathrm{I}}'}{2}z^2\mathcal{L}_1'[h_{1\mathrm{I}}], \tag{7.2.4}$$

respectively. The linear operator, $\mathcal{L}_1$, is defined as in (4.1.5) and is repeated here for clarity

$$\mathcal{L}_1[\Phi] = \left[\frac{\mathrm{d}^2}{\mathrm{d}r^2} + \frac{1}{r}\frac{\mathrm{d}}{\mathrm{d}r} - \frac{m^2}{r^2} - G\right]\Phi. \tag{7.2.5}$$

Notice that the eigenvalue problem (5.2.6), pressure and velocity components (7.2.1)–(7.2.4) are all independent of the capillary number C due to the chosen velocity scale in the fixed contact angle model.

In the thin film limit, the velocity and pressure along the free surface are constructed from the eigenfunction, $h_{1\mathrm{I}}(r)$, where the derivatives with respect to r are calculated numerically using a finite difference approximation. In § 4.1.3 we discussed the form of the velocity components given that the eigenfunction is of the form $h_1(r) = k_m r^m$ close to $r = 0$, giving

$$u_1(r,z) = k_m\left(\frac{z^2}{2} - h_0 z - \frac{\alpha}{3}\right)mGr^{m-1}, \tag{7.2.6}$$

$$v_1(r,z) = k_m\left(\frac{z^2}{2} - h_0 z - \frac{\alpha}{3}\right)\mathrm{i}mGr^{m-1}, \tag{7.2.7}$$

$$w_1(r,z) = k_m\frac{z^2}{2}mGr^m, \tag{7.2.8}$$

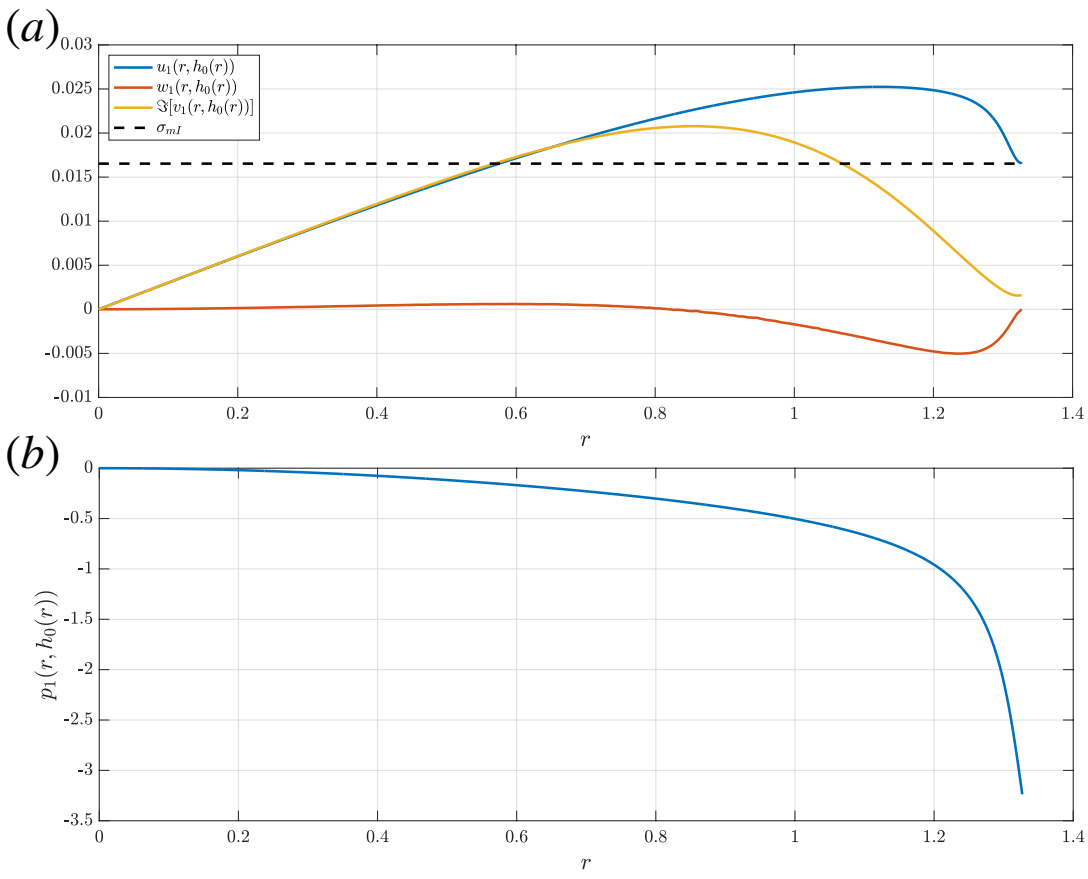


FIGURE 7.2: (a) Velocity and (b) pressure perturbations of the thin film problem (I) for $m = 2$, $\phi_{\mathrm{I}} = 2, G_{\mathrm{I}} = 10$ and $\alpha = 1 \times 10^{-3}$. The velocity and pressure are constructed using the eigenfunction, h_1, which is a solution of the eigenvalue problem (5.2.6). Figure (a) also shows the corresponding eigenvalue of (5.2.6).

where the axial equation has been simplified using $h_0'(r) \sim r$ when $r \ll 1$. Therefore, for each non-axisymmetric mode the axial velocity at the origin is zero, and for each mode $m = 2, 3, 4, \ldots$ all three velocity components are zero at the origin. The corresponding pressure close to the origin is

$$p_1(r, z) = k_m G r^m. \tag{7.2.9}$$

Figure 7.2 (a) shows the thin film velocity components when $\phi_{\mathrm{I}} = 2$, $G_I = 10$, $\alpha_{\mathrm{I}} = 1 \times 10^{-3}$ and $m = 2$, constructed from the eigenfunction, h_1, using (7.2.2)–(7.2.4). The real part of the radial and axial velocities and the imaginary part of the azimuthal velocity are shown, with the corresponding other parts being zero. First we observe that the velocity at the origin is zero, as expected for solutions

with $m = 2, 3, 4, ...$, satisfying the velocity regularity condition (3.1.12).

The axial velocity at the contact line, $w_{1\mathrm{I}}(R_0, 0)$, is zero satisfying the no-penetration condition (3.1.6). Furthermore, the effect of the slip is demonstrated since both the radial and azimuthal velocities are non-zero at the contact line. The eigenvalue, $\sigma_{m\mathrm{I}}$, is also shown in figure (7.2) with a black dashed line and meets $u_{1\mathrm{I}}$ at the contact line, demonstrating that the contact line kinematic condition (4.1.16) is satisfied. We see that close to the origin both the radial and azimuthal velocities are approximately linear, consistent with the r^{m-1} behaviour predicted by (7.2.6, 7.2.7). Although not clearly visible on the figure 7.2 (a) the axial velocity component also performs as predicted by (7.2.8). Figure 7.2 (b) shows the $O(\epsilon)$ pressure, $p_{1\mathrm{I}}(r)$, for the same case, constructed using (7.2.1). The pressure close to the origin is quadratic, in agreement with (7.2.9). Note that, in each of these figures the axes are nondimensionalised using the contact angle as a small lubrication parameter.

7.2.2 Verification of implementation

In § 6.3.2 we described how the $\mathcal{O}(1)$ contact angle model is nondimensionalised differently to the previously discussed thin film models and therefore transformations are required between quantities in each nondimensional space. The transformations for each variable are derived in appendix C, where each variable of the thin film model is denoted with subscript I, while those of the $O(1)$ contact angle model are denoted with subscript II.

The weak form (7.1.33) of the perturbation equations of motion (7.1.4)–(7.1.7) subject to appropriate boundary conditions was derived in § 7.1.3. Subsequently, we described how the method used to find the growth rate, $\sigma_{m\mathrm{II}}$, relies on knowledge of the perturbed free surface, $h_{1\mathrm{II}}(r)$. In the thin film limit, when the contact angle, $\theta_c \ll 1$, we have solutions for each velocity component (7.2.2)–(7.2.4), and the pressure (7.2.1). The thin film velocity components and pressure are functions of the perturbed free surface, $h_{1\mathrm{I}}(r)$, which we previously the solved an eigenvalue problem (5.2.6) to find. Therefore, to verify the finite element implementation described in § 7.1 we consider systems where the contact angle is small, comparing the numerical velocity and pressure to the analytical thin film solutions for each test functions (7.1.41) following appropriate transformation.

Specifically, given a set of nondimensional parameters, ϕ_{I}, G_{I}, and α_{I} we choose a small contact angle, $\theta_c \ll 1$, and calculate the corresponding parameters ϕ_{II}, G_{II} using (C.0.2). We use these parameters and the small contact angle to solve for the equilibrium free surface shape, $h_{0\mathrm{II}}$, producing a mesh from the solution. Next, using the method described in § 7.1.4 we assemble a set of Bessel functions, calculating the curvature (7.1.44) of each one and subsequently solving the problem described by the weak formulation (7.1.33). To ensure solutions are comparable to those in the thin film limit we again use the Greenspan slip function [31], so that

$$s(h_{0\mathrm{II}}) = \frac{\alpha_{\mathrm{II}}}{3h_{0\mathrm{I}}}. \tag{7.2.10}$$

Comparable thin film solutions are found by transforming each test function so that $f_{(m,n)\mathrm{I}} = \theta_c^{-2/3} f_{(m,n)\mathrm{II}}$, and analytically calculating the velocity components and pressure (7.2.1)–(7.2.4) for each (m, n) combination using each transformed solution in place of $h_{1\mathrm{I}}$.

Figure 7.3 shows the transformed real part of the radial and axial velocities and the imaginary part of the azimuthal velocity on the equilibrium free surface, $z = h_0(r)$ using transformation in appendix C. These solutions are found using the finite element method described above and each component is plotted with a solid coloured line. We apply the transformations (C.0.10) to the radial and azimuthal velocity components, (C.0.11) for the axial velocity component and (C.0.5) for the radial coordinate, r_{II}, so that solutions reside in the same nondimensional space as the thin film solutions. We present solutions within this space since it allows each velocity solution to be presented on the same figure; we know from the axial velocity transformation that w_{II} will be an order of magnitude smaller than the radial and azimuthal velocities and therefore would not be discernible within the nondimensional space of model II.

Each column in figure 7.3 corresponds to the first four non-axisymmetric wavenumbers, $m = 1, 2, 3, 4$ while each row is given by the Bessel modes, $n = 0, 1, 2$. The thin film velocity, $\boldsymbol{u}_{\mathrm{I}}$ given by (7.2.2)–(7.2.4), for transformed free surface perturbation, $f_{(m,n)\mathrm{I}} = \theta_c^{-2/3} f_{(m,n)\mathrm{II}}$, is also shown in each figure in various dashed black lines. The parameters used to produce 7.3 where $\phi_{\mathrm{I}} = 2$, $G_{\mathrm{I}} = 10$, with contact angle $\theta_c = 0.04$, which corresponds to $\phi_{\mathrm{II}} = 3.2 \times 10^{-3}$, $G_{\mathrm{II}} = 1.17$. The finite element mesh has uniform element size, meaning no refinement was used,

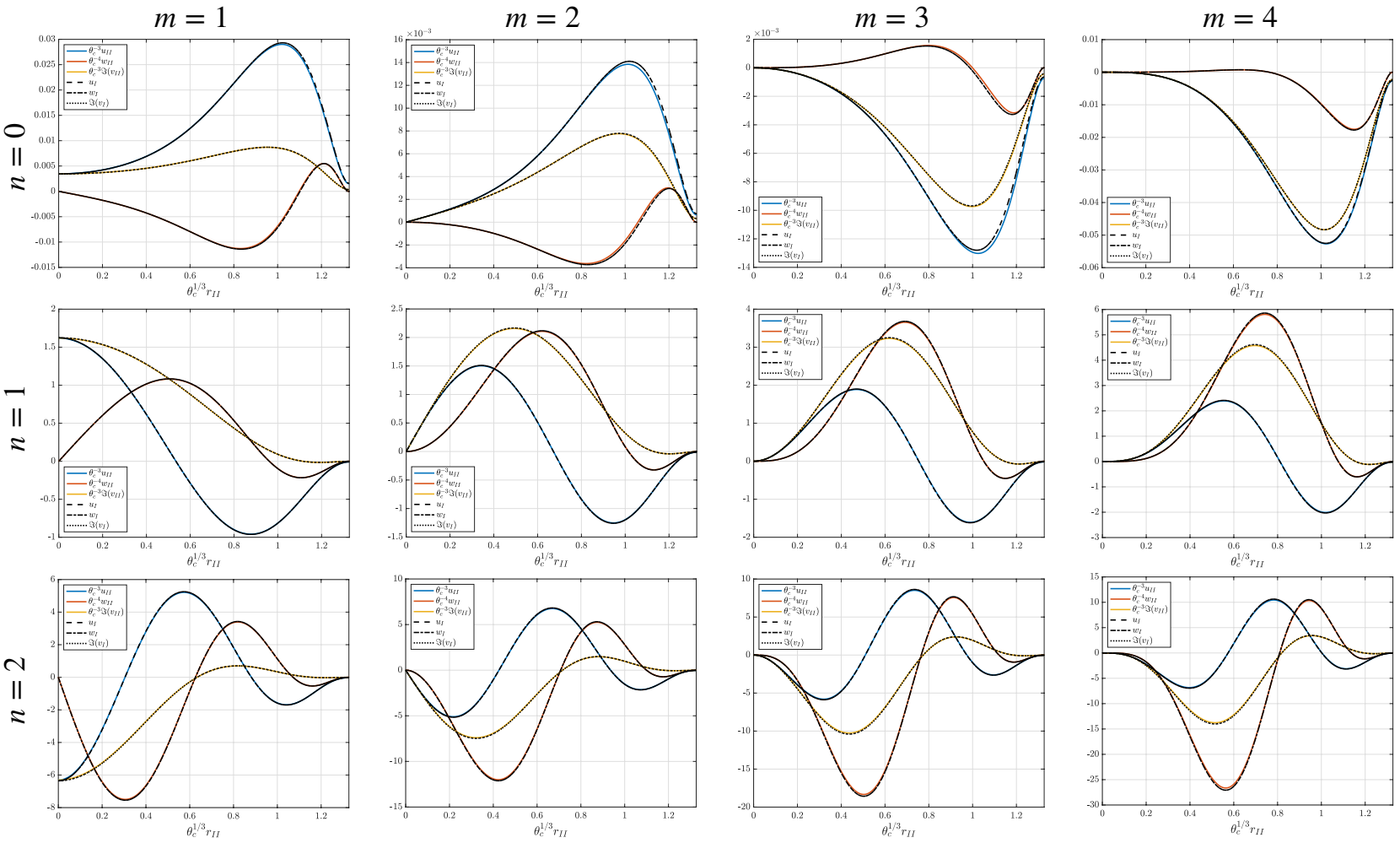


Figure 7.3: Comparison between the transformed numerical velocity components from the finite element implementation, $\boldsymbol{u}_{\mathrm{II}}$, and the thin film velocity (7.2.2)–(7.2.4) for the first four non-axisymmetric wavenumbers and first three Fourier–Bessel modes. Note that, the thin film velocities are constructed using the transformed test function $f_{(m,n)\mathrm{I}} = \theta_c^{-2/3} f_{(m,n)\mathrm{II}}$. Each plot was produced using $\theta_c = 0.04$, $\phi_{\mathrm{I}} = 2$, and $G = 10$.

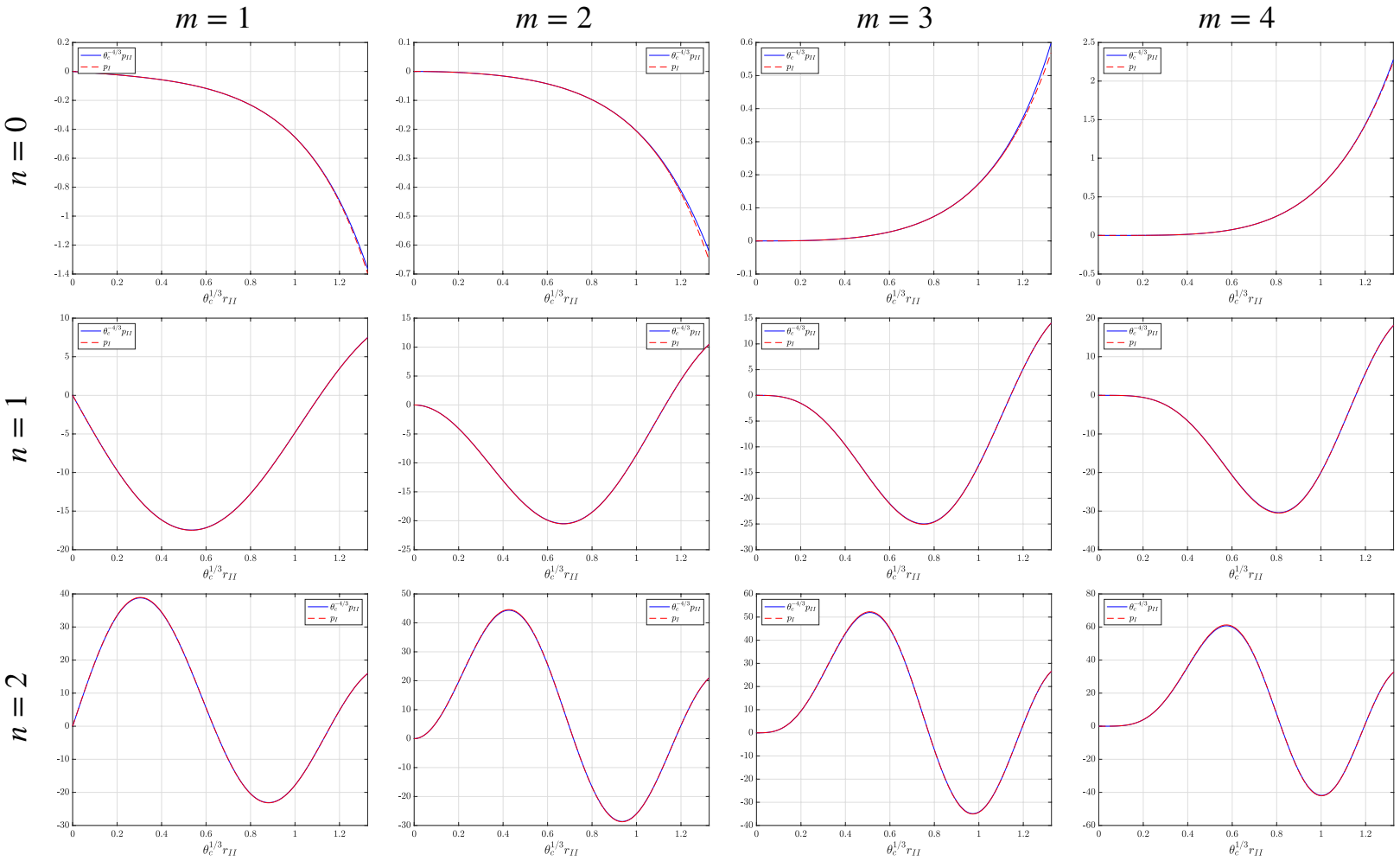


Figure 7.4: Comparison between the transformed numerical pressure p_{II} and the thin film velocity (7.2.1) for the first four non-axisymmetric wavenumbers and first three Fourier–Bessel modes. Each pressure function corresponds to the same case as figure 7.3, were $\theta_c = 0.04$, $\phi_{\mathrm{I}} = 2$, and $G = 10$.

and had $N = 9254$ elements. Due to the contact angle being small, the maximum height of the free surface is $h_{0\mathrm{II}} \approx 0.029$, and the resultant the maximum velocity magnitude on the free surface is $|\boldsymbol{u}_{\mathrm{II}}| = \mathcal{O}(10^{-6})$ when $n = 0$. Nevertheless, figure 7.3 shows that the agreement between the agreement between the transformed numerical velocity solutions and thin film velocity (7.2.2)–(7.2.4) is good.

The functions $f_{(m,n)}$ were constructed from Bessel functions to satisfy both the velocity regularity condition (7.1.19) and the combined contact angle condition (7.1.15). When $m = 1$, in the first column of figures, we observe that the radial and azimuthal velocity components, u_1 and v_1, at the origin are non-zero for each Bessel mode, while the axial velocity, w_1, at $r = 0$ is zero with the non-zero slope. Conversely, when $m = 2, 3, 4, ...$ each velocity component is zero at the origin and furthermore $w_r = 0$ in each of these cases. Specifically, we see the behaviour predicted by the asymptotic solutions (7.2.6)–(7.2.8) whereby the radial and azimuthal velocities look like r^{m-1} close to the origin, while the axial velocity behaves like r^m for each Bessel mode, n. Therefore, in each case the velocity is regular at the origin.

The above observations are physically consistent and could be anticipated by considering the shape of each perturbation visualised in figure 4.1. The centre of mass of perturbations $m = 2, 3, 4, ...$ lies exactly on the axis of rotation, $r = 0$. Therefore the radial and azimuthal velocities must be zero at the origin. Furthermore, in these cases the axial velocity must have zero slope to ensure w_1 is differentiable at the origin. Conversely, an $m = 1$ perturbation is a translation of the centre of mass away from centre of rotation meaning radial and azimuthal velocities can be induced at $r = 0$. Furthermore, for the same reason the axial velocity need not have zero slope at the origin in this case.

In each case within figure 7.9, the axial velocity at the contact line $r = R_0$, is zero, satisfying the no-penetration condition (6.1.4). The radial and azimuthal velocities at the contact line are non-zero due to the slip conditions (6.1.2), most visible in the first row of figures where $n = 0$. We see that for the chosen parameters a positive radial velocity at the contact line is induced when $n = 0$ and $m = 1, 2$, meaning these are the only two unstable configurations. Each other figure shows that the radial contact line velocity is negative and therefore the configuration is stable. The neutral stability curves shown in Figure 4.3 show that $m = 1$ and

Contact angle	δ	N
0.010	0.00406	10003
0.022	0.00437	9933
0.048	0.00501	9999
0.105	0.00562	10016
0.229	0.00630	10044
0.500	0.00715	10027

Table 7.1: Contact angle, θ_c, target element size, δ and resultant number of elements, N, used to produce figure 7.5.

$m = 2$ are indeed the only two unstable configurations within the thin film limit.

Figure 7.4 shows the comparison between thin film pressure solutions (7.2.1), and the transformed numerical solution along the free surface, $h_0(r)$, for wavenumbers $m = 1, 2, 3, 4$ and the Bessel modes, $n = 0, 1, 2$. Each figure corresponds to the velocity plot on the same row and column in figure 7.3. Again we observe good agreement between the small contact angle limit and the full model with a small contact angle. Furthermore, note that the asymptotic behaviour (7.2.9) that $p_1 \propto r^m$ when $r \ll 1$ is demonstrated for each Bessel mode with wavenumber m. This can be best seen in the column where $m = 1$, where the pressure demonstrates linear behaviour when r is small.

We stated above that the two cases which have positive radial contact line velocity, and are therefore unstable, are when $n = 0$, $m = 1, 2$. Note that, in these cases the free surface pressure is qualitatively different, such that a negative pressure is induced at the contact line. In other cases, when $n = 0$, $m = 3, 4, ...$ the pressure at the contact line is positive. The opposing signs of the pressure and radial velocity at the contact line is demonstrated by the solution within the thin film limit, where we see from (7.2.1, 7.2.2) that

$$u_{1\mathrm{I}}(R_0, 0) = -\frac{\alpha_{\mathrm{I}}}{3}\frac{\mathrm{d}p_{1\mathrm{I}}}{\mathrm{d}r}\bigg|_{r=R_0}. \tag{7.2.11}$$

Therefore, positive contact line velocities induce negative pressure gradients at the contact line.

The thin film model (I) is derived under the assumption that the fixed contact

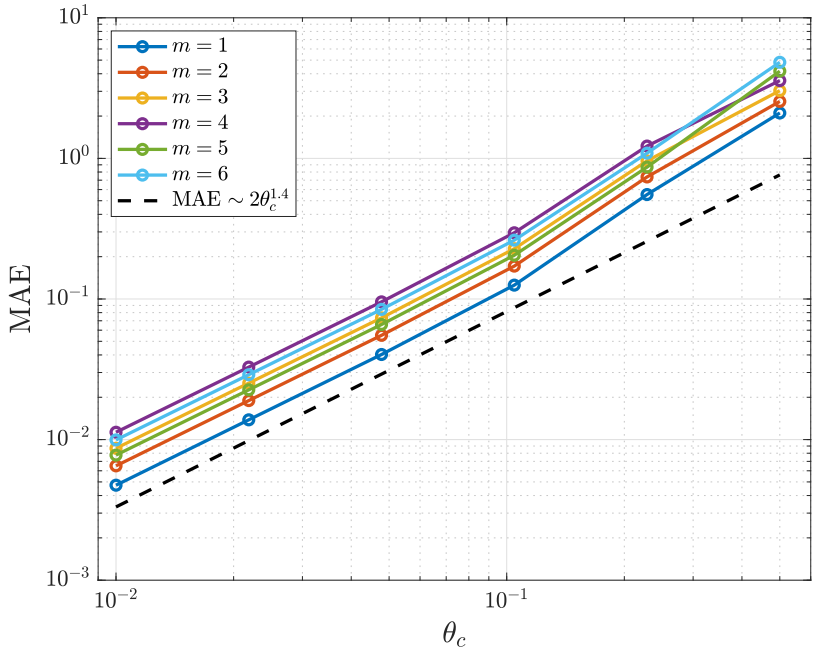


Figure 7.5: Mean average error of the first six non-axisymmetric wavenumbers $m = 1, 2, ..., 6$ against the contact angle, θ_c. The case presented is for $\phi_{\mathrm{I}} = 2$, $G_{\mathrm{I}} = 10$.

angle is small and so we expect that the error between solutions will decrease as the contact angle decreases. The mean absolute error (MAE) over the first seven Bessel modes is defined as

$$\mathrm{MAE} = \frac{1}{7}\sum_{n=0}^{6} \left|\sigma_{\mathrm{I}(m,n)} - \theta_c^{-3}\sigma_{\mathrm{II}(m,n)}\right|, \tag{7.2.12}$$

for each wavenumber, m. The growth rates, $\sigma_{(m,n)}$, are defined as the radial contact line velocity (7.1.45) of their respective solution, whether it be from (I) thin film model (7.2.2) or (II) the full numerical solution. The growth rate, $\sigma_{(m,n)\mathrm{II}}$ has been transformed using the radial velocity scaling (C.0.10). It is important to remember that $\sigma_{\mathrm{I}(m,n)}$ comes from substituting the normalised functions (7.1.41) into the expression for the thin film radial velocity (7.2.3) and are not solutions of the eigenvalue problem (5.2.6).

Figure 7.5 shows the MAE as the contact angle is varied for each wavenumber, $m = 1, 2, ..., 6$. The parameters used in each plot are $\phi_{\mathrm{I}} = 2$, $G_{\mathrm{I}} = 10$, which are transformed according to (C.0.2) and a mesh produced at each contact angle. The resolution of each mesh, δ, is constant so that no refinement is used, and is

optimised so that the number of elements is as close to $N = 1 \times 10^4$ as possible. Table 7.1 shows the resolution and subsequent number of elements, N, for each contact angle used to produce figure 7.5. We see that, as anticipated, the MAE reduces with contact angle for each wavenumber. The convergence is linear on logarithmic axes in the range $\theta_c \in [10^{-2}, 10^{-1}]$, with exponent $n = 1.4$. Therefore, in this region MAE $\propto \theta_c^{1.4}$ for each wavenumber. Note that this rate of convergence is lower than that of the equilibrium solutions, where in § 6.3.2 we determined that solutions converge like θ_c^2. The convergence rate of numerical solutions may be limited by the convergence of the finite element solutions themselves.

Overall, we have shown that the numerical method described in § 7.1 recovers the analytical thin film solutions (7.2.1)–(7.2.4), when given the same function, $f_{(m,n)}$, in replacement of h_1, showing good agreement for sufficiently small contact angles. Therefore, we have demonstrated that numerical solution of the system the equations and boundary conditions has been correctly implemented.

7.2.3 Comparison of eigensolutions

In the thin film limit we found numerical solutions to the eigenvalue equation (5.2.6), returning the eigenfunction h_{1e}, and the eigenvalue σ_e. The subscript 'e' denotes solutions of the eigenvalue equation (5.2.6).

The functions $f_{(m,n)}$ (7.1.41) are constructed to satisfy the boundary conditions imposed on the free surface perturbation h_1, and sum to give h_1 (7.1.42) . However, the coefficient of each term in the series $k_{(m,n)}$ is unknown in general. We saw in figure 7.1 that the first non-zero function in the sum (7.1.42) is monotonic. Specifically, if $m + R_0 \cot(\theta_c) h_0''(R_0) < 0$ then the only monotonic function is given by $n = 0$, whereas if $m + R_0 \cot(\theta_c) h_0''(R_0) > 0$ the only monotonic functions is given by $n = 1$. In § 4.4 we discussed the shape of the eigenfunction, h_{1e}, shown in figure 4.4, which are also monotonic. Although figure 4.4 is for the solutions to a similar problem where the contact angle is modelled with the Tanner law, the eigenfunctions when the fixed contact angle is imposed compare qualitatively. Therefore, when the contact angle is small we can compare the first non-zero function in the sum (7.1.42) to the eigenfunction, h_{1e}, of the eigenvalue equation (5.2.6), following transformation using the contact angle.

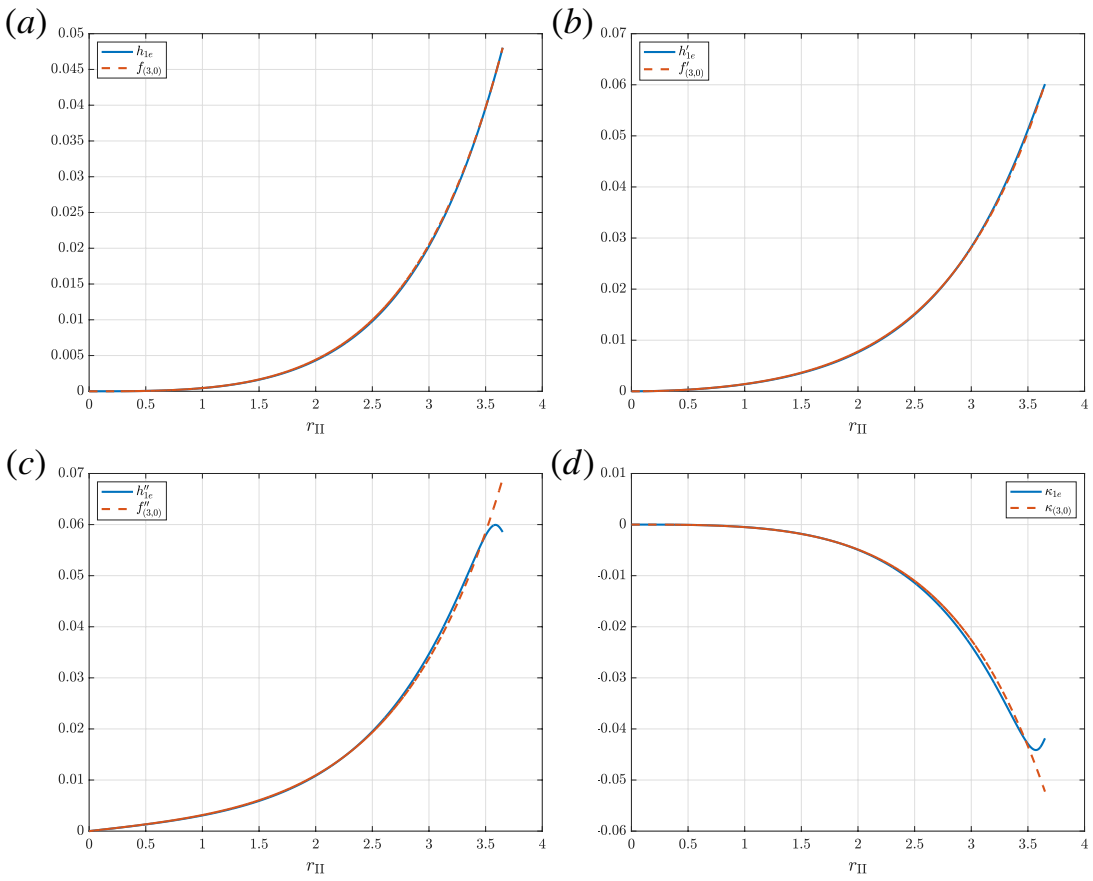


Figure 7.6: (a) Comparison of the first non-zero function in the sum (7.1.42) and the transformed solution of the eigenvalue problem (5.2.6). The remaining figures show the comparison between the (b) first derivatives, (c) second derivatives and (d) curvature (7.1.12) of the same functions. Each figure is for the case where $\phi_{\mathrm{I}} = 2$, $G_{\mathrm{I}} = 10$, $m = 3$ and $\theta_c = 0.048$.

Figure 7.6 (a) shows the comparison between the first nonzero term in the sum (7.1.42) and the transformed eigenfunction when $\phi_{\mathrm{I}} = 2$, $G_{\mathrm{I}} = 10$, $m = 3$ and $\theta_c = 0.048$. When the first nonzero function is transformed according to (C.0.7), the agreement between the numerical solution, h_{1e}, and the function constructed purely from the boundary conditions, $f_{(3,0)}$, is good. Figures 7.6 (b, c) show the comparison of the first and second derivatives of the same functions. The derivatives of h_{1e} are calculated numerically using a finite difference scheme, whereas the derivatives of the function, $f_{(3,0)}$, are performed analytically. We also observe good agreement between the first derivatives, shown in figure 7.6 (b). It is expected that the functions and their first derivatives will agree well at the contact line due to the Robin boundary condition (7.1.15) being satisfied in each case. Also, qualitative agreement at the origin is expected by construction, however the

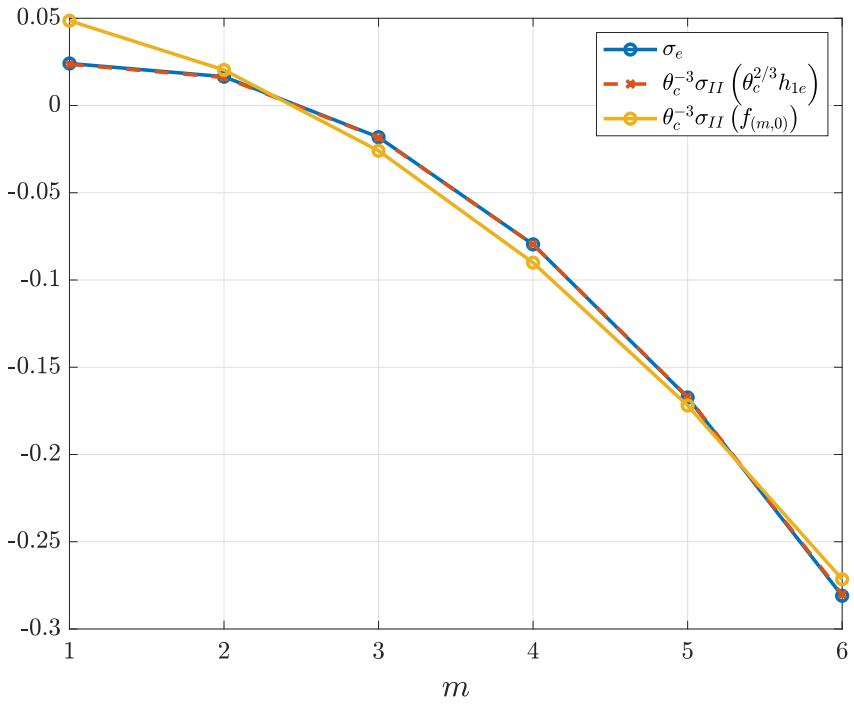


Figure 7.7: Comparison of thin film eigenvalue σ_{me} (blue) to transformed numerical growth rate for Bessel mode $n = 0$ (yellow), where $\phi_{\mathrm{I}} = 2$, $G = 10$, $\alpha_I = 1 \times 10^{-3}$ and $\theta_c = 0.048$, for the first six non-axisymmetric wavenumbers, m. Also shown is the transformed growth rate, having used the transformed eigenfunction, $\theta_c^{2/3} h_{1e}$, in place of $f_{(m,n)}$ (red).

overall level of agreement in figures 7.6 (a, b) is surprising. The second derivatives agree well when $r_{\mathrm{II}} < 3.5$ but diverge from one another close to the contact line at $r_{\mathrm{II}} = R_0 = 3.65$. Near the origin the behaviour of each function is linear, consistent with the second derivative of r^m when $m = 3$. Figure 7.6 (d) compares the curvature (7.1.44) of $f_{(3,0)}$ to the $\mathcal{O}(\epsilon)$ curvature within the thin film limit, given by $\kappa_{1e} = \mathcal{L}_1(h_{1e})$, where $\mathcal{L}_1$ is given by (7.2.5). There is also error within the $\mathcal{O}(\epsilon)$ curvature of the free surface close to the contact line, caused by differences between the second derivatives of each function, which in turn will lead to error within the velocity at the contact line and therefore the growth rate.

Next, we can compare the resultant growth rates and assessing how the difference in $\mathcal{O}(\epsilon)$ curvature indicated in figure 7.6 (d) manifests in the velocity at the contact line. Figure 7.7 shows the eigenvalues of (5.2.6) against wavenumber for the same case where $\phi_{\mathrm{I}} = 2$, $G_{\mathrm{I}} = 10$, shown in blue. Also shown are the numerical growth rates corresponding to the first non-zero function $f_{(m,n)}$ has been used as the free

surface perturbation, shown in yellow. For the case considered the contact angle is $\theta_c = 0.048$ so that $R_0 \cot(\theta_c) h_0''(R_0) = -4.58$. Therefore, for $m = 1, 2, 3, 4$ the $n = 0$ mode is used to calculate the velocity and subsequently the growth rate. Whereas, for $m = 5, 6, ...$ we used $n = 1$, since there are no real roots to (7.1.39) in this case. Given these functions, the numerical growth rates, σ_{II}, are transformed using (C.0.17) so that solutions in the same nondimensional space as the thin film growth rates, σ_e, and therefore comparable. We see that solutions using the first terms of the Fourier–Bessel sum compare well to the thin film numerical solutions both qualitatively and quantitatively. The error in the solution is due to the difference in $\mathcal{O}(\epsilon)$ curvature, which in turn is due to the difference in the second derivatives between h_{1e} and $f_{(m,n)}$, demonstrated in figures 7.6 (c, d).

We construct Bessel functions which satisfy the boundary conditions since the perturbed free surface shape, h_1, is unknown. Within the thin film limit, the eigenfunction, h_{1e}, is known and so we can test our implementation in a different way, by transforming this function according to (C.0.7), and using it to solve the full equations in our finite element implementation. The eigenfunction, h_{1e}, is itself an approximation since it is derived neglecting $\mathcal{O}(\theta_c^2)$ terms, however we mitigate this error by considering a case where the contact angle is small. Figure 7.7 also shows the numerical growth rates where the transformed eigenfunction $\theta_c^{2/3} h_{1e}$ has been used to solve for the velocity and pressure, shown with a dashed red line. We observe that the agreement is good, verifying that the finite element implementation can recover the correct growth rates when given the correct free surface perturbation, h_{1e}. In the case presented, the sum of the percentage error over the first six wavenumbers is 0.24%.

Overall, to further verify our numerical method when the contact angle is not necessarily small, we compared the growth rates to results from the thin film model previously studied. We found that when the contact angle is small the first non-zero function in the constructed sum (7.1.42) compares well to the eigenfunction, h_{1e}, which arises from solving the eigenvalue equation (5.2.6) within the thin film limit. Furthermore, we showed that constructed monotonic function, $f_{(m,n)}$, produces growth rates which agree well with the eigenvalues, σ_e, of (5.2.6) when the contact angle is small following appropriate transformations. Finally, using the transformed eigenfunction we showed that the finite element method produces growth rates comparable to the eigenvalues with a small percentage error.

7.3 Linear stability results

We now consider results of the linear stability of non-axisymmetric perturbations to the equilibrium solutions defined in § 6.3, where the contact angle is $\mathcal{O}(1)$. In this section we solely consider quantities in the nondimensional space of the $\mathcal{O}(1)$ contact angle model (II) and so drop the subscripts hereafter.

In § 7.2.3 we discussed how the first non-zero function, $f_{(m,n)}$, in the Fourier–Bessel series (7.1.42) is monotonic and occurs for $n = 0$ or $n = 1$, depending on the sign of $m + R_0 \cot(\theta_c) h_0''(R_0)$. We saw that this monotonic function compares well to the eigensolutions when the contact angle is small, subsequently returning growth rates which also compare well (see figure 7.7). Therefore, in this section we will only consider the monotonic function in the Fourier–Bessel series, assuming that it compares well to the eigenfunction when the contact angle is not small.

Figure 7.8 shows the numerical solution for the three velocity components and the pressure, on the mesh defined by the equilibrium solution for $\phi = 3.14$, $G = 10$, and $\theta_c = \pi/3$. The specific case presented is for $m = 3$ and $n = 0$, so that the free surface is perturbed by $f_{(3,0)}$. We take the slip function to be constant, $s(h_0) = \beta$, since the previously used Greenspan slip law is generally used where the film height is small. However, the results are qualitatively the same, whether the Navier or Greenspan slip laws are used. We have defined the instability of the system as whether the contact line advances or recedes in time, quantified by the radial contact line velocity, $u_1(R_0, 0)$. In figure 7.8 the radial velocity at the contact line is negative, indicated in blue, which in our definition means that the system is stable. However, there is a region of positive velocity above indicated in red, which may indicate that the method of instability is a rolling over the contact line, rather than the contact line itself moving. The azimuthal velocity, $v_1^\dagger(r, z)$, shown in figure 7.8 (b) is always positive, with maximum velocity on the free surface in the region $h_0'(r)$ changes sign. The axial velocity, $w_1(r, z)$, is shown in figure 7.8 (c). Immediately, we see that the no-penetration condition is satisfied, with zero velocity along $z = 0$. Similarly to the radial velocity there are regions of positive and negative axial velocity. Figure 7.8 (d) shows the pressure, which similarly to the radial velocity changes sign close to the contact line.

Next, we consider the behaviour of the solutions close to the axis of rotation, $r = 0$.

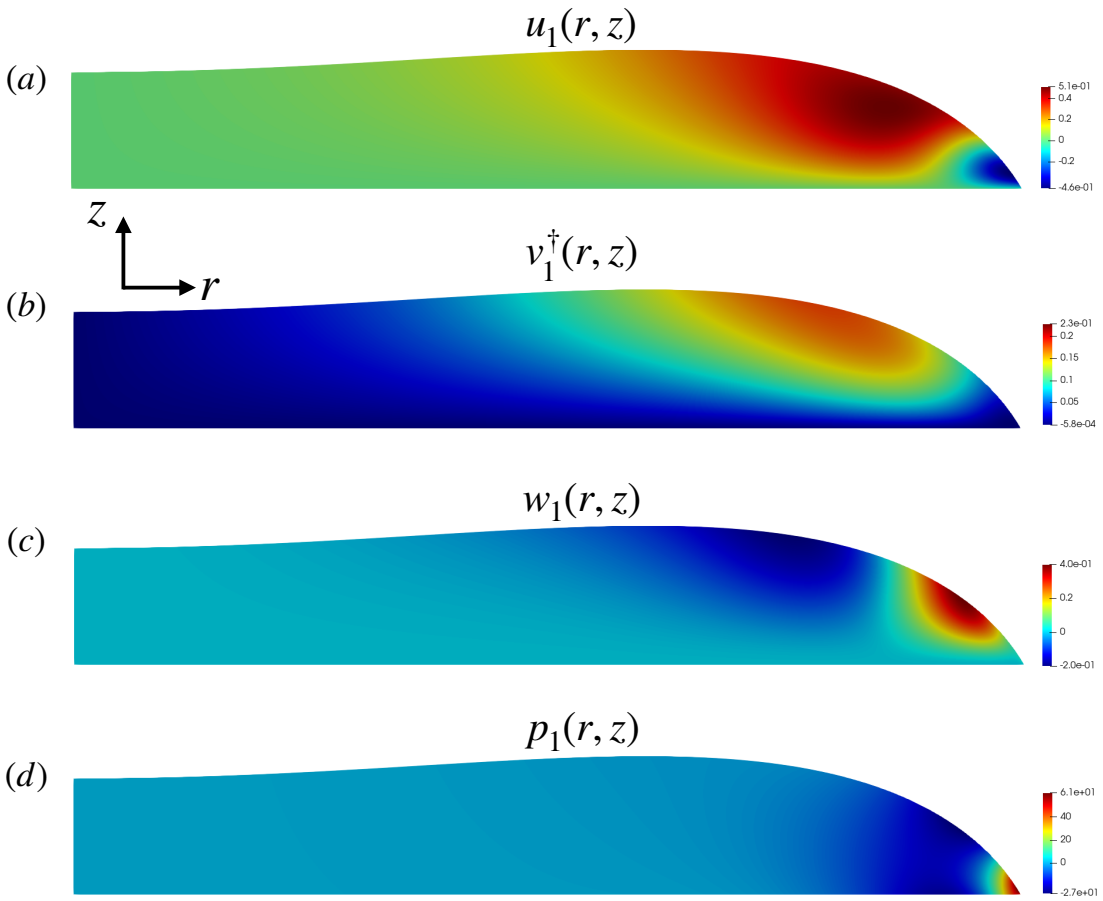


Figure 7.8: Solution for the velocity components and pressure on a mesh defined by the equilibrium solution when $\phi = 3.14$, $G = 10$, and $\theta_c = \pi/3$. The specific case presented is for $m = 3$, $n = 0$, so that the free surface is perturbed by $f_{(3,0)}$, while slip length is $\beta = 0.01$.

Figure 7.9 shows the three velocity components and the pressure along the free surface, $h_0(r)$, for the same equilibrium solution as in figure 7.8, where $\phi = 3.14$, $G = 10$, $\theta_c = \pi/3$. Figures 7.9 (a)–(d) show the solutions for wavenumbers $m = 1, 2, ..., 6$, plotted on logarithmic axes, demonstrating the behaviour close to the origin, $r = 0$. In this case $R_0 \cot(\theta_c) h_0''(R_0) = -24.3$, so that the $n = 0$ Bessel mode is the first non-zero function for each wavenumber shown. Figure 7.9 (a) shows the radial velocity, $u_1(r, z)$, and demonstrates the behaviour along the free surface near the origin. For each wavenumber, the radial velocity is linear on logarithmic axis with gradient of $m - 1$, demonstrated by the black dashed lines, meaning that the radial velocity behaves like r^{m-1} along the free surface, $h_0(r)$, close to the origin. Similarly, the azimuthal velocity, $v_1^\dagger(r, z) = \mathrm{i}v_1(r, z)$, shows the same behaviour in figure 7.9 (b) for each wavenumber. The axial velocity and pressure

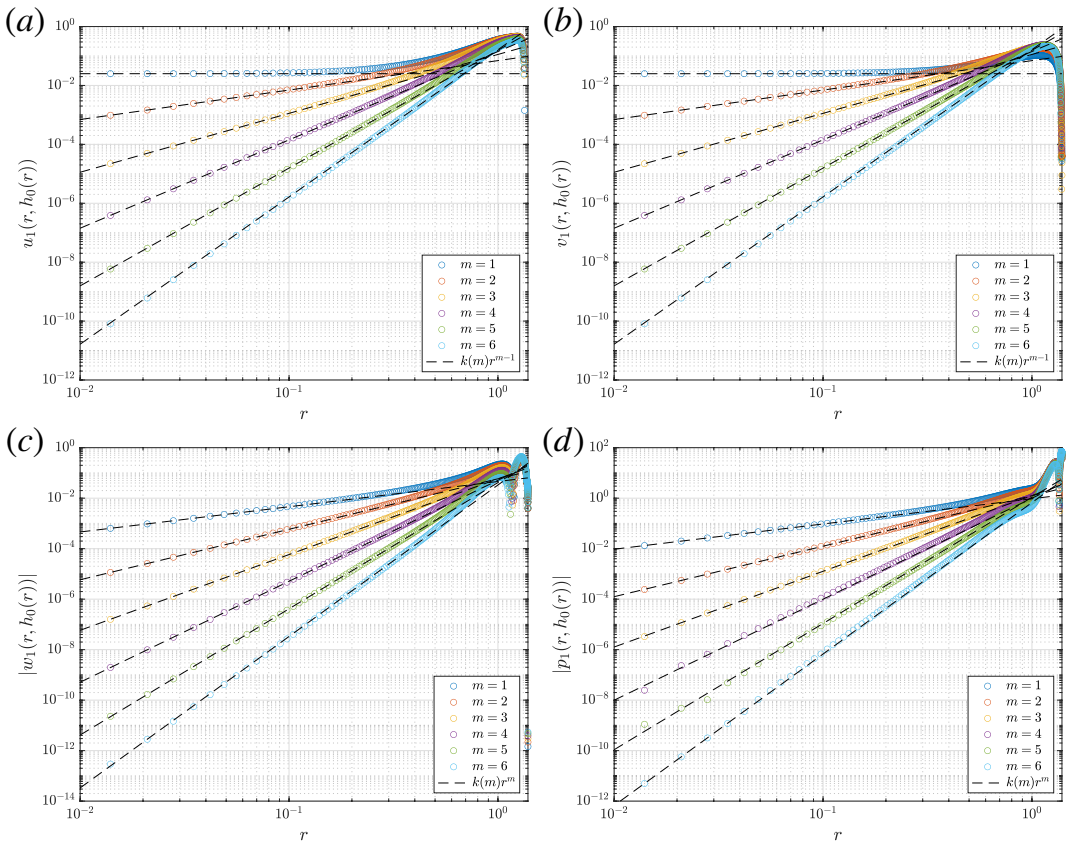


Figure 7.9: Behaviour of (a)–(c) velocity components and (d) pressure near the origin for the same nondimensional parameters used to produce figure 7.8, for each wavenumber $m = 1, 2, ..., 6$.

solutions shown in figures 7.9 (c, d) indicate that these quantities behave like r^m along the free surface and close to the origin. Therefore, the velocity is regular at the origin for each wavenumber, so that (7.1.19) is satisfied. Furthermore, we find that the behaviours for the velocity and pressure found within the thin film limit, given by (7.2.6)–(7.2.9) are retained when the contact angle is large.

In § 6.3 we discussed how for each contact angle, θ_c, and Bond number, G, there exists a range of nondimensional rotation rates, ϕ, for which equilibrium solutions exist. The minimum value is always $\phi = 0$, corresponding to no rotation, whereas the maximum ϕ_m is determined numerically using a golden search algorithm. However, we determined that similarly to in the thin film limit, there is a range $\phi_c \leqslant \phi < \phi_m$ for which multiple solutions for R_0 exist, indicated in figure 6.2. Therefore, the full range of solutions is given between the maximum value of R_0, which exists where $h_0(0) = 0$, and the minimum value of R_0, corresponding to

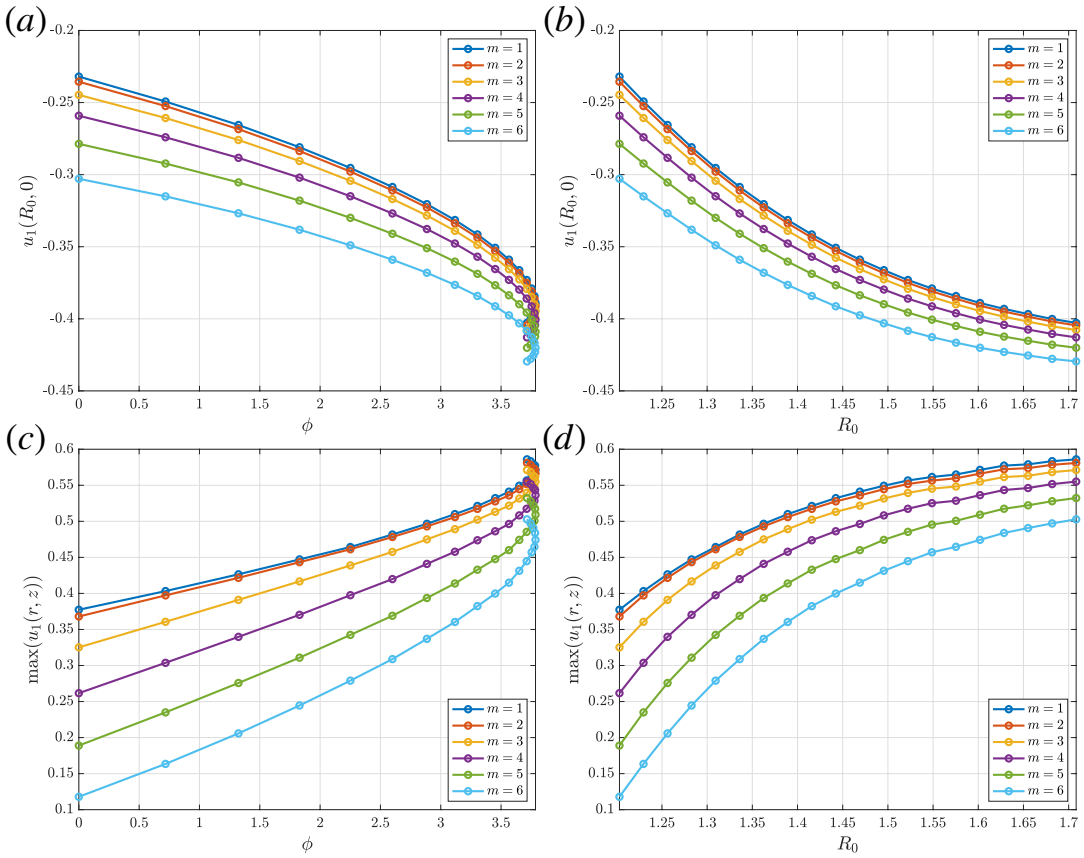


Figure 7.10: Solutions of (7.1.33) with Bond number, $G = 10$, contact angle, $\theta_c = \pi/3$, Navier slip length $\beta = 0.01$, and Bessel mode $n = 0$ for the first six non-axisymmetric wavenumbers. (a ,b) Show the radial contact line velocity as (a) the centrifugal number, ϕ, and (b) the resultant contact line position, R_0 are varied. Figures (c, d) show the maximum radial velocity as (c) ϕ, and (d) R_0 are varied.

where $\phi = 0$. Given a Bond number and a contact angle we can produce meshes between these maximum and minimum values, and for each one construct the first non-zero Bessel function in the series (7.1.42) given a wavenumber, m, and assessing the trend in the solutions.

Figure 7.10 (a, b) show the contact line velocity, $u(R_0, 0)$, plotted against (a) ϕ and (b) R_0 for the first six non-axisymmetric wavenumbers when $n = 0$. In this case a contact angle, $\theta_c = \pi/3$, and a Bond number $G = 0$ were used. For each centrifugal number, ϕ, the mesh is produced, optimising the number of elements to be approximately $N \approx 2000$ by using a target element size at $\delta \approx 0.02$. We impose Navier slip so that the slip function is constant $s(h_0) = \beta = 0.01$. In each figure 7.10 (a, b) we observe for each system the contact line velocity is negative, with greater wavenumbers having more negative velocities. In figure 7.10 (b),

where the contact line velocity is plotted as a function of R_0, each function is decreasing within the range of possible solutions. Therefore, under our definition of contact line instability, whereby the radial contact line must be positive, each solution is stable. Physically, larger values of ϕ correspond to greater rotation rates and therefore we would expect greater radial velocities as ϕ increases. The results shown in figure 7.10 (a, b) appear to contradict this. However, there is evidence to suggest that the method of instability is in fact a rolling of the ridge over the contact line. We can see this in figure 7.8 (a), which shows a region of positive velocity at the ridge. Rolling motion at the contact line is common when the contact angle is large in flows down an inclined plane [52]. Rolling of the contact line has also been observed experimentally in spin coating in both glycerol solutions [66] and silicon oils [61, 64] of various volumes.

To characterise how a rolling instability may occur we consider the maximum radial velocity induced by the monotonic function $f_{(m,n)}$, where $n = 0$ or $n = 1$. Figures 7.10 (c, d) show the maximum radial velocity as a function of (c) the centrifugal number, ϕ, and (d) the mean radius, R_0, for the same case as figures 7.10 (a, b). In figure 7.10 (c) we see that the maximum radial velocity increases with ϕ in the region $0 \leqslant \phi < \phi_c$ for each wavenumber, with greater velocities induced for $m = 1$. In the region where $\phi_c \leqslant \phi < \phi_m$ there exists multiple solutions, where the upper branch has larger R_0, and the resultant maximum radial velocities are greater. When the maximum radial velocity is plotted against R_0 in figure 7.10 (d), it increases for each wavenumber with the induced velocity decreasing as the wavenumber increases. The results are physically consistent when the maximum radial velocity is considered; larger rotation rates induce larger radial velocities.

We observe similar results when the Bond number, G, is varied. Figure 7.11 (a) shows the radial velocity at the contact line as a function of the Bond number, G, for contact angle, $\theta_c = \pi/3$, centrifugal number, $\phi = 2.4$, Bessel mode, $n = 0$, and wavenumbers $m = 1, 2, ..., 6$. We again use a Navier slip law where $s(h_0) = \beta$, where $\beta = 0.01$ and each mesh has approximately $N = 1 \times 10^4$ elements. Larger Bond numbers, corresponding to larger volumes, have more negative radial contact line velocities and are therefore more stable. The results are contrary to physical interpretation and dynamics observed experimentally in chapter 2, which suggest that larger volumes are have greater growth rates at the same rotation

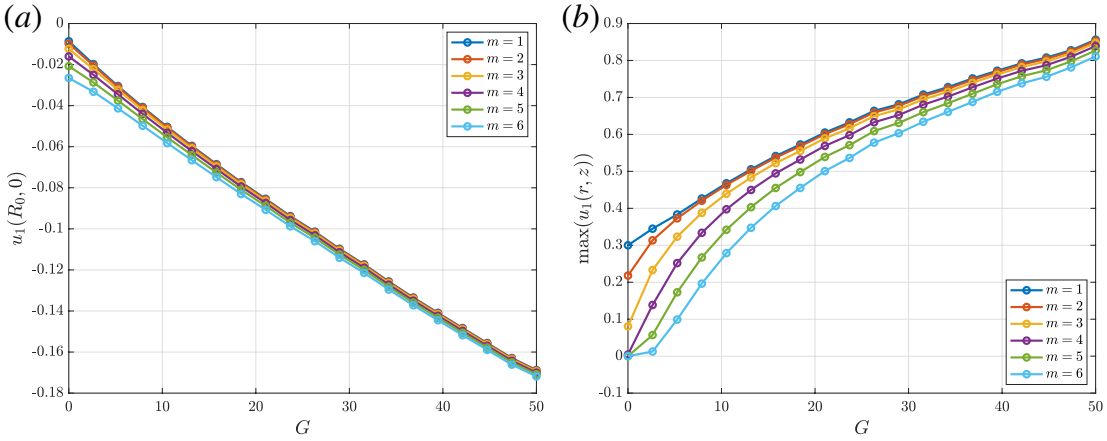


Figure 7.11: Solutions (7.1.33) with centrifugal number, $\phi = 2.4$, contact angle, $\theta_c = \pi/3$, Navier slip length $\beta = 0.01$, and Bessel mode $n = 0$ for the first six non-axisymmetric wavenumbers. (a) Shows the radial contact line velocity while (b) shows the maximum velocity within the domain as G is varied.

rate. However, the maximum radial velocity, shown in figure 7.11 (b), aligns with the physical interpretation of varying the Bond number, where we observe larger radial velocities as G is increased. In this case we observe at each G the greatest radial velocity is induced by an $m = 1$ perturbation, contrary to experimental observations. The maximum radial velocity of each mode decreases sequentially as the wavenumber is increased for fixed G.

When the contact angle is small, we observed the radial contact line velocity can be positive (see figure 7.3), with the interpretation that since the contact line can move radially outwards, it is linearly unstable. However, for large contact angles we observe that the radial velocity at the contact line is negative, as shown in figures 7.10 (a, b). Therefore, there must be a critical contact angle for which the sign of the radial velocity at the linearised contact line, $u_1(R_0, 0)$, changes sign. We consider solutions at the same point in nondimensional parameter space, where given the Bond number and contact angle the centrifugal number is maximum, ϕ_m. In the thin film limit, we saw that at this point in parameter space there are always unstable wavenumbers for any Bond number, shown in figures 5.3 (d)–(f).

Figure 7.12 shows scaled radial contact line velocity as a function of the contact angle for the first four non-axisymmetric wavenumbers, $m = 1, 2, 3, 4$, which are unstable when the contact angle is small. The Bond number and Bessel mode used are $G = 10$, $n = 0$, respectively, and each mesh has approximately $N = 1 \times 10^4$

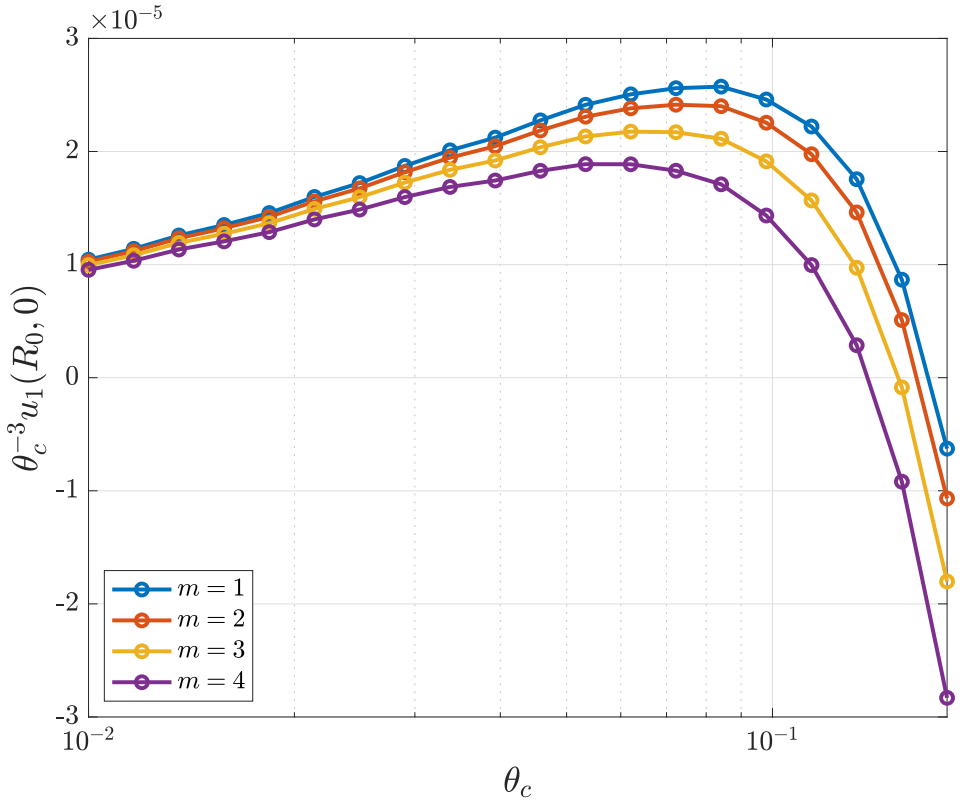


Figure 7.12: Scaled radial velocity as the contact angle is varied, for $G = 10$, and Greenspan slip length of $\alpha = 1 \times 10^{-3}$. Each data point was produced by finding the maximum ϕ given the contact angle, solving the weak formulation (7.1.33) on a mesh with approximately $N = 1 \times 10^4$ elements, when $n = 0$.

elements. It is important to note that in each case the Greenspan slip law has been used, so that $s(h_0) = \alpha/(3h_0)$, where $\alpha = 1 \times 10^{-3}$. For large contact angles the results are qualitatively similar to when the Navier slip law is used, but for small contact angles only the Greenspan slip law allows non-zero contact line velocities, discussed in § 5.1.2. The velocities are scaled with θ_c^{-3} so that the radial velocity is the same order of magnitude for each contact angle. We see that there is a change in sign for each mode at approximately $\theta_c = 0.15$, with all velocities beyond the crossing point being negative. The threshold is marginally different for each wavenumber, with $m = 1$ changing sign at the greatest contact angle, while $m = 4$ changing sign for the smallest contact angle. Therefore, a qualitative change in solutions occurs for contact angles larger than 0.15, where as discussed above the method of instability may transition to rolling over the contact line, rather than the contact line having positive radial velocity. When the contact

angle is larger than this threshold, the observations made of figure 7.10 are typical of any valid combination of ϕ and G.

Overall, our preliminary solutions indicate that the previous definition of the growth rate may be insufficient to capture what occurs when the contact angle is large. We determined it may be more appropriate to define the growth rate of the system as a function of the maximum radial velocity, due to the velocity solutions indicating rolling at the contact line. Further work is recommended to understand this. One method to do such could be to advect the mesh using the velocity flow, assessing how an initial perturbation grows in time. It is important to remember that the solutions presented in this chapter rely on the knowledge of the perturbation of the free surface before solving for the velocity and pressure fields. To circumvent this problem, we constructed a set of Bessel functions which satisfy the derived boundary conditions at $\mathcal{O}(\epsilon)$. To avoid this, it may be more appropriate to assemble the system of equations and boundary conditions into an eigenvalue problem for the free surface shape, h_1, and growth rate, σ_m, for a given wavenumber.

7.4 Summary

In this chapter we have discussed the linear stability of equilibrium solutions presented in § 6.3, subject to non-axisymmetric perturbations. The existing literature surrounding the fingering instability of rotating droplets, discussed in chapter 1, focuses on thin film solutions of the governing equations. Therefore, the linear stability analysis for large contact angles performed within this chapter is a novel contribution to the literature.

The equilibrium solutions, determined in § 6.3, were perturbed making a normal mode assumption, deriving the $\mathcal{O}(\epsilon)$ equations of motion and boundary conditions, where $\epsilon \ll 1$. The finite element analysis of the problem at leading order in ϵ, described in § 6.4, provided a basis from which the numerical method described in this chapter was developed for the $\mathcal{O}(\epsilon)$ equations and boundary conditions. We used a novel method of determining the linear stability, constructing the free surface perturbation, $h_1(r)$, to satisfy the $\mathcal{O}(\epsilon)$ boundary conditions using a Fourier-Bessel series, and solve the resultant weak formulation for the pressure

and velocity fields.

First, we considered configurations with small contact angles and compared the resultant velocity and pressure fields to the analytic solutions derived in the thin film limit. We saw that when the contact angle is small, and given the same function $f_{(m,n)}$, the agreement between the numerical and analytic solutions is good. To further verify our numerical method, we compare the growth rates from the first non-zero function in the Fourier–Bessel series (7.1.42) to results from the thin film model previously studied. Since the models are nondimensionalised differently, transformations exist between the cases, described in appendix C. The growth rates are calculated using the finite element method described above, and scaled with the contact angle, showing good agreement to the eigenvalues of (5.2.6) when the contact angle is small.

We discussed solutions where the contact angle is $\mathcal{O}(1)$, finding that the instability is characterised by rolling over the contact line, rather than outward movement of the contact line itself. To assess the size of the instability we consider the maximum radial velocity, showing this increases as the mean radius of the contact line, R_0, increases. Finally, we varied the contact angle to assess where the radial velocity at the contact line changes sign. This indicates the transition between an instability where the contact line moves radially outwards when the contact angle is small, and a rolling instability for larger contact angles.

Further work is recommended on this topic, suggested routes being advection of the boundary in time according to the velocity field, or solving the full eigenvalue problem rather than constructing the free surface perturbation, h_1, from Bessel functions.

Chapter 8

Comparison with experimental results and discussion

In § 2.1.2 we described the method of using Fourier analysis to extract information from video sequences data characterising the front instability of spun up drops of viscous fluid with different volumes at varying rotation rates. Specifically, we extracted the amplitude of each Fourier mode and assessed how each mode grows in a short time following spin-up, using a linear fitting to calculate the dimensional growth rates from the data.

Subsequently, we developed two models; the thin film model presented in chapters 3, 4 and 5, herein referred to as model I, and the $\mathcal{O}(1)$ contact angle model presented in chapters 6, 7, and referred to as model II. Both models assume that viscosity dominates, and therefore inertial terms are neglected due to the Reynolds number, Re, being sufficiently small.

In this chapter we compare aspects of each model to the experimental results presented in § 2.3.

8.1 Equilibrium solutions

In § 2.1.2 for a given image extracted from the recorded video file, we explained how to use Fourier analysis to find the mean radius of the contact line, a_0. We presented the results in § 2.3, considering both the stationary radii prior to the detection of any motion, and the spin-up radii when the disc reached the target

rotation rate.

Recall that for model I the equilibrium solutions are defined in terms of two nondimensional parameters, the nondimensional rotation rate, ϕ_{I}, named the centrifugal number, and the nondimensional measure of gravity to surface tension, G_{I}, the Bond number, repeated here

$$\phi_{\mathrm{I}} = \frac{\rho\Omega^2 V}{\gamma\theta_c^2}, \quad G_{\mathrm{I}} = \frac{\rho g V^{2/3}}{\gamma\theta_c^{2/3}}. \tag{8.1.1}$$

In model II, we no longer assume that the contact angle is small and as a result nondimensionalised the system of equations in an alternative way, described in § 6.2. The resultant nondimensional parameters, analogous to those in (8.1.1) are

$$\phi_{\mathrm{II}} = \frac{\rho\Omega^2 V}{\gamma}, \quad G_{\mathrm{I}} = \frac{\rho g V^{2/3}}{\gamma}. \tag{8.1.2}$$

Notice that in this latter case the contact angle, θ_c, does not appear in either nondimensional quantity, instead appearing in the boundary conditions. In each model the length is nondimensionalised by the volume of fluid, V. Typical experimental values of each physical quantity are listed in table 2.1. Subsequently, for each model we determined the nondimensional hydrostatic equilibrium solution shape, $h_0(r)$, and resultant nondimensional mean radius, R_0, and building a parameter space as each nondimensional parameter is varied, shown in figures 3.4 and 6.9. Recall that, to derive these equilibrium solutions, we assumed the system was at rest within the rotating frame of reference. The main result from the equilibrium analysis of each model is that for each Bond number there is a corresponding maximum centrifugal number, beyond which equilibrium solutions, that is those with zero velocity at leading order in ϵ, do not exist.

8.1.1 Stationary solution

Recall from § 2.3.2 that we determined the mean radius, a_0, of each experiment in the frames prior to spin-up, so that the initial condition of the experiments can be assessed. Specifically, we discussed how the size of the initial radius of the contact line varies for the same target volume. The results are presented in figure 2.8 (a), and reproduced in figures 8.1 (a, b), where we see that larger volume droplets have

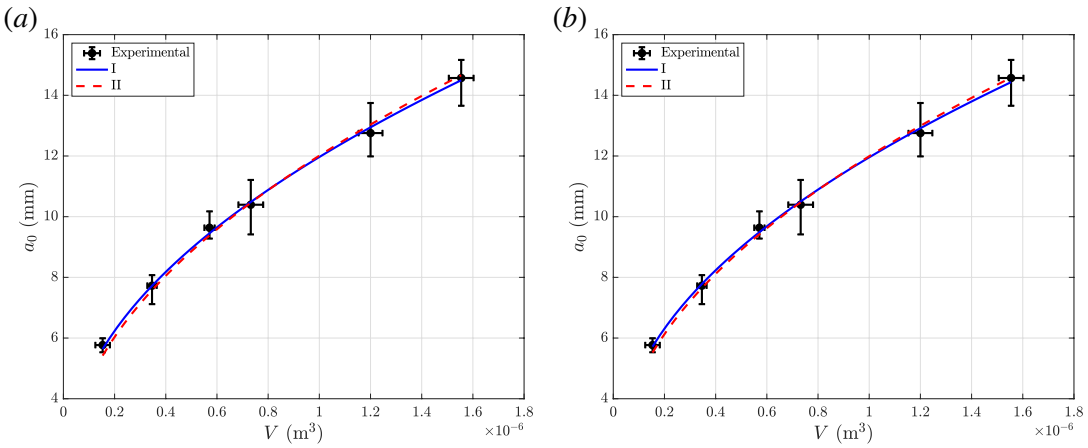


Figure 8.1: Comparison of mean fluid radius to both the thin film model I, and $\mathcal{O}(1)$ contact angle model II, when $\phi = 0$, where (a) the contact angle and (b) both the contact angle and surface tension coefficient are used as fitting parameters.

Model	Fitting parameters	θ_c (rad)	γ (kg s^{-2})	SS residuals (mm^2)
I	1 (θ_c)	1.342	0.0630	0.099
II	1 (θ_c)	1.318	0.0630	0.298
I	2 (θ_c, γ)	1.247	0.0797	0.083
II	2 (θ_c, γ)	1.213	0.0801	0.177

Table 8.1: Summary of parameters used to produce figure 8.1, and the resultant sum of squared (SS) residuals between the model predictions and the experimental data.

larger initial radii.

Since we are considering the radius of the fluid before any rotation has occurred, the rotation rate is $\Omega = 0$, and hence $\phi = 0$ in each model. We fit each model to the data using a nonlinear curve fitting method, using the contact angle, θ_c, as an adjustable parameter, whereas the value other physical quantities are taken from table 2.1. Figure 8.1 (a) shows the dimensional comparison between the experimental data and each model, where the model I is shown with a blue solid line, and model II shown with a red dashed line. We see good agreement for each model, and the resultant contact angle and corresponding sum of squared (SS) residuals are listed in the first two rows of table 8.1. We see that in both cases the contact angle is large with $\theta_c \approx 1.3$. It is therefore perhaps surprising how well the thin film model performs, since it is derived under the assumption of a small

contact angle.

The value for the surface tension, γ, reported in table 2.1 is for a pure glycerol solution, whereas the fluid used for the experiments is prepared using a small amount of dye, the surface tension of which is larger than glycerol. Therefore, it is likely that the overall surface tension is larger than the reported value, and γ is subsequently used as an extra fitting parameter to the data. The results are listed in the final two rows of table 8.1, where there are two fitting parameters and the comparison is plotted in figure 8.1 (b). We see that, as anticipated, in each case the fitted value of $\gamma \approx 0.080$ is larger than the previous table value of $\gamma = 0.063$, with a lower sum of squared residuals than the case where only the contact angle is fitted for each model, indicating better agreement. When both the surface tension coefficient and contact angle are fitted, we see in table 8.1 that the contact angle is approximately $0.1\,\text{rad} \approx 6\,^\circ$ lower than when only the contact angle is fitted.

In the modelling, we assumed the system is in equilibrium in order to find the base state. Before any rotation occurs this is a good assumption, and we see that the modelling reflects that, showing good agreement between both models and the experimental data.

8.1.2 Non-zero rotation

Recall that in each experiment, the time $t = 0$ is defined from the frame where the target rotation rate, Ω, is first achieved. The method for calculating where the target rotation rate is reached was detailed in § 2.3.2. The amplitude of the $m = 0$ Fourier mode at $t = 0$ is denoted R_0. Figure 2.8 (b) shows how R_0 varies with rotation rate and volume.

The data from the stationary comparison indicates that the surface tension is greater than the value reported as an estimated lower bound in table 2.1 for pure glycerol. Therefore, when fitting the models to the spin-up radius data the surface tension coefficient, γ, and the contact angle, θ_c, are used as fitting parameters, where again we use a nonlinear curve fitting algorithm. To account for variations in the preparation of fluid and atmospheric conditions between experimental sets, we determine the fitting parameters for each volume individually, as well as all

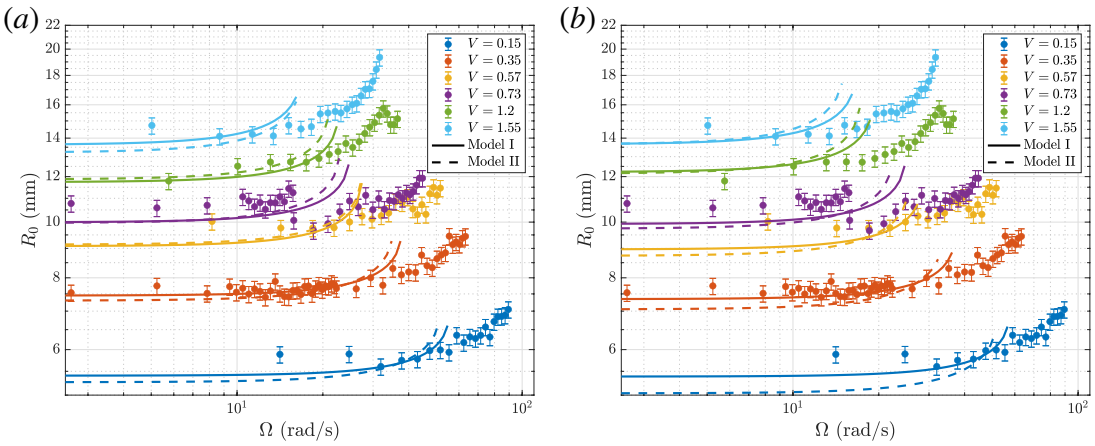


Figure 8.2: Comparison between the experimental spin-up radius and the prediction of the both models I and II, where (a) each experimental set is fitted individually, and (b) the data is fitted all together.

Figure 8.2 (a) shows prediction of both models against the data where each experimental set has been fitted individually. The prediction of models I and II are shown in solid and dashed lines, respectively, with colour corresponding to the appropriate volume. Figure 8.2 (b) shows the model predictions for a single contact angle and surface tension coefficient over all data sets. Immediately, we see in each figure that for each volume that both models are limited to a smaller range of rotation rates than the experimental data. This feature is expected, since we found in § 3.4 that for each Bond number, G, there is a maximum centrifugal number, ϕ, for which equilibrium solutions exist, corresponding to a maximum rotation rate. The values of the contact angle and the surface tension coefficient are reported in table 8.2, for each experimental set and model, along with the sum of squared residuals. The final row of the table shows the results when the data is fitted using all data points together, for each model corresponding the figure 8.2 (b). The residuals are calculated between the model and the data points which are lower than the maximum rotation rate the model predicts, and data points which are beyond this threshold are ignored.

The values of the contact angle for model I lie within a range of 0.11 rad, which is approximately 6 °, whereas for model II the resultant contact angles vary between 1.187 and 1.479, a difference of approximately 16 °. The surface tension coefficient varies more substantially in both cases, a suprising result given the fluid was

Volume (ml)	Model	θ_c (rad)	γ (kg s^{-2})	SS residuals (mm^2)
0.15	I	1.500	0.0635	0.403
	II	1.334	0.0805	0.610
0.35	I	1.396	0.0795	0.877
	II	1.290	0.0932	1.787
0.57	I	1.453	0.0674	1.103
	II	1.187	0.1105	1.113
0.73	I	1.449	0.0719	9.753
	II	1.328	0.0849	9.623
1.20	I	1.497	0.0925	0.993
	II	1.276	0.1250	1.427
1.55	I	1.501	0.0682	2.682
	II	1.479	0.0843	2.771
Overall	I	1.501	0.0673	20.095
	II	1.501	0.0677	28.371

Table 8.2: Summary of the parameters used to produce figures 8.2 (a, b), and the resultant sum of squared (SS) residuals between the model and experimental data.

prepared in the same way for each experiment. Furthermore, the fitted contact angles are similar to those from the stationary comparison, shown in figure 8.1.

Considering figure 8.2 (a), we see that the agreement is good within the range where the model is valid. Moreover, we see that each model predicts the spin-up radius better for lower rotation rates, with the model over-predicting the spin-up radius for larger rotation rates. The worst corresponding SS residuals value for both models is where $V = 0.73\,\text{ml}$, shown in purple on figure 8.2 (a), for which the data is most skewed. For each experimental set the contact angle predictions for model I are greater those of model II, while the reverse is true for the surface tension coefficient. Furthermore, for each set other than $V = 0.73\,\text{ml}$, the SS residuals is greater for model II than for model I indicating that the agreement between model I and the data is marginally better. These results are unexpected, since model II includes terms which are neglected in model I.

The agreement when the data is fitted overall, shown in figure 8.2 is also good for both models. Again, model I performs better than model II with a smaller

SS residuals value, although the contact angle and surface tension are similar. The sum of the SS residuals when the data is fitted individually for model I is $15.81\,\mathrm{mm}^2$, which is lower than the overall value of $20.10\,\mathrm{mm}^2$, indicating a better fit. Similarly, for model II the sum of SS residuals when individually fitted is $17.33\,\mathrm{mm}^2$ whereas the overall value is $28.371\,\mathrm{mm}^2$.

Experimentally, the acceleration (2.1.2) was chosen to limit contact line spreading within the spin-up phase of the experiment. However, during this phase it is likely that velocities were induced within the fluid relative to the rotating base. A key modelling assumption in each model was that the velocity within the rotating frame of reference is zero, and therefore the system is in equilibrium. Hence, although experimentally we attempted to limit magnitude of induced velocity, the modelling assumptions do not align perfectly with those observed in the experiment, and therefore are a potential source of error. In § 8.1.1 we saw that prior to any movement of the disc, when the system is at rest, both models predict the location of the contact line well.

When fitting the equilibrium models to the experimental data at spin-up we have assumed that the equilibrium contact angle is independent of the rotation rate. However, there are indications that for more viscous fluids the contact angle increases with rotation [64]. Therefore, it may not be appropriate to fit each data set with a single contact angle, and the resultant larger values of the surface tension coefficient act to counteract this effect.

In summary, we see that both the thin film model I and the $\mathcal{O}(1)$ contact angle model II perform well at predicting the location of the linearised contact line, R_0, and although the assumption that the contact angle is small is not met, model I performs marginally better in comparison to the data. However, both models are limited due to the assumption that the system is in equilibrium, whereas in the experiment it is likely that velocities are induced during the spin-up phase of the experiment.

8.2 Axisymmetric spreading

In § 2.3.3 we found that from the spin-up radius the axisymmetric Fourier mode spreads like

$$a_0(t) = R_0 + kV^n\Omega^4 t, \tag{8.2.1}$$

where the values of the coefficient, k, and exponent, n, are presented in table 2.3. Overall, we found that $k = 11.73$, $n = 1.57$ fits the data well.

The linear stability analysis assumes an initial condition which has zero velocity within the rotating frame of reference. We have seen in § 8.1.2 that this may not be realised, due to the error between the mean radius at spin up, and the dimensional equilibrium contact line position. The mathematical analysis concerning the neutral stability of the axisymmetric mode in the thin film limit, performed in §§ 4.3, 5.4, indicated that solutions are mostly stable to axisymmetric perturbations, with stable solutions only appearing for radii greater than R_{0c}, the radius at the maximum value of ϕ. We do not see this behaviour within the experiments, and see that the amplitude of the axisymmetric Fourier mode always grows in time from the spin-up radius, R_0.

The qualitative disagreement in axisymmetric spreading further indicates that the initial condition of the experiment was not in equilibrium, although the spin-up radius, R_0, is relatively well approximated by models making this assumption, demonstrated in § 8.1.2.

8.3 Non-axisymmetric spreading

In this section we compare the numerical growth rates from the experimental data, presented in § 2.3, to the eigenvalues calculated from the linear stability problem within the thin film limit described in chapter 4 for non-axisymmetric perturbations. In this section we will only consider solutions to thin film model I, since we found in § 7.3 that model II does not produce results which are qualitatively comparable to the experiments for large contact angles.

In § 2.3.4 we presented the linear growth rates and dominant Fourier modes for each experiment as both the volume and rotation rate were varied. The main

qualitative result from the non-axisymmetric analysis was that as the rotation rate increased, the dominant mode also increased sequentially from $m = 1$ for each volume considered. Furthermore, the threshold rotation rate for a mode to become dominant decreases as the droplet volume was increased. As anticipated, the growth rate of a given mode increased for greater rotation rates. However, the rate at which this growth occurs decreased, indicating there may exist an upper limit on the growth rate of each mode which is dependent on the volume and physical properties of the fluid.

Throughout chapters 4 and 5 when considering thin film model I we developed multiple sub-models to describe the linear stability of a rotating droplet about the equilibrium position derived in § 3.4. We initially considered a model within the quasi-steady limit $C = 0$ in § 4.2, concluding that the unconditionally dominant mode is $m = 1$, corresponding to a translation of the centre of mass away from the axis of rotation. Hence, the qualitative behaviour of the experiments cannot be captured by this model, since experimentally we see the dominant mode increasing with the rotation rate.

The models we discussed that are capable of capturing the qualitative behaviour of the experiments are the models with non-zero capillary number; the 'general Tanner model' described in § 4.4, the 'fixed contact angle model' described in § 5.2, and the more general model form of the latter models which includes Coriolis forces, presented in § 5.3. In each case we showed that the linear stability problem reduces to a fourth order eigenvalue problem for the growth rate, σ_m, given a wavenumber, m, amongst other physical parameters.

Next, we will discuss which model is most appropriate by considering the values of the resultant nondimensional parameters, and subsequently assess how the models perform against the experimental data.

8.3.1 Physical properties

To perform a comparison between the experimental data and thin film models there are a number of physical parameters to be set. Namely, the contact angle, θ_c, the surface tension coefficient, γ, the contact line speed, κ, the Greenspan slip length, α, and the Tanner exponent, q. The contact angle, θ_c, and the surface

tension coefficient, γ, are taken as the values from table 8.2 for the overall fit of the data so that the sum of squared residuals between the experimental and model equilibrium contact line positions is minimised.

The capillary number is defined in table 8.3, when the Tanner boundary condition (3.1.10) is used and involves measure of contact line speed, κ. The speed, κ, is not a material constant [3] and is therefore determined experimentally. Through our experimental analysis of axisymmetric solutions, we determined a power law (8.2.1) of how the axisymmetric mode grows in time so that the measure of contact line speed used in the model is $\kappa = \kappa_e \theta_c^{-q} = kV^n \Omega^4 \theta_c^{-q}$, where n and k are reported above in § 8.2. The Tanner exponent q is commonly taken as $q = 1$ or $q = 3$ [32, 31], and as discussed in § 4.2, changing q does not affect the stability and instead acts as a multiplier to the eigenvalues. De Gennes [1] concludes that $q = 3 \pm 0.5$ using experimental data of Hoffman [45], while Hocking [33] and Ehrhard and Davies [32] suggest that $q = 3$ is most appropriate to model the contact line dynamics. Therefore, we take $q = 3$ for our comparison.

Recall in § 5.1 we established that for the Tanner model with non-zero capillary number, referred to as the 'general Tanner model' and discussed in § 4.4, that the slip parameter, α, has no effect on the stability of eigenvalues but increasing α increases the absolute value of σ_m. Therefore, the Greenspan slip coefficient, α, is used as a fitting parameter to the data, in a nonlinear least squares sense.

8.3.2 Nondimensional parameters

The modelling identifies several nondimensional groups, the form of which are reported in table 8.3 along with the corresponding balance of forces. Before comparing the thin film model I to the experimental data we must consider the magnitude of each of these nondimensional quantities, assessing the validity of each model within the thin film limit from throughout chapters 4 and 5 given the assumptions made during the derivation.

The centrifugal and Ekman numbers are functions of the rotation rate, Ω, while the Reynolds and capillary numbers are dependent on rotation rate through the chosen velocity scale, U, via the contact line speed, κ, which is taken from the axisymmetric spreading data (8.2.1). Therefore, for each experimental set at fixed

Parameter	Form	Name	Balance
L	$\left(\frac{V}{\theta_c}\right)^{1/3}$	Length scale	N/A
U	$\kappa\theta_c^q$	Velocity scale	N/A
ϕ	$\frac{\rho\Omega^2 L^3}{\gamma\theta_c}$	Centrifugal number	Rotation to surface tension
G	$\frac{\rho g L^2}{\gamma}$	Bond number	Gravity to surface tension
Re	$\frac{\rho U L}{\mu}$	Reynolds number	Inertia to viscosity
Ek	$\frac{\mu}{\rho\Omega L^2}$	Ekman number	Viscosity to rotation
C	$\frac{\mu U}{\gamma\theta_c^3}$	Capillary number	Viscous drag to surface tension

Table 8.3: Summary of relevant dimensional and nondimensional parameters used in the thin film modelling (I), indicating the form, name and force balance.

volume the centrifugal, Reynolds, Ekman, and capillary numbers all vary with rotation rate, while the Bond number remains fixed. Table 8.4 reports the resultant nondimensional parameters for each volume, where the physical properties of the fluid other than the surface tension coefficient are taken from table 2.1. The maximum and minimum values of the nondimensional centrifugal, capillary and Reynolds numbers are reported, within the range in which model I is valid. The Ekman number varies inversely with rotation rate, and so the maximum and minimum values of the inverse of the Ekman number are reported meaning that each maximum column corresponds to the maximum rotation rate within the parameter space.

The maximum value of capillary number, C, is small for each experimental set, with $C < 0.05$ in each case. In § 5.2 we discussed a thin film model, where the contact angle remains fixed, rather than being related to the contact line speed using the previously used Tanner law. We concluded that eigenvalues for the same parameters align for capillary numbers of $\mathcal{O}(1)$ and above, that is, sufficiently

Volume (ml)	G	ϕ		C		Re		Ek^{-1}	
		min	max	min	max	min	max	min	max
0.15	4.0182	0.2552	3.9181	1.743×10^{-4}	0.0411	2.338×10^{-4}	0.0551	0.3646	1.4285
0.35	6.9172	0.0198	3.5702	7.306×10^{-7}	0.0238	1.286×10^{-6}	0.0420	0.1162	1.5620
0.57	9.6543	0.3172	3.5793	1.510×10^{-4}	0.0192	3.141×10^{-4}	0.0400	0.5061	1.6999
0.73	11.3956	0.0418	3.2071	2.350×10^{-6}	0.0138	5.308×10^{-6}	0.0313	0.1915	1.6772
1.20	15.8412	0.3315	3.0565	1.190×10^{-4}	0.0101	3.169×10^{-4}	0.0269	0.5855	1.7779
1.55	18.8221	0.3270	2.9844	1.033×10^{-4}	0.0086	2.999×10^{-4}	0.0250	0.6072	1.8341

Table 8.4: Summary of the resultant nondimensional parameters for model I, defined in table 8.3, for each experimental set. Where parameters vary with rotation rate, the maximum and minimum values are presented. Pure glycerol was used and the densities and viscosities were calculated using formulas within [98].

fast contact line speeds, κ. Since capillary numbers for the experimental data are orders of magnitude smaller than the transitional value, the fixed contact angle model is not valid within this regime for the thin film model I. In § 4.2 we considered the quasi-steady limit $C = 0$, recovering results of McKinley and Wilson [43], when $G = 0$, and finding equivalent results to McKinley and Wilson [42] for $G > 0$ subject to a change in nondimensional variables. We found that the $m = 1$ mode, corresponding to a translation of the centre of mass of the fluid, is always the most unstable mode, independent of all physical parameters. In figure 2.10 we saw that for each experimental run, the most unstable Fourier mode increased with the rotation rate. Therefore, the quasi-steady model presented in § 4.2 is insufficient to describe the qualitative nature of the experimental data, especially for greater rotation rates when the capillary number is $\mathcal{O}(10^{-2})$. We showed in § 4.4.1 that when $C \lesssim \mathcal{O}(10^{-3})$ the quasi-steady Tanner model compares well to the general Tanner model. Hence, for smaller contact line speeds, and therefore smaller rotation rates, the quasi-steady model will compare well to the general Tanner model, whereas for larger rotation rates the quasi-steady model will overestimate the growth rates.

When nondimensionalising model I in § 3.2, we initially made the Stokes flow approximation by assuming that the Reynolds number was sufficiently small, while the Ekman number sufficiently large,

$$\theta_c^2 \mathrm{Re} \to 0, \quad \frac{\theta_c^2}{\mathrm{Ek}} \to 0. \tag{8.3.1}$$

The experimental values presented in table 8.4 show that for each set that the Reynolds number is small for values within the range of validity of the model. The maximum value of $\theta_c^2 \mathrm{Re} = 0.12$ appears for $V = 0.11\,\mathrm{ml}$ and $\Omega = 55.4\,\mathrm{rad\,s^{-1}}$ due to larger rotation rates being considered for this smaller volume. The small values of the Reynolds number verify that in this configuration viscosity dominates inertia. Therefore, although the contact angle, θ_c, itself is not small, with the accepted value being $\theta_c = 1.5$, we see that the experimental Reynolds numbers shown in table 8.4 are sufficiently small enough for (8.3.1) (a) to hold true.

The Ekman number describes the balance between viscous and Coriolis forces. In § 5.3 we detailed a model including the previously neglected terms involving the Ekman number. We found that as anticipated the inclusion of the Coriolis

effect resulted in complex eigenvalues, where the imaginary part corresponded to precession of modes within the rotating frame. The conclusions of this section were that if $\mathrm{Ek}/\theta_c^2 > 0.1$, then the imaginary part of the eigenvalue is negligible, while the real part is well approximated by solutions within the limit (8.3.1) (b). Using the values in table 8.4 we see that the minimum value is $\mathrm{Ek}/\theta_c^2 = 0.24$, when $V = 1.55\,\mathrm{ml}$ and $\Omega = 15.2\,\mathrm{rad\,s^{-1}}$. Furthermore, in the numerical analysis of the experimental data no precession of modes was observed. Therefore, it is well founded to neglect the Coriolis effect, as was done in the model presented in § 4.4, as the Ekman number is sufficiently large enough to be approximated using (8.3.1) (b).

Overall, we have established that the general Tanner model, presented in § 4.4 is the most appropriate to fit to the data considering the magnitude of the nondimensional quantities reported in table 8.4. In this model, the contact angle is modelled with the Tanner law, resulting in a small but finite capillary number, while and both limits (8.3.1) are taken and justified.

8.3.3 Comparison to experimental data

Equilibrium solutions exist in limited region of parameter space compared to the set of rotation rates investigated experimentally. This was discussed in § 8.1.2, and is demonstrated in figure 8.2. Therefore, the linear stability analysis is also limited to a subset of rotation rates, since for greater rotation rates there is no physical base solution from which to perturb. Figure 8.3 shows the dimensional growth rates against rotation rate for the first four Fourier modes within the range of physical equilibrium solutions. The experimental results were first presented in figure 2.11 where the independent variable in each plot was, $\phi^* = \Omega^2 V$. The general Tanner model prediction is also shown for the first four wavenumbers using solid lines with colour corresponding to the same Fourier mode.

Recall that, modes with amplitude less than the noise level a short time after spin-up are not shown on figure 8.3, since they are not required to resolve the boundary at this time. However, the Tanner model can predict negative eigenvalues, so that perturbations decay in time. This may be due to the boundary conditions, since our modelling neglects contact line hysteresis. As discussed in § 1.2.1, contact angle hysteresis is the phenomenon where the contact angle is not unique and

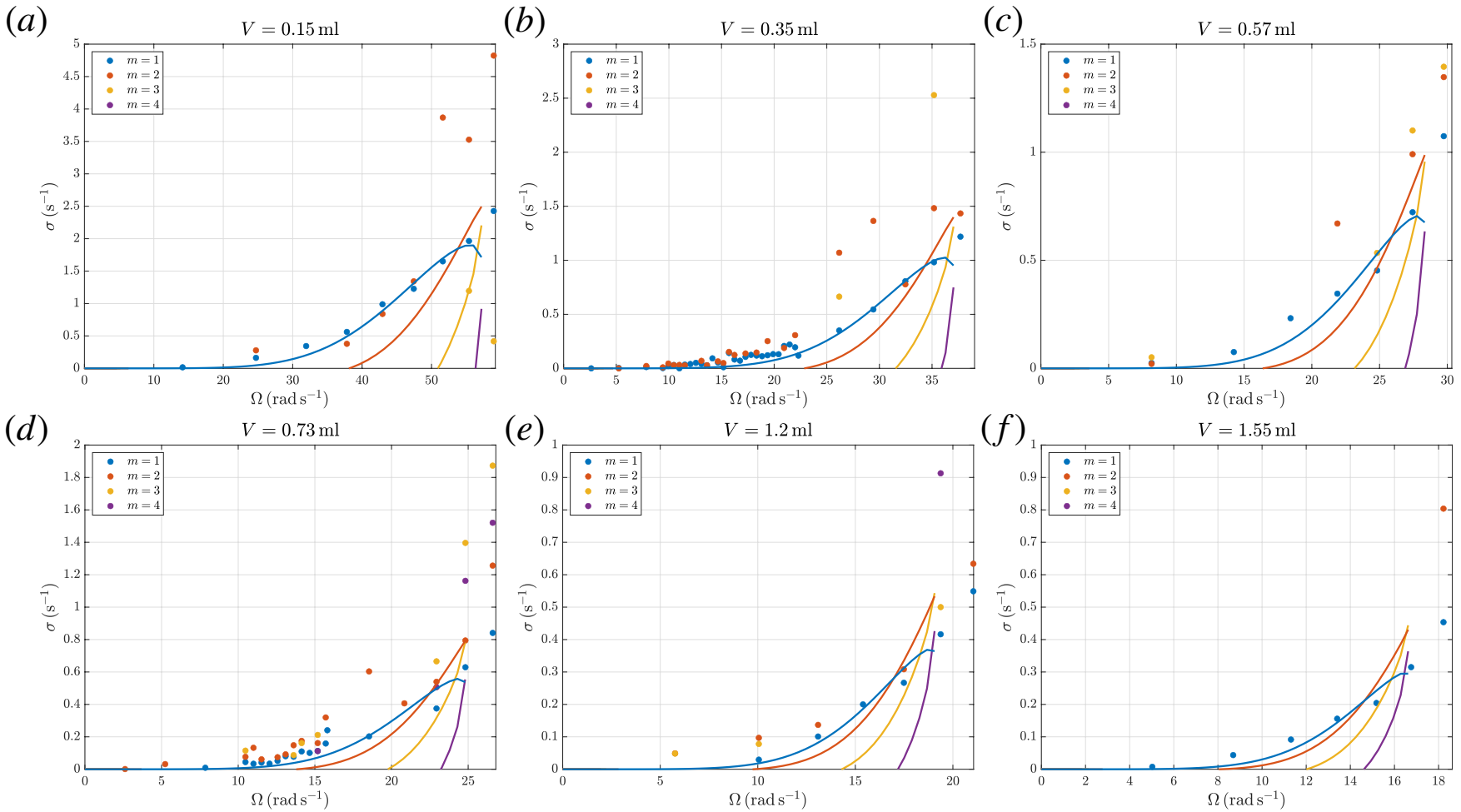


Figure 8.3: Dimensional comparison of the predictions of the general Tanner model and the experimental data for each volume considered. The slip coefficients used for each figure are reported in table 8.5 whereas the contact angle and surface tension coefficients are taken from table 8.2.

must be greater than a critical value, known as the advancing contact angle, in order for the contact line to move. If the contact angle is below this threshold the contact line will be stationary. Therefore, by neglecting this feature, the contact line can otherwise recede at a rate given by the negative eigenvalue, σ_m. Subsequently, negative eigenvalues are not shown on figures 8.3 (a)–(f) and we only discuss positive eigenvalues, corresponding to those which rise above the noise level of the data following spin-up.

The values of the fitting parameter, α, for each experimental set are presented in table 8.5. We see that for each experiment the fit to the data is optimum when the nondimensional slip length $\alpha \approx 0.01$. The corresponding dimensional slip length is also presented in table 8.5, which are orders of magnitude smaller than the mean radius of the droplet for each experimental set. The magnitude of the slip length is consistent with the findings of Wilson *et al.* [85] when comparing to the experimental data of Fraysse and Homsy [58] and Spaid and Homsy [60] in the context of purely axisymmetric spreading.

The sum of squared residuals between the model I and data where $m = 1$ is also presented in table 8.5, with each value being small, indicating a good fit. This is demonstrated in each of the figures 8.3 (a)–(f), where we see that the Tanner model agrees well with the data for the $m = 1$ mode. Furthermore, for the $m = 1$ mode in particular the modelling captures the experimental observation of an upper limit on the growth rate, with a maximum value depending on the experimental parameters. For greater wavenumbers, $m = 2, 3, 4, ...$, there are inconsistencies in the prediction and the experimental data. Although the model captures the qualitative nature of the experiments, that the most unstable mode increases with rotation rate, it fails to predict the growth rates of higher modes accurately. Consequently, the threshold for a mode to become dominant is also not predicted well in general. This may be due to inaccuracies in the initial condition of the experiment, discussed in § 8.1.2, which subsequently introduce error into the results of the linear stability analysis. We saw in figure 8.2 that the error between the model I prediction and experimental data is greatest for larger rotation rates, within the range of physical solutions. Since this is also the region in which higher mode instabilities occur this is a likely cause for the discrepancy for higher mode instabilities.

Volume (ml)	α (nondim)	α (mm^2)	SS residuals, $m = 1$ (s^{-2})
0.15	0.0109	0.535	0.0625
0.35	0.0099	0.835	0.0967
0.57	0.0113	1.333	0.0207
0.73	0.0099	1.381	0.0575
1.20	0.0100	1.939	0.0027
1.55	0.0098	2.258	0.0036

Table 8.5: Nondimensional and dimensional Greenspan slip coefficients used to produce figure 8.3 for each experimental set. The slip coefficient is nondimensionalised using the length scale given in table 8.3. Also shown in the sum of squared (SS) residuals between the experimental data and the thin film model for the $m = 1$ mode.

Figure 8.4 shows two specific cases where the amplitude of the unstable Fourier modes in a short time following spin-up are plotted against time. Also shown on each figure is the model prediction of how the amplitude of the Fourier modes grow in time, from the general Tanner model, using the parameters detailed above. Therefore, a direct comparison between the amplitude of the Fourier modes and the model prediction can be observed, eliminating error in numerically calculating growth rates from the data as is done to produce figure 8.3.

Figure 8.4 (a) shows the experiment where $V = 0.15\,\text{ml}$ and $\Omega = 55.4\,\text{rad}\,\text{s}^{-1}$. In this case the first three non-axisymmetric Fourier modes are shown, since in a short time after spin up no other modes exceed the noise level, indicated in black. The amplitude of the Fourier modes are shown on a semi-logarithmic axes, so that an exponential perturbation will appear linear in time, with initial slope equal to the growth rate of a given Fourier mode. We see that the agreement is good between the model and prediction for $m = 1$ and $m = 3$, whereas the agreement for $m = 2$ is not as good. However, the modelling does correctly predict that the $m = 2$ mode is the most unstable, having the greatest slope. The absolute error between the predicted and experimental values of the spin-up radius, R_0, is $\Delta R_0 = 0.443\,\text{mm}$, showing good agreement. Figure 8.4 (b) is similar and shows the case where $V = 0.57\,\text{ml}$ and $\Omega = 27.4\,\text{rad}\,\text{s}^{-1}$ where the first four non-axisymmetric Fourier modes are shown. Note that, in figure 8.3 (c) for this specific case the $m = 4$ is not accepted due to the amplitude rising greater than the noise level after the prescribed time δt; however, we present it on this figure

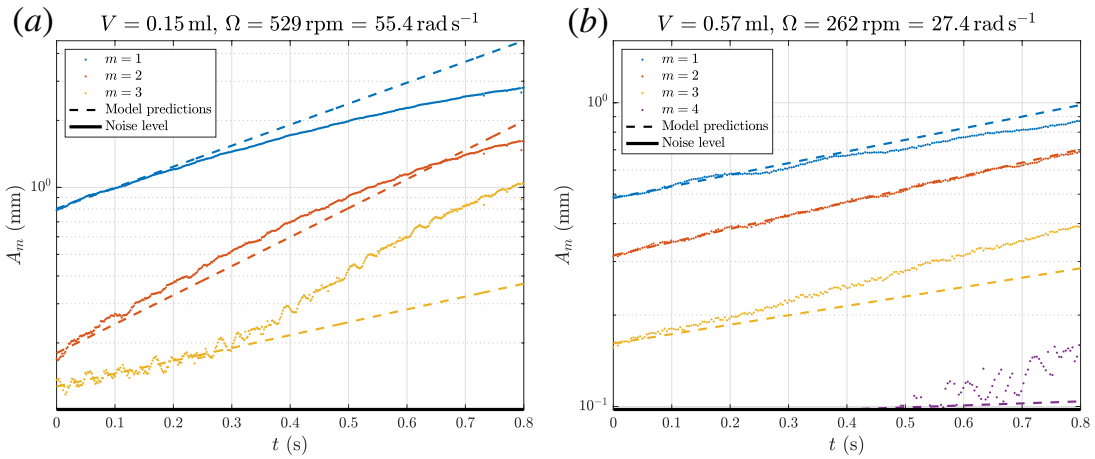


Figure 8.4: Plot of the unstable Fourier modes in a short time following spin-up, also shown is the prediction of the thin film general Tanner model, shown in dashed lines for each wavenumber $m = 1, 2, 3$.

for completeness. In this case we see that the agreement is good for $m = 1$ and $m = 2$, but not as good for $m = 3$ and $m = 4$. In the latter two cases although the numerical agreement of the growth rate is off, the model correctly predicts the stability of these modes, with both being unstable and growing in time. In this case the absolute error in the equilibrium solution between experiment and model is $\Delta R_0 = 0.525\,\text{mm}$, again showing good agreement.

Overall, we see that for the presented two cases where the spin-up radius is well approximated by the model, that the agreement between the amplitudes of Fourier modes and the model prediction is good. Specifically, when the contact line speed is taken from the axisymmetric spreading data, the contact angle and surface tension coefficient are taken to reflect the equilibrium data, and Greenspan slip coefficient is taken from a nonlinear least squares fit to the non-axisymmetric data.

8.3.4 Contact angle varying with rotation

We have discussed the equilibrium and linear stability results above under the assumption that the contact angle, θ_c, does not vary with rotation. Furthermore, from the two cases considered in figure 8.4 we saw that the growth rates from the experiment and thin film model compare well when the error in the equilibrium solution is small. Therefore, instead of assuming a constant contact angle, we choose the contact angle so that the experimental equilibrium radius, R_{0e}, is

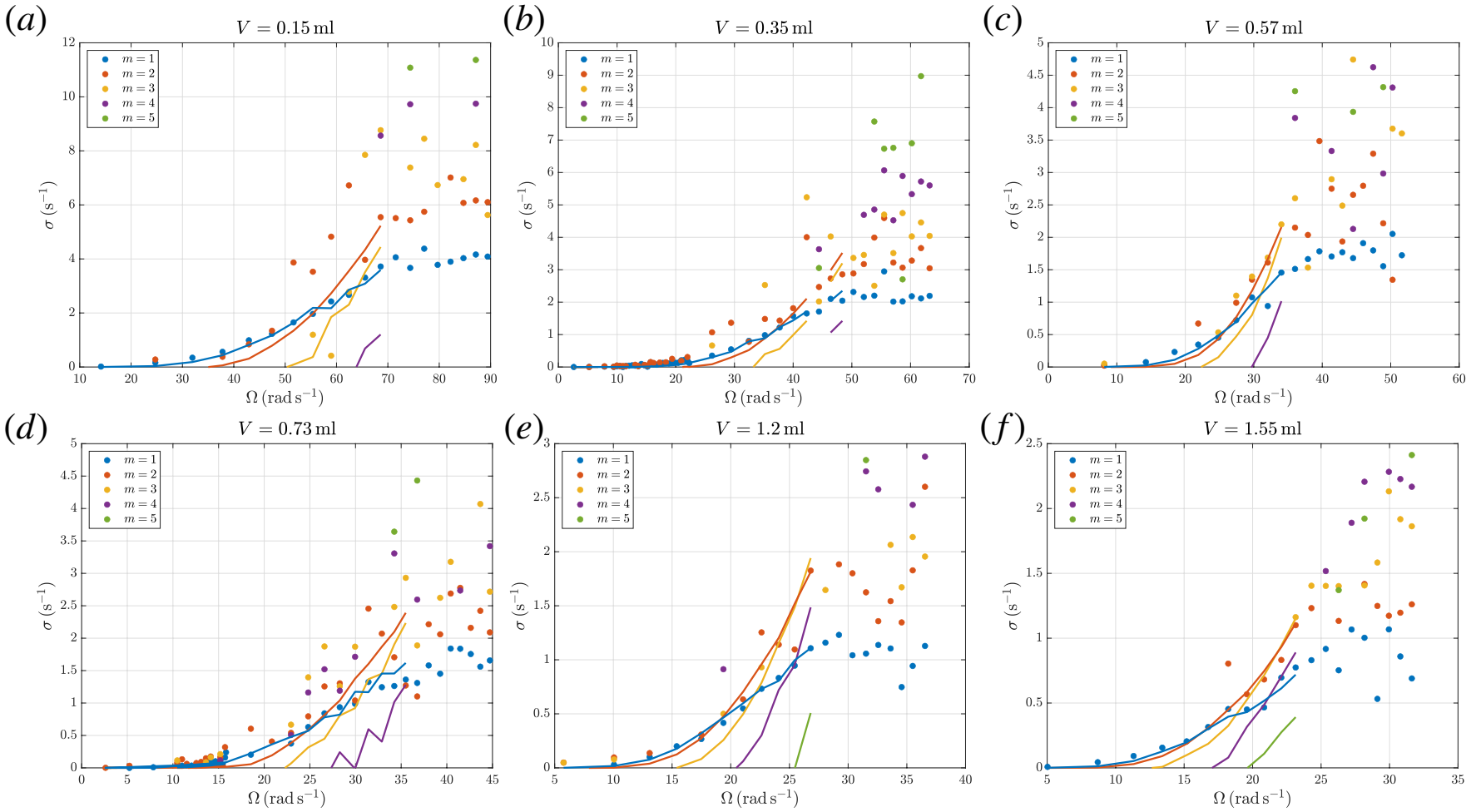


Figure 8.5: Dimensional comparison of the general Tanner model and the experimental data for each experiment when the contact angle is taken from the solution of (8.3.2).

exactly reproduced by the model. To do this, we numerically solve the transcendental equation

$$R_{0e} = \left(\frac{V}{\theta_c}\right)^{1/3} R_{0\mathrm{I}}\left(\frac{\rho\Omega^2 V}{\gamma\theta_c^2}, \frac{\rho g V^{2/3}}{\gamma\theta_c^{2/3}}\right), \tag{8.3.2}$$

for each experiment. The solution $R_{0\mathrm{I}}$ is found by solving the contact angle condition at leading order in ϵ (3.4.10a), given the nondimensional parameters, ϕ and G which depend on the contact angle as shown. The coefficient of $R_{0\mathrm{I}}$ is the lengthscale, L, which also depends on the contact angle.

Subsequently, the linear stability problem can be solved where the surface tension coefficient is taken from the table 2.1 rather than fitted to the data as before. The contact line speed is once again taken from the axisymmetric spreading data, while the remaining physical quantities are taken from table 2.1. The Greenspan slip coefficient used a fitting parameter to the data, where again we find the optimum fit in each case when $\alpha \approx 0.01$. The results are presented in figure 8.5, where we see that again for each volume there exists a maximum rotation rate the model can exist for. In comparison to the results presented in figure 8.3, the range in which solutions exist is extended since we do not constrain the contact angle to be below $\pi/2$. In this case the restriction comes where there is no value of θ_c that can solve (8.3.2), given the physical parameters. The lack of solution of (8.3.2) causes the gap in the prediction in figure 8.5 (b). We observe that when the contact angle is taken to exactly match the equilibrium solution, the model better fits the data for higher wavenumbers, while the agreement in the $m = 1$ mode is again good. Along with better quantitative agreement for higher wavenumbers, we also see that the threshold for a wavenumber to become dominant is also better predicted in comparison to the results presented in figure 8.3. This can especially be seen in figure 8.5 (f) where $V = 1.55\,\mathrm{ml}$ where we see that both the threshold for the dominant mode between the $m = 1, 2$ and $m = 2, 3$ is well predicted by the model in this case.

For larger rotation rates the solutions to (8.3.2) are greater than the allowed range of $0 < \theta_c < \pi/2$, for which solutions are not multi-valued close to the contact line. The solutions to (8.3.2) are shown in figure 8.6, for each volume, where we see that the contact angle, θ_c, increases with rotation rate, rising above $\pi/2$, which is also shown in black. Larger contact angles being required may be due to the initial condition of the experiment, where as discussed in § 8.1.2, the system appears to

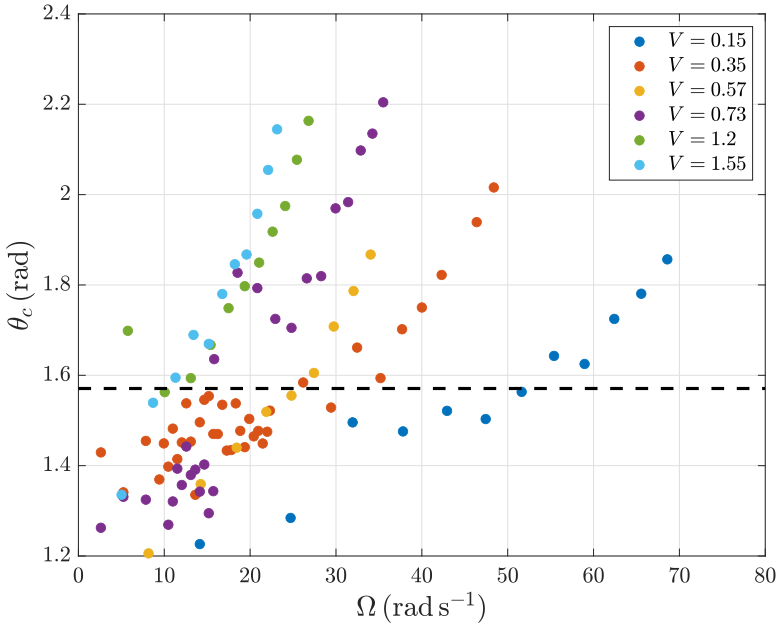


Figure 8.6: Solutions of (8.3.2) for the contact angle, θ_c, against the rotation rate, for each volume. The threshold of $\theta_c = \pi/2$ is also shown in a black dashed line.

not be at rest at the start of the experiment. However, the modelling assumes that at $t = 0$ the system is in a state of rest within the rotating frame of reference. Therefore, the fitting of artificially large contact angles appears to rectify this discrepancy, allowing the equilibrium contact line position to be greater so that the modelling of equilibrium solutions agrees with the experiment.

8.4 Summary

In this chapter we have simultaneously compared the experimental data for initial drop radii and subsequent numerical nonaxisymmetric growth rates, first presented in § 2.3, to the equilibrium solutions presented in § 3.4 and respective eigenvalues calculated from the linear stability problem of the general Tanner model of § 4.4. None of the previous studies detailed in chapter 1 have compared both the equilibrium and growth rates simultaneously. Furthermore, the early modelling of fingering instabilities by Troin *et al.* [59] has been shown to compare well with several experimental studies [58, 53, 68], however prior to this thesis no model has been shown to sufficiently model both equilibrium and linear stability favorably.

When comparing the equilibrium solutions we saw that both the thin film model I and the $\mathcal{O}(1)$ contact angle model II perform well at predicting the equilibrium contact line position, R_0. However, we demonstrated that both models have limitations due to the non-physical assumption that the system is in equilibrium, since in reality velocities are induced during the spin-up phase of the experiment.

We discussed the free parameters in the model, taking the contact line speed directly from the axisymmetric spreading data, and both the contact angle and surface tension coefficient from the nonlinear least squares fit between the equilibrium solutions and the experimental spin-up radii. Following this, we discussed the size of the nondimensional parameters justifying why the general Tanner model is most appropriate to fit to the data over models within different areas of the parameter space discussed in this thesis.

We found that within the range of solutions allowed due to the size of the contact angle, the qualitative agreement between the experiment and thin film general Tanner model was good, with good quantitative agreement for the $m = 1$ mode, where the nondimensional Greenspan slip coefficient, α, was similar for each experimental set.

Finally, we took the contact angle such that for each experiment the equilibrium contact line position from the model is equal to the spin-up radius from the experiment. Under this approximation we saw the quantitative agreement for $m = 1, 2, 3$ is good, with the model better predicting the thresholds where the dominant wavenumber changes. However, we found that for the equilibrium radius to be taken from the experiment the contact angles are unphysical for greater rotation rates. We posited that the contact angle is greater to offset the discrepancy between the initial condition of the experiment, which is unsteady, and the equilibrium solutions of the model, which are steady. Furthermore, it is important to remember that in the thin film model the contact angle is assumed small, whereas the experimental data indicates that the contact angle is large. Therefore, although the agreement is found to be good there is likely to be some error introduced by the modelling approximation made.

Chapter 9

Conclusions and closing remarks

9.1 Thesis summary

The aim of this thesis was to understand the contact line instability of a viscous fluid under rotation. We performed both experimental and mathematical analysis as both the volume of droplet and rotation rate of the plate were varied. We considered different regions of the parameter space to previous experimental and mathematical studies, which generally consider small volumes and contact angles. In doing so we attempted to understand the limitations of the commonly used thin film model, as well as considering the qualitative differences when the contact angle is large.

In chapter 2 we set out the experimental methodology to investigate the contact line instability when a viscous fluid of a prescribed macroscopic volume is spun at a chosen rotation rate. Fourier analysis was used to find the amplitude Fourier modes which contribute to the shape of the contact line. First, we considered the spin-up radius, observing that the spin-up radius increases with both rotation and volume. We assessed the axisymmetric spreading from the spin-up frame, finding a power-law for growth which showed good agreement with the data. The spreading rate was found to be different from the results of Holloway *et al.* [62] who considered microscopic volumes of silicon oils. The experiments performed showed a distinct difference in the onset of instability, such that the onset of instability was almost instantaneous in contrast to experiments on small volumes who observe a long axisymmetric phase before onset of instability.

The magnitude of the non-axisymmetric instability was quantified by taking the logarithm of the amplitudes of non-axisymmetric modes $m = 1, 2, 3, ...$ over time, obtaining the growth rates of each relevant mode. Subsequently, the dominant growth mode was determined and presented as functions of both the rotation rate and volume. The main result from the non-axisymmetric analysis being that the threshold rotation rate for a mode to become dominant decreases as the volume increases. Specifically, this meant that the dominant wavenumber increased with rotation rate for fixed volume, in contrast to previous results by Melo *et al.* [26] and Fraysse and Homsy [58] who reported the dominant wavenumber as independent of rotation rate and volume, while considering smaller volumes, $\mathcal{O}(10^{-2})$ ml, of Silicon oils. We determined that the dominant wavenumber is also a function of drop volume in the studied configuration. The fluid in much of the previous experimental studies discussed in chapter 1 are non-Newtonian silicon oils, using microscopic droplets [26, 58, 60, 62] or macroscopic droplets [61, 64, 67, 63]. Veretennikov *et al.* [66] performed similar experiments to those presented in chapter 2, using macroscopic volumes of glycerol, however the rotation rates investigated were too low to observe the higher mode instabilities observed in our experiments. Therefore, the experiments we performed were within an unexplored region of parameter space and produced novel qualitative differences in the onset of instability and quantitative differences in the spreading rate and fingering instability as a function of rotation rate and drop volume.

In order to make comparisons with the experimental data, in chapter 3 we derived a model for the evolution of the free surface, $h(r, \varphi, t)$, and contact line, $R(\varphi, t)$, of a fixed volume of viscous fluid in solid body rotation on a solid plate. In this chapter we made a lubrication approximation, assuming that the radial length scale is significantly larger than the axial length scale and identifying the contact angle as an appropriate lubrication parameter. The contact line dynamics were modelled using a macroscopic slip law whereas the contact angle was related to the contact line speed using the Tanner law, where contact line hysteresis was neglected. We identified three key parameters, the centrifugal, Bond and capillary numbers; nondimensional measures of the rotation rate, volume, and viscous contact line speed against surface tension, respectively. We discussed the equilibrium solutions determined by McKinley *et al.* [42, 43], where the fluid is in solid body rotation, presenting the results as a parameter space in which physical, hydrostatic

solutions exist. The key result from this equilibrium analysis is that each Bond number has a corresponding maximum value of the centrifugal number. In terms of physical parameters, each volume has a maximum rotation rate beyond which no equilibrium solution is possible for which the contact angle is small.

Chapters 4 and 5 concerned the linear stability analysis of the equilibrium solutions of McKinley *et al.* [42, 43], detailed in § 3.4. We used a Greenspan slip condition [31] in replacement of a more commonly used Navier slip condition to avoid the contact line speed being zero, leading to purely stable eigenvalues. Within the quasi-steady limit we presented analytic solutions for the free surface perturbation and the growth rate for different wavenumbers, m, recovering the solutions of McKinley *et al.* [42] when $m = 0$ and McKinley and Wilson [43] for Bond number $G = 0$, while presenting novel solutions for $G > 0$. Within the quasi-steady limit we found that the $m = 1$ mode is unconditionally unstable and dominant over the entire parameter space provided any rotation occurs. Each larger wavenumber can be both linearly stable and unstable within the parameter space depending on the rotation rate and volume, indicated by neutral stability curves presented in § 4.3. The neutral stability curves were found to be independent of capillary number, slip length and Tanner exponent. When the capillary number is positive the derived eigenvalue equation was solved numerically using a finite difference scheme, detailed in appendix B. The case where $G = 0$ had previously been studied by McKinley and Wilson [43], whereas the analysis presented in § 4.4 discussed novel solutions when $G > 0$. We found that the inclusion of capillary effects allows the dominant mode to rise from $m = 1$ as both the centrifugal and Bond numbers are increased, in line with experimental observations detailed in chapter 2.

The linear stability model was extended in chapter 5, where we first showed how the Greenspan slip law allows non-zero radial velocities at the contact line, contrary to the widely used Navier slip condition which leads to a qualitative change in the boundary conditions and purely stable eigenvalues. In § 5.2 we discussed novel solutions where the contact angle remains fixed, replacing the previously used Tanner law. We determined that the equilibrium solutions, as well as the neutral stability curves within the parameter space, are unchanged from the Tanner model. Furthermore, we verified that the results of fixed contact angle model are equivalent to the Tanner model in the large capillary limit; when the capillary number is $\mathcal{O}(1)$ and above, consistent with non-rotating analysis of Ehrhard and

Davis [32] and Myers *et al.* [77, 78]. Next, we considered a model retaining previously neglected terms corresponding to the Coriolis force, defining a threshold in terms of the nondimensional Ekman number above which the effect of including the Coriolis force is negligible. Previous studies assume the Coriolis force terms are negligible [19, 90], however we have demonstrated through direct comparison of solutions that taking the limit $\mathrm{Ek}' \to \infty$ in § 3.2 is a reasonable approximation to make. The final extension we considered was the quasi-steady limit where an ODE for the evolution of the contact line was derived for axisymmetric perturbations. We compared numerical solutions of the derived ODE to the solutions of the linear stability problem, showing that for sufficiently small perturbations to the contact line the growth or decay of perturbations is accurately predicted by the previously determined exponential growth rate. Furthermore, we demonstrated why the axisymmetric mode is neutrally stable at the maximum rotation rate within the previously defined parameter space.

Having completed our analysis within the thin film limit, we proceeded to discuss solutions where the contact angle is no longer assumed to be small. Existing literature, detailed in chapter 1, focuses on thin film solutions of the governing equations. In chapter 6 we nondimensionalised the system of equations and boundary conditions in an alternative way to chapter 3, with the contact angle functioning as an arbitrary boundary condition, rather than within the nondimensional quantities as in chapter 3. Following the same procedure as McKinley *et al.* [42, 43] and § 3.4, we determined novel solutions for the steady, axisymmetric, equilibrium free surface and the constant equilibrium contact line position. The resultant parameter space of solutions and the trends as each of the nondimensional quantities were varied were found to be qualitatively comparable results to those in the thin film limit. Specifically, for fixed volume and contact angle there exists a maximum rotation rate, above which equilibrium solutions cannot exist. We determined that larger contact angles can support equilibrium solutions at greater rotation rates, while also finding that the thin film model performs well for contact angles less than $\theta_c = \pi/2$. Therefore, in terms of prediction of equilibrium solutions, the thin film solutions determined by McKinley *et al.* [42, 43] and detailed within § 3.4 are found to be a good approximation of the full system, and have the advantage of providing an analytical form rather than the purely numerical solutions when the contact angle is arbitrary. At the end of chapter 6, we developed a numerical

finite element method to solve a set of Stokes equations on a mesh defined by an equilibrium solution. By doing so, we recovered the expected leading order velocity and pressure solutions, while providing a foundation method for solving the perturbation equations in chapter 7.

In chapter 7 we discussed the linear stability of the novel equilibrium solutions presented in § 6.3, subject to non-axisymmetric perturbations. We constructed the perturbation to the free surface using Bessel functions, satisfying the $\mathcal{O}(\epsilon)$ boundary conditions, and solve the resultant weak formulation for the pressure and velocity fields within a mesh defined by the equilibrium solution. We used the solutions within the thin film limit to verify the numerical method before discussing results with $\mathcal{O}(1)$ contact angles. When the contact angle is sufficiently large, the evidence suggests that the instability transitions from slip at the contact line to a rolling of the contact line, with negative radial velocity at the contact line for all values of the centrifugal and Bond numbers for which equilibrium solutions exist. The results are in qualitative agreement with previous experiments where rolling of the contact line has been observed experimentally using both glycerol [66] and silicon oils [61, 64] of various volumes and rotation rates. The linear stability analysis for large contact angles identified the limitation of the thin film models discussed in chapters 4 and 5, such that the rolling motion at the contact line is not captured. However, the thin film models provides advantages in terms of tractability and relative simplicity, with analytic equilibrium solutions and a simplified eigenvalue equation solved using a finite difference method.

Chapter 8 concerned the comparison between the mathematical models and the experimental data. Previous studies detailed in chapter 1 have not compared both the equilibrium and growth rates simultaneously as has been done in this work. Furthermore, verification of a thin film linear stability analysis of the closed form equilibrium solutions derived by McKinley *et al.* [42, 43] has not been performed prior to this thesis. In chapter 8 we first considered the fluid radii before any movement is detected, when no rotation is present. We found that the both the thin film and large contact angle models discussed in chapters 3 and 6 show good agreement to the data for each volume considered. The contact angle was found to be large, however despite this the thin film model performs well indicating that neglecting of $\mathcal{O}(\theta_c^2)$ terms was well founded in this case. Next, we considered the spin-up radius see that again both models perform well at predicting the location

of the linearised contact line, R_0, as a function of the rotation rate within the range of possible solutions. Specifically, the thin film model is found to perform marginally better than the large contact angle solutions, indicating the strength of the approximation made rather than identifying any underlying weaknesses. Finally, we compared the growth rates of non-axisymmetric modes between the experimental data and the mathematical models. Taking the contact line speed directly from the axisymmetric spreading data and the contact angle from the leading order fit, we discussed the size of the nondimensional parameters and determined that the general Tanner model (see § 4.4) is the most appropriate model to reflect the data. The large contact angle model could not provide a sufficient qualitative comparison to the experimental data due to the solutions being limited to where the contact angle is fixed. We found good qualitative agreement between the thin film general Tanner model and the data, with good quantitative agreement for the $m = 1$ mode within the range of possible solutions, even though the contact angle is not small. When the contact angle is taken so that the leading order radius is exactly the experimental spin-up radius, the quantitative agreement is good for the first three wavenumbers and the dominant mode as a function of rotation rate is well predicted for each volume. However, in this case the resultant contact angles can be unphysical for greater rotation rates. A possible explanation of this is that the contact angle acts to offset the discrepancy between the assumed steady initial condition of the model, and the unsteady experimental initial condition. This analysis demonstrated that the strength of the thin film model is in its relative simplicity, and although in some regimes it may be insufficient it was capable of qualitative and quantitative match to the experimental data we collected.

9.2 Closing remarks and future work

There are many possible avenues for further development of the mathematical models in this thesis. In chapter 8 we discussed that the discrepancy between leading order solutions and the experimental spin-up radius is likely caused due to velocities being induced during the acceleration phase of the experiment. The mathematical modelling in this thesis assumes that the rotation rate is achieved instantaneously, and therefore it may be interesting to investigate the acceleration phase with the aim of understanding how the contact line instability is affected.

The industrial process which is a foundation for this investigation generally includes an evaporative phase [17]. Therefore, a possible extension to the presented models is to couple the equations of motion with a diffusion equation for fluid concentration, modelling the effect of evaporation in similar fashion to previous studies by Meyerhofer [18], Jenekhe and Schuldt [21] and Riesfeld *et al.* [23, 24].

In each comparison of the leading order models to the experimental data we determined that the contact angle is large. However, the model presented in chapter 7, which described the linear stability of the system when the contact angle is $\mathcal{O}(1)$, proved insufficient to describe the experimental data for a number of reasons. First, the free surface perturbation was constructed to satisfy the boundary conditions, which proved successful when the contact angle is small, but produced inconsistent results for larger contact angles. Therefore, it is instructive to assemble and solve the full eigenvalue problem for the free surface perturbation and growth rate, using the framework provided in this thesis. Second, we found that due to the capillary number being small, the fixed contact angle model was insufficient to reproduce the experimental data, since it is valid where the capillary number is large. Therefore, similarly to the thin film case it would be natural to consider a Tanner boundary condition to model the contact angle, when solving the full eigenvalue problem for $\mathcal{O}(1)$ contact angles.

Appendix A

Derivation of Governing Equations

Considering the rotating system described in § 3.1 and shown in figure 3.1, the rotation rate is constant about the vertical axis, so that the rotation vector is $\boldsymbol{\Omega} = \Omega\hat{\boldsymbol{z}}$. We define the rotation angle, $\psi(t) = \Omega t$, and introduce unit vectors $\hat{\boldsymbol{i}}$ and $\hat{\boldsymbol{j}}$ in the rotating frame defined as

$$\hat{\boldsymbol{i}}(t) = \cos(\psi(t))\hat{\boldsymbol{x}} + \sin(\psi(t))\hat{\boldsymbol{y}}, \tag{A.0.1}$$

$$\hat{\boldsymbol{j}}(t) = -\sin(\psi(t))\hat{\boldsymbol{x}} + \cos(\psi(t))\hat{\boldsymbol{y}}, \tag{A.0.2}$$

expressed in terms of stationary frame unit vectors $\hat{\boldsymbol{x}}$ and $\hat{\boldsymbol{y}}$. Figure A.1 shows a diagram of this rotating coordinate system. Differentiating the above unit vectors with respect to time gives

$$\frac{\mathrm{d}}{\mathrm{d}t}\hat{\boldsymbol{i}}(t) = \Omega(-\sin(\psi(t))\hat{\boldsymbol{x}} + \cos(\psi(t))\hat{\boldsymbol{y}}) = \Omega\hat{\boldsymbol{j}}, \tag{A.0.3}$$

$$\frac{\mathrm{d}}{\mathrm{d}t}\hat{\boldsymbol{j}}(t) = -\Omega(\cos(\psi(t))\hat{\boldsymbol{x}} + \sin(\psi(t))\hat{\boldsymbol{y}}) = -\Omega\hat{\boldsymbol{i}}. \tag{A.0.4}$$

This can be generalised such that

$$\frac{\mathrm{d}\hat{\boldsymbol{p}}}{\mathrm{d}t} = \boldsymbol{\Omega} \times \hat{\boldsymbol{p}}, \tag{A.0.5}$$

where $\hat{\boldsymbol{p}}$ is either rotation unit vector, (A.0.1) or (A.0.2). If we define a function within the rotating frame using $\hat{\boldsymbol{i}}$, $\hat{\boldsymbol{j}}$, and $\hat{\boldsymbol{k}} = \hat{\boldsymbol{z}}$,

$$\boldsymbol{f}(t) = f_1(t)\hat{\boldsymbol{i}} + f_2(t)\hat{\boldsymbol{j}} + f_3(t)\hat{\boldsymbol{k}}, \tag{A.0.6}$$

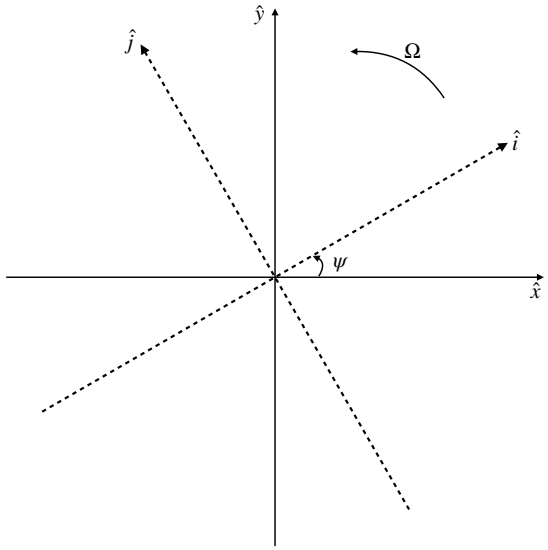


Figure A.1: Top view of coordinate system rotating about the vertical axis with constant rotation rate Ω. Here solid lines are at time $t = 0$ while the dashed line at some time $t > 0$, so that we have rotation angle $\psi = \Omega t$.

and examine the derivative with respect to time, using the product rule and (A.0.6)

$$\begin{aligned}
\frac{\mathrm{d}\boldsymbol{f}}{\mathrm{d}t} &= \frac{\mathrm{d}f_1}{\mathrm{d}t}\hat{\boldsymbol{i}} + f_1\frac{\mathrm{d}\hat{\boldsymbol{i}}}{\mathrm{d}t} + \frac{\mathrm{d}f_2}{\mathrm{d}t}\hat{\boldsymbol{j}} + f_2\frac{\mathrm{d}\hat{\boldsymbol{j}}}{\mathrm{d}t} + \frac{\mathrm{d}f_3}{\mathrm{d}t}\hat{\boldsymbol{k}} + f_3\frac{\mathrm{d}\hat{\boldsymbol{k}}}{\mathrm{d}t} && \text{(A.0.7)}\\
&= \frac{\mathrm{d}f_1}{\mathrm{d}t}\hat{\boldsymbol{i}} + \frac{\mathrm{d}f_2}{\mathrm{d}t}\hat{\boldsymbol{j}} + \frac{\mathrm{d}f_3}{\mathrm{d}t}\hat{\boldsymbol{k}} + \left[\boldsymbol{\Omega}\times\left(f_1(t)\hat{\boldsymbol{i}} + f_2(t)\hat{\boldsymbol{j}} + f_3(t)\hat{\boldsymbol{k}}\right)\right] && \text{(A.0.8)}\\
&= \left[\left(\frac{\mathrm{d}}{\mathrm{d}t}\right)_R + \boldsymbol{\Omega}\times\right]\boldsymbol{f}(t), && \text{(A.0.9)}
\end{aligned}$$

where terms in the rotating frame are denoted subscript R. Therefore, if we have a direction vector $\boldsymbol{r}$ defined in the rotating coordinate system, the velocity vector in a stationary frame, denoted subscript i, is given by

$$\boldsymbol{v_i} = \frac{\mathrm{d}\boldsymbol{r}}{\mathrm{d}t} = \left(\frac{\mathrm{d}\boldsymbol{r}}{\mathrm{d}t}\right)_R + \boldsymbol{\Omega}\times\boldsymbol{r}, \tag{A.0.10}$$

and hence, the rotating frame velocity is

$$\boldsymbol{v}_R = \boldsymbol{v_i} - \boldsymbol{\Omega}\times\boldsymbol{r}. \tag{A.0.11}$$

We can find the acceleration by differentiating (A.0.10) again, recalling that the rotation is constant,

$$\boldsymbol{a_i} = \frac{\mathrm{d}\boldsymbol{v_i}}{\mathrm{d}t} = \left[\left(\frac{\mathrm{d}}{\mathrm{d}t}\right)_R + \boldsymbol{\Omega}\times\right](\boldsymbol{v}_R + \boldsymbol{\Omega}\times\boldsymbol{r}) \tag{A.0.12}$$

$$= \frac{\mathrm{d}\boldsymbol{v}_R}{\mathrm{d}t} + 2\boldsymbol{\Omega}\times\boldsymbol{v}_R + \boldsymbol{\Omega}\times(\boldsymbol{\Omega}\times\boldsymbol{r}). \tag{A.0.13}$$

For a fluid particle, we look in a Lagrangian frame of reference moving with the fluid flow, hence

$$\left(\frac{\mathrm{D}\boldsymbol{u}}{\mathrm{D}t}\right)_i = \left(\frac{\mathrm{D}\boldsymbol{u}}{\mathrm{D}t}\right)_R + 2\boldsymbol{\Omega}\times\boldsymbol{v}_R + \boldsymbol{\Omega}\times(\boldsymbol{\Omega}\times\boldsymbol{r}). \tag{A.0.14}$$

Performing Newton's second law on a fluid parcel in a stationary frame under gravity and substituting (A.0.14), for the acceleration in the stationary frame gives

$$\rho\left(\frac{\mathrm{D}\boldsymbol{u}}{\mathrm{D}t}\right)_R = -\nabla p - \rho\boldsymbol{\Omega}\times(\boldsymbol{\Omega}\times\boldsymbol{x}) - 2\rho\boldsymbol{\Omega}\times\boldsymbol{u} - \rho g\hat{\boldsymbol{z}} + \mu\nabla^2\boldsymbol{u}. \tag{A.0.15}$$

The left hand side is analogous to mass multiplied by acceleration in the rotating frame, and is equal to the sum of static pressure, centrifugal force, Coriolis force, gravitational force and viscous forces.

Appendix B

Discretisation of eigenvalue problem

In this appendix we detail the discretisation of the eigenvalue problem (4.1.4) both for axisymmetric and non-axisymmetric perturbations. In § 4.1.3 we described the boundary conditions depending on the wavenumber, m. In the axisymmetric case where $m = 0$, the eigenvalue equation (4.1.4) is coupled with an integral condition for the conservation of volume (4.1.27), while when $m \geqslant 1$, the boundary conditions are more simple to discretise.

For clarity, the eigenvalue problem (4.1.4) is repeated here

$$\mathcal{L}_2[\mathcal{L}_1(h_1)] = C\sigma_m h_1, \tag{B.0.1}$$

where the linear operators $\mathcal{L}_1$ and $\mathcal{L}_2$ are defined as,

$$\mathcal{L}_1[\Phi] = \left[\frac{\mathrm{d}^2}{\mathrm{d}r^2} + \frac{1}{r}\frac{\mathrm{d}}{\mathrm{d}r} - \frac{m^2}{r^2} - G\right]\Phi, \tag{B.0.2}$$

$$\mathcal{L}_2[\Phi] = -\left[\left\{\frac{1}{3}h_0^3 + \frac{\alpha}{3}h_0\right\}\frac{\mathrm{d}^2}{\mathrm{d}r^2} + \frac{1}{r}\left(r\left\{\frac{1}{3}h_0^3 + \frac{\alpha}{3}h_0\right\}\right)'\frac{\mathrm{d}}{\mathrm{d}r} - \frac{m^2}{r^2}\left\{\frac{1}{3}h_0^3 + \frac{\alpha}{3}h_0\right\}\right]\Phi, \tag{B.0.3}$$

respectively.

B.1 Non-axisymmetric perturbations

We start with the simpler case where perturbations are non-axisymmetric, for wavenumbers $m = 1, 2, 3, \ldots$. The boundary conditions to the eigenvalue equation

(B.0.1), first stated in § 4.1.3, are the velocity regularity conditions which depend on m,

$$m = 1: \quad h_1(0) = 0, \quad h_1''(0) = 0, \quad h_1'''(0) = 0, \tag{B.1.1}$$

$$m = 2: \quad h_1(0) = 0, \quad h_1'(0) = 0, \quad h_1'''(0) = 0, \tag{B.1.2}$$

$$m \geqslant 3: \quad h_1(0) = 0, \quad h_1'(0) = 0, \quad h_1''(0) = 0, \tag{B.1.3}$$

and the combined Tanner condition (4.1.15),

$$\sigma_m h_1(R_0) = -q \left\{ h_0''(R_0) h_1(R_0) + h_1'(R_0) \right\}. \tag{B.1.4}$$

The fixed domain $[0, R_0]$ defined by the leading order solution is represented by N points, denoted r_i, with a finite difference of $\mathrm{d}r = R_0/(N-1)$ between points. The corresponding value of $h_1(r_i)$ is denoted h_i. The boundary conditions at $r = 0$ are discretised to second order accuracy using forward finite differences. Therefore, the first three derivatives of h_1 at $r = 0$ are approximated as

$$h_1(r_1 = 0) = h_1, \tag{B.1.5}$$

$$h_1'(r_1 = 0) = \frac{-3h_1 + 4h_2 - 1h_3}{2\mathrm{d}r}, \tag{B.1.6}$$

$$h_1''(r_1 = 0) = \frac{2h_1 - 5h_2 + 4h_3 - h_4}{\mathrm{d}r^2}, \tag{B.1.7}$$

$$h_1'''(r_1 = 0) = \frac{-5h_1 + 18h_2 - 24h_3 + 14h_4 - 3h_5}{\mathrm{d}r^3}, \tag{B.1.8}$$

where depending on the wavenumber, three of the above four expressions are set equal to zero. At the other end of the domain, there is a single boundary condition (B.1.4), which is discretised about the point $r_N = R_0$ using a second order backward finite difference approximation,

$$\sigma_m h_N = -\frac{q h_{N-2}}{2\mathrm{d}r} + \frac{2q h_{N-1}}{\mathrm{d}r} - q \left\{ h_0''(R_0) + \frac{3}{2\mathrm{d}r} \right\} h_N. \tag{B.1.9}$$

The eigenvalue equation (B.0.1) is of the form

$$C\sigma_m h_1 = f_4(r)\frac{\mathrm{d}^4 h_1}{\mathrm{d}r^4} + f_3(r)\frac{\mathrm{d}^3 h_1}{\mathrm{d}r^3} + f_2(r)\frac{\mathrm{d}^2 h_1}{\mathrm{d}r^2} + f_1(r)\frac{\mathrm{d}h_1}{\mathrm{d}r} + f_0(r)h_1, \tag{B.1.10}$$

where the subscript of the coefficient functions, f_i, represents the order of the corresponding derivative. Each derivative is discretised using a five point central

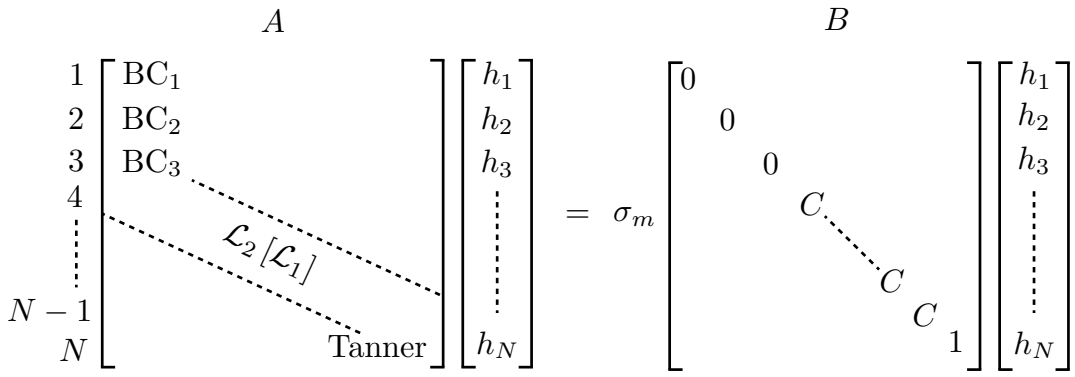


Figure B.1: Schematic diagram of the structure of the discretisation of the eigenvalue problem (B.0.1), for non-axisymmetric perturbations $m = 1, 2, 3, ...$

difference interpolant, surrounding r_i, while the coefficient function is evaluated at r_i. When a central difference approximation cannot be used at r_{N-1}, a five point backward difference approximation is used. The eigenvalue problem and boundary conditions are assembled into a generalised eigenvalue matrix problem, $Ah = \sigma Bh$, where A and B are $N \times N$ matrices, and h is a row vector. The first three rows in the hand matrices correspond to the boundary conditions at $r = 0$, while the final row represents to the combined Tanner condition (B.1.9). The remaining $N - 4$ rows are given by the finite difference approximation of the eigenvalue equation (B.0.1), where rows 4 to $N - 2$ in A represent the approximation of the linear operator using central differences, while row $N - 1$ uses a backward finite difference scheme. Each of the boundary conditions which could be applied at $r = 0$ do not contain the eigenvalue, σ_m, and therefore the first three rows in the right hand matrix, B, contain only zeros. However, the Tanner boundary condition (B.1.9) does contain σ_m, and so the entry on row N column N of B is one. The remaining entries in rows 4 to $N-1$ in the right hand matrix B are given by C down the leading diagonal. Figure B.1 shows a diagram of the structure of each of the matrices A and B as described above.

B.2 Axisymmetric perturbations

The four boundary conditions for the eigenvalue equation (B.0.1) when considering axisymmetric perturbations are two regularity conditions at $r = 0$ (4.1.29) (a, b), an integral condition (4.1.29) (c), and the combined Tanner condition (4.1.15).

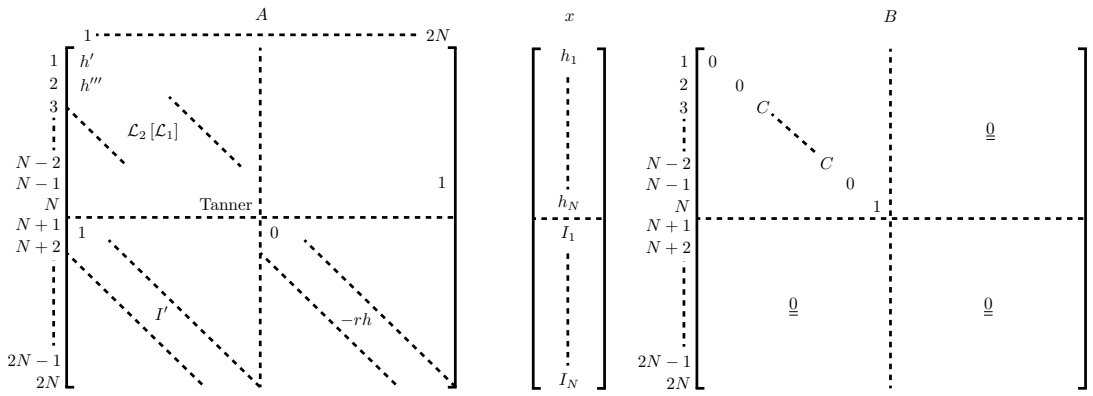


Figure B.2: Schematic diagram of the structure of the discretisation of the eigenvalue problem (B.0.1), for axisymmetric perturbations $m = 0$.

To impose the integral condition we define the variable I, which represents the indefinite integral

$$I = \int rh_1(r)\,\mathrm{d}r, \tag{B.2.1}$$

which, by differentiating and enforcing appropriate boundary conditions, results in a differential equation and boundary condition which represents the integral boundary condition (4.1.29) (c),

$$\frac{\mathrm{d}I}{\mathrm{d}r} - rh_1 = 0, \quad I(0) = 0, I(1) = 0. \tag{B.2.2}$$

The integral ODE (B.2.2) is coupled with the eigenvalue equation (4.1.4) and the remaining boundary conditions.

When discretising the ODE for I (B.2.2) it is important to avoid a checkerboarding problem, which occurs where the values of I at odd numbered nodes are independent of those at the even numbered nodes. Hence, we discretise (B.2.2) at the midpoints between grid points

$$I_1 = 0, \tag{B.2.3}$$

$$\frac{I_{i-1} + I_i}{\mathrm{d}r} - r_{i-\frac{1}{2}}\left[\frac{h_{i-1}}{2} + \frac{h_i}{2}\right] = 0, \quad i = 2, ..., N \tag{B.2.4}$$

$$I_N = 0, \tag{B.2.5}$$

giving a total of $N + 1$ equations. The differentiability and symmetry conditions (4.1.29) (a, b) are discretised using forward finite differences while the combined

Tanner law is discretised using backward finite differences, giving another 3 equations. The remaining $N-4$ equations come from eigenvalue equation which is discretised centrally using a five point interpolant for each derivative, while the coefficient of each derivative is evaluated at the point, r_i. This gives a total of $2N$ equations, formed into a generalised eigenvalue problem of the form $Ax = \sigma Bx$, where the first N entries in the eigenfunction x give $h_1(r)$, while the second N entries give I. The right hand matrix, B, is largely zeros other than on the leading diagonal on rows $i = 3, ..., N-2$, where it is C, due to the right hand side of the eigenvalue equation (B.0.1), and $i = N$ where the entry is 1 to reflect the combined Tanner condition (4.1.15). Figure B.2 shows the structure of each of the matrices A and B along with the eigenfunction x, as described above.

Note that, in both the axisymmetric and non-axisymmetric cases the difference in the implementation between the combined Tanner boundary condition (4.1.15) and the combined fixed contact angle condition (5.2.5) amounts to changing a single value in the matrix B and taking $C = 1$. Specifically, in both the axisymmetric and non-axisymmetric case the entry on row N column N is changed from a one to a zero when the fixed contact angle condition is imposed.

Appendix C

Transformations for comparison of models

Since the thin film model I and model with $\mathcal{O}(1)$ contact angle II are nondimensionalised in different ways, we must first establish the transformations between cases. Considering the nondimensional parameters ϕ and G in the thin film case

$$\phi_{\mathrm{I}} = \frac{\rho\Omega^2 V_f}{\gamma\theta_c^2}, \quad G_{\mathrm{I}} = \frac{\rho g V_f^{2/3}}{\gamma\theta_c^{2/3}}, \tag{C.0.1}$$

and in the $\mathcal{O}(1)$ contact angle case

$$\phi_{\mathrm{II}} = \frac{\rho\Omega^2 V_f}{\gamma}, \quad G_{\mathrm{II}} = \frac{\rho g V_f^{2/3}}{\gamma}. \tag{C.0.2}$$

Therefore, we find that

$$\phi_{\mathrm{II}} = \theta_c^2\phi_{\mathrm{I}}, \quad G_{\mathrm{II}} = \theta_c^{2/3} G_{\mathrm{I}}. \tag{C.0.3}$$

In both cases, the lengthscale is determined using the volume,

$$V_f^{1/3} = \theta_c^{1/3} L_{\mathrm{I}} = L_{\mathrm{II}} \quad \Rightarrow \quad L_{\mathrm{II}} = \theta_c^{1/3} L_{\mathrm{I}} \tag{C.0.4}$$

Next, the dimensional radial length scales like

$$r = L_{\mathrm{II}} r_{\mathrm{II}} = L_{\mathrm{I}} r_{\mathrm{I}} = \theta_c^{-1/3} L_{\mathrm{II}} r_{\mathrm{I}} \quad \Rightarrow \quad r_{\mathrm{II}} = \theta_c^{-1/3} r_{\mathrm{I}}. \tag{C.0.5}$$

Whereas, the vertical length scale

$$z = h(r,\varphi,t) = L_{\mathrm{II}} h_{\mathrm{II}}(r_{\mathrm{II}},\varphi,t) = \theta_c L_{\mathrm{I}} h_{\mathrm{I}}(r_{\mathrm{I}},\varphi,t) = \theta_c^{2/3} L_{\mathrm{II}} h_{\mathrm{I}}(r_{\mathrm{I}},\varphi,t) \tag{C.0.6}$$

therefore

$$h_{\mathrm{II}}(r_{\mathrm{II}},\varphi,t) = \theta_c^{2/3} h_{\mathrm{I}}(\theta_c^{-1/3} r_{\mathrm{I}},\varphi,t). \tag{C.0.7}$$

The scalings for each of the derivatives of h are calculated using the chain rule giving the nth derivative as

$$\frac{\partial^n h_{\mathrm{II}}}{\partial r_{\mathrm{II}}^n} = \theta_c^{\frac{2+n}{3}} \frac{\partial^n h_{\mathrm{I}}}{\partial r_{\mathrm{I}}^n}. \tag{C.0.8}$$

The velocity scales are

$$U_{\mathrm{I}} = \frac{\gamma\theta_c^3}{\mu}, \quad U_{\mathrm{II}} = \frac{\gamma}{\mu} \quad \Rightarrow \quad U_{\mathrm{II}} = \theta_c^{-3} U_{\mathrm{I}}, \tag{C.0.9}$$

hence, the horizontal velocity scales like

$$u(r,z) = U_{\mathrm{I}} u_{\mathrm{I}} = U_{\mathrm{II}} u_{\mathrm{II}} = \theta_c^{-3} U_{\mathrm{I}} u_{\mathrm{II}} \quad \Rightarrow \quad u_{\mathrm{II}} = \theta_c^3 u_{\mathrm{I}}, \tag{C.0.10}$$

while the vertical velocity scales like

$$w(r,z) = \theta_c U_{\mathrm{I}} w_{\mathrm{I}} = U_{\mathrm{II}} w_{\mathrm{II}} = \theta_c^{-3} U_{\mathrm{I}} w_{\mathrm{II}} \quad \Rightarrow \quad w_{\mathrm{II}} = \theta_c^4 w_{\mathrm{I}}. \tag{C.0.11}$$

The pressure scale in each case is given by

$$P_{\mathrm{I}} = \frac{\mu U_{\mathrm{I}}}{L_{\mathrm{I}}\theta_c^2}, \quad P_{\mathrm{II}} = \frac{\mu U_{\mathrm{II}}}{L_{\mathrm{II}}} = \frac{\mu U_{\mathrm{I}}}{L_{\mathrm{I}}\theta_c^{10/3}} \quad \Rightarrow \quad P_{\mathrm{II}} = \theta_c^{-4/3} P_{\mathrm{I}}, \tag{C.0.12}$$

using the relationships (C.0.4, C.0.9). Therefore,

$$p = P_{\mathrm{I}} p_{\mathrm{I}} = P_{\mathrm{II}} p_{\mathrm{II}} = \theta_c^{-4/3} P_{\mathrm{I}} p_{\mathrm{II}} \quad \Rightarrow \quad p_{\mathrm{II}} = \theta_c^{4/3} p_{\mathrm{I}}. \tag{C.0.13}$$

If we consider the dimensional slip conditions used in the thin film model I

$$u = \frac{\alpha}{3h}\frac{\partial u}{\partial z}, \quad v = \frac{\alpha}{3h}\frac{\partial v}{\partial z}. \tag{C.0.14}$$

Since u, v scale in the same way we need only consider one of the slip laws in both transformations

$$u_{\mathrm{I}} = \frac{\alpha}{3L_{\mathrm{I}}^2\theta_c^2 h_{\mathrm{I}}}\frac{\partial u_{\mathrm{I}}}{\partial z_{\mathrm{I}}} = \frac{\alpha_{\mathrm{I}}}{3h_{\mathrm{I}}}\frac{\partial u_{\mathrm{I}}}{\partial z_{\mathrm{I}}}, \quad u_{\mathrm{II}} = \frac{\alpha}{3L_{\mathrm{II}}^2 h_{\mathrm{II}}}\frac{\partial u_{\mathrm{II}}}{\partial z_{\mathrm{II}}} = \frac{\alpha_{\mathrm{II}}}{3h_{\mathrm{II}}}\frac{\partial u_{\mathrm{II}}}{\partial z_{\mathrm{II}}}, \tag{C.0.15}$$

hence

$$\alpha = \alpha_{\mathrm{I}} L_{\mathrm{I}}^2\theta_c^2 = \alpha_{\mathrm{II}} L_{\mathrm{II}}^2 \quad \Rightarrow \quad \alpha_{\mathrm{II}} = \theta_c^{4/3}\alpha_{\mathrm{I}}. \tag{C.0.16}$$

Within each model the growth rate is given by the velocity at the contact line, and therefore

$$\sigma_{\mathrm{II}} = \theta_c^3\sigma_{\mathrm{I}}. \tag{C.0.17}$$

Overall, we have identified appropriate transformations so that approximate solutions within the thin film limit can be compared to the full numerical solution within nondimensional space, thereby verifying the numerical method.

Bibliography

[1] P.G. De Gennes. Wetting: statics and dynamics. *Reviews of Modern Physics*, 57(3):827, 1985.

[2] T.G. Myers. Thin films with high surface tension. *SIAM Review*, 40(3):441–462, 1998.

[3] S.H. Davis. Interfacial fluid dynamics. In G.K. Batchelor H.K. Moffatt, M.G. Worster, editor, *Perspectives in Fluid Dynamics : A collective introduction to current research*, chapter 1, pages 1–51. Cambridge University Press, Cambridge, 2003.

[4] A. Oron, S.H. Davis, and S.G. Bankoff. Long-scale evolution of thin liquid films. *Reviews of Modern Physics*, 69(3):931–980, 1997.

[5] R.V. Craster and O.K. Matar. Dynamics and stability of thin liquid films. *Reviews of Modern Physics*, 81(3):1131–1198, 2009.

[6] C.W. Frank, V. Rao, M.M. Despotopoulou, R.F.W. Pease, W.D. Hinsberg, R.D. Miller, and J.F. Rabolt. Structure in thin and ultrathin spin-cast polymer films. *Science*, 273(5277):912–915, 1996.

[7] D.B. Hall, P. Underhill, and J.M. Torkelson. Spin coating of thin and ultrathin polymer films. *Polymer Engineering & Science*, 38(12):2039–2045, 1998.

[8] F.A. Denis, P. Hanarp, D.S. Sutherland, and Y.F. Dufrêne. Fabrication of nanostructured polymer surfaces using colloidal lithography and spin-coating. *Nano Letters*, 2(12):1419–1425, 2002.

[9] S. Arscott. The limits of edge bead planarization and surface levelling in

spin-coated liquid films. *Journal of Micromechanics and Microengineering*, 30(2):25003–25013, 2020.

[10] P. Jasinski, S. Molin, M. Gazda, V. Petrovsky, and H.U. Anderson. Applications of spin coating of polymer precursor and slurry suspensions for solid oxide fuel cell fabrication. *Journal of Power Sources*, 194(1):10–15, 2009.

[11] J. Britt and C. Ferekides. Thin-film CdS/CdTe solar cell with 15.8% efficiency. *Applied Physics Letters*, 62(22):2851–2852, 1993.

[12] J.H. Heo, D.H. Song, and S.H. Im. Planar $CH_3NH_3PbBr_3$ hybrid solar cells with 10.4% power conversion efficiency, fabricated by controlled crystallization in the spin-coating process. *Advanced Materials*, 26(48):8179–8183, 2014.

[13] F. Yang, D.W. Kang, and Y.S. Kim. Improved interface of $ZnO/CH_3NH_3PbI_3$ by a dynamic spin-coating process for efficient perovskite solar cells. *RSC Advances*, 7(31):19030–19038, 2017.

[14] Y. Kim, A. DiVenere, G.K.L. Wong, J.B. Ketterson, S. Cho, and J.R. Meyer. Structural and thermoelectric transport properties of Sb_2Te_3 thin films grown by molecular beam epitaxy. *Journal of Applied Physics*, 91(2):715–718, 2002.

[15] D.B. Mitzi, L.L. Kosbar, C.E. Murray, M. Copel, and A. Afzali. High-mobility ultrathin semiconducting films prepared by spin coating. *Nature*, 428(6980):299–303, 2004.

[16] J. Moreira, A.C. Vale, and N.M. Alves. Spin-coated freestanding films for biomedical applications. *Journal of Materials Chemistry B*, 9(18):3778–3799, 2021.

[17] M.D. Tyona. A theoritical study on spin coating technique. *Advances in Materials Research*, 2(4):195–208, 2013.

[18] D. Meyerhofer. Characteristics of resist films produced by spinning. *Journal of Applied Physics*, 49(7):3993–3997, 1978.

[19] A.G. Emslie, F.T. Bonner, and L.G. Peck. Flow of a viscous liquid on a rotating disk. *Journal of Applied Physics*, 29(5):858–862, 1958.

[20] R.G. Larson and T.J. Rehg. Spin coating. *Liquid Film Coating: Scientific Principles and their Technological Implications*, pages 709–734, 1997.

[21] S.A. Jenekhe and S.B. Schuldt. Coating flow of non-Newtonian fluids on a flat rotating disk. *Industrial & Engineering Chemistry Fundamentals*, 23(4):432–436, 1984.

[22] C.J. Lawrence. The mechanics of spin coating of polymer films. *The Physics of Fluids*, 31(10):2786–2795, 1988.

[23] B. Reisfeld, S.G. Bankoff, and S.H. Davis. The dynamics and stability of thin liquid films during spin coating. I. Films with constant rates of evaporation or absorption. *Journal of applied physics*, 70(10):5258–5266, 1991.

[24] B. Reisfeld, S.G. Bankoff, and S.H. Davis. The dynamics and stability of thin liquid films during spin coating. II. Films with unit-order and large peclet numbers. *Journal of applied physics*, 70(10):5267–5277, 1991.

[25] A. Münch, C.P. Please, and B. Wagner. Spin coating of an evaporating polymer solution. *Physics of Fluids*, 23(10):102101, 2011.

[26] F. Melo, J.F. Joanny, and S. Fauve. Fingering instability of spinning drops. *Physical Review Letters*, 63(18):1958–1961, 1989.

[27] E.B. Dussan. On the spreading of liquids on solid surfaces: static and dynamic contact lines. *Annual Review of Fluid Mechanics*, 11:371–400, 1979.

[28] T. Young. An essay on the cohesion of fluids. *Philosophical Transactions of the Royal Society of London*, 95:65–87, 1805.

[29] W.A. Zisman. Surface energetics of wetting spreading and adhesion. *Journal of Paint Technology*, 44:42–57, 1972.

[30] L.H. Tanner. The spreading of silicone oil drops on horizontal surfaces. *Journal of Physics D: Applied Physics*, 12(9):1473–1484, 1979.

[31] H.P. Greenspan. On the motion of a small viscous droplet that wets a surface. *Journal of Fluid Mechanics*, 84(1):125–143, 1978.

[32] P. Ehrhard and S.H. Davis. Non-isothermal spreading of liquid drops on horizontal plates. *Journal of Fluid Mechanics*, 229(1):365–388, 1991.

[33] L.M. Hocking. The wetting of a plane surface by a fluid. *Physics of Fluids*, 7(6):1214–1220, 1995.

[34] C.W. Extrand. Model for contact angles and hysteresis on rough and ultraphobic surfaces. *Langmuir*, 18(21):7991–7999, 2002.

[35] L. Gao and T.J. McCarthy. Contact angle hysteresis explained. *Langmuir*, 22(14):6234–6237, 2006.

[36] G. Whyman, E. Bormashenko, and T. Stein. The rigorous derivation of Young, Cassie–Baxter and Wenzel equations and the analysis of the contact angle hysteresis phenomenon. *Chemical Physics Letters*, 450(4):355–359, 2008.

[37] L. Makkonen. A thermodynamic model of contact angle hysteresis. *The Journal of Chemical Physics*, 147(6):64703, 2017.

[38] S. Wu and M. Ma. A contact angle hysteresis model based on the fractal structure of contact line. *Journal of Colloid and Interface Science*, 505:995–1000, 2017.

[39] P. Yue. Thermodynamically consistent phase-field modelling of contact angle hysteresis. *Journal of Fluid Mechanics*, 899:A15, 2020.

[40] H.B. Eral, D.J.C.M. 't Mannetje, and J.M. Oh. Contact angle hysteresis: a review of fundamentals and applications. *Colloid and Polymer Science*, 291(2):247–260, 2013.

[41] C.W. Extrand. Origins of wetting. *Langmuir*, 32(31):7697–7706, 2016.

[42] I.S. McKinley, S.K. Wilson, and B.R. Duffy. Spin coating and air-jet blowing of thin viscous drops. *Physics of Fluids*, 11(1):30–47, 1999.

[43] I.S. McKinley and S.K. Wilson. The linear stability of a drop of fluid during spin coating or subject to a jet of air. *Physics of Fluids*, 14(1):133–142, 2002.

[44] K.E.R. Boettcher and P. Ehrhard. Contact-line instability of liquids spreading on top of rotating substrates. *European Journal of Mechanics-B/Fluids*, 43:33–44, 2014.

[45] R.L. Hoffman. A study of the advancing interface. i. interface shape in liquid—gas systems. *Journal of Colloid and Interface Science*, 50(2):228–241, 1975.

[46] S.F. Kistler. Hydrodynamics of wetting. *Wettability*, 6:311–430, 1993.

[47] L.M. Hocking. A moving fluid interface. Part 2. The removal of the force singularity by a slip flow. *Journal of Fluid Mechanics*, 79(2):209–229, 1977.

[48] L.M. Hocking. Sliding and spreading of thin two-dimensional drops. *The Quarterly Journal of Mechanics and Applied Mathematics*, 34(1):37–55, 1981.

[49] L.M. Hocking and A.D. Rivers. The spreading of a drop by capillary action. *Journal of Fluid Mechanics*, 121:425–442, 1982.

[50] L.M. Hocking. The spreading of a thin drop by gravity and capillarity. *The Quarterly Journal of Mechanics and Applied Mathematics*, 36(1):55–69, 1983.

[51] C. Huh and L.E. Scriven. Hydrodynamic model of steady movement of a solid/liquid/fluid contact line. *Journal of Colloid And Interface Science*, 35(1):85–101, 1971.

[52] E.B. Dussan V. and S.H. Davis. On the motion of a fluid-fluid interface along a solid surface. *Journal of Fluid Mechanics*, 65(1):71–95, 1974.

[53] M.A. Spaid and G.M. Homsy. Stability of Newtonian and viscoelastic dynamic contact lines. *Physics of Fluids*, 8(2):460–478, 1996.

[54] W.B. Hardy. The spreading of fluids on glass. *The London, Edinburgh, and Dublin Philosophical Magazine and Journal of Science*, 38(223):49–55, 1919.

[55] D. Beaglehole. Profiles of the precursor of spreading drops of siloxane oil on glass, fused silica, and mica. *The Journal of Physical Chemistry*, 93(2):893–899, 1989.

[56] E.O. Tuck and L.W. Schwartz. A numerical and asymptotic study of some third-order ordinary differential equations relevant to draining and coating flows. *SIAM Review*, 32(3):453–469, 1990.

[57] M.N. Popescu, G. Oshanin, S. Dietrich, and A.M. Cazabat. Precursor films in wetting phenomena. *Journal of Physics: Condensed Matter*, 24(24):243102, 2012.

[58] N. Fraysse and G.M. Homsy. An experimental study of rivulet instabilities in centrifugal spin coating of viscous Newtonian and non-Newtonian fluids. *Physics of Fluids*, 6(4):1491–1504, 1994.

[59] S.M. Troian, E. Herbolzheimer, S.A. Safran, and J.F. Joanny. Fingering instabilities of driven spreading films. *Europhysics Letters*, 10(1):25–30, 1989.

[60] M.A. Spaid and G.M. Homsy. Stability of viscoelastic dynamic contact lines: An experimental study. *Physics of Fluids*, 9(4):823–832, 1997.

[61] M.W Wang and F.C. Chou. Fingering instability and maximum radius at high rotational bond number. *Journal of the Electrochemical Society*, 148(5):G283, 2001.

[62] K.E. Holloway, P. Habdas, N. Semsarillar, K. Burfitt, and J.R. de Bruyn. Spreading and fingering in spin coating. *Physical Review E*, 75(4):046308, 2007.

[63] K.E. Holloway, H. Tabuteau, and J.R. de Bruyn. Spreading and fingering in a yield-stress fluid during spin coating. *Rheologica Acta*, 49:245–254, 2010.

[64] F.C. Chou, C.C Lai, and T.S. Zen. Dynamic contact angle of spreading thin film on a rotating disk. *Japanese Journal of Applied Physics*, 47(12R):8989, 2008.

[65] M. Blank and P. Ehrhard. Experiments on the spreading of silicone oil droplets on horizontal rotating plates. *Proceedings in Applied Mathematics and Mechanics*, 14(1):677–678, 2014.

[66] I. Veretennikov, A. Agarwal, A. Indeikina, and H.C. Chang. Unusual contact-line dynamics of thick films and drops. *Journal of Colloid and Interface Science*, 215(2):425–440, 1999.

[67] M. Kulkarni, S. Sahoo, P. Doshi, and A.V. Orpe. Fingering instability of a suspension film spreading on a spinning disk. *Physics of Fluids*, 28(6):63303, 2016.

[68] S. Sahoo, A.V. Orpe, and P. Doshi. Spreading dynamics of superposed liquid drops on a spinning disk. *Physics of Fluids*, 30(1):12110, 2018.

[69] C. Josserand and S.T. Thoroddsen. Drop impact on a solid surface. *Annual Review of Fluid Mechanics*, 48:365–391, 2016.

[70] J.Y. Li, X.F. Yuan, and Q. Han. Time evolutions of water drops impacting on a rotating disk. *Advanced Materials Research*, 354:609–614, 2012.

[71] J.Y. Li, X.F. Yuan, Q. Han, and G. Xi. Impact patterns and temporal evolutions of water drops impinging on a rotating disc. *Proceedings of the Institution of Mechanical Engineers, Part C: Journal of Mechanical Engineering Science*, 226(4):956–967, 2012.

[72] S. Moghtadernejad, M. Jadidi, Z. Johnson, T. Stolpe, and J. Hanson. Droplet impact dynamics on an aluminum spinning disk. *Physics of Fluids*, 33(7):72103, 2021.

[73] Y. Pan, Z. Wang, X. Zhao, W. Deng, and H. Xia. On axisymmetric dynamic spin coating with a single drop of ethanol. *Journal of Fluid Mechanics*, 951:A30, 2022.

[74] T.J. Rehg and B.G. Higgins. The effects of inertia and interfacial shear on film flow on a rotating disk. *The Physics of Fluids*, 31(6):1360–1371, 1988.

[75] A. Acrivos, M.J. Shah, and E.E. Petersen. On the flow of a non–Newtonian liquid on a rotating disk. *Journal of Applied Physics*, 31(6):963–968, 1960.

[76] E. Momoniat and D.P. Mason. Investigation of the effect of the Coriolis force on a thin fluid film on a rotating disk. *International Journal of Non-Linear Mechanics*, 33(6):1069–1088, 1998.

[77] T.G. Myers and J.P.F. Charpin. The effect of the Coriolis force on axisymmetric rotating thin film flows. *International Journal of Non-Linear Mechanics*, 36(4):629–635, 2001.

[78] T.G. Myers and M. Lombe. The importance of the Coriolis force on axisymmetric horizontal rotating thin film flows. *Chemical Engineering and Processing: Process Intensification*, 45(2):90–98, 2006.

[79] O.K. Matar, G.M. Sisoev, and C.J. Lawrence. Thin film flow over spinning discs: The effect of surface topography and flow rate modulation. *Chemical Engineering Science*, 63(8):2225–2232, 2008.

[80] A. McIntyre and L.N. Brush. Spin-coating of vertically stratified thin liquid films. *Journal of Fluid Mechanics*, 647:265–285, 2010.

[81] B.S. Dandapat and S.K. Singh. Two-layer film flow on a rotating disk: A numerical study. *International Journal of Non-Linear Mechanics*, 46(1):272–277, 2011.

[82] BS Dandapat and SK Singh. Two-layer film flow over a rotating disk. *Communications in Nonlinear Science and Numerical Simulation*, 17(7):2854–2863, 2012.

[83] P. Gurrala, P. Katre, S. Balusamy, S. Banerjee, and K.C. Sahu. Evaporation of ethanol-water sessile droplet of different compositions at an elevated substrate temperature. *International Journal of Heat and Mass Transfer*, 145:118770, 2019.

[84] Y.O. Tu. Contact line slippage of fluid flow on a rotating disk. *Journal of Colloid and Interface Science*, 116(1):237–240, 1987.

[85] S.K. Wilson, R. Hunt, and B.R. Duffy. The rate of spreading in spin coating. *Journal of Fluid Mechanics*, 413:65–88, 2000.

[86] C.J. Lawrence and W. Zhou. Spin coating of non–Newtonian fluids. *Journal of Non–Newtonian Fluid Mechanics*, 39(2):137–187, 1991.

[87] J.P.F Charpin, M. Lombe, and T.G. Myers. Spin coating of non–Newtonian fluids with a moving front. *Physical Review E*, 76(1):016312, 2007.

[88] B. Hu and S.L. Kieweg. The effect of surface tension on the gravity-driven thin film flow of Newtonian and power-law fluids. *Computers & fluids*, 64(15):83–90, 2012.

[89] H.E. Huppert. Flow and instability of a viscous current down a slope. *Nature*, 300(5891):427–429, 1982.

[90] J.A. Moriarty, L.W. Schwartz, and E.O. Tuck. Unsteady spreading of thin liquid films with small surface tension. *Physics of Fluids A: Fluid Dynamics*, 3(5):733–742, 1991.

[91] P.N. Konon, E.I. Mogilevskiy, G.N. Sitsko, and V.Y. Shkadov. Equilibrium of liquid drop on rotating disc. *Moscow University Mechanics Bulletin*, 75:102–109, 2020.

[92] I.S. McKinley and S.K. Wilson. The linear stability of a ridge of fluid subject to a jet of air. *Physics of Fluids*, 13(4):872–883, 2001.

[93] I.S. McKinley. Studies in thin film flows. *PhD Thesis, University of Strathclyde*, 1999.

[94] L.W. Schwartz and R.V. Roy. Theoretical and numerical results for spin coating of viscous liquids. *Physics of Fluids*, 16(3):569–584, 2004.

[95] H.C. Cho, F.C. Chou, M.W Wang, and C.S. Tsai. Effect of Coriolis force on fingering instability and liquid usage reduction. *Japanese Journal of Applied Physics*, 44(4L):L606, 2005.

[96] H.C. Cho and F.C. Chou. Rivulet instability with effect of Coriolis force. *Journal of Mechanics*, 22(3):221–227, 2006.

[97] K. Takamura, H. Fischer, and N.R. Morrow. Physical properties of aqueous glycerol solutions. *Journal of Petroleum Science and Engineering*, 98:50–60, 2012.

[98] A. Volk and C.J. Kähler. Density model for aqueous glycerol solutions. *Experiments in Fluids*, 59(5):A75, 2018.

[99] W. Burger and M.J. Burge. *Digital image processing: an algorithmic introduction using Java*. Springer, 2016.

[100] J. Canny. A computational approach to edge detection. *IEEE Transactions on Pattern Analysis and Machine Intelligence*, PAMI-8(6):679–698, 1986.

[101] L. Ding and A. Goshtasby. On the Canny edge detector. *Pattern Recognition*, 34(3):721–725, 2001.

[102] W. Gao, X. Zhang, L. Yang, and H. Liu. An improved sobel edge detection. In *2010 3rd International conference on computer science and information technology*, volume 5, pages 67–71. IEEE, 2010.

[103] L. Yang, X. Wu, D. Zhao, H. Li, and J. Zhai. An improved Prewitt algorithm for edge detection based on noised image. In *2011 4th International congress on image and signal processing*, volume 3, pages 1197–1200. IEEE, 2011.

[104] L.M. Hocking and M.J. Miksis. Stability of a ridge of fluid. *Journal of Fluid Mechanics*, 247:157–177, 1993.

[105] T.A. Driscoll, N. Hale, and L.N. Trefethen. Chebfun guide, 2014.

[106] J. Kiefer. Sequential minimax search for a maximum. *Proceedings of the American Mathematical Society*, 4(3):502–506, 1953.

[107] V. John. Slip with friction and penetration with resistance boundary conditions for the Navier–Stokes equations - numerical tests and aspects of the implementation. *Journal of Computational and Applied Mathematics*, 147(2):287–300, 2002.

[108] C. Geuzaine and J.F. Remacle. Gmsh: A 3-D finite element mesh generator with built-in pre- and post-processing facilities. *International journal for numerical methods in engineering*, 79(11):1309–1331, 2009.

[109] M.G. Larson and F. Bengzon. *The finite element method : theory, implementation, and applications*. Springer, 2013.

[110] M. S. Alnaes, J. Blechta, J. Hake, A. Johansson, B. Kehlet, C. Richardson A. Logg, J. Ring, M. E. Rognes, and G. N. Wells. The FEniCS project version 1.5. *Archive of Numerical Software*, 2015.

[111] M.S. Alnæs, A. Logg, K.B. Ølgaard, M.E. Rognes, and G.N. Wells. Unified form language: A domain-specific language for weak formulations of partial differential equations. *ACM Transactions on Mathematical Software*, 40(2):1–37, 2014.

[112] C. Taylor and P. Hood. A numerical solution of the Navier-Stokes equations using the finite element technique. *Computers & Fluids*, 1(1):73–100, 1973.

[113] D. Boffi. Three-dimensional finite element methods for the Stokes problem. *SIAM Journal on Numerical Analysis*, 34(2):664–670, 1997.

[114] F. Bowman. *Introduction to Bessel functions*. Dover Publications, New York, 1958.